



**HAL**  
open science

# Customizable latent heat thermal energy storage and transfer system for air-cooling in buildings: design and thermal analysis

Maria de Los Ángeles Ortega del Rosario

## ► To cite this version:

Maria de Los Ángeles Ortega del Rosario. Customizable latent heat thermal energy storage and transfer system for air-cooling in buildings: design and thermal analysis. Mechanics [physics]. Université de Bordeaux, 2018. English. NNT : 2018BORD0197 . tel-01945962

**HAL Id: tel-01945962**

**<https://theses.hal.science/tel-01945962>**

Submitted on 5 Dec 2018

**HAL** is a multi-disciplinary open access archive for the deposit and dissemination of scientific research documents, whether they are published or not. The documents may come from teaching and research institutions in France or abroad, or from public or private research centers.

L'archive ouverte pluridisciplinaire **HAL**, est destinée au dépôt et à la diffusion de documents scientifiques de niveau recherche, publiés ou non, émanant des établissements d'enseignement et de recherche français ou étrangers, des laboratoires publics ou privés.

THÈSE PRÉSENTÉE  
POUR OBTENIR LE GRADE DE  
**DOCTEUR DE**  
**L'UNIVERSITÉ DE BORDEAUX**

ÉCOLE DOCTORALE SCIENCES PHYSIQUES ET DE L'INGENIEUR  
SPÉCIALITÉ : MÉCANIQUE

Par Maria De Los Ángeles ORTEGA DEL ROSARIO

**Système de stockage et transfert d'énergie par chaleur latente  
adaptable au rafraîchissement d'air en bâtiments :**  
**Conception et analyse thermique**

Sous la direction de : Denis BRUNEAU  
co-directeur : Patrick SÉBASTIAN)

Soutenue le 23 octobre 2018

Membres du jury :

M. NADEAU, Jean-Pierre	Professeur Emérite	ENSAM	Président
Mme. MUSSY, Marjorie	Directrice de Recherche	CEREMA Nantes	Rapporteur
M. ZALEWSKI, Laurent	PU	Université d'Artois	Rapporteur
M. BRUNEAU, Denis	Professeur d'ENSA	ENSAP Bordeaux	Examineur
M. RODRIGUEZ, Julio	Professeur	UTP Panamá	Examineur
M. SÉBASTIAN, Patrick	Maître de Conférence	Université de Bordeaux	Examineur
M. JOMAA, Wahbi	PU	Université de Bordeaux	Invité
M. RAJI, Saed	Ingénieur de Recherche	Nobatek-INEF4	Invité
M. BONNAMY, Paul	Ingénieur de Recherche	Nobatek-INEF4	Invité



# **Système de stockage et transfert d'énergie par chaleur latente adaptable au rafraîchissement d'air en bâtiments : Conception et analyse thermique**

**Résumé :** Ces travaux de thèse visent à concevoir et étudier une unité d'échangeur de chaleur air-MCP en tant que solution passive à la problématique du contrôle de confort thermique dans les bâtiments pendant l'été, fournissant des directives de conception et une intégration facile aux bâtiments. Les MCP présentent une grande capacité de stockage par unité de volume, ce qui leur permet de contribuer à la réduction de la consommation d'énergie liée aux applications de rafraîchissement. Bien qu'ils présentent certains inconvénients, en tant que faible conductivité thermique, notamment dans les PCM commerciaux, une conception bien détaillée est nécessaire pour atteindre des performances thermiques adéquates.

La première partie de cette thèse examine les systèmes existants à travers une étude bibliographique, mettant en évidence la relation géométrique avec la physique et la performance thermique. Cette recherche a fourni les bases pour le développement d'une conception d'une unité air-MCP, suivant une méthodologie de résolution de problèmes développée par le laboratoire I2M. Une matrice de mots-clés a été obtenue à partir des phénomènes physiques et de l'analyse fonctionnelle de l'unité. À partir de cette matrice, l'analyse des brevets a inspiré la conception qui a abouti à un échangeur de chaleur air-PCM à faisceau tubulaire avec des tubes verticaux alignés perpendiculairement au flux d'air.

Le développement d'outils de conception et d'intégration dans les bâtiments a été recherché au moyen d'une modélisation permettant de prédire avec précision les performances thermiques du système. Les modèles simplifiés sont préférés pour cette tâche. Néanmoins, ils peuvent sous-estimer les performances réelles si les phénomènes physiques impliqués ne sont pas correctement comptabilisés. Alors, des approches expérimentales locales et globales ont été utilisées pour parvenir à une compréhension de la physique associée aux cycles de charge et de décharge dans l'unité air-MCP. Pour cela, un banc d'essai a été installé, mesurant la température et le débit d'air dans différentes conditions d'entrée, accompagné d'un suivi visuel à travers des images numériques. Les traitements d'images et des données ont été utilisés pour obtenir des indicateurs de performance thermique et des corrélations équivalentes en utilisant des nombres adimensionnels connus pour les mécanismes de transfert de chaleur convectifs-conducteurs dans le PCM.

Ces découvertes ont permis de développer des modèles de résistance thermique et d'enthalpie qui rendent compte de la complexité des phénomènes impliqués dans l'unité pour la prédiction de la performance. Enfin, la performance thermique du système a été testée dans deux applications de bâtiments : en tant qu'unité mobile dans une maison PEH à Gradignan dans un bureau du labo I2M.

**Mots clés :** Matériau à changement de phase, cylindrique, bâtiments, stockage de chaleur, faisceau de tubes, conception





# Customizable latent heat thermal energy storage and transfer system for air-cooling in buildings: design and thermal analysis

**Abstract:** The present work aims to design and study an air-PCM heat exchanger unit as a passive solution for thermal comfort assessment in buildings during summertime, providing tools to ease the design and building integration. The PCM present a large storage capacity per volume unit whereby, they can contribute to the reduction of the energy consumption related to cooling applications. Although, they show some drawbacks, as a low thermal conductivity in commercial PCM, so a well-thought design of these kind of systems is necessary to achieve adequate thermal performances.

The first part of this thesis surveys the existing systems through a literature review, highlighting the geometry relation with the physics and thermal performance. This search provided the bases for the development of an air-PCM unit design, following a problem-solving methodology developed by the I2M laboratory. A keyword matrix was obtained from the physical phenomena and functional analysis of the unit. From this matrix, the patents analysis provided inspiration for the design resulting in a tube bundle air-PCM heat exchanger with vertical tubes aligned perpendicular to the airflow.

The development of design and integration in buildings tools was sought through a modeling that can accurately predict the thermal performance of the system. Simplified models are preferred for this task. Nevertheless, they can under predict the actual performance if the physical phenomena involved is not properly accounted. Then, local and global experimental approaches were used to achieve an understanding of the physics associated with charging and discharging cycles in the unit. For this, a test bench was installed, measuring temperature and airflow under different inlet conditions, accompanied by a visual tracking through digital images. Image and data processing were used to obtain thermal performance indicators and equivalent correlations using known dimensionless numbers for convective-conductive heat transfer mechanisms in the PCM.

These findings allowed the development of thermal models based on energy balances, that accounted the complexity of phenomena involved in the unit for performance prediction. Finally, the thermal performance of the system was tested in two buildings applications: as a mobile unit in a PEH house in Gandingan and as an active façade in a building in Talence.

**Keywords :** Phase change materials, cylindric, buildings, air-PCM heat exchangers, tube-bundle, design

---

**Institut d'Ingénierie et Mécanique de Bordeaux - Département TREFLE**

URM 5295, Esplanade des Arts et Métiers, 33405 TALENCE Cedex, France



# **Sistema de almacenamiento de energía por calor latente adaptable al acondicionamiento de aire en edificios a través de la utilización de materiales de cambio de fase: diseño y análisis térmico**

**Resumen:** El presente trabajo tiene como objetivo diseñar y estudiar una unidad intercambiador de calor aire-PCM como presentan una solución pasiva al confort térmico en edificios durante el verano, proporcionando herramientas para facilitar el diseño y la integración en edificios. Los PCM una gran capacidad de almacenamiento por unidad de volumen, por lo que pueden contribuir a la reducción del consumo de energía relacionado con las aplicaciones de refrigeración. Estos materiales presentan algunos inconvenientes en cual su uso, como una baja conductividad térmica, típica en PCM comerciales, por lo es necesario un diseño que tome en cuenta esta problemática para lograr rendimientos térmicos adecuados.

La primera parte de esta tesis examina los sistemas existentes a través de una revisión de la literatura, destacando la relación de geometría con los fenómenos físicos y el rendimiento térmico. Esta búsqueda proporcionó las bases para el desarrollo de un diseño de unidad aire-PCM, siguiendo una metodología de resolución de problemas desarrollada por el laboratorio I2M. Se obtuvo una matriz de palabras clave a partir de los fenómenos físicos y el análisis funcional de la unidad. A partir de esta matriz, el análisis de patentes proporcionó inspiración para el diseño que dio como resultado un intercambiador de calor PCM de aire y haz de tubos verticales alineados perpendicularmente al flujo de aire.

El desarrollo del diseño y la integración en herramientas de edificios se buscó a través de un modelo que pudiese predecir con precisión el rendimiento térmico del sistema. Los modelos simplificados son los preferidos para esta tarea. Sin embargo, su poder de predicción puede verse afectada si los fenómenos físicos involucrados no se contabilizan adecuadamente. Es por ello que se utilizaron enfoques experimentales locales y globales para lograr una comprensión de la física asociada con los ciclos de carga y descarga en la unidad. Se realizó una instalación de un banco de pruebas, que permitió mediciones de temperatura y flujo de aire en diferentes condiciones de entrada, acompañado de un seguimiento visual a través de imágenes digitales. El procesamiento de imágenes y datos se utilizó para obtener indicadores de rendimiento térmico y correlaciones a partir de números adimensionales relacionados con mecanismos de transferencia de calor por convección y conducción en el PCM.

Estos hallazgos permitieron el desarrollo de modelos térmicos para la predicción del rendimiento, basados en balances de energía de cada volumen de control. Finalmente, el rendimiento térmico del sistema se probó en dos aplicaciones de edificios: como una unidad móvil en una casa PEH en Gradignan y dentro de una oficina del laboratorio I2M.

**Palabras clave:** Materiales de cambio de fase, cilindros, edificios, intercambiador de calor aire-PCM, haz de tubos, diseño



This thesis has been prepared at

**Institut d'Ingénierie et Mécanique de Bordeaux - Département TREFLE**

ENSAM

Esplanade des Arts et Métiers

33405 TALENCE Cedex

France

☎ (33)(0)05 56 84 54 19

Web Site <https://i2m.u-bordeaux.fr/>





*Je dédie ce travail  
à tous ceux qui le méritent*





# Remerciements

Je tiens d'abord à remercier à mon bien-aimé directeur de Thèse, M. Denis Bruneau, pour avoir fait confiance à mon potentiel pour mener à bien ce travail et tout le temps dédié à m'encadrer. C'est grâce à vous que j'ai eu l'opportunité de venir ici en France, et ça va rester comme un point très important dans ma vie. À mon bien-coaimé codirecteur de thèse. M Patrick Sébastian, pour tous les échanges toujours plein de nouvelles connaissances pour moi. Sachez que j'ai beaucoup appris de vous, en tant qu'étudiant, comme dans mon travail de thèse. Je tiens vraiment à vous remercier pour la liberté que vous deux m'avez laissée pour mener à bien ce travail, mais en même temps, que vous étiez toujours là quand j'avais besoin d'aide.

Je tiens également à remercier à mon jury de thèse. À mes rapporteurs Mme. Marjorie Musy et M. Laurent Zalewski, pour avoir pris le temps de lire et jugé cette thèse. J'ai bien apprécié la clarté et pertinence de toutes vos remarques, dans le rapport comme dans la soutenance, qui vont sûrement m'aider dans la suite.

Je tiens à remercier au directeur du labo, M. Jean-Christophe Batsale, pour m'avoir accueilli au sein de l'I2M, et d'être là si on avait des questions, même si vous avez trop de choses à faire. À M. Jean-Pierre Nadeau, de qui j'ai non seulement appris une nouvelle façon de penser aux problèmes d'ingénierie, mais aussi dans différentes situations de la vie. Merci aussi d'avoir présidé mon jury de thèse. À M. Julio Rodríguez, pour m'encadrer en Panama, m'encourager venir faire une thèse, et venir aussi à la juger, Je suis sûre qu'on continuera quand j'arrive au Panama.

À M. Wahbi Jomaa, pour le soutien et pour nous avoir donné la permission de venir tous les week-ends. Merci aussi de faire parti de mon jury. Du côté Nobatek, je remercie à Paul Bonammy, pour m'avoir patiemment enseigné l'utilisation des instruments (et d'avoir eu à le faire en anglais, car je ne parlait pas français, tout au début). Ton aide au début de ma thèse a été fondamentale pour le développement expérimental de cette thèse. J'ai bien apprécié ta présence dans mon jury. À Saed Raji, merci pour les échanges et pour faire partie de mon jury. À Isabelle Iratchet et Jérôme Lopez, pour le soutien administratif quand a été nécessaire.

Du côté labo, je remercie d'abord à Muriel ; on ne pourrait pas arriver sans vous à nous en sortir. Aussi à Audrey et Cyril pour le support technique. Bien sûr, je tiens à remercier sincèrement les doctorants avec qui j'ai partagé ces quatre années, depuis mon arrivée au labo pendant mon stage de master : Antonio, Tom, Xavier, Ulises, Yousseff, Mehdi, Meherez, Antone, Stéphanie, Ludovic, Tan, Térrence, Mohamed, Charlotte, Zakaria, Bauka, Clément, Sébastian, Romain, Sarah, Sagen, Grace, Stéphane, Cécile, Jorge, Vincent, Thomas, Dung ... Du côté GRECCAU, à Aline, Catherine, Abdulaziz, Assia, Ferrán...

Je voudrais particulièrement remercier ceux avec qui j'ai partagé plus de temps : Maimouna, merci pour toutes tes histoires et la patience. Je pense que c'est grâce à toi que j'ai énormément appris le français. Jeremy, merci pour tout le temps partagé (montagne et escalade) et pour avoir essayé de sauver mon ordi (R.I.P), également à Hugo et les vacances d'hiver. José, venga hombre, créeme que las idas al laboratorio los findes se hicieron menos pesadas con los cuentos

que siempre tenías. Talking about weekends, I want to thank Yibiao for the time shared and for listening to my speech, that was really nice to meet you. Yingying, with whom I shared office. Thanks for the dumplings :).

J'aimerais aussi remercier les permanents : Azita, Jean-Rodolphe, Didier, Henri, Valat, Jean-François Bonnet, . . . . Aussi au team EBS : Tingting, Laurent, Alain Sempey, à Alain Sommier pour l'assistance avec la calibration.

D'ailleurs j'aimerais remercier Mme. Valérie Pernot pour tout le soutien et l'assistance des mon arrivé ici à Bordeaux. Pour l'aide technique à M. J-M. George, Alain Oschsenoffer, et très particulièrement à Sam, avec qui j'ai partagé salle de Manip. A mis amigos en Panamá, a todos los miembros de la TUNA, a Oscar, Marcus, Moi, Roberto, Antonio, Daniel (aunque estés en Paris). Ustedes han sido un soporte fundamental durante mi tiempo aquí, los sentí muy cerca, aun cuando estuviésemos a más de 8 000 km de distancia.

A Luis, Ana Emilia y a Manuel, quiero agradecerles particularmente por escucharme en los momentos más difíciles. A Shannon, mi amiga en Bordeaux, gracias por el apoyo, por ser siempre tan cheerleader conmigo y darme ánimos en todo momento, sobre todo justo antes de mi sustentación, nunca olvidaré eso. A Vicky, por tratar de siempre estar allí, de que no olvidara que todavía soy joven y de estar siempre disponible cuando iba de vacaciones a Panamá, eres la mejor. A mi familia en Europa con quien emprendí también esta aventura: a Ezequiel, siento que nuestra amistad creció de un modo que no hubiese imaginado antes en este tiempo que estuvimos por acá, y a Lian, por supuesto, no tengo palabras para escribir lo que significó tu apoyo durante este tiempo, sobre todo en los momentos más oscuros (añadir a esta línea lágrimas).

A Miguel .

Por último quiero agradecer a mi familia. Mami, siempre te has sacrificado por mí y durante esta aventura, no ha sido la excepción. Eres la mejor mami del mundo. Papi, gracias por todo, sé lo difícil que ha sido esto también para ti, todo el sacrificio y lo mucho que nos hemos extrañado, también eres el mejor. Los amo. A mis abuelitos que siempre oraron por mí y sé lo mucho que ha significado para ustedes: Alfonsa, Eladio, Bienve y Doro. Siento mucho todo este tiempo que hemos sacrificado juntos. A mis tíos y amigos, por siempre estar pendiente. A los que perdí durante este tiempo (Rooney y Giamby) y con quienes no he podido estar (Fulita, Niño, Morris, Manchis, Fourier y Kepler). Y a Mininin, por algo siempre has viajado conmigo.

Cette page a été la dernière page rédigée sur ce mémoire, mais peut-être, l'une des plus difficiles car ils sont plus de quatre ans, de souvenirs et des personnes, au-delà de ceux que j'ai mentionné. Enfin à vous tous un grand merci.





# Contents

<b>Abstract</b>	<b>vii</b>
<b>Remerciements</b>	<b>xiii</b>
<b>Contents</b>	<b>xvii</b>
<b>Résumé détaillé de la thèse</b>	<b>xxiii</b>
<b>Nomenclature</b>	<b>1</b>
<b>Introduction</b>	<b>7</b>
Current Problematic: Global outlook . . . . .	7
Phase change materials for cooling and heating applications . . . . .	8
PCM systems for building applications developed by I2M of Bordeaux . . . . .	9
Box shape tube bundle: <i>Napevomo house</i> . . . . .	9
Slabs PCM system: <i>Sumbiosi house</i> . . . . .	11
Further Research . . . . .	12
Departure point for the present work . . . . .	13
Problem statement . . . . .	13
Thesis Objectives . . . . .	14
Thesis Structure and Methodology . . . . .	14
Methodology . . . . .	14
<b>1 Theoretical background and literature review</b>	<b>17</b>
1.1 Scope . . . . .	17
1.2 Phase Change Materials . . . . .	18
1.2.1 Organic materials . . . . .	18
1.2.2 Inorganic materials . . . . .	20
1.2.3 Eutectic materials . . . . .	20
1.3 Encapsulation of phase change materials . . . . .	21

1.4	Physical phenomena during phase change . . . . .	23
1.4.1	Dimensionless numbers associated with phase change . . . . .	25
1.4.2	Experimental Approaches . . . . .	26
	Melting in rectangular vessels . . . . .	27
	Melting in spherical capsules . . . . .	28
	Melting in cylindrical vessels . . . . .	28
1.4.3	Numerical Approaches . . . . .	29
1.4.4	Empirical correlations for conduction and convection during phase change . . . . .	31
1.4.5	Visual tracking of the melting front . . . . .	34
1.5	Basic concepts in Image Processing . . . . .	36
1.6	Concluding Remarks . . . . .	39
<b>2</b>	<b>Air-PCM heat transfer unit definition</b>	<b>43</b>
2.1	Scope . . . . .	43
2.2	Design of an air-PCM heat exchanger unit . . . . .	44
2.2.1	Methodology for the design of an air-PCM unit . . . . .	44
2.2.2	System Overview . . . . .	45
2.2.3	Physical phenomena involved in phase change applications for cooling and heating . . . . .	46
	Global Phenomena . . . . .	46
	Local Phenomena . . . . .	47
2.2.4	General Analysis . . . . .	48
	Operational Architecture (Structural Analysis) . . . . .	48
2.2.5	Functional Analysis . . . . .	49
2.2.6	Keywords search and analysis . . . . .	51
	Matrix Description . . . . .	51
	Matrix Analysis . . . . .	52
	Selection of the line of evolution . . . . .	55
2.3	Concluding remarks and perspectives . . . . .	59
<b>3</b>	<b>Experimental Approaches</b>	<b>61</b>
3.1	Scope . . . . .	61
3.2	Experimental setup and procedures . . . . .	62
3.2.1	Design of the experiment . . . . .	62
3.2.2	Experimental setup . . . . .	64
	Experimental Apparatus . . . . .	64
	Air-PCM heat exchanger . . . . .	66

	PCM selection . . . . .	67
	Metrology of the experimental setup . . . . .	68
3.2.3	Experimental Procedure . . . . .	71
	Airflow rate measurements . . . . .	71
	Temperature measurements . . . . .	75
	Testing protocol . . . . .	75
3.3	Experimental results and discussion . . . . .	76
3.3.1	Melting cycle results . . . . .	77
	Temperature measurements: . . . . .	77
	Image Analysis . . . . .	78
3.3.2	Solidification cycle results: . . . . .	86
	Temperature measurements . . . . .	86
	Image Analysis . . . . .	86
3.4	Thermal performance of the unit . . . . .	93
3.4.1	Data processing for thermal performance evaluation . . . . .	93
	Global Domain . . . . .	93
	Local Domain . . . . .	94
3.4.2	Results and Analysis of the thermal performance evaluation . . . . .	98
	Global Domain . . . . .	98
	Local Domain . . . . .	102
3.5	Physical phenomena identification . . . . .	111
3.5.1	Physical phenomena related to phase change . . . . .	111
3.5.2	Dimensionless numbers associated with an air-PCM heat exchanger . . . . .	112
3.5.3	Results from the phenomena identification by dimensionless numbers . . . . .	113
3.6	Concluding remarks . . . . .	113
<b>4</b>	<b>Modeling of a tube bundle type air-PCM unit</b> . . . . .	<b>115</b>
4.1	Scope . . . . .	115
4.2	Experimental Correlations . . . . .	116
4.2.1	Previous analysis before obtaining the correlations . . . . .	116
4.2.2	Statistical tests to validate the multiple linear regression . . . . .	117
4.2.3	Results from the correlations for the melting fraction . . . . .	118
4.3	Thermal resistance model . . . . .	121
4.3.1	Problem statement for the model . . . . .	121
4.3.2	Resolution methodology . . . . .	121
4.3.3	Assumptions . . . . .	122
4.3.4	Mathematical formulation . . . . .	123



Air sub-domain: . . . . .	123
Wall sub-domain: . . . . .	123
PCM sub-domain: . . . . .	124
4.3.5 Initial and boundary conditions . . . . .	124
4.3.6 Numerical Resolution . . . . .	125
4.3.7 Validation of the model . . . . .	127
Validations from the First tube . . . . .	129
Results from the eighth tube . . . . .	130
Global validation of the heat exchanger . . . . .	133
4.4 Non-isothermal phase change with natural convection model . . . . .	135
4.4.1 Main assumptions for the model . . . . .	135
4.4.2 Energy conservation in the air . . . . .	136
4.4.3 Energy conservation in the wall and PCM . . . . .	136
4.4.4 Supplementary assumptions . . . . .	136
4.5 Concluding remarks . . . . .	137
<b>5 Building Applications</b>	<b>139</b>
5.1 Scope . . . . .	139
5.2 Mobile air-PCM unit . . . . .	140
5.2.1 PCM containers . . . . .	141
Filling of the tubes with RT21 . . . . .	141
Filling the tubes with SP25E . . . . .	142
5.2.2 Unit Structure . . . . .	142
5.2.3 Experimental setup and Procedure . . . . .	143
5.2.4 Results under controlled conditions : Office room at I2M laboratory . . . . .	146
Results and analysis . . . . .	146
5.2.5 Results under real conditions : Sumbiosi PEH . . . . .	150
Platform overview . . . . .	150
Metrology of the platform . . . . .	151
Results and analysis . . . . .	152
5.3 Concluding Remarks . . . . .	155
<b>General Conclusions</b>	<b>157</b>
Limitation of the Research . . . . .	158
Regarding the design . . . . .	158
Regarding the experimental approaches . . . . .	158
Regarding the modeling approaches . . . . .	159

Regarding the building application . . . . .	159
Perspectives and future research . . . . .	159
Regarding the design . . . . .	159
Regarding the experimental approaches . . . . .	159
Regarding the modeling approaches . . . . .	160
Regarding the building application . . . . .	160
<b>Bibliography</b>	<b>161</b>
<b>List of Tables</b>	<b>173</b>
<b>List of Figures</b>	<b>175</b>
<b>A Calibration</b>	<b>185</b>
A.1 Temperature calibrations . . . . .	185
A.2 Velocity and airflow calibrations . . . . .	185
<b>B Modeling Results</b>	<b>189</b>
B.1 Melting correlations results . . . . .	189
B.2 1-D thermal resistance modeling results . . . . .	189
<b>C Pure conduction enthalpy method modeling</b>	<b>195</b>
C.1 Enthalpy method modeling . . . . .	195
C.1.1 Mathematical formulation . . . . .	195
C.1.2 Numerical Solution . . . . .	196
Melting fraction update . . . . .	197
Discretization in each finite-volume : Temperature field . . . . .	198
Discretization in each finite-volume : melting fraction field . . . . .	200
C.1.3 Conductivity value . . . . .	200
<b>D Mobile air-PCM unit</b>	<b>201</b>
D.1 Selection of the PET tubes . . . . .	201
D.1.1 Partnership for manufacturing . . . . .	202
D.1.2 Short-term reliability test . . . . .	202
D.2 Air-PCM unit Plans . . . . .	203
D.3 Visual tracking of phase change for the air-PCM unit . . . . .	205
D.3.1 Solidification cycle . . . . .	205
D.3.2 Melting cycle . . . . .	209

**Index**

**215**

**Contents**

**217**

# Résumé détaillé de la thèse

## Introduction

Le secteur résidentiel et du bâtiment est un acteur important de la consommation énergétique actuelle, qu'en 2015 encore, il représentait environ 22% de la consommation totale d'énergie. Associés à cette consommation il y a une production des gaz à effet de serre que représente environ d'un 17% de la production mondiale de CO<sub>2</sub> [6]. Alors, plusieurs solutions pour l'amélioration des technologies liées à ces secteurs sont objet de recherche aujourd'hui, l'un entre eux, les matériaux à changement de phase ou MCP.

L'intérêt de l'utilisation des MCP en bâtiments, c'est parce qu'ils permettent de stocker une grande quantité d'énergie en petits volumes à une température d'opération presque constante. Donc, leur utilisation en bâtiment peut amener à une réduction de la consommation d'énergie électrique du même qu'une diminution des émissions des gaz à effet de serre.

Il existe une grande variété de ces matériaux, où la température de changement de phase choisie est dépendante de l'application, et pour le cas des applications en bâtiment cette température est liée aux conditions de confort dans l'endroit de l'application. On peut classer les MCP en matériaux organiques, inorganiques et eutectiques [97]. De façon générale, un matériau peut être considéré comme MCP s'il répond à certains critères comme [121] : une grande capacité de stockage par chaleur latente, des changements de volume petits, qu'il a une stabilité chimique, qu'il ne soit pas corrosif, non-toxique, ininflammable et non-explosif.

Outre la nature du MCP, pour ce type d'applications, il faut aussi considérer l'encapsulation du MCP. Comme le MCP suivre un changement d'un état solide à un état liquide, il a besoin d'un contenant qui empêche les fuites de liquide. En plus, l'encapsulation maintient le MCP isolé des environnements environnants, garantissant ainsi une composition correcte du MCP, qui aurait autrement changé en raison du mélange avec le fluide externe. La sélection peut se faire autour de sa taille, du matériau de cette encapsulation ou de la géométrie sélectionnée. Cette sélection joue un rôle très important sur la performance finale du système avec du MCP.

Aujourd'hui il existe plusieurs formes d'intégrer les MCP aux bâtiments. Par exemple, le MCP peut être mélangé avec les matériaux de construction, où le MCP est normalement sous une forme liquide, de poudre ou microencapsulé. Dans des autres applications, le MCP se présente de façon encapsulée à l'intérieur du bâtiment, généralement dans des parois, fenêtres, toitures et planchers.

Ils peuvent se présenter aussi en applications où le MCP est encapsulé dans un système échangeur-stockeur. Ce dernier est suivant utilisé pour des applications de confort de l'air pendant l'été qui est aussi généralement couplé avec des stratégies de ventilation naturelle nocturne dans le bâtiment.

À partir des travaux menés par le laboratoire liés à l'utilisation des systèmes actif air-MCP pour le rafraîchissement d'air en bâtiment, notamment avec un système intégré à la maison

Napevomo, pour le concours Solar Decathlon en 2010, avec une géométrie de faisceau de tubes carrés [86], et puis avec la maison Sumbiosi en 2012, avec une système à plaques parallèles [87] ; il a été remarqué la suite de la recherche liée à ces systèmes : dans une coté une évolution de la géométrie vers une adéquation entre performance et intégrabilité au bâtiment, et de l'autre côté, le développement d'outils d'aide à la conception et au dimensionnement. Ces besoins de recherche nous donnent à nous le cadre de ces travaux de thèse.

Dans ces travaux, la sélection de la géométrie est menée à partir d'une méthodologie de conception qui cherche une adaptation aux bâtiments en termes de distribution spatiale et performance. Les outils d'intégration et dimensionnement se feront à partir d'une modélisation qui aide à prédire la performance globale du système à partir de paramètres procédés et de géométrie.

Pour que la modélisation reste assez simplifiée et adaptée aux outils métiers, il faudra une recherche de phénomènes physiques, de sorte que cette modélisation peut prendre en compte l'ensemble de phénomènes associés au changement de phase, notamment les effets de la convection naturelle dans le MCP sur la performance du système. Ces démarches nous donnent finalement les objectifs du travail de thèse :

- Identifier et décrire les phénomènes physiques liés au fonctionnement d'un échangeur de chaleur air-PCM dans les domaines local et global.
- Développer des modèles phénoménologiques et de performance basée sur des indicateurs clé.
- Concevoir, construire et tester la faisabilité et les performances d'un système air-PCM.

## **Chapitre 1 : *Contexte théorique et littérature***

Le premier chapitre de cette thèse appelé « *Theoretical background and literature review* » est consacré à une recherche bibliographique et des concepts clés pour la compréhension de ces types de systèmes. Ici, nous présentons des études faites pour la compréhension des phénomènes physiques associés au changement de phase, y compris les différents types d'approches : analytique, expérimental et numérique. La recherche de la littérature nous amène à voir les difficultés de développer des études sur ces types de systèmes généralement associés à [85] :

1. La non-linéarité du problème résultant du mouvement de l'interface solide-liquide lors du changement de phase.
2. Connaissance insuffisante du processus de transfert de chaleur à l'interface solide-liquide, en raison de la convection naturelle dans le MCP liquide.
3. Incertitude de la résistance thermique de l'interface entre le conteneur et le PCM solide.
4. Changement de volume avec le changement de phase.
5. La présence de vides dans le PCM solide.

Finalement cette recherche nous amène à choisir certains points de départ dans le développement de cette thèse, comme les bases pour la sélection de la géométrie du système et la forme d'évaluer l'expérimentation et modélisation, qui seront approfondies au cours des chapitres suivants.

## Chapitre 2 : Définition de l'échangeur de chaleur air-PCM

Le deuxième chapitre « *Air-PCM heat transfer unit definition* » est dédié à la sélection d'une géométrie adaptée aux applications en bâtiments. La méthodologie suivie ici, est issue d'un ensemble de trois analyses : une analyse architecturale, une analyse fonctionnelle et une analyse de phénomènes physiques. Le système à concevoir s'agit d'un échangeur-stockeur air-MCP qui a comme but général le rafraîchissement de l'air à l'intérieur d'un bâtiment, pendant la journée durant la période estivale. Suite à cette utilisation, les MCP sont devenus dans un état liquide, alors pendant la nuit, le système doit régénérer ces MCP pour une nouvelle utilisation. Le système doit aussi fonctionner avec le minimum possible de pertes. Le choix de géométrie doit être largement adaptable aux bâtiments, avec la possibilité d'un choix de MCP commerciales, comme moyen de stockage.

### Analyse architecturale

De cette analyse ils sont sortis les trois parties principales de notre système :

1. L'entrée d'air, qui est liée aux conditions instantanées du bâtiment, c'est-à-dire, la température d'air intérieur  $T_{in}$  et la vitesse d'air à l'entrée  $v_{air}$ .
2. L'échangeur air-MCP où il aura lieu les échanges entre l'air et les MCP à travers d'une surface d'échange  $A$ .
3. La sortie d'air ou climatisation, qui va assurer le confort thermique indépendamment des facteurs environnementaux.

### Analyse Fonctionnelle

L'analyse fonctionnelle décrit les différentes situations de vie de notre système, avec leurs fonctions et restrictions. Du système à concevoir, la fonction de service est le rafraîchissement d'air pendant l'été. Dans la figure [r.i](#), on présente les situations de vie associées au fonctionnement actif du système.

L'étude de ces deux analyses ensemble nous donne les objectifs généraux de notre système :

1. Stocker l'énergie
2. Transférer la chaleur

### Analyse de phénomènes physiques

Les phénomènes physiques liés à ce type de systèmes sont dépendants de la sélection de la géométrie du contenant de MCP. Alors ici, on présente une approche générale de ces phénomènes, qu'on peut observer dans la figure suivante. Si on schématise le système avec les parties décrites dans l'analyse architecturale, et on fractionne les MCP dans des contenants de formes inconnues (qu'on représente ici en forme carrée), on peut voir qu'à l'intérieur de ce système, il aura des phénomènes qui ont un impact global, comme celles associées aux échanges entre l'air et les contenants avec du MCP, et aussi bien qu'il y aura des phénomènes qui sont directement liés à l'interne du contenant. Ceci nous amène à diviser l'étude de phénomènes en deux domaines : global et local.



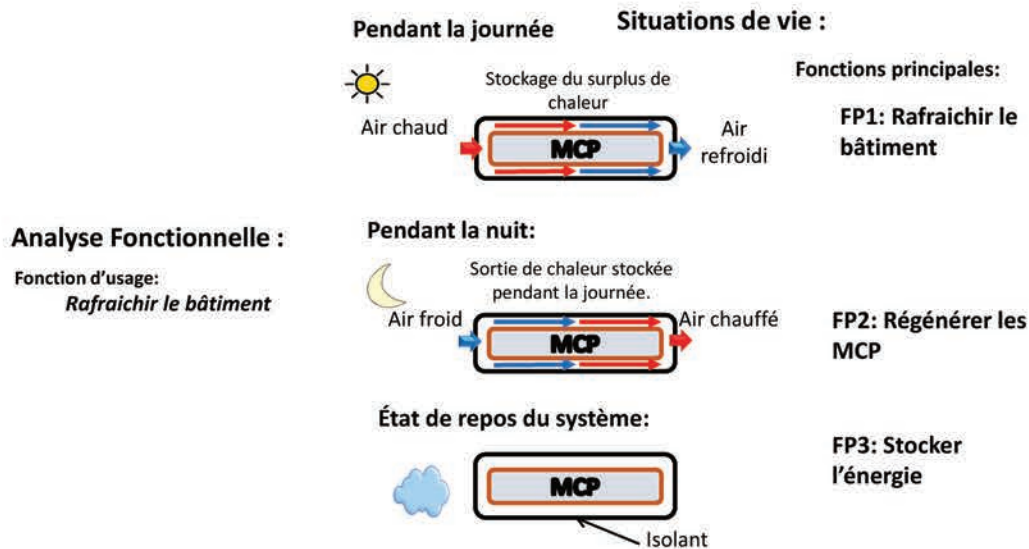


Figure r.i – Analyse fonctionnelle du système.

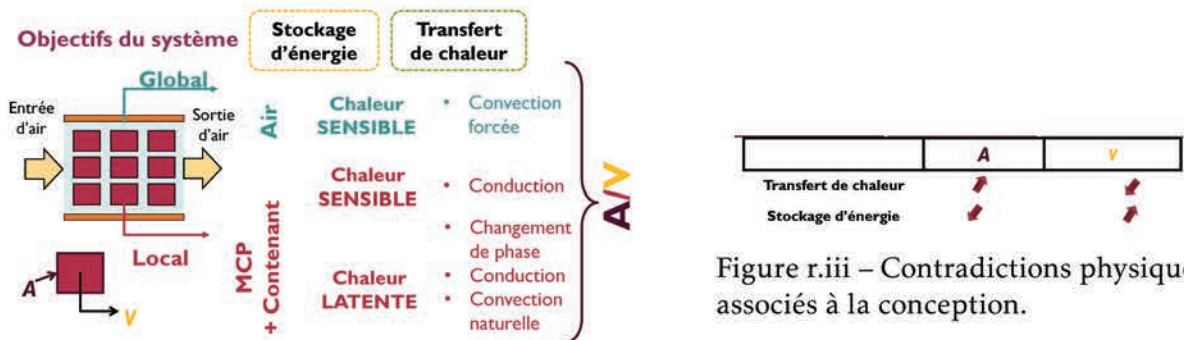


Figure r.ii – Analyse des phénomènes physiques en deux domaines : global et local.

Alors, dans cette partie, l'étude est consacrée à la recherche d'une géométrie adaptable aux objectifs préalablement définis. Alors, une analyse des lois physiques associées à ces phénomènes comme celles décrites dans la recherche de la littérature, nous donne le rapport entre la surface d'échange et le volume du contenant ( $A/V$ ), comme paramètres pertinents à la sélection de la géométrie à partir des notions de la performance globale du système.

Pour avancer vers la sélection de la géométrie finale ce deux paramètres ont été associés aux objectifs du système. Cette association se présente dans la figure r.iii. Si on observe, dans un côté le transfert de chaleur croît avec la surface d'échange et décroît avec l'augmentation du volume, de l'autre une surface d'échange importante va diminuer la capacité de stockage du l'augmentation de pertes de chaleur à travers de cette surface. Cette petite analyse nous amène à une contradiction physique à l'heure de choisir la géométrie.

Il existe plusieurs manières de surmonter ces contradictions dans le domaine de conception. Ici, on a choisi de s'aider avec une méthode développée il y a quelques années par le labo I2M, lié à la recherche de brevets comme source d'inspiration pour la résolution de problèmes en ingénierie. Cette méthode s'agit d'un outil qu'à partir d'une base de mot clés initiale, va générer une base de données complète, qui nous donnera des idées pour la résolution de la

problématique de choix de géométrie.

Finalement, un arbitrage a été fait qui a donné comme résultat la sélection d'une géométrie en faisceau de tubes cylindriques verticaux, distribués soit en quinconces ou soit en ligne, qui à son tour peut être dans une position fixe ou mobile sur son propre axe axial.

### Chapitre 3 : *Approches Experimentales*

Dans le chapitre trois appelé « *Experimental Approaches* » il est présenté l'expérimentation menée dans un banc d'essai composé d'un prototype d'échangeur air-MCP avec un faisceau de 99 tubes en verre remplis de MCP, alignés de forme parallèle. Ce banc a répondu à un besoin de reproduire les conditions réelles d'un système, air-MCP à l'intérieur d'un bâtiment.

L'étude expérimentale a été menée dans deux domaines : globale et locale. Les objectifs de cette étude sont de déterminer les paramètres procédés pour la modélisation (domaine global) et de mettre en évidence les phénomènes liés au changement de phase (domaines global et local). Donc, ce banc d'essai a permis trois types de mesures : température, vitesse et images numériques (photographies).

L'instrumentation pour les mesures de températures a été faite avec des thermocouples type K, calibrés avec un banc thermostaté au laboratoire. Six tubes ont été instrumentés permettant de mesurer la température axiale du MCP, de la paroi en verre à l'intérieur et l'extérieur ainsi que la température de l'air dans un point autour du tube. Une cartographie de 25 points a été faite pour avoir un profil de la vitesse de l'air à l'entrée avec un anémomètre à fil chaud Kimo®. Des mesures de débit ont été faites à la sortie du banc d'essai avec un anémomètre à hélice Kimo®.

Les données ont été analysées en deux étapes : une analyse des données brutes, c'est-à-dire, les mesures directes des capteurs et de photographies, qui nous donne une interprétation primaire des phénomènes, et une analyse à partir des résultats du traitement de données, avec de paramètres choisis comme indicateurs de la performance du système dans les deux domaines d'étude.

À partir de ces premiers résultats, nous avons constaté que, bien que les mesures de température globale nous permettent d'observer le comportement global du système, elles sont insuffisantes pour prédire l'état actuel du MCP. C'est là que les mesures locales interviennent, ce qui donne une notion plus détaillée des différentes étapes du changement de phase dans les MCP. Les images sont venues compléter l'analyse primaire des phénomènes.

D'ici, on constate que la fusion suit différents régimes qui donnent comme résultat différents les formes du MCP solide tout au long du cycle, et que pourtant définir de façon simple la position de l'interface entre la partie solide et liquide par des méthodes simplifiées peut être une tâche compliquée. Cependant, à partir de cette analyse, il reste des questions concernant la phénoménologie, telle que le moment du début du changement de phase et la quantification des effets de conduction et de convection pendant le cycle.

Ensuite, l'analyse de la performance du système est faite à l'aide des paramètres indicateurs qui sont proposés à l'échelle globale, à savoir : la puissance de rafraîchissement  $P_{cool}$ , et la durée de fonctionnement et  $\Delta t_{op}$  ; puis à l'échelle locale : la fraction de masse liquide dans le système. Les paramètres globaux du système sont trouvés à partir des mesures de température et de vitesse, tandis les paramètres locaux sont trouvés aussi à l'aide des photographies prises.

La sélection de  $T_{in}$  et  $v_{air}$  comme paramètres procédés amène à une mesure de la performance de notre système. Alors, la performance globale résulte d'un compromis entre  $P_{cool}$  et  $\Delta t_{op}$ . La



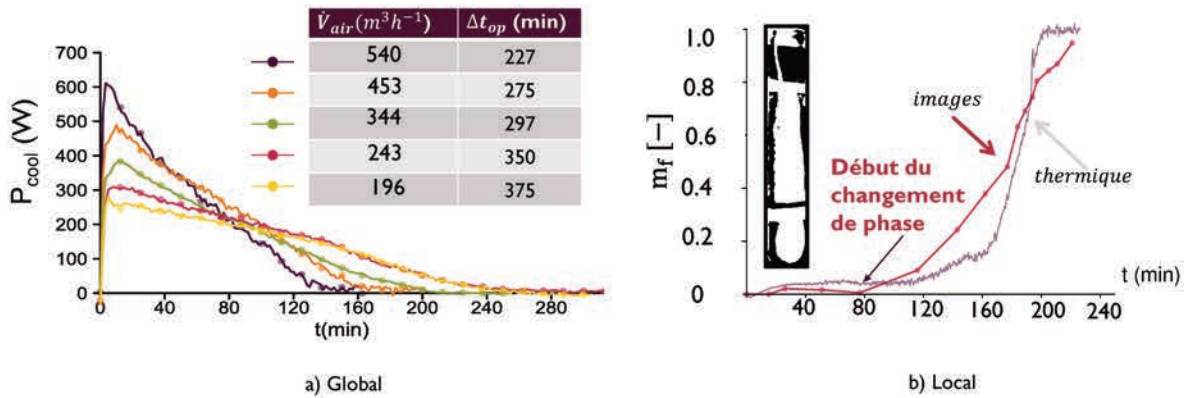


Figure r.iv – Synthèse de résultats des expériences a l'échelle a) Globale et b) Locale.

fraction liquide  $m_f$  est trouvée par trois méthodes : par bilan thermique, par bilan thermique avec une approche de front de fusion unidirectionnelle dans le sens radial, et par traitement des images. Ce traitement est fait à partir de la méthode de binarisation seuillage du tube qu'ont été aussi instrumenté. A la fin ces trois méthodes sont comparées, ce qui nous a permis d'identifier le temps de début de changement de phase.

Finalement, ce chapitre s'achève par l'étude de nombres adimensionnels tels que Stefan  $Ste$ , Fourier  $Fo$ , Biot  $Bi$  et Rayleigh  $Ra$ ; cela a permis la quantification de certains phénomènes tels que le sens de la conduction dans la paroi du tube et la présence d'une convection naturelle importante dans le MCP liquide.

En synthèse, les phénomènes plus importants à considérer sont : la convection forcée entre l'air et les tubes, la conduction radiale à travers de la paroi des tubes, et les effets de convection naturelle dans le MCP liquide à l'échelle locale.

## Chapitre 4 : Modélisation d'un type d'échangeur air-MCP composé d'un faisceau de tubes cylindriques

Le quatrième chapitre « *Modeling of a tube bundle type air-PCM* » décrit la mise en modèle du système étudié.

Dans la première partie de ce chapitre, une modélisation empirique a l'échelle locale est présentée à travers d'une notion des corrélations qui sont recherchés entre les nombres de Rayleigh, Fourier et Stefan et la fraction de MCP liquide. Ces relations sont aussi étudiées de manière statistique à travers de différents tests de validité statistique.

Une seconde méthode de modélisation est proposée afin de prédire le comportement global du système. Ce *modèle de dimensionnement* cherche à prédire la performance du système à travers des indicateurs vus dans la partie expérimentale, à savoir :  $P_{cool}$  et  $\Delta t_{op}$  à partir des paramètres procédés  $T_{in}$  et  $v_{air}$ , paramètres géométriques et propriétés du MCP.

L'unité la plus petite qui décrit les échanges entre l'air et le contenant, c'est un tube avec 3 volumes de contrôle : l'air, la paroi et le MCP. Si on suppose des échanges 1-D radiale conductive, avec une température de MCP constante, et qu'on néglige le stockage par énergie sensible, on peut exprimer les bilans énergétiques de chacun de ces volumes. Dans l'air, ce bilan est donné en termes de la convection entre l'air et la paroi. Ce flux convectif, peut exprimer la chaleur



entrant dans les tubes, par de notions de résistances thermiques. Cette chaleur vient à la fois être responsable du passage de MCP de la phase solide à la phase liquide, et pourtant peut nous donner la position de l'interface solide-liquide.

Alors cette modélisation locale peut exprimer le comportement global si on fait l'hypothèse que le transfert entre les tubes d'une même ligne est négligeable. Dans ce cas, avec la résolution d'un tube, on peut avoir la résolution de toute la ligne en multipliant par le nombre de tubes de cette ligne. Comme cet échangeur est disposé de tel façon que l'état du système à la sortie d'une ligne est l'état d'entrée de la ligne suivante, on peut aussi de cette manier arriver à prédire le comportement de la première ligne à la dernière, et pourtant le comportement global de tout le système.

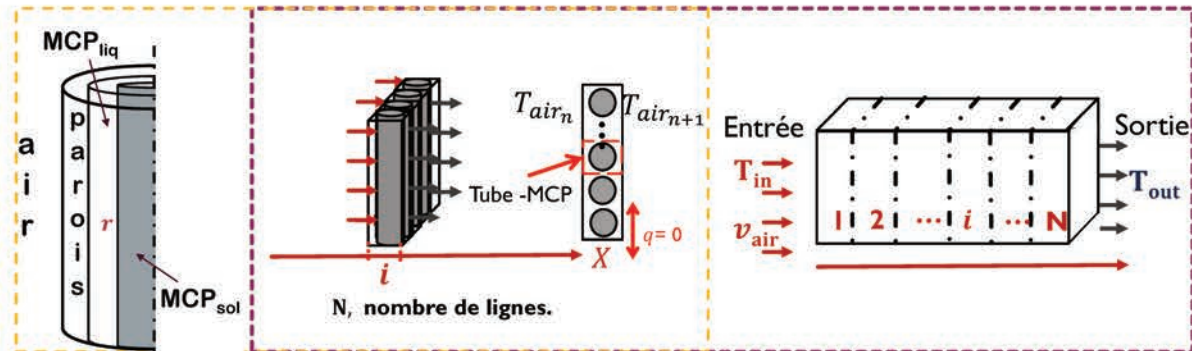


Figure r.v – Synthèse de résultats des expériences à l'échelle a) Globale et b) Locale.

La modélisation a été testée pendant le changement de phase et comparée avec des expériences de fusion menées dans le laboratoire. Ici, on voit de ces résultats, que le modèle ne prévoit bien la diminution de rayon, qu'en la réalité varie de façon compliquée, alors il ne peut pas être précis, du le fait qu'il ne prend pas en compte des effets d'hétérogénéité et phénomènes complexes. Cependant, on voit que la modélisation, respecte le bilan énergétique globale, et alors il arrive à une prédiction correcte de la durée de fonctionnement.

Alors si on compare les résultats de la modélisation avec les mesures de température à l'entrée et la sortie on voit une prédiction satisfaisante en termes de température ( $RMSE = 0,31^{\circ}C$ ), ce qui conduit également à une prédiction satisfaisante de la puissance de rafraîchissement. Néanmoins les problèmes de prédiction locale, cette modélisation qui a comme but l'intégration dans un outil d'aide à l'intégration en bâtiment et de dimensionnement des échangeurs, présente des résultats satisfaisants en ce qui concerne la prédiction du comportement global du système sous des indicateurs de durée de fonctionnement et de puissance de refroidissement. Le modèle présenté ici reste avec une notion très simplifié, bien adaptée aux outils métiers, et avec une prédiction globale satisfaisante.

Étant donné que cette modélisation s'avère insuffisante en termes de compréhension une troisième modélisation est proposée à la fin de ce chapitre comme perspectif. Ce modèle de compréhension cherche à intégrer les corrélations précédemment établies pour la fraction liquide dans une modélisation qui suivre le même principe de celle qu'on vient de décrire. Les différences principales entre ces deux modèles sont que le deuxième prendre en compte le stockage dans la paroi, et les données d'entrée de la température de MCP sont données à la fois par l'analyse de DSC du matériau et par la corrélation, ce qui va permet à la fin la prise en compte de phénomènes de changement de phase a une température non-uniforme et la convection dans le MCP liquide, avec un modèle qui reste toujours assez simple et adaptable



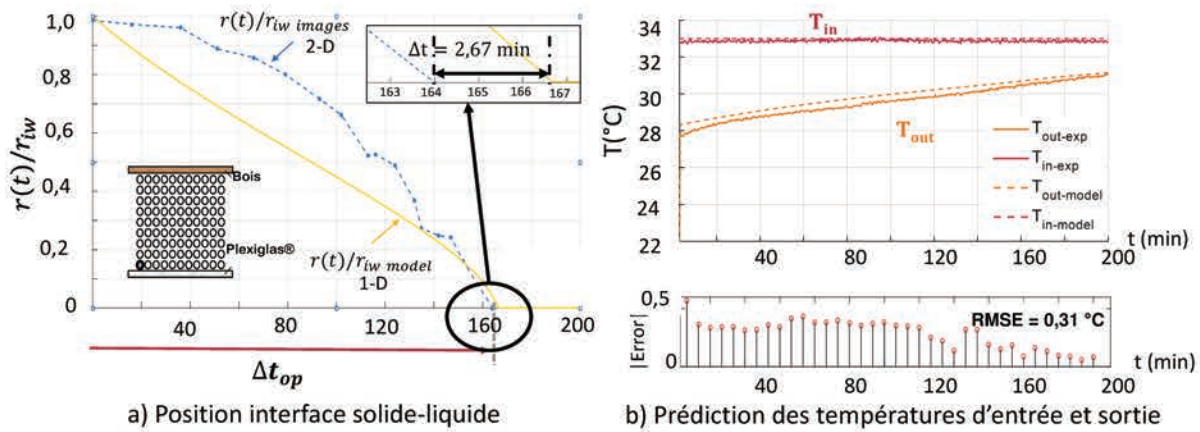


Figure r.vi – Synthèse de résultats de la modélisation à l'échelle a) Locale et b) Globale.

aux outils métiers.

## Chapitre 5 : Applications en bâtiments

Une dernière chapitre « *Building Applications* » présente le développement et tests préliminaires d'une unité mobile de MCP. Ici on présente de la conception à l'utilisation de ce prototype dans deux cas réels : dans un bureau du labo I2M et dans une maison à énergie positive située à Gradignan, Bordeaux.

Pour ces applications, l'échangeur avec une structure en Aluminium fabriquée aux ateliers de l'ENSAM Bordeaux et intégré de tubes cylindriques en PET distribués en quinconces, a été rempli avec deux types de MCP RT21 pour l'application « bureau » et SP25 pour l'application « maison ». Dans cette deuxième application, le fonctionnement a été couplé aux stratégies de ventilation naturelle nocturne de la maison. Il est montré que l'échangeur aide à maintenir des conditions de confort au sein de l'ambiance pendant les heures les plus chaudes de la journée, et une régénération des MCP est possible pendant la nuit.

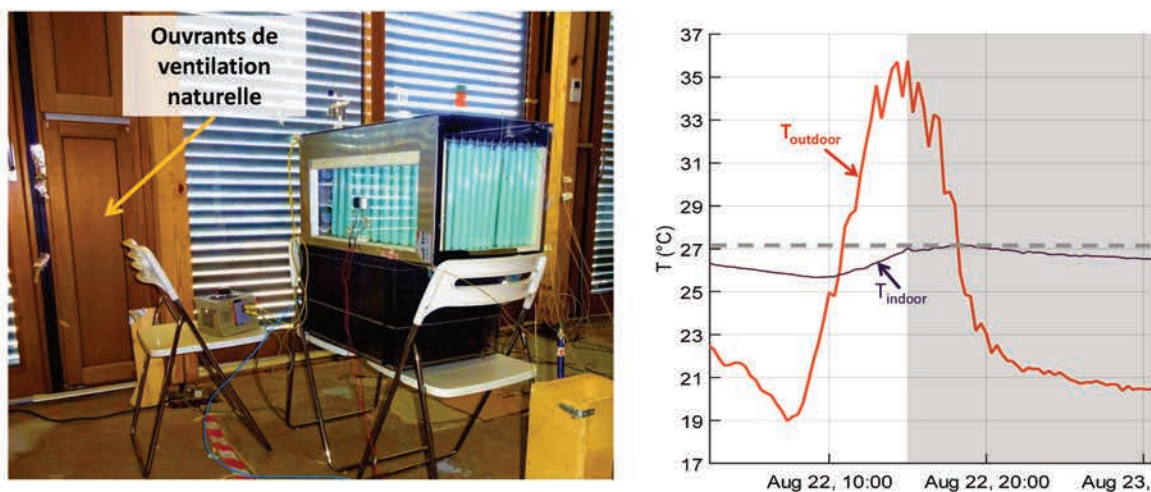


Figure r.vii – Test en application « maison » avec les résultats pour la journée du 22 août 2017.

## Conclusions et perspectives

Le présent travail a été développé dans le cadre d'une recherche d'une géométrie qui permet une adéquation entre performance et intégrabilité au bâtiment, et aussi du développement d'outils d'aide à la conception et au dimensionnement. Alors il a visé à surmonter les complexités liées à l'intégration d'un système air-MCP, en particulier, pour la construction d'applications en réalisant une compréhension approfondie des phénomènes physiques associés. Pour atteindre cet objectif, deux axes d'action ont été développés conjointement : un axe scientifique et un axe d'application.

La thèse a commencé par une recherche bibliographique. La connaissance générale du changement de phase est tout à fait disponible ; néanmoins, lorsqu'on aborde une solution particulière, on peut remarquer qu'il existe encore de manques dans les connaissances qui représentent des opportunités pour des études ultérieures. C'est le cas du système air-PCM développé au cours de ce travail. La forme du contenant sélectionnée a été couverte de manière expérimentale et numérique dans la littérature, mais seules quelques études ont abordé des systèmes similaires, et toutes se concentrant uniquement sur le comportement global du système et non sur les phénomènes physiques locaux.

Dans ce travail, nous avons présenté une méthodologie qui visait à trouver une géométrie assurant des performances thermiques avantageuses et pouvant être adaptée par la suite pour s'intégrer aux objectifs énergétiques du bâtiment. La conception finale obtenue, qui utilise des tubes verticaux au sein d'un faisceau de tubes, correspond aux géométries d'échange de chaleur utilisées pour d'autres applications thermiques. Elle est en outre facilement adaptable aux applications actives et passives de systèmes macro-encapsulés dans les bâtiments.

La partie expérimentale développée pendant ces travaux a été essentielle pour la poursuite du développement de cette thèse et l'essentiel de la compréhension des phénomènes physiques. Pour obtenir ces résultats, nous utilisons des mesures de température, vitesse de l'air et photographies. Le traitement ultérieur de ces mesures nous a permis de traduire ces phénomènes en différents types d'indicateurs de performances du système étudié et de les quantifier. On a trouvé ici que la conduction et la convection jouent toutes deux un rôle important au cours des différentes étapes du cycle de fusion du MCP à l'échelle locale.

Une modélisation a été proposée dans le but d'accomplir les objectifs initiaux de la recherche. Les résultats obtenus avec ce modèle montrent qu'un modèle simplifié basé sur une approche conductrice 1-D avec une notion de résistances thermiques peut expliquer la performance globale d'un échangeur de chaleur air-PCM. Cependant, cela pourrait être insuffisant pour décrire le comportement local dans un conteneur. Nous considérons cela comme l'une des découvertes majeures des travaux actuels, car il nous révèle que, pour le dimensionnement ou la conception d'outils, il peut suffire simplifier les phénomènes locaux, même s'il existe des mécanismes complexes, tels que des mécanismes de convection naturelle.

Finalement avec la construction et mise en place d'un prototype d'échangeur air-MCP composé d'un faisceau de tubes cylindriques verticaux, nous avons constaté que ce type de systèmes présentent un potentiel de développement, car ils pouvaient contribuer à maintenir le confort thermique pendant la période souhaitée.

Alors en synthèse, ces travaux ont mené à :

1. Sélection d'une géométrie adaptable aux applications de bâtiments,
2. Développement d'un modèle de dimensionnement
3. Compréhension des phénomènes physiques associés au changement de phase.

#### 4. Développement d'un modèle de compréhension

Dans les travaux futurs, il reste encore à développer une modélisation qui peut prendre en compte l'ensemble des phénomènes associés au changement de phase, qui reste toujours simple pour être intégrée comme outil métier. Une modélisation de ce type a été proposée ici, laissant comme perspective le développement numérique et sa validation. Des tests plus détaillés et dans une plus longue période sont à l'avenir pour les prototypes développés.

# Nomenclature

## LATIN LETTERS

$L_c$	Characteristic length	[m]
$C, a, b, x$	Coefficients referring to empirical correlations	[-]
$h_{air}$	Convective heat transfer coefficient	[W·m <sup>-2</sup> ·K <sup>-1</sup> ]
$S$	Cross-section surface area	[m <sup>2</sup> ]
$D$	Diameter	[m]
$\mathcal{S}$	Dimensionless pitch	[-]
$\mathcal{A}$	Enthalpy-temperature coefficient	[-]
$\mathcal{B}$	Enthalpy-temperature independent term	[-]
$n$	Exponent related to empirical correlations	[-]
$m$	Exponent related to convection	[-]
$g$	Gravity constant	[m·s <sup>-2</sup> ]
$q$	Heat transfer rate	[W]
$I$	Refers to image	
$L$	Latent heat	[J·kg <sup>-1</sup> ]
$W$	Losses	[W]
$m$	Mass	[kg]
$\dot{m}$	Mass flow rate	[kg·s <sup>-1</sup> ]
$C$	Melting correlation constant	[-]

---

$m_f$	Melting fraction	[-]
$n_t$	Number of tubes	[-]
$P$	Power	[W]
$r$	Radii of tubes	[m]
$h$	Sensible heat capacity	[J·kg <sup>-1</sup> ]
$X$	Space in x-coordinate	[m]
$c_p$	Specific heat	[J·kg <sup>-1</sup> ·K <sup>-1</sup> ]
$h$	Specific enthalpy	[J·kg <sup>-1</sup> ]
$A$	Surface area	[m <sup>2</sup> ]
$T$	Temperature	[°C]
$k$	Thermal conductivity	[W·m <sup>-1</sup> ·K <sup>-1</sup> ]
$Q$	Thermal energy or heat	[J]
$R$	Thermal resistance	[K·W <sup>-1</sup> ]
$e$	Thickness	[m]
Th	Threshold	[-]
$t$	Time	[s/min/h]
$H$	Total enthalpy	[J·kg <sup>-1</sup> ]
$v$	Velocity	[m·s <sup>-1</sup> ]
$V$	Volume	[m <sup>3</sup> ]
$\dot{q}$	Volume flow rate	[m <sup>3</sup> ·h <sup>-1</sup> ]

**GREEK LETTERS**

$\phi$	Availability	[-]
$\rho$	Density	[kg·m <sup>-3</sup> ]
$\mu$	Dynamic viscosity	[Pa·s]
$\varepsilon$	Effectiveness	[-]
$\eta$	Efficiency	[-]
$\beta$	Expansion coefficient	[K <sup>-1</sup> ]
$\alpha$	Thermal diffusivity	[m <sup>2</sup> ·s <sup>-1</sup> ]
$\delta$	Amount of already melted PCM	[m/m <sup>2</sup> /m <sup>3</sup> ]
$\Delta$	Difference	[-]

**SUBSCRIPTS**

<i>cum</i>	Cumulated value
<i>E</i>	East node
<i>e</i>	Eastern boundary
<i>ow</i>	External face of the tube
<i>ext</i>	Exterior
<i>hex</i>	Heat exchanger
<i>in</i>	Inlet
<i>iw</i>	Internal face of the tube
<i>l</i>	Liquid
<i>L</i>	Longitudinal
<i>max</i>	Maximum value
<i>k</i>	Number of iterations



<i>OP</i>	Operation
<i>out</i>	Outlet
<i>P</i>	Present node
<i>r</i>	Recover
<i>air</i>	Refers to air
<i>cycle</i>	Refers to the cycle of cooling/heating of the PCM
<i>H</i>	Refers to the height
<i>D</i>	Refers to the hydraulic diameter
<i>pcm</i>	Refers to the phase change material
<i>wall</i>	Refers to the wall surface of the PCM containers
<i>hyd</i>	Relative to the hydraulic diameter
<i>tube</i>	Relative to the tube of PCM
<i>s</i>	Stored/solid
<i>T</i>	Transversal
<i>W</i>	West node
<i>w</i>	Western boundary

#### **ABBREVIATIONS AND ACRONYMS**

BN	Binary image
CFD	Computational fluid dynamics
Cond	Conduction
PC	Constraint
C	Physical Contradiction
Iblur	Filtered image
FC	Forced convection

---

BW	Gray-scale image
HVAC	Heating ventilation and air conditioning
HW	Hot wire
LHTES	Latent heat thermal energy storage
LMTD	Logarithmic mean temperature difference
NC	Natural convection
NTU	Number of transfer units
O	Objectives
1-D	One-dimensional
PCM	Phase change materials
PC	Physical constraints
PET	Polyethylene terephthalate
PF	Principal functions
PID	Proportional-integral-derivative
RGB	Red-green-blue channels
cool	Refers to the cooling of the air
heat	Refers to the heating of the air
RE	Relative error
RMSE	Root mean square error
2-D	Two-dimensional
3-D	Three-dimensional
VP	Vane probe

**DIMENSIONLESS NUMBERS**

$Bi$  Biot

$Fo$  Fourier

$Gr$  Grashof

$Nu$  Nusselt

$Pr$  Prandtl

$Ra$  Rayleigh

$Re$  Reynolds

$Ste$  Stefan

# Introduction

## Current Problematic: Global outlook

The increase of the world energy consumption represents a significant concern nowadays, considering that still in 2015, 82% of the energy production was based on fossil fuels. The building and residential sectors represented around 22% of the total energy consumption. Most of the energy demand for these sectors comes from heating, ventilation and air-conditioning applications (HVAC), making them a major contributor to global greenhouse gases emissions, which for these sectors, it was associated with 17% of the CO<sub>2</sub> emissions in 2015, besides the fact that these building-related CO<sub>2</sub> emissions have continued to rise by nearly 1% per year, since 2010 [6].

The balance of the current situation increases the pressure to adopt the necessary actions, such as those established recently at the Paris Agreement (COP21), that limits the increase of the greenhouse emissions to avoid climate change, by holding the increase in the global average temperature to well below 2°C [19]. These factors make the search for a reduction on the energy consumption related to HVAC and the improvement of the efficiency of technologies used in these applications a current trend.

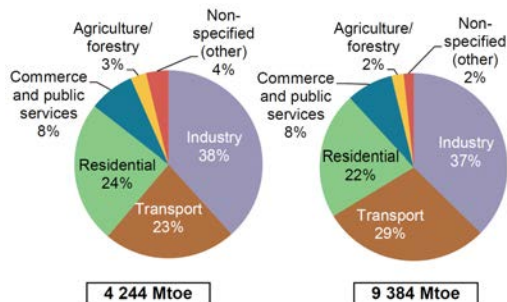


Figure i.8 – World overview of the total final consumption by sector. The residential sector ranked third in 2015 (22%).

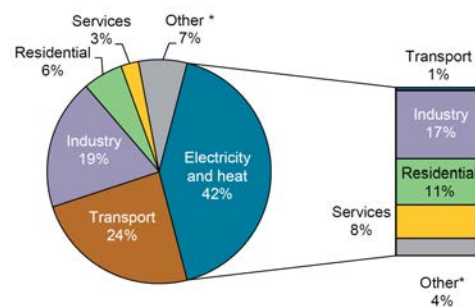


Figure i.9 – World CO<sub>2</sub> emissions from fuel combustion by sector, 2015.

The building and residential sectors are expected to play a significant role in achieving substantial energy and emissions reduction in the future. Hence, several solutions have been developed in different research programs around the globe during the last decades, some of them based on innovative solutions, which responded to zero or nearly zero greenhouse gases emissions; others, are based on the enhancement of already known systems and techniques, which can be applied as low consumption auxiliary systems. Since the building is a complex system composed itself in several sub-systems, these ameliorations focus on the various subsystems that make them up such as [13]:

- the amelioration of the building envelope and the use of passive cooling, reducing the heat gains and minimizing the cooling loads,
- the HVAC systems, increasing the energy efficiency of the cooling systems, and
- the integration of renewable energy sources.

## Phase change materials for cooling and heating applications

We call phase change materials (PCM) those materials with the potential of storing or releasing a significant amount of energy during phase change. This storage capacity is significantly larger if we compared to conventional construction materials [9], as can be observed in figure i.10. These materials can be classified into organic, inorganic and eutectic materials, existing in a wide variety of products and within a wide range of melting temperatures, making them useful in several thermal applications.

This large energy storage capacity can be used for cooling and heating systems in a building as latent heat thermal energy storage (LHTES) if the melting temperature matches the local environmental conditions. During summertime, these materials can prevent overheating of the indoor air by storing the surplus heat during the day, and by potentially reducing the heating needs during the night during the wintertime.

Since their use as a system can match the peak energy load periods, they can reduce and shift the maximum air temperature within a building [59], [9], as observed in figure i.11. Therefore, they can be exploited as an alternative to mitigate the increasing demand for HVAC systems in buildings. By doing so, they would offer thermal comfort, potentially saving energy.

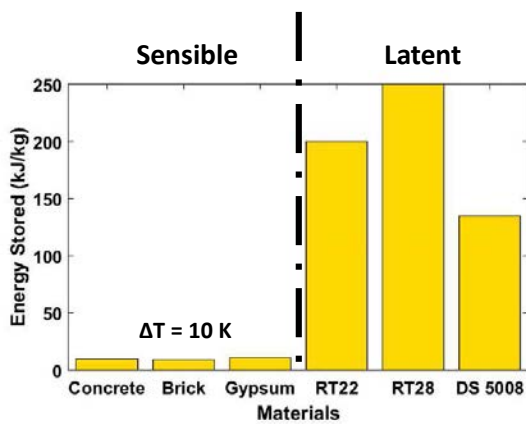


Figure i.10 – Comparison of the heat storage capacity between construction materials and some commercial PCM.

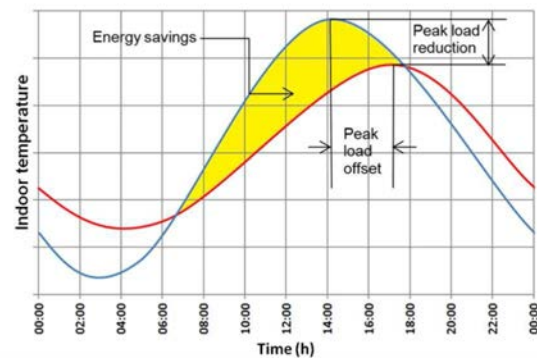


Figure i.11 – Potential peak load shifting and energy savings due to the use of PCM in building applications.

Several methods of incorporating the PCM in buildings applications have been conducted since 1975, [54], and since then, a diversity of PCM products and containers have been explored, allowing a greater and better integration in buildings. Among these techniques we have [122]:

1. *The impregnation of PCM into the construction materials* [50], [115]. In here, the PCM can be incorporated by simply mixing it with the construction materials, if they are presented

in liquid or powder form. They can also be immersed, where the PCM penetrate the pores of the construction material.

2. *Integrated into the building envelope.* The PCM can be integrated into the internal and external structure of the building such as floors, walls, ceilings, plaster, windows, paint, and others, increasing the building thermal mass [45]. According to Akeiber et al. [9], the most common approach detected in the literature is to integrate the PCM into the wall structure, due to ease setup and incorporation.
3. *Free cooling applications.* Matching the PCM storage capacity with nocturnal ventilation techniques could allow the use of the cold energy available during the nights for later use during the daytime. Despite the different varieties of PCM that can be used for free cooling applications, they follow the same basic principle: the hot air, a product of the high temperatures of the day interacts with the PCM. The surplus heat is absorbed by the PCM in an endothermic process, resulting in the melting of the material. Consequently, the air loses heat to the PCM resulting in a lower temperature of it. By doing this process, this interaction can achieve the cooling of the place. After that, during the night, the cold air regenerates the PCM, leaving them ready for next use.

In general, these uses can be classified as passive or active systems. Passive storage in buildings allows the storage of a high quantity of energy, giving thermal stability inside the building. Thermal mass refers to a typical building structure that adds inertia to the temperature variation [9]. When PCM is added to the building structure, it increases the thermal mass and prevents the heat from reaching the occupied space

Increasing the thermal mass of a building can be useful in light-weight buildings with low thermal inertia. These buildings are usually subjected to a considerable temperature fluctuation during the summertime due to overheating by solar radiation [76].

Its operation can also be found as part of an active cooling system. These applications need the help of a mechanical device to achieve the PCM thermal energy charging or discharging. In this case, PCM can be installed in storage units, in HVAC systems or it can be used as a heat-cold storage tank in solar cooling technique [103]. According to Souayfane et al. [103], these systems have been investigated numerically in many studies, and barely any free cooling system was applied in a real experimental case for building [118]. Extensive literature reviews about the use of PCM in building applications can be found in [9], [76], [118], [102], and [103].

## **PCM systems for building applications developed by I2M of Bordeaux**

Since 2009, the I2M laboratory in partnership with Nobatek-Inef4 Society, and other educational institutions have been developing PCM systems for building thermal comfort during the summertime. In this section, we present an overview of the systems developed before this present work.

### **Box shape tube bundle: *Napevomo house***

The first LTHES device was conceived as an auxiliary air cooling system for the Napevomo house, a positive energy house (PEH) built within the framework of the competition Solar Decathlon Europe 2010. The competition took place in Madrid, Spain in June 2010 and after the competition, the house was rebuilt at the Arts et Métiers Campus in Bordeaux. Napevomo is a single house with a living area of 47m<sup>2</sup> designed to accommodate two people (see figure [i.12](#)

[72]). The energy needs of this house were covered by a solar co-generation system producing electrical power and hot water for the house, a couple of PCM systems that covers the needs of air conditioning of the house and an HVAC system responsible for ensuring that household demand is satisfied at all times. In here we detail only the PCM systems. Bruneau et al. [11] present further detail about the Napevomo house and the thermal systems within it.

The Napevomo PCM systems were designed as a simple shell and tube exchanger using the NTU-effectiveness as the sizing method, usually used for conventional heat exchangers. The scientific and technical works related to the design, construction, and installment of this systems were addressed during the Ph.D. thesis of Serge Ekomy Ango [86]. The features of this device were set up by the geographical, climatic, and technical conditions of the competition, and the house energy requirements. Among the different rules, the competition required to maintain the indoor air temperature below 25 °C throughout the day, while promoting low energy consumption [87]. Therefore, the principle of operation of the system mainly consisted of cooling down the air during the day, maintaining it within the thermal comfort by regulating the indoor air temperature, and regenerate the PCM during the night by intaking the cold outdoor air, as shown in figure i.13.

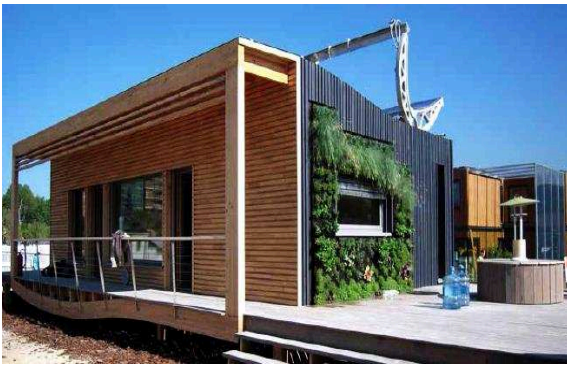


Figure i.12 – Napevomo house at the Solar Decathlon competition.

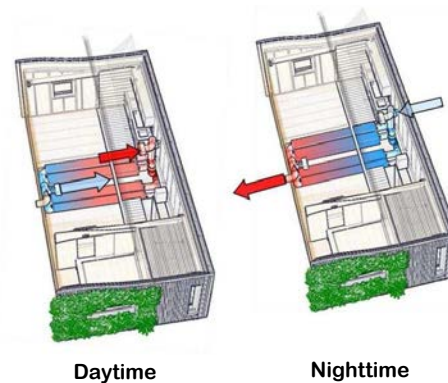


Figure i.13 – Principle of operation of the air cooling system using PCM at the Napevomo house.

The air-cooling system consists of four LHTES devices, each of them containing a horizontal energy storage device, namely a box-section tube bundle filled with paraffin wax, with a parallel air flow [11] (see figures i.14 and i.15). The system is integrated within the house floor. Two paraffin waxes were selected as storage material, the paraffin Rubitherm® RT21 [88], with a latent heat capacity of 134 kJ kg<sup>-1</sup> and a melting temperature range around 21°C, which responded directly to the actual weather conditions at the competition place, and Rubitherm® RT28 HC [25], with latent heat capacity of 245 kJ·kg<sup>-1</sup> and a melting temperature range around 28°C, in case of higher temperatures.

The PCM containers present a box shape tubes geometry made of aluminum. These geometric and material choices were based on the material thermal properties, e.g., heat conductivity, the compatibility with the PCM, the price and the manufacturing feasibility of each piece, since they would be manufactured at Arts et Métiers workshop. During the manufacturing of these systems, it was also included a paraffin filling process and the addition of deflectors to create a torturous effect between the air and the tubes, increasing the turbulence and thus, improving the heat exchange between them. This was made with the purpose of overcome the drawback that implies the low conductivity of the paraffin material (0,2 W·m<sup>-1</sup>·K<sup>-1</sup>).





Figure i.14 – One box shape tube bundle containing the PCM.



Figure i.15 – The view of an open heat exchanger and a closed heat exchanger connected to an air network.

### Slabs PCM system: *Sumbiosi house*

In 2012, I2M built a second house, Sumbiosi, for the Solar Decathlon Europe, a competition also held in Madrid, Spain. Sumbiosi is a modular house with a living area of 70 m<sup>2</sup> designed to accommodate 3 people permanently and up to 5 people temporarily (see figure i.20).



Figure i.16 – Sumbiosi house at the Solar Decathlon Europe 2012.



Figure i.17 – LHTES test bench used in the Sumbiosi house.

After the results obtained by the PCM system developed for the Napevomo house, it was decided to also include among the thermal systems composing this positive energy house, a PCM system coupled with a natural ventilation strategy as an auxiliary source for thermal comfort during summertime. For this prototype, a preliminary design process was followed focusing on the geometric parameters of this new system to enhance the thermal performance. The design methodology was based on a functional analysis of the PCM system. Some of the general service functions defined during the design were as follows:

- During the designing and manufacturing process, the system should consist of materials easily obtainable and inexpensive, that also consider the volume changes of PCM.
- Regarding the assembly and disassembly, it must contain components that are easy to transport and install.
- During the daytime, the system has to cool down the place, while melting the PCM.



- During the night, the PCM should be regenerated (the PCM must be solidified).
- During the storage process, the energy should be stored avoiding possible losses.

This design aimed to improve the thermal performance optimizing the geometric features of the system. Therefore, for this design, the selection of the container looked up for a geometry that allows a large heat transfer surface area. The slab type containers feature this condition; then a corrugated slab type was explored as the PCM containers for this device.

The house LHTES system consisted of three energy storage devices each of them consisting of ten racks made of five rough aluminum slabs filled with RT21 paraffin wax. Two positions were tested for these slabs: horizontal and vertical. Among the attractive features of this design are the thermal properties of the container material, the rough surface of the slabs and the fragmented modular system, that increases the turbulence of the airflow, and then, enhance the heat transfer. One major disadvantage of this configuration is the ratio between storage capacity of the device and the volume occupied by it. Slabs containers present a reduced storage capacity if compared with other classical geometries, where the large heat transfer surface area which is desirable during the cooling process, can be counterproductive since this geometry can increase the potential losses during the energy storage.

The working principle of the device within the house follows the same principle presented for the Napevomo house [100]. A schematic of this operation principle of the PCM system is presented in figure i.18. Although for Sumbiosi, the PCM system was installed as part of the envelope of the house on the East façade wall [96] (see figure i.19).

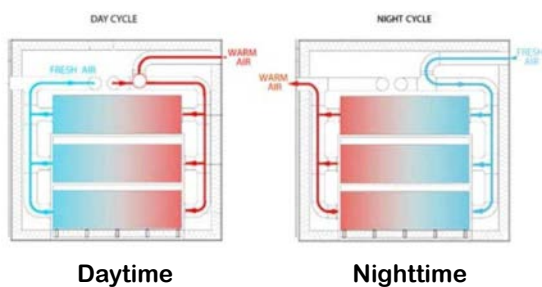


Figure i.18 – Operation principle of the Sumbiosi House during the Solar Decathlon 2012.



Figure i.19 – PCM system embedded in the Sumbiosi house wall at the IUT campus in Bordeaux.

## Further Research

Once both competitions were over, both houses were re-installed in Bordeaux, and further evaluation of the cooling potential of these systems was performed. These PCM prototypes were the subject of study of a thesis authored by Fabien Rouault [87]. This work coupled an experimental and numerical development of air-PCM systems for building applications. The experiments were carried out as a support for the modeling. These models were enhanced by the use of a decision support system following optimization techniques, which allows the designer to compute the best geometric distribution of container, the selection of the material and the global architecture of the system.

These studies resulted in tools that coupled with the modeling of the air-PCM systems using energy conservation models with already existing building software. The importance of this

work lies in the integration of such models in this software specially designed to fulfill the needs of architects and building engineers.

### Departure point for the present work

Before the development of the present work another evolution of the type of containers and geometry of PCM systems was contemplated and in developing at the I2M laboratory. In this context, some laboratory tests were carried out using cylindrical bags that were manufactured in situ, as a part of a Master Thesis [67]. These bags were installed in a test bench, as a part of a PCM modular system easy to install and uninstall, with components that were easy to replace. It was of paramount importance a proper sealing of the plastic bags because if not, the liquid PCM could leak out of the bags. Since it was not possible to ensure the dependability of the plastic bags, then it was not followed further by this container proposal.

These projects, the PCM systems developed for the Napevomo and Sumbiosi houses, as well as this PCM test bench using cylindrical bags, have served as the basis for the development of this thesis work. This thesis aims for a next evolution in the containers used for PCM, by further exploring the physical phenomena effects of the thermal performance of air-PCM systems for building applications [26].



Figure i.20 – Plastic bags used as PCM containers [67].

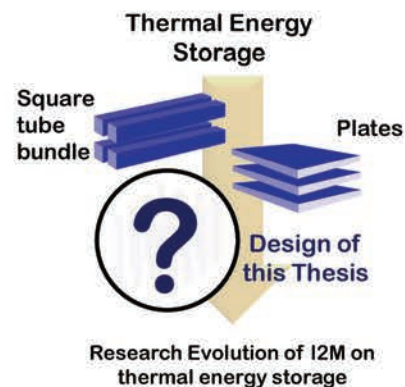


Figure i.21 – Evolution line of the LHTES systems developed by the I2M laboratory [26].

### Problem statement

The use of practical and straightforward models can ease the designing and integration of PCM systems for building applications. To develop these models we need a proper understanding of the phase change phenomena in order to predict the thermal performance of the system, meaning that we need to overcome the complexities inherent to phase change. Then, identifying and coupling the local and global phenomena associated with the operation of PCM systems could help to overcome such complexities, increasing the performance of the models.



## Thesis Objectives

We can summarize the thesis objectives as:

1. To identify and describe the physical phenomena involved in the operation of an air-PCM heat exchanger at the local and global domains.
2. To develop phenomenological and performance models based on key indicators.
3. To design, build and test the feasibility and performance of an air-PCM system.

## Thesis Structure and Methodology

The present work has been divided into two axes of research. The principal axis is related to the development of the scientific procedure. This axis includes the understanding of physical phenomena. The second axis includes the work carried out in parallel for the development of the thermal application of air-PCM systems in buildings. In figure i.22 is presented the research axes and the general structure of this present work.

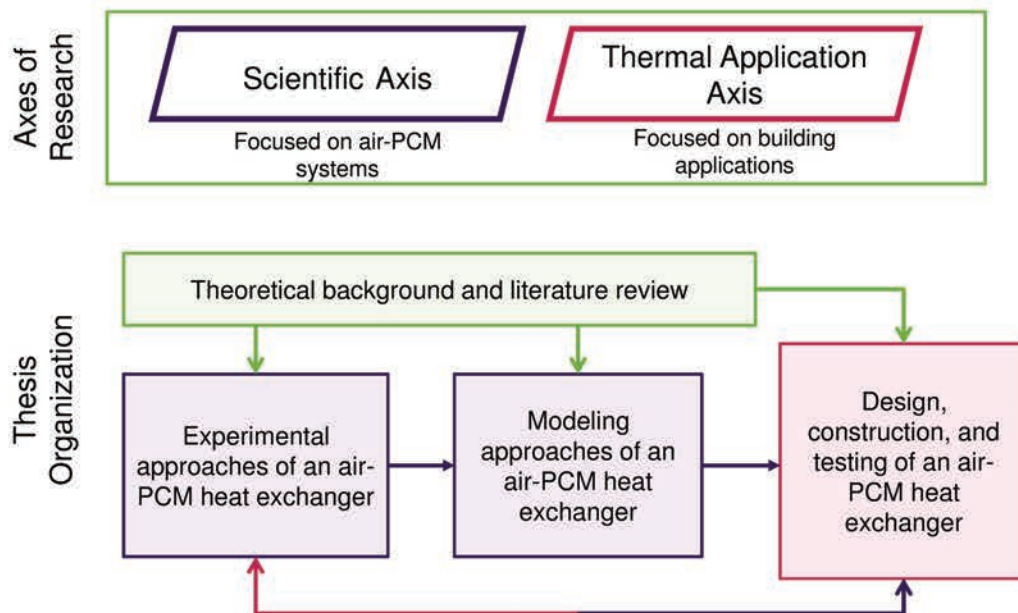


Figure i.22 – Axes of research and thesis structure.

## Methodology

These methods can be organized into four steps:

1. Design Methodology, that includes the selection of the container geometry and further arrangement adaptable for building integration.
2. Modeling of an air-PCM unit, that can be easily integrated to design and sizing tools.
3. Physical phenomena understanding.
4. Construction of an air-PCM prototype unit

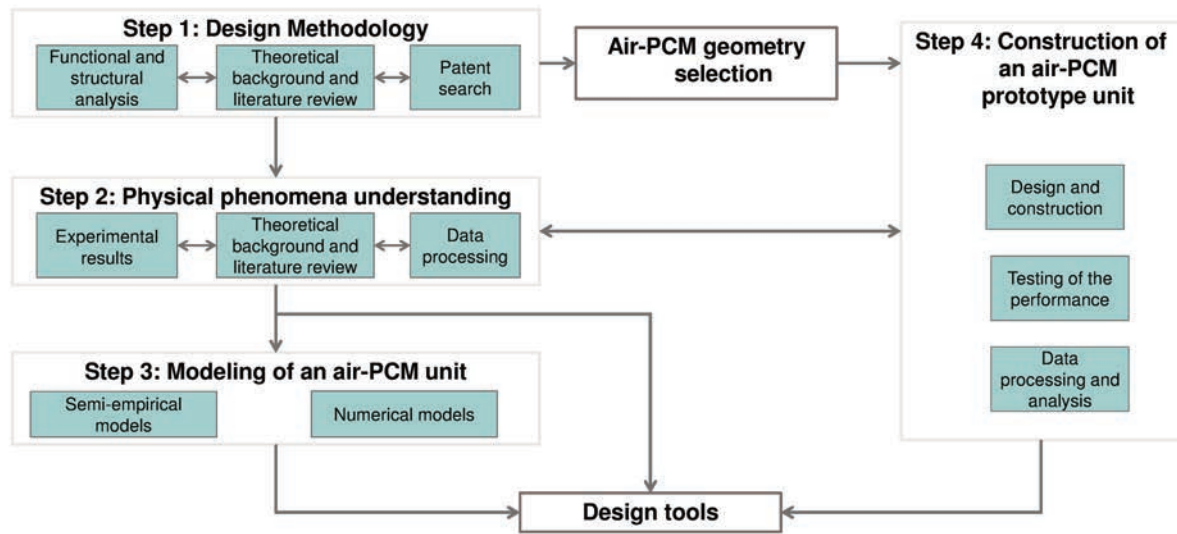


Figure i.23 – Scientific approaches for the development of the present work.

The scientific approach followed for the development of the thesis methodology is summarized in figure i.23.

Among the approaches and methods used for the developing of the present work we have:

1. Design methods (General and Functional analysis, Keywords search of innovative ideas) to obtain a proposal of the air-PCM unit.
2. Experimental measurements of air velocity and temperature, from an air-PCM unit (test bench) with controlled inlet conditions, during melting and solidification.
3. Digital photographs during each cycle to record the phase change.
4. Dimensionless and statistical analysis to obtain key parameters from experiments that address the complexity of the phenomena (conduction and convection during phase change) through correlations instead of the use of mass transport and other complex phenomena.
5. Thermal resistance and energy balance (using Fourier's and Newton's laws of heat transfer) for both, experimental data treatment and numerical modeling.
6. Data collection from real building experiences.



La chaleur pénètre, comme la gravité, toutes les substances de l'univers, ses rayons occupent toutes les parties de l'espace. L'objet de notre ouvrage est d'exposer les lois mathématiques que suit cet élément.

---

Jean-Baptiste Joseph Fourier

# 1

## Theoretical background and literature review

### 1.1 Scope

To accomplish the objectives set for this work, we need to fully understand the phenomenology associated with phase change and PCM systems. This understanding allows us not only to have a proper knowledge that prepares the ground for further experiments and models, but it also serves as the basis for the design of PCM systems.

In this chapter, we present in parallel, the theoretical background related to phase change materials and its thermal applications, as well as, a literature review related to experimental analysis, modeling and building applications. The first part intends to present all the necessary knowledge that even if its well known, it is vital in the understanding and development of phase change. The last part presents the approaches and solutions implemented during the last decades by different authors, which would allow us to get a better insight into our problem.

## 1.2 Phase Change Materials

When a material undergoes a change of phase, an endothermic or exothermic process occurs, leading the material to store or release a considerably high amount of energy in the form of heat, which generally occurs at a single temperature or within a fixed range of temperature. This type of heat is known as latent heat; the heat storage capacity per unit mass during phase change is inherent to each material.

The concept of phase change materials circumscribes those materials that undergo a solid-liquid transformation at a temperature within the operating range of a selected thermal application [44]. Their attractiveness lies in the fact that they can store a significant amount of energy in small volumes while remaining at an almost constant temperature. This attractiveness represents the major advantage of these materials as storage medium if compared with the thermal storage by sensible heat, where we need a broad temperature difference or large volumes to achieve considerable heat storage.

The PCM can be found in a wide range of temperatures and chemical compositions, whereby they can be used for numerous applications, such as [94]: building air conditioning, electronics cooling, waste heat recovery, textiles, preservation of food, solar energy storage, fabrics, and others.

Since these PCM materials can store large amounts of energy within reduced volumes, their use in building applications can potentially generate energy savings and a reduction on the greenhouse gases emissions by matching their use with the energy demands of the building. However, to select a PCM as a suitable material for LHTES applications, we have to consider if this PCM fulfill the thermal, physical, kinetic and chemical criteria to be selected as heat storage materials. Some of these criteria were gathered by Zalba et al. [121], and listed as follows:

- The melting point must be within the desired operating temperature range.
- The material must possess a high latent heat of fusion per unit mass. This way a smaller amount of material could store a given amount of energy.
- Small volume changes during phase transition.
- The material must exhibit little or no sub-cooling during freezing.
- Chemical stability, no chemical decomposition and corrosion resistance to construction materials.
- Contain non-poisonous, non-flammable and non-explosive elements/compounds.

Over the last 40 years, different classes of materials, including hydrates salts, paraffin waxes, fatty acids, eutectic of organics and inorganic compounds, and polymers have been considered as potential PCM. Abhat [3] in 1983 classified PCM into two categories: organic and inorganic materials. Later in 2009, Sharma et al. [97], extended this classification into three categories: organic, inorganic and eutectic, with subcategories in each of them, as shown in figure 1.1 [97], [106]. In this section we present a brief description of those categories:

### 1.2.1 Organic materials

Organic PCM are further described as paraffin and non-paraffins. They present congruent melting, which means that melting and solidification repeatedly occur without phase segregation and degradation of their latent heat of fusion; also they present little or no supercooling effects,

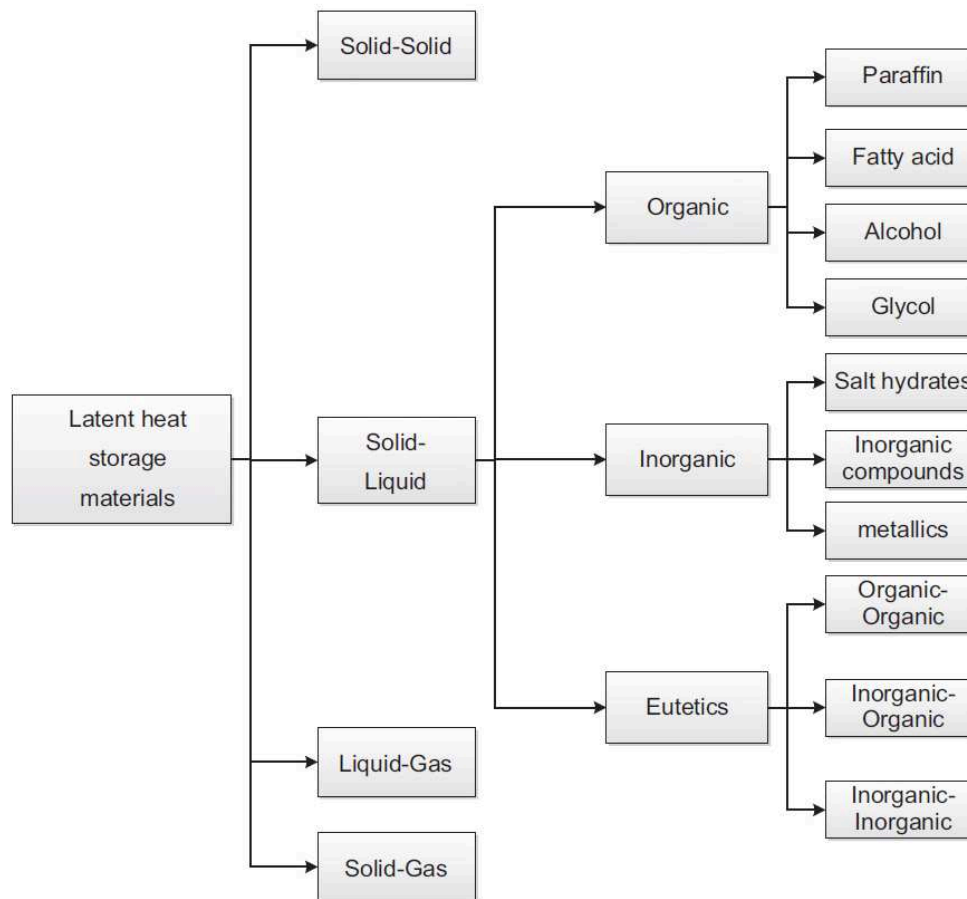


Figure 1.1 – Classification of latent heat storage materials.

and they are usually noncorrosive materials. These organic PCMs are sub-divided into the following categories:

- **Paraffins.** They consist of a mixture of *n*-chain alkanes  $\text{CH}_3 - (\text{CH}_2) - \text{CH}_3$ . The paraffin is available in a large temperature range as shown in figure 1.2, which make them attractive for several thermal applications. They also present a reasonable cost, a predictable behavior, reliability, they are non-corrosive, and chemically inert below 500 °C. The commercial use of paraffin comes from the distillation of crude oil. Although their use as thermal storage material is attractive, they present some drawbacks such as low thermal conductivity, and in some cases, they are not compatible with plastic containers.
- **Non-paraffins.** In this group are included materials such as esters, fatty acids, alcohols, and glycols. They are the most numerous of the phase change materials with highly varied properties, representing the largest category of candidate's materials for phase change storage [97]. Among their properties we have: a high heat of fusion, low thermal conductivity, varying level of toxicity, inflammability and instability at high temperature. From this group, the fatty acids are attractive for thermal energy storage due to their higher heat of fusion, compared to paraffin. These PCMs also show reproducible behaviors during melting and solidification, with no supercooling. However, their cost is about 2-2,5 times the cost of paraffin.



### 1.2.2 Inorganic materials

They are further classified as salt hydrate and metallics.

- **Salt hydrates.** These materials are alloys of inorganic salts and water forming a typical crystalline solid of the formula  $AB \cdot nH_2O$ . Since most of the hydrate salts present poor nucleating properties, they show supercooling in the liquid before solidification. Their most attractive properties are their high latent heat of fusion per unit volume, relatively high thermal conductivity and small volume changes on melting. Some of them present congruent behaviors, while others are incongruent. The major issue with them is that most of the salt hydrates that are suitable as storage materials melt incongruently.
- **Metallics.** In this category are included low melting metals and metals eutectics. Their major advantage is their high thermal conductivity. Although, they present major issues as storage materials such as their generally high weight, low heat of fusion per volume unit and low specific heat.

### 1.2.3 Eutectic materials

Eutectic materials are made from a minimum melting composition of two or more components, each of which melts and freezes congruently. During the crystallization phase, a mixture of the components is formed, hence acting as a single component. Their major attractiveness is their ability to obtain more desired properties such as a specific melting point or a higher heat storage capacity per unit volume [59]. The thermophysical properties of eutectic is still a field for further investigations for thermal energy storage as many combinations have yet to be tested and proved.

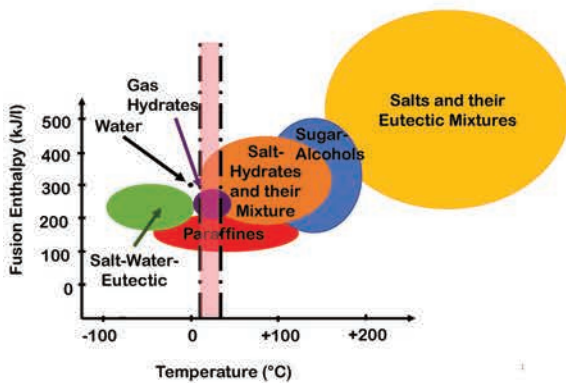


Figure 1.2 – Different types of PCM according to their melting temperature and enthalpy.

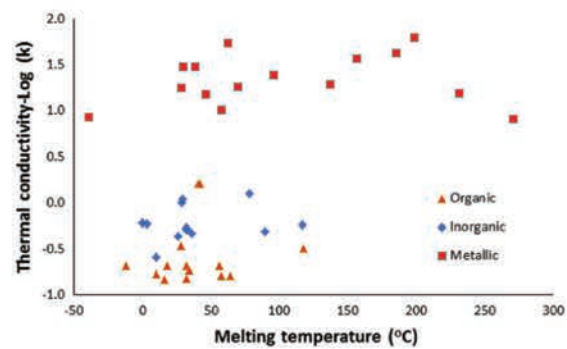


Figure 1.3 – Thermal conductivity distribution for different types of PCM.

The final selection of the PCM material would depend on several factors, including cost, thermal, mechanic, kinetic, physical and chemical properties, which are related to the final application in which the material is going to be used. In order to highlight the advantages and disadvantages of these materials, Kalnæs and Jelle [59] gathered the principal features of each type of material. These features are summarized in table 1.1.

The effectiveness of a heat transfer process can be affected by the thermal conductivity of the material, and with PCM this is not an exception. Therefore, when selecting the material, it

must be analyzed if the design of the system is sufficient to guarantee a good heat transfer with the conductivity of the selected material. If not, we must look for another material, increase the conductivity of the material, for instance, by adding conductive particles, or re-condition the design of the system to enhance heat transfer. In figure 1.3 it is shown the logarithm of the thermal conductivity  $\text{Log}(k_{pcm})$  of PCM regarding the melting temperature. Unsurprisingly, the metallic type PCM present the higher conductivities among them [106].

Furthermore, figure 1.2 results useful for PCM selection, showing the PCM ranges according to their melting temperatures and enthalpies of fusion. In the pink area lies those materials that can be suitable for building applications, allowing us to focus on the PCM available types for these applications [28].

Table 1.1 – Overview of the advantages and disadvantages of each PCM group of materials (developed by Kalnæs and Jelle).

Organic	Inorganic	Eutectic
<b>Advantages</b>		
No supercooling	High volumetric latent heat	
No phase segregation	storage capacity	
Large temperature range	Higher thermal conductivity than organic PCM	Sharp melting points
Compatible with conventional construction materials.	Low cost	Properties can match specific requirements
Chemically stable	Non-flammable	
Recyclable	Sharp phase change	
High heat of fusion		
<b>Disadvantages</b>		
Flammable	Corrosive to metals	
Low thermal conductivity	Phase segregation	Limited data and information
Low volumetric latent heat	Supercooling	High cost
storage capacity	High volume change	

### 1.3 Encapsulation of phase change materials

Encapsulation is the process of covering the PCM with a suitable coating or shell material [94]. Since the most common PCM used as thermal energy storage material undergo a solid-liquid phase change, the PCM needs to be encapsulated; otherwise, the liquid PCM would leak out. Besides preventing liquid leakage, the encapsulation keeps the PCM isolated from the surroundings, ensuring the correct composition of the PCM, which would otherwise have changed due to the mixing with the external fluid.

The encapsulation has a direct effect on the thermal performance of the PCM. Their properties directly affect the performance of heat transfer and energy storage. Encapsulation of PCM can be classified according to their size, material, and geometric properties.

#### (a) PCM encapsulation based on size

Based on the size of the container, the encapsulation of the PCM can be classified in:

1. macro-encapsulation (*above 1,0 mm*),
2. micro-encapsulation (*1-1000  $\mu\text{m}$* ), and
3. nano-encapsulation (*1-1000 nm*).

For thermal storage, macro-encapsulation is the conventional way of encapsulating the PCM since it does not require a complicated process. The typical containers used for PCM are rectangular vessels, spheres, and cylindrical vessels (cylinders, tubes, annular containers). Several studies of each of these containers can be found in the literature, being the cylindrical and rectangular configurations the most found among them [7]. The macro-encapsulation of PCMs can avoid large phase separations, increase the rate of heat transfer and provide a self-supporting structure for the PCM [85].

On the other hand, micro-encapsulation presents higher rates of heat transfer; they are thermally more reliable and stable than macro-encapsulated PCM [8] [12]. Nevertheless, they present a more complicated manufacturing process. Moreover, there are also available studies on nano-encapsulated PCM, presenting even better results regarding the heat transfer rates than macro and micro-encapsulation. However, their study is still at the laboratory scale; therefore, further research is needed on this subject to be considered as commercially feasible. A complete review about nano-encapsulation in buildings can be found in [61].

#### (b) PCM encapsulation based on the material

The material plays an important role in heat transfer and mechanical performance of a PCM container. It has to ensure at least acceptable heat transfer rates, as well as withstanding the changes in pressure and temperature during the phase change. The most common materials used as PCM containers are polypropylene, polyolefin, polyamide, silica, polyurea, urea-formaldehyde, copper and aluminum [94]. Several authors have studied the performance of these materials as PCM containers, based on heat transfer performance and mechanical properties such as thermal conductivity, chemical stability with the PCM, the compressibility of the material, and deformation [20] [119] [22] and [107]. Some properties that must present the container material were listed by Salunkhe and Shembekar [94] and are presented hereunder:

1. The material should have sufficient structural and thermal strength to withstand the phase change process of PCM.
2. It should retain their thermophysical properties at the micro and nano level.
3. It should be leak proof.
4. It should not react with the PCM.
5. It should be a good water diffusion barrier.
6. It should have higher thermal conductivity.

Metallic containers are usually an attractive choice due to their thermal and mechanic characteristics. Although, they are not a viable option if the PCM is corrosive. Similarly, plastic is an attractive choice due to their weight; however, they present poor thermal conductivity, and for organic PCM it must first be analyzed if the type of plastic is compatible with the PCM because they present a similar structure than the organic PCM; this could lead to diffusion or chemical reaction.

#### (c) PCM encapsulation based on the geometry

As it was already stated, the most common geometries for PCM containers are spheres, cylinders, plates, and tubes. These geometries are popular due to the ease of manufacturing and handling that they entail. However, we can also find variations of these geometries as PCM containers.

The physical phenomena that are commonly associated to phase change, i.e., melting and solidification controlled by conductive and convective heat transfer mechanisms are heavily affected by the geometry and geometric disposition of the container regarding the gravity phenomenon. Therefore if these phenomena are described inadequately, it would result in an inaccurate prediction of the thermal performance [7]. Since one of the objectives of this present work is the identification of the physical phenomena occurring during phase change, more details are presented in further sections.

So far, we have presented an overview of the general concepts related to phase change, which concepts are common to all of the applications where they are generally used. Before going further in the phenomenology associated with these materials, we present a review of the use of PCM in building applications, which allows us to focus our detailed search of the phenomena, taking into account the application in which it will perform.

## 1.4 Physical phenomena during phase change

Whether we are studying melting or solidification, phase change results in a complex problem mainly because it involves the presence of more than one phase, creating a boundary between them, that varies in time and space. If our goal is to ease the designing and use of PCM systems, we should provide users with tools that, despite the complexities of the process, can acceptably predict the behavior and performance without going into tedious methods. To achieve this, we need a deep understanding of the phenomena so that these phenomena can be simplified without affecting their effect on phase change.

According to Regin [85], the heat transfer analysis of the phase change problem is much more complicated than single phase problems due to:

1. The non-linearity of the problem resulting from the motion of the solid-liquid interface during phase change.
2. Inadequate knowledge of the heat transfer process at the solid-liquid interface, because of the buoyancy-driven natural convection in the liquid PCM.
3. Uncertainty of the interface thermal resistance between the container and the solid PCM.
4. Volume change with the change of phase (upon shrinkage).
5. The presence of voids in the solid PCM.

Several physical phenomena are inherent to PCM during melting and solidification. Their effects in phase change and therefore, in the modeling of these processes vary according to the specific conditions of the problem, such as the shape of containers, storage material, geometry arrangement, thermal applications among others, which leads to retain or discard such phenomena under certain circumstances. In here we briefly mention the most important phenomena to be retained.

1. ***Moving solid-liquid interface.*** The position of the solid-liquid interface not only distinguishes one phase from the other, but it also reflects the quantity of the PCM that has already melted or solidified at a certain instant. This measure is of great importance



because it can reveal the amount of heat that has been stored or discharged from the PCM. This is probably the most important feature to determine during phase change [124], leading to the need for a prediction of this parameter as accurate as possible.

2. **Density change in phase change.** During the phase change, we can identify two types of density changes in the material [10]: (i) due to change of temperature in a phase, since density depends on the temperature, and (ii) due to the difference between the solid and liquid density at the melting temperature. Solid density is usually higher for most PCM, whereas the water is a notable exception [124]. When melting occurs, the PCM occupies more volume, increasing the pressure on the container; whereas for solidification, when shrinkage occurs, the PCM occupy less volume, under-pressurizing the container. This last entails void formation (bubbles or gaps from the vapor of the material and other gases) within the PCM. These voids are more likely to be formed between the PCM and the container since the weakest forces of adhesion are between them.
3. **Buoyancy effects in the melt region.** The temperature difference not only leads to a change in the density of the PCM, but it also induces flows in the liquid PCM due to the presence of gravity, promoting the natural convection. These flow interactions with the remaining solid, create 2-D melting patterns. These patterns are linked to the amount of PCM remaining on the process by a certain instant; therefore, it should be addressed when studying phase change. The role of natural convection in solidification is much less important and in many cases may be discarded [124].
4. **Phase change over a wide temperature range.** Pure substances offer a sharply, well-defined phase change temperature, which is desirable for most of the thermal applications since the temperature of operation can be well predicted. However, these materials present a high cost, making them impractical solutions as a storage material. Nevertheless, there are commercial PCM that present attractive phase change temperature ranges. In either way, this parameter must be taken into account during the design and modeling of PCM systems.
5. **Enthalpy hysteresis.** Some PCM can present subcooling or superheating effects during phase change, where phase change does not occur at the expected temperature. For instance, for building applications, this is a phenomenon which should be avoided in the PCM.

Melting and solidification for several shapes of containers and PCM have been widely studied. The first to acknowledge the moving boundary problem of phase change was Jožef Stefan, and since then, this problem has been called the "*Stefan Problem*."

Usually, if we want to understand a physical problem, we resort to experimental and analytical approaches to accomplish this task. The problem with the analytical solutions for the Stefan problem is that they are mostly available for one-dimensional cases, and for simple boundary conditions. They have been addressed in the literature, especially in heat transfer textbooks as the theoretical solution of phase change problems [21], [10], [77]. Therefore, for air-PCM applications, the phase change comprehension relies mostly on experimental and numerical approaches. These approaches usually express the performance in terms of melting fraction, temperature profiles, operation time and melting rate or power [7]. Besides, these approaches are often associated with a group of dimensionless numbers used in the study of PCM. Before explaining these approaches, we define these dimensionless numbers in the following section.

### 1.4.1 Dimensionless numbers associated with phase change

The dimensionless numbers are algebraic expressions, generally in the form of fractions, where the numerator and denominator are powers of physical quantities with the total physical dimension equal to unity [90]. These numbers are obtained by dimensional analysis and by a scaling of the governing equation of a specific phenomenon.

Their use is well extended in the fields of chemistry, transport of momentum, heat, and mass, since they simplify the description of phenomena and the governing equations to a reduced number of variables. Besides, they provide a clear physical interpretation of the phenomenon under study.

In an LHTES system where a single container is in contact with an external fluid, from which it will be transferred the necessary heat to the phase change to happen, the heat and mass transport can be explained by the Reynolds, Prandtl, and Nusselt numbers.

The Reynolds number  $Re$  determines whether a flow is laminar or turbulent. It can be defined as :

$$Re = \frac{D_{hyd} \cdot v_{max}}{\nu_{fluid}} \left[ \frac{\text{convection}}{\text{viscosity}} \right] \quad (1.1)$$

where  $D_{hyd}$  is the hydraulic diameter,  $v_{max}$  is the maximum velocity of impact between the fluid and the container, and  $\nu_{fluid}$ , the dynamic viscosity of the fluid.

The Prandtl number  $Pr$  approximates the ratio of momentum diffusivity to thermal diffusivity. Low  $Pr$  means effective heat conduction with dominant thermal diffusivity. High  $Pr$  means effective heat convection with dominant momentum diffusivity. The Prandtl number is given by:

$$Pr = \frac{\nu}{\alpha} \left[ \frac{\text{momentum diffusion}}{\text{heat diffusion}} \right] \quad (1.2)$$

The Nusselt number determines the ratio of actual heat transferred by a moving fluid to the heat transfer that would occur by conduction and it is defined by:

$$Nu = \frac{h_{air} \cdot D_{hyd}}{k_{air}} \left[ \frac{\text{conductive thermal resistance}}{\text{convective thermal resistance}} \right] \quad (1.3)$$

where  $h_{air}$  is the overall convective heat transfer coefficient, and  $k_{air}$  is the air conductivity.

The Biot number,  $Bi$ , defines the ratio of the heat transfer resistances inside of and at the surface of a body. This can determine whether or not the temperatures inside a body will vary significantly in space, from a thermal gradient applied to its surface. With this number, we can define if the heat transfer across the tube wall can be considered as unidimensional conduction, and it can be defined as:

$$Bi = \frac{L_c \cdot h_{air}}{k_{wall}} \left[ \frac{\text{conductive thermal resistance}}{\text{convective thermal resistance}} \right]. \quad (1.4)$$

Regarding the phenomena occurring within the PCM container, we first consider here the Stefan number  $Ste$  which is associated with the phase change, it expresses the ratio between the sensible heat and latent heat available from the PCM. This Stefan number is a dimensionless form of the temperature difference between the outer surface of the tube and the PCM melting

temperature given by:

$$Ste = \frac{c_{p_{pcm}} \cdot [T_{wall} - T_{pcm}]}{L} \left[ \frac{\text{sensible heat}}{\text{latent heat}} \right]. \quad (1.5)$$

We also consider the Fourier number,  $\mathcal{Fo}$ , as a dimensionless measure of time. It expresses the ratio between the amount of heat transmitted to the body and the sensible storage capacity of the body, and it is defined by:

$$\mathcal{Fo} = \frac{\alpha_{pcm} \cdot t}{L_{c_{pcm}}^2} \left[ \frac{\text{unsteadiness}}{\text{mass diffusion}} \right] \quad (1.6)$$

where  $\alpha_{pcm}$  is the thermal diffusivity of the PCM, and  $L_{c_{pcm}}$  is the characteristic length of the PCM, which corresponds to the length through which conduction occurs.

Both the Fourier number together with the Stefan number, are sufficient to describe the heat transfer when the phase change is only considered by conduction [17]. Finally, if we want to account the presence of natural convection during phase change, Rayleigh number  $\mathcal{Ra}$ , which defines the ratio of buoyancy forced and thermal momentum diffusivity, and it is related to the effects of natural convection in the liquid PCM. Rayleigh number is defined as:

$$\mathcal{Ra} = \frac{g \cdot \rho^2 \cdot c_p \beta \cdot [T_{ow} - T_{pcm}] \cdot L_c^3}{\mu \cdot k} \left[ \frac{\text{buoyancy force}}{\text{viscous force}} \right]. \quad (1.7)$$

### 1.4.2 Experimental Approaches

Early experimental studies were carried out by Sparrow et al. [104], for pure and impure substances used as PCM. Besides, Farid et al. [42], Zalba et al. [121], and Stritih et al. [105] conducted studies in systems with PCM to determine the phenomena involved in phase change. Their results show different heat transfer mechanisms governing melting and solidification.

Zalba et al. [121], observed that the thickness of the encapsulation, the inlet air temperature, and the airflow have a significant influence on the solidification process, whereas for melting, the inlet air temperature showed more significant than the encapsulation thickness. They also showed that solidification is mainly dominated by conduction while melting by convection.

Similar results were found by Stritih [105], who performed experimental studies on melting and solidification on rectangular containers. During their studies, they found heat transfer correlations, relating the Nusselt number as a function of the Rayleigh number. From these correlations made for melting and solidification, it can be observed that the natural convection during melting is almost ten times higher than natural convection during solidification.

Ettouney et al. [34], found that, for a vertical double pipe configuration, the natural convection was dominant during melting for upward flow of the heat transfer fluid, whereas, for downward flow, it was negligible. Thus these experimental studies relate conduction as the main heat transfer mechanism during the solidification process, while convection to melting process.

The heat transfer rates during melting and solidification are greatly affected by the geometric configuration and orientation of the container regarding the gravity, as well as the thermal boundary conditions between the fluid and the container. They play a significant role in the evolution of the shape of the remaining solid, the movement of the currents of liquid PCM and the liquid-solid interface, and the thermal characteristics of the PCM during phase change. In

general, the heat transfer rate is higher in the upper portion of all containers where natural convection dominates [27].

In general, we can classify heat transfer problems during phase change as [7]:

- conduction controlled phase change,
- convection controlled phase change, and
- conduction and convection controlled phase change.

In the next section, we cover further details about the phase change phenomena dividing the process according to the container shape. We decided to evaluate the phenomena according to this parameter, since, as we have already stated, the container geometry affects heat transfer, and therefore the thermal performance.

### Melting in rectangular vessels

Rectangular shape for PCM containers has been widely studied. Their use as PCM containers has been widely spread since they are easy to obtain and manufacture. Their thermal behavior can be categorized, according to their thermal boundary, into two types of phase change [27]:

1. constant heat flux, and
2. constant temperature.

Jany and Bejan [56] in 1987 presented a scaling theory of melting with natural convection in an enclosure heated from the side, which can be well applied to rectangular vessels. They show that the phenomenon consists of a sequence of four regimes:

1. the pure conduction regime,
2. the mixed regime, where the upper portion of the liquid gap is controlled by convection and the lower portion by conduction,
3. the convection regime, and
4. the last or "shrinking solid" regime.

An early study performed by Zhang et al. [123] presents experimental results of the melting process within a rectangular vessel filled with *n*-octadecane ( $C_{18}H_{38}$ ). Discrete sources heated one wall of this container at a constant rate. Their main findings include the observation of the significant role of natural convection and the Stefan number during melting, making the liquid-solid interface more pronounced when this number increases.

Later, Faraji and El Qarnia studied numerically the phenomenon of melting of *n*-eicosane within a rectangular vessel heated with three protruding heat sources with a constant volumetric heat generation from one side. The other sides were thermally insulated. They described three stages during melting. At the early stage, conduction was predominant at the bottom part of the PCM. They describe a second stage where natural convection was involved. During this stage, the liquid streamlines became relatively packed next to the active wall and the melting front, which leads to a relatively fast-moving flow next to those boundaries. During the third stage, the location of the intersection of the melting front and non-active vertical wall moved downward.

Yanxia et al. performed an experimental study on the thermal characteristics of the melting process of ethanolamine–water binary mixture used as PCM. This PCM was contained in a rectangular vessel heated from a vertical side. Their experiments indicated a heat transfer enhancement due to natural convection, compared with only conduction-dominated phase change. They described that the mechanism of pure conduction only occurred during the initial stage of melting and a conduction–convection coupled model was necessary for predicting



melting process accurately at later stages.

### Melting in spherical capsules

Melting in spherical capsules can be classified into two groups [27]:

1. constrained melting, and
2. unconstrained melting.

The first type occurs in experimental studies where a thermocouple is placed inside the capsule; the positioning of the thermocouple prevent the PCM from sinking or raising to the bottom or top of the sphere due to gravity. The second group of melting occurs where there is no anchor inside the capsule. In this case, the PCM will sink or rise and experience thermal contact with the wall.

### Melting in cylindrical vessels

Regarding the airflow direction, the cylindrical containers are usually arranged horizontally or vertically. The effects of gravity, diameter size, and heat exchanges are different for these two configurations; therefore, different melting patterns and performances are obtained.

Bareiss and Beer [15] performed experiments to test melting inside a cylindrical container. They found that as long as conduction is the controlling mechanism heat transfer can be expressed by correlating the Nusselt number to the Rayleigh number. When convection is controlling phase change, then, the Nusselt number is a function of the Stefan, Fourier, and Rayleigh numbers, as well as the height-to-diameter aspect ratio,  $H/D$ . They observed that for longer tubes, the melting layer found in the top of the tube does not increase significantly.

During the early studies performed by Sparrow et al. [104], [33], these authors carried out a melting cycle for a vertical cylinder, analyzing the natural convection effects. Besides, they focused on finding the shape of the remaining solid during melting. This process was done by interrupting the melting process at various stages and then observing the solid taken outside the tube. They suggested a strong relationship between the melting fraction and the dimensionless numbers of Fourier, Stefan, and Grashof. From these results they stated that melting in vertical cylinders includes three effects that can be observed:

1. Natural convection in the melt phase (liquid PCM).
2. The downward melting at the upper section of the tube.
3. The change of density of the PCM as it melts.

Furthermore, these authors observed a conical pattern in the remaining solid, which became more visible as the amount of liquid increased in the cylinder. Menon et al. [91] also observed this conical pattern for a similar study using commercial paraffin wax in slender tubes of small diameters between 1,91 cm and 3,18 cm; and heights between 30,5 cm and 61 cm. They reported that the melting fraction is also a function of the height-to-diameter aspect ratio,  $H/D$ .

Wu and Lacroix [62] performed a numerical study of natural convection controlling melting of a PCM, with isothermal boundaries. They found that heat transfer is dominated by conduction when the container is heated from the top. They also find that the melting patterns of those containers heated from different sides are far more complicated by those single side heated containers.

In a more recent study, Jones et al. [57] performed a study using a wide tube of 6,3 cm of

inner diameter and 5,98 cm of height. From their results, they expressed the melting fraction as a function of the Fourier and Stefan numbers, where conduction controls the phase change.

Shmueli et al. [98], performed a numerical study using the enthalpy-porosity approach on insulated tubes heated from the bottom and isothermally heated sides. These authors found that as melting progresses, natural convection in the liquid dominates, the remaining solid takes a conical shape, and it shrinks from the top to the bottom.

Later, Katsman et al. [64] performed a study for four different unclosed tubes of inner diameters between 0,9 cm and 3,92 cm; and a height of 17 cm of PCM. For the wider tubes in this study, they found melting patterns similar to those early reported by Menon et al. [91] and Sparrow et al. [33]. Nonetheless, for the small-diameter tubes, they observed radial melting pattern instead of the conical pattern reported in previous studies. From this observation, they concluded that conduction is the main heat transfer mechanism during melting of slender tubes of small diameter. They suggested that these vertical cylindrical containers are more suitable for heat storage applications.

More recently, Riahi et al. [108] performed a numerical study to develop tools that could recreate the same results as those obtained experimentally by Jones et al.[57].

In summary, these studies have shown that melting inside a vertical cylinder is a multi-dimensional phenomenon, and simplification into a one-dimensional problem could lead to an incorrect performance prediction. On the other hand, if the model obtained for a single container is too complex, the computational time required to predict its performance, under a more realistic model, could be excessive.

### 1.4.3 Numerical Approaches

Numerical solutions present the challenge of simultaneously solve the energy balance in the liquid and solid domains of the PCM, and at the same time try to track the solid-liquid interface position. Numerical models can be divided into:

- **Fixed grid method** (i.e. weak solution). For these methods, the spatial discretization is presented as a fixed space grid. The moving boundary between the liquid and solid phase is usually addressed using an auxiliary function [92]. Several methods have been developed using this configuration, within which we have:

#### (a) The enthalpy method

First proposed by Eyres [112] in 1946. This method expresses the phase change problem addressing the sensible and heat storage by the enthalpy term of the energy conservation equation. This method deals with the phase change interface by creating a mushy zone between the solid and the liquid and using the same governing equations for both phases. It can be simply expressed as:

$$\rho_{pcm} \cdot \frac{\partial H_{pcm}}{\partial t} = \nabla \cdot (k_{pcm} \cdot \nabla T_{pcm}) \quad (1.8)$$

where  $H_{pcm}$  is the total enthalpy,  $\rho_{pcm}$  is the density of the PCM,  $k_{pcm}$  is the thermal conductivity of the PCM. This method gained popularity with the approach developed by Voller [116], which proposed a rapid implicit solution technique for the enthalpy formulation of conduction controlled phase change problems. This method is usually

solved using finite difference schemes [116], [125], [85] or finite volume schemes [78], [116], [117], [55].

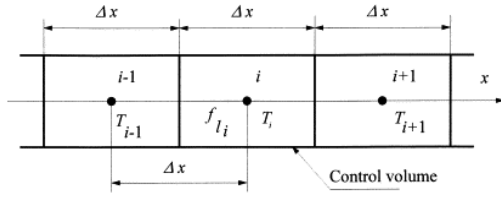


Figure 1.4 – A typical control volume grid for finite difference methods [125].

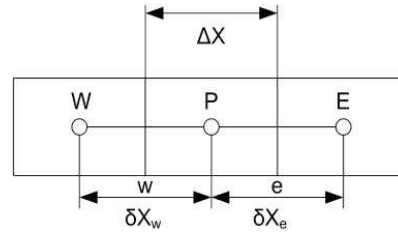


Figure 1.5 – A typical control volume grid for finite volume methods [92].

### (b) The heat capacity method

This method uses analytical/empirical relationships and numerical approximations. In here, the heat capacity term in the governing equation imitates the effect of total enthalpy (sensible and latent heat) by increasing the heat capacity value during the phase changing stage. Generally, two approaches are used for this method: the apparent heat capacity and the effective heat capacity [117], [54]. The general form for conduction controlled phase change can be written as:

$$\rho_{pcm} \cdot c_{p^A} \cdot (T_{pcm}) \cdot \frac{\partial T_{pcm}}{\partial t} = \nabla \cdot (k_{pcm} \nabla T_{pcm}) \quad (1.9)$$

where  $c_{p^A}$  refers to the heat capacity.

### (c) Analytical/empirical relationships

These methods include a wide range of approaches depending on the objective of the modeling. Some of them use the material characteristics to determine thermal properties. For instance, the heat capacity of the PCM can be determined from the differential scanning calorimeters (DSC), and then approximate the heat capacity of the PCM using a simple, direct relationship with the introduction of a fictitious melting temperature range [82], [117].

Analytical models using thermal resistance are also found in the literature. Dubovsky et al. [30], developed an analytical model for an air-PCM heat exchanger using cylindrical vessels.

Other models are based on empirical correlations that allow accounting specific phenomena during phase change, without covering in detail the governing equations of these phenomena. Often these correlations are expressed as a function of dimensionless parameters. The attractiveness of these methods lies in the possibility to adapt those correlations to other numerical methods, simplifying in some cases the modeling of the phenomena. This approach has been widely used for accounting the buoyancy effects of the natural convection within the liquid PCM [42]. In the following sections, we detail further these approaches.

- **Deforming grid methods or front tracking scheme** (i.e. strong solution). These methods develop grids that move along with the boundary layer, and therefore the position of this moving boundary is found explicitly [92], and they can be classified into two approaches.

The first approach uses a local mesh refined method, i.e., h-method; it begins with a fixed grid, and at each iteration, points are added or removed to match the actual situation. The main issue with this approach is that since the number of grid changes at each time step, it could have difficulties in maintaining the data structure.

The second method used, which try to overcome this difficulty is the r-method, also known as the moving mesh method. This method starts with a uniform mesh and then moves the mesh points, keeping the mesh topology and the number of mesh points fixed as the solution evolves. Further information about these method can be found in [68] and [83].

- **First law and second law problems.** The first law models are based on the energy conservation within the phase change, and compare the efficiency of the process to the amount of energy that can be stored in the PCM [31]. Since they do not consider the effect of time duration through which the heat is stored or retrieved, the temperature at which the heat is supplied, and the temperature of the surroundings, they can be complemented by the second law models. They together are used for the optimal design of these systems.

The first law efficiency ( $\eta$ ) of a thermal energy storage system is defined by [31] as:

$$\eta = \frac{Q_r}{Q_s} \quad (1.10)$$

where  $Q_r$  is the total thermal energy extracted in the PCM using the heat recovery process, and  $Q_s$  is the total heat stored by the phase-change material during the heat storage process.

The second law can be expressed in terms of the availability recovered ( $\phi_r$ ) or added ( $\phi_s$ ) during heat transfer by:

$$\psi = \frac{\phi_r}{\phi_s}. \quad (1.11)$$

From equations 1.10 and 1.11 it can be inferred that the first law efficiency is an indicator on how energy is utilized, whereas the second law efficiency indicates how well the availability of energy is used.

#### 1.4.4 Empirical correlations for conduction and convection during phase change

LHTES systems are currently used for a large number of applications, not only in the building sector but in several thermal applications. This is why focusing on finding practical design tools for these systems remains a realm of study. According to Joybary et al., [69] design tools for heat exchangers can be classified into two categories:

- *The simplified methods.* These methods include the traditional sizing methods such as the effectiveness-number of transfer units ( $\epsilon - NTU$ ) method, and the logarithmic mean temperature difference (*LMTD*).
- *The complex methods.* In here we take into account the methods that solve the phase change problem by explicitly solving the governing equations. These methods usually rely on CFD simulations.

The simplified methods have been attractive through years because they can be quickly implemented. They often rely on pure conduction approaches to acknowledge phase change. The main issue with these methods for air-PCM heat exchangers is that their direct used tends to

oversimplify the phase change process, usually neglecting the natural convection in the liquid PCM.

On the other hand, CFD offers a detailed simulation of the phenomena occurring during phase change, including heat, mass and momentum transport; nonetheless, the computational time can be excessive for this type of systems. These methods may result in impractical tools for certain cases.

If the computational time is a critical matter for modeling, one solution proposed is the enhancement of traditional simplified methods by accounting complex phenomena such as natural convection. For instance, Tay et al. [109] compared 3-D CFD simulations and 1-D  $\varepsilon$ -NTU with experimental data and found that when the buoyancy effects of natural convection were accounted, 1-D  $\varepsilon$ -NTU could accurately predict the performance of heat exchangers.

Some authors like Farid et al. [41] and Joybari et al. [69] have reported different approaches to understand and model melting and solidification including the effects of natural convection and two-dimensional melting. Most of these approaches rely on correlations, which can be applied to a single container or a whole system.

These correlations aim to simplifying through the definition of a single parameter or few parameters, the effects of natural convection in terms that can be easily exploitable. That is why they are usually expressed in terms of well known dimensionless numbers, which allow its use in other conditions and a physical significance of the phenomenon that we want to model. Two practical parameters that can be found in the literature are the use of an effective thermal conductivity  $k_{eff}$  and the melting fraction of the PCM  $m_f$ .

#### (a) The effective thermal conductivity $k_{eff}$

The effective thermal conductivity was used since the early studies of Farid et al., [41], [43] [42], and has been widely use for accounting natural convection since then [85]. The effective thermal conductivity is defined as the equivalent thermal conductivity that a motionless fluid in the gap would need to transfer the same amount of heat as the (real) natural convection case [5]. This approach accounts for the natural convection in pure conduction models, where the effective thermal conductivity is expressed as a function of the Rayleigh number, as follows:

$$k_{eff} = k_{pcm_l} \cdot \mathcal{Nu}_{\mathcal{NC}} \quad (1.12)$$

where  $\mathcal{Nu}_{\mathcal{NC}}$  is expressed as:

$$\mathcal{Nu}_{\mathcal{NC}} = \mathcal{C} \cdot [\mathcal{Ra}]^n. \quad (1.13)$$

In equation 1.12,  $k_{pcm_l}$  is the thermal conductivity of the liquid phase of the PCM and  $\mathcal{Nu}_{\mathcal{NC}}$  is the Nusselt number accounting for the effects of natural convection.

The major advantage of this concept is that it can be easily integrated to conductive models by replacing the thermal conduction of the material, by an effective conduction term taking into account natural convection and the variations of the melting front in more than one dimension. Saeed Mostafavi Tehrani et al. [111] shows a review of the typical experimental values found in the literature for different shapes of containers.

Nevertheless, despite the attractiveness of this approach, Joybari et al. [69] suggest some disadvantages of the effective thermal conductivity, such as:

1. Experimental data should be available a priori to evaluate the thermal conductivity.
2. Derivation of effective thermal conductivity is experimentally tedious.

3. A constant value cannot be designated to the effective thermal conductivity for a fluid that varies in temperature.
4. It cannot provide information about the melting front location.

(b) **The melting fraction of the PCM  $m_f$**

The second approach seeks to express the melting fraction  $m_f$  showing the effects of phase change controlled by combined conduction and convection mechanisms. Even though the melting fraction is not a new concept, and have been studied since the early works of Sparrow et al. [104], its use as a mean to express natural convection in conductive models is quite recent [69].

Sparrow et al. [104] and [33], developed experimental melting fraction correlation for pure and non-pure substances within a cylindrical container. They expressed melting fraction as a function of the cumulative energy of the process ( $E_{pcm}$ ) versus the maximum energy that can be stored by the material ( $E_L$ ) given by:

$$m_f \sim \frac{E_{pcm}(t)}{E_L} \quad (1.14)$$

Their results show that the melting fraction can be expressed as a product of powers of the dimensionless quantities  $\mathcal{F}oSte$ , which accounts the conductive mechanisms of phase change and,  $\mathcal{R}a$ , which accounts for natural convection in the liquid PCM.

Choi et al. [58] also developed an experimental correlation of the melting fraction (for melting and solidification), this time, for a rectangular container. Their correlation expresses the melting fraction  $m_f$  as a product of the powers of the dimensionless numbers  $\mathcal{F}o$ ,  $Ste$  and,  $\mathcal{R}a$ . Later Wang et al. [120] found a similar expression for rectangular containers. In their case, the authors assumed constant density during phase change, and therefore the melting fraction was expressed as a function of the change of volume  $V_{pcm}(t)$ , versus the total volume of the container  $V_{total}$ .

$$m_f \sim \frac{V_{pcm}(t)}{V_{total}}. \quad (1.15)$$

Katsman et al. [64] developed a more complex correlation of the melting fraction to include the effects of the downward and annular melting directions within tubes in shell and tube containers. They followed the initial expression obtained early by Sparrow [104], and adding the effects of the different patterns of the melting by including two Rayleigh numbers with two different characteristic lengths ( $L_c$ ): one based on the height and the other based on the hydraulic diameter.

Assis et al. [14] and [32] develop correlation form experimental and numerical studies for spheres. These studies also express the melting fraction as a variation of the expression developed by Sparrow [104].

More recently, Fan et al. [52] developed correlations to cylindrical containers. The authors expressed the melting fraction as the traditional product of power. Finally, the most recent study found was develop by Joybari et al. [69] in which he expresses numerically the melting fraction including the effects of natural convection as a function of the melting fraction obtained by pure convection ( $m_{f_{pc}}$ ) and the shell-to-tube radius ratio ( $R$ ).

The choice of the approach used to account natural convection will depend on the interest of the model and the experimental data available. Nevertheless, there is a major problem with



the developing of empirical and numerical correlation to describe some processes during phase change. The available data from the literature has not been correlated, making it difficult to compare the results obtained from different authors. The two main reasons for this are [7]:

- The use of different types of PCM with different heat transfer characteristics.
- The use of different dimensionless parameters and ranges.
- The non-use at all of the dimensionless parameters, making it impossible to extend the knowledge to applications beyond the original source

Therefore, the use of these correlations should be careful and always check the validity of them for the range studied. In table 1.2, we condensed some of the correlations found in the literature for melting fraction.

Table 1.2 – Summary of developed correlations for melting and solidification for PCM.

Reference	Study	Container Type	Correlation	Remark
Sparrow [104]	E	C	$m_f = FoSte \cdot Gr^{\frac{1}{8}}$	Melting with natural convection
Choi [58]	E	R	$m_f = C \cdot Fo^a \cdot Ste^b \cdot Re^c$	Solidification
Wang [120]	E	R	$m_f = C \cdot Fo^a \cdot Ste^b \cdot Ra^c$	Melting and solidification
Katsman [64]	E	ST	$m_f = FoSte^{0,75} \cdot Ra_D^{0,1} \cdot \exp\left(\frac{C}{Ra_H}\right)$	Melting for different diameters
Assis [14]	E and N	S	$m_f = 1 - \left[1 - a \cdot FoSte^b\right]^c$	Melting with NC
Assis [32]	E and N	S	$m_f = 1 - \left[1 - d \cdot FoSte^a \cdot Gr^b\right]^c$	Solidification
Fan [52]	E	C	$m_f = a \cdot FoSte^b \cdot Ra^b$	Melting with NC
Joybari [69]	N	C	$m_f = C \cdot R^m \cdot m_{fpc}^n$	Melting with NC

Note: The letters E and N, in the column study, represent Experimental and Numerical, respectively. In container type C, S, R, and ST, represents cylindrical, spherical, rectangular and shell tube, respectively.

#### 1.4.5 Visual tracking of the melting front

Visual tracking of the melting front has been found in the literature as a method to observe the phenomena controlling melting and solidification of PCM. An early study developed by Abdel-Wahed et al.[2], allowed visual information on the natural convection during the outward melting of solids around a cylinder, showing a particular interest about the effect of subcooling (see figure 1.6. After that, some studies tracked the melting fraction from experiments by interrupting the process and removing the remaining solid like Sparrow[104] (see figure 1.7). After that, some studies used transparent containers to have a direct observation of phase change, and then extract the information about the melting front position, like the one developed by Regin et al. [85] (See figure 1.8. Despite a large amount of information that can be obtained from the direct analysis of those images, we need to quantify the phenomena occurring during phase change. One way to do this is through image processing. Jones et al.[57] offered the tracking of the melting front for a wide cylinder by using image processing (see figure 1.9). Nevertheless, his study was performed under fully controlled and constant conditions, within a

wide cylinder with several thermocouples under ideal conditions, if compared to an air-PCM heat exchanger. Furthermore, other studies developed for this matter are the ones of Katsman et al. [64] (see figure 1.10), for cylindrical containers, Tan et al. [37], for spherical containers, Shmueli et al. [98] for cylindrical containers (see figure 1.12), and Bashar [16], for rectangular containers, as shown in figure 1.13.

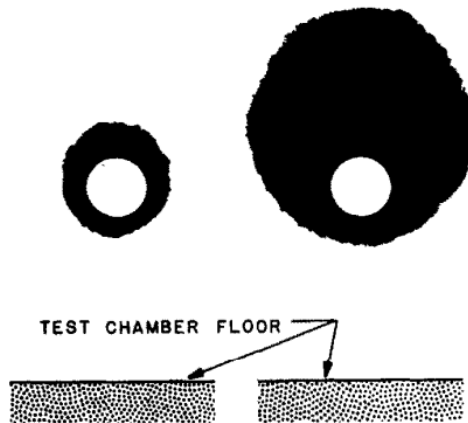


Figure 1.6 – Photographic study on melting about an embedded horizontal heating cylinder performed by Wahed.

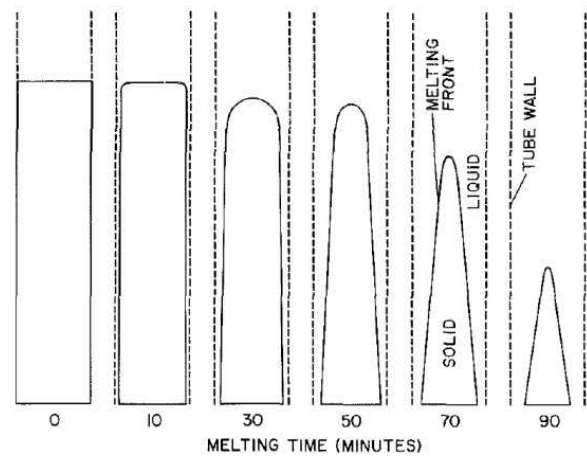


Figure 1.7 – Representation of the melting shapes and time history performed by Sparrow et al.

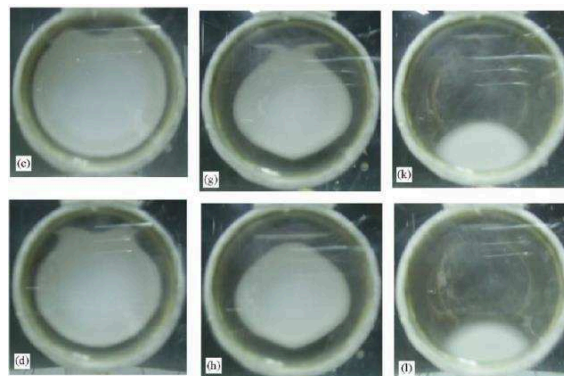


Figure 1.8 – Instantaneous photographs of the melting of paraffin wax inside a horizontal cylindrical capsule performed by Regin et al.

One reason that these studies have not been more spread is that according to some authors, carry on experimental studies coupled with data and image processing to obtain information such as the melting front position and the instantaneous melting fraction can result in a difficult task, in particular when several inlet conditions are observed [69]. Then, it is rather preferred to perform numerical studies for these cases. Nevertheless, performing experimental studies allow observing complex phenomena difficult to simulate because some situations have not been widely covered in the literature.

The latter is the case of melting on air-PCM heat exchangers composed of vertical cylindrical containers. One analytical study [30] and two numerical studies with experimental validation, performed by Sherer et al. [55] (see figure 1.14) and Promopattum et al. [38] (see figure 1.15), were found in the literature at the present time of this review. These studies do not perform further experimental analysis on the phenomena occurring during phase change in this type of



air-PCM heat exchangers.

Since these works goal is to develop further understanding of the phenomena involved during phase change in air-PCM heat exchangers, we could take advantage of some techniques such as image processing. In the next section, we will present a brief explanation of these techniques.

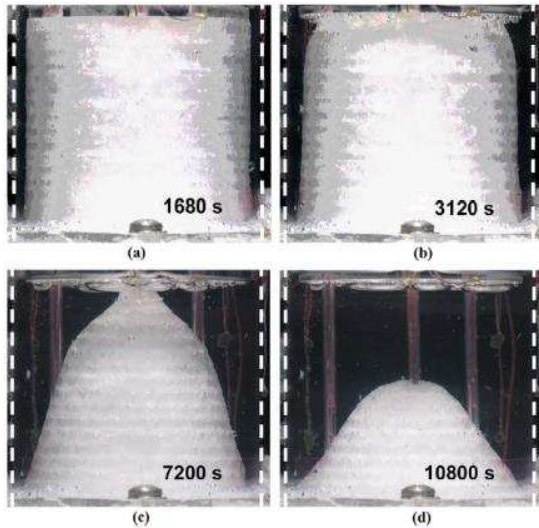


Figure 1.9 – Photographs taken during the melting of wax within the cylindrical enclosure for a wall temperature at four different times performed by Jones et al.

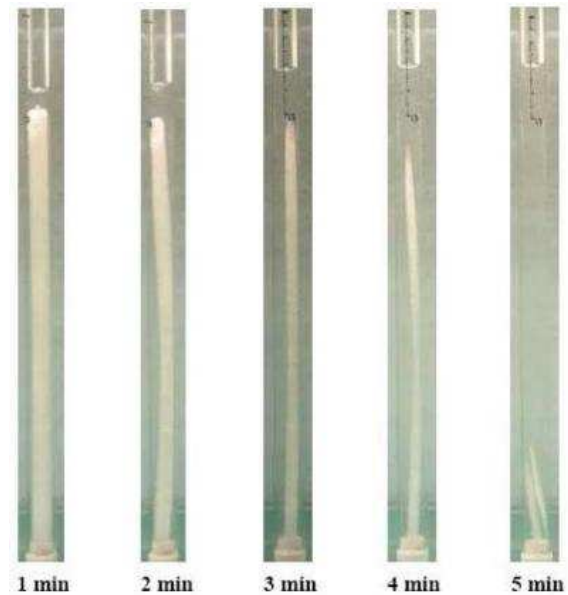


Figure 1.10 – Typical melting patterns in a narrow tube found by Katsman.

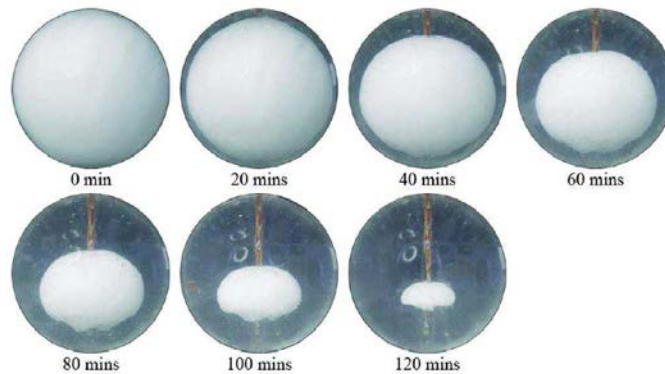


Figure 1.11 – Instantaneous photographs of the melting of PCM inside the spherical capsule performed by Tan et al.

## 1.5 Basic concepts in Image Processing

A digital image can be considered as a discrete representation of data possessing both spatial (layout) and intensity (color) information, which for instance can be represented as two-dimensional series of positions or a matrix  $I(x, y)$ . A pixel is the basic unit of information within the image at a given spatial resolution and quantization level. Each pixel within an image carries an amount of information about this image. This information content of pixel varies according to the type

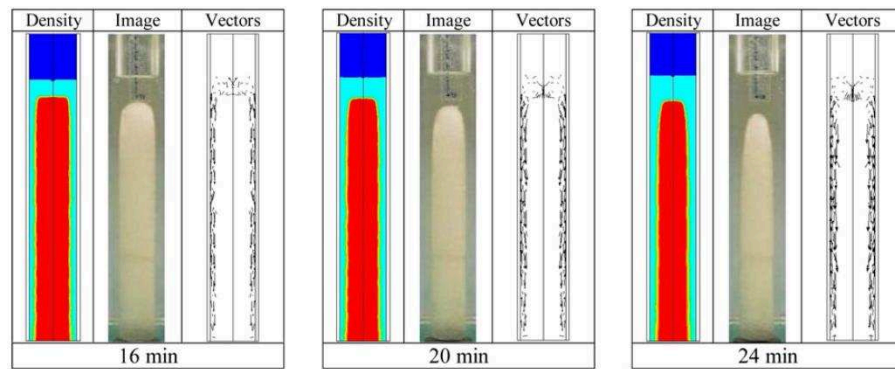


Figure 1.12 – Simulated density distributions and vector maps vs. experimental images performed by Shmueli et al.

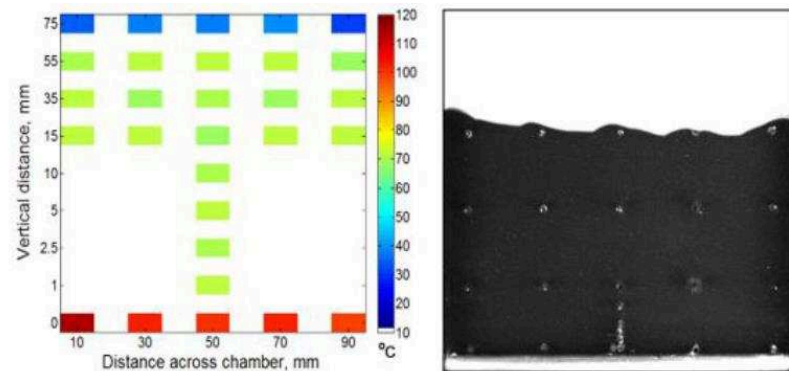
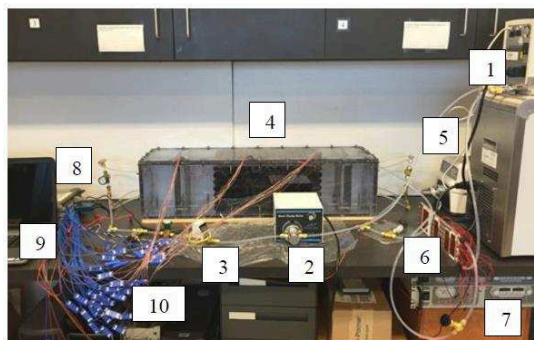


Figure 1.13 – Colormaps of the temperature field and image of the melting of PCM performed by Bashar.



- |                       |                                      |
|-----------------------|--------------------------------------|
| 1 – Thermostatic bath | 6 – Cold plate with attached heaters |
| 2 – Gear pump         | 7 – Power supplies                   |
| 3 – Flow meter        | 8 – Data acquisition system          |
| 4 – TES unit          | 9 – Computer                         |
| 5 – Gear pump         | 10 – TES thermocouple wires          |

Figure 1.14 – Experimental system for validation of the modeling developed by Sherer.

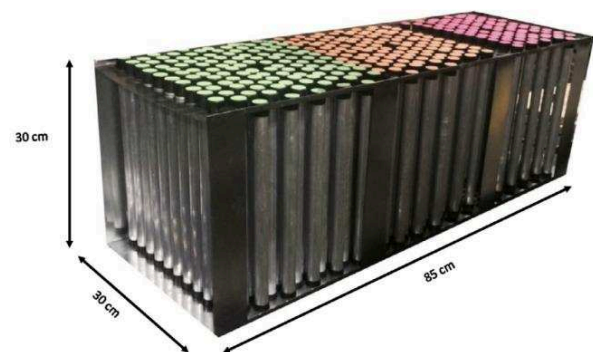


Figure 1.15 – Real scale prototype of the phase change material heat exchanger used by Promappatum.

of image [101]. There are several types of images depending on the application such as Infrared (IR), Medical imaging, 3-D images and other. In here, we only focus on those concerning our study. According to the data type some examples of images are:

- **RGB or true color image.** They consist of 3-D arrays that assign three numerical values

to each pixel, each value corresponding to the red, green and blue (RGB) image channel component respectively. These are the type of images that we commonly obtain when we take photos. The RGB color space is based upon the portion of the electromagnetic spectrum visible to humans. Each channel can display between 256 values of intensity (0-255); therefore, graphics file formats store RGB images as 24-bit images, where the red, green, and blue components are 8 bits each. This yields a potential of 16 million colors.

- **Intensity or grayscale images.** They are 2-D arrays assigning one numerical value to each pixel which is representative of the intensity at this point. Each pixel can contain between 256 values of intensity (0-255); therefore we have a single numerical value at each pixel location.
- **Binary Images.** They are 2-D arrays assigning one numerical value from the set  $\{0, 1\}$  to each pixel in the image. They are sometimes referred to as logical images. In these images, black color corresponds to zero "0", and white corresponds to one "1."

Since the RGB images that we commonly obtain, contain a huge amount of information, for further processing they are usually converted into a grayscale image, since it contains less information than a color image. Even though we reduce the amount of information, the majority of important features is maintained, such as edges, regions, blobs, junctions, and others.

As in other fields, where we separate the specific phenomena that we want to study, the same happens in the image processing. This process is called enhancement, where we manipulate different techniques to improve the visualization and quantification of the features that we want to extract from the image. The basic enhancement techniques are based on filtering. The filter applied depends mainly on the feature that we want to extract. Some filters are dedicated to noise removal or edge detection, for instance. One example of filtering for noise removal is the Gaussian Filter. It has the effect of smoothing the image, and is commonly used in edge detection algorithms.

For our case of study if we want to separate solid from the liquid phase, then it is important if we can detect the edges between these two images or if we can separate one region from the other. In image treatment this can be executed by two approaches [101]:

- **Edge/boundary methods.** This approach is based on the detection of edges as a mean to identifying the boundary between regions.
- **Region-based methods.** This approach assigns pixels to a given region based on their degree of mutual similarity.

Within an image, an edge can be considered as a discontinuity or gradient within the image [18]. Therefore most of the edge detection filters consist of derivative filters for discontinuities. They give a response when points of discontinuity are found in the image, and no response for perfectly smoothed regions. They are divided in first-order edge detection and second-order edge detection. Among the first group, we have the Roberts, Prewitt, and Sobel filters. Examples of second-order filters are the Laplacian and the Laplacian of Gaussian filters. Among them is the *Canny edge detector* which is considered the best edge detection method up to date, since they search for low error rates.

Another conventional approach used is the *Intensity thresholding*. The idea of the intensity thresholding is based on the intensity of a pixel: a threshold is used to separate the luminous regions from dark ones. A value of the threshold is selected such that, if a pixel possesses a value higher than the threshold, it is assigned to one region, while if it falls below the threshold, then it is assigned to another region [18].

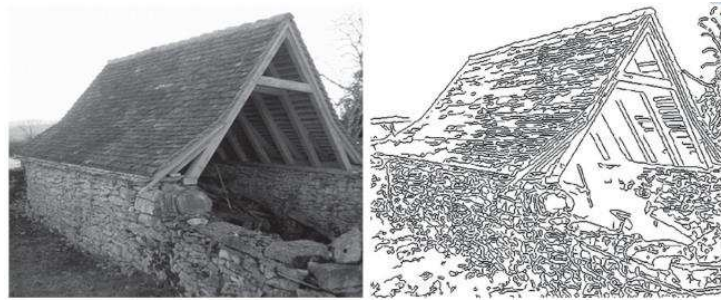


Figure 1.16 – Intensity image and Canny segmentation filter by Bergounioux.

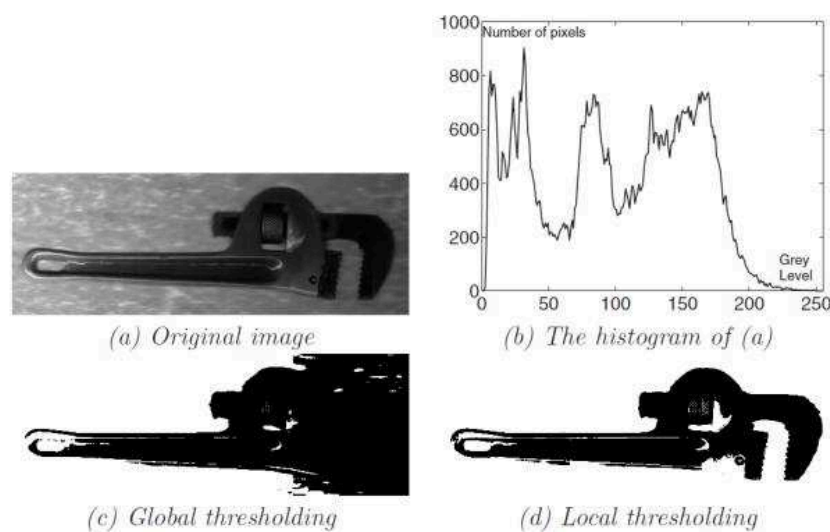


Figure 1.17 – Simple thresholding versus hysteresis thresholding by Petrou and Petrou.

## 1.6 Concluding Remarks

Regarding the general organization of this thesis, we have already stated that to develop design tools for air-PCM systems, we need a robust understanding of the physical phenomena involved in these systems. To achieve this, we rely on the theoretical background, experiments and modeling of such systems.

Therefore, in this chapter, we aimed to cover the general concepts regarding phase change and its thermal applications, with an especial focus on building applications. To do this, we surveyed what has been done so far in this subject, in a way that allows us to identify the opportunities on the designing and scientific contribution, as well as those aspects where current knowledge may be insufficient. Thus, we can make the following remarks.

*Regarding the general concepts on phase change materials:*

- When studying phase change materials, it must be considered as a single system with its encapsulation. The interactions between them affect the physical and chemical performance of the PCM. The geometry, size, and orientation of the container affect the heat

transfer performance, while the selection of the encapsulation material, also affects the chemical stability of the PCM-encapsulation system. Therefore when selecting a PCM as storage material, it must be included an analysis of its performance with a specific type of container.

- Since PCM are found in a broad range of phase change temperatures, the selection of the material, must be coupled with the desired application; otherwise, the system would not work.

*Regarding the building application,*

- The potential of storing large amounts of energy of PCM have been used to achieve the thermal comfort in summertime and wintertime. Their use as a part of a passive system seeks to increase the thermal mass of the building. Thus, it can be considered as part of the building barrier that attenuates the rapid increase of the indoor temperature of the building during summertime, due to the high outdoors temperatures; and as thermal isolation during wintertime.
- When we use PCM as an active system, we can think about it as an air-conditioning unit, where we store the surplus heat contained in the indoor air, and by doing this, we can reduce the indoor temperature and achieve thermal comfort. The advantage of this use is that its use can be controlled, matching its use with the peak load.
- One challenge that was identified from this review is that we want to develop simple tools of design for a system that includes a storage medium, a material that carries complex phenomena, such as more than one phase, change of density and moving boundary, and we want to keep this tools as simple and accurate as possible.

*Regarding the phase change materials*

- According to the studies surveyed during this review, melting results in a more complex phenomenon than solidification; in here, natural convection plays a more significant role. Therefore, more efforts have been made towards the inclusion of natural convection during melting, for the prediction of heat transfer performance.
- Another parameter which has been a subject of great interest is the tracking of the melting front position since it reveals the storage potential of the material by measuring the remaining amount of PCM in its initial state.
- Regarding the study approaches, we can state that the main problem found with experimental approaches, besides the complexities of measuring and costs of such phenomena, is that it is not easy to extrapolate the results obtained by one study under certain conditions, to other studies. This problem is linked to the effect that has the encapsulation-PCM system in the heat transfer performance.
- Respecting the numerical approaches, different methods have been addressed to describe and solve phase change; some of them focus on reducing the complexity (by sacrificing accuracy) in order to achieve a quick and simple response. Others focus on accounting mass and heat transport (including Navier and Stokes equations) but sacrificing computation time and simplicity. Nevertheless, the approach used depends on the final applications and the possibilities of the study. Even if both approaches have been widely covered, the numerical approach results in most common use in recent years; the experiments are mostly used for modeling validation.

- To overcome some of the problems stated for experimental and numerical approaches, some authors have appeal to the obtention of empirical and numerical correlations. They represent a solution "in between of" these two approaches, where the complexity of the phenomena can be reduced, facilitating the implementation of simple models. Since these correlations usually rely on dimensionless parameters, it can, by some means, allow the extrapolation of results obtained by other authors.

Finally, we noticed that, even though image analysis of phase change, has been an early method of accounting the physical phenomena, it has been used mostly as a qualitative tool, rather than been approached by image processing techniques, which can result in a quantitative tool.

This literature review leaves us questions that can be exploited as future research points, showing us those points where there is a lack of knowledge. They will be further explored during this work.





Design is a fundamental human activity, relevant and useful to everyone. Anything humans create — be it product, communication or system — is a result of the process of making inspiration real.

---

Maggie Macnab

# 2

## Air-PCM heat transfer unit definition

### 2.1 Scope

In this chapter we highlight the procedure and results for the designing of a customizable air-PCM system adapted to thermal systems on building applications. We carry out this design by making using three analysis: structural, functional and physical phenomena. Then, to solve the problem, we make interfere a methodology recently developed at the I2M laboratory. The main feature of this methodology is that it uses a patent search of key concepts related to the problem to solve, as a source of innovative solutions.

We adapted this methodology for our case of study, giving us guidelines and some criteria that help us with the designing decisions. In this way, the final design of the air-PCM system is not only guided by the phenomenology and traditional decision criteria for those type of systems but also the result of a search among innovative systems derived from the patent analysis.



## 2.2 Design of an air-PCM heat exchanger unit

### 2.2.1 Methodology for the design of an air-PCM unit

#### (a) System Overview:

The adapted methodology begins with the definition of the overall concept of the system. This step presents the system overview, where are well established the context, the problematic and the requirements of the product. This step is the starting point of the method since it provides information related to global expectations for the final product.

#### (b) General analysis:

The methodology continues with the general analysis of the system. This general analysis includes the definition of the operational architecture of the unit and the functional analysis of the system. In general terms, this section describes how the system will fit into the world, defining the external conditions, and establishing some scenarios in which the system will be used, showing its primary objectives [93]. At the end of this step, the requirement statements will be established, allowing the search for design opportunities.

#### (c) Inspiration methodology Keyword analysis:

The I2M laboratory developed an inspiration methodology, which from the search of patents proposes solutions for problems in engineering, such as the designing of new products. This methodology consists of hierarchical guidelines, which take into account the requirements initially raised for the project. Since this methodology was developed during the Ph.D. works of Valverde [114], in here we adapted some of the steps of this methodology to match our needs in the designing of an air-PCM system as a solution for thermal comfort during summertime in buildings.

Furthermore, the concepts obtained from the general analysis can be arranged as a matrix or dataset of keywords, gathering the similar concepts under a specific group. If prior knowledge of the system is available, then, the concepts extracted from this theoretical and practical knowledge can be used to enrich the dataset. By grouping these concepts, we can describe a hierarchical classification of keywords. This dataset becomes then, the initial matrix of keywords and the basis for further analysis. We call these concepts keywords because they serve as an entry for further queries related to the system. These queries provide further knowledge about the system, becoming a practical way to find innovative solutions and lines of evolution.

To increase the keywords and therefore the opportunity to find an innovative solution we can rely on the analysis of Patent Classification Codes (PCC). Furthermore, these words can be extended using a lexical database. Besides, innovation principles, evolution laws, and eco-friendly aspects can also be included in this search. Then, at the end of these processes, we will not only have the traditional, well-known concepts related to the system but also, related words that may describe the same concept in other fields. This latter allows covering a greater extension of existing systems.

This step of the methodology followed the work developed by Valverde in 2015 [114], who proposes obtaining the keyword dataset from the sources mentioned earlier. This step is an iterative process that conducts into the creation of a discovery matrix. This matrix reveals the opportunities of innovation. In our case, this matrix help us to focus our search on the design of an air-PCM unit in this work.

The classification system that is implemented to rank these keywords consist of six categories. These categories are defined as [114]:

- nouns,
- verbs/adjectives,
- physical phenomena characteristics,
- technological systems,
- types (system related),
- complements of the problem.

Within each category, there is also a hierarchy that allows separating the origin of the keyword. For this, the matrix relies on a visual classification through the use of CAPITALIZED words, **bold** words and *italic* words.

Valverde [114] set two conditions as stopping points for the iterative process: one for a specific search, and the other one, for the global analysis of patents. For the former, the stopping point can be identified when all the searches throw the same concepts. A high incidence of patents containing the same technologies and phenomena may indicate, on the one hand, that these patents can be called classics for this function. On the other hand, it is likely not to be necessary, performing a new search with the words that come out of these patents. This search could be stopped, when the discovery matrix is filled, linking most of the physical phenomena with the associated technologies which have been found. If there is any black space, it could be due to two reasons: some technical impossibilities or scientific lock-ups; or could be as well, some opportunities to innovate.

In our case, once the discovery matrix is filled, we analyze the keywords to look for possible solutions for the proposed system. It is not surprising that several types and tendencies of solutions can appear as a solution. Thus, in order to focus our search, a set of initial requirements could be specified in advance, if there are some limitations to address on the design. Now that each step of the methodology has been defined, we can proceed to explain the design process.

### 2.2.2 System Overview

We propose to design a system consisting of a heat exchanger containing phase change materials. With the integration of PCM in heat exchangers, we aim to exploit the large energy storage capacity during phase change, as a cooling source for indoor air during warm days.

To begin the designing process, the first question that we must ask is *What do we need from the system?* To answer this question, we enlist the tasks and objectives that the system being designed must fulfill as follows:

- During the daytime, the system should cool down the place by storing the surplus heat in the PCM. Melting occurs as a consequence of this storage.
- During nighttime, regenerate the PCM using the cold nocturnal air since we need them for future use.
- Try to keep the cooling/heating potential of the unit achieved during phase change, during the standby periods. This means: keep as low as possible the losses of the system.
- The system must be able to be compatible with the use of commercial PCM.
- The design should allow the integration in different types of building applications, either as an active unit or as part of the building structure.

In brief, the resulting design must consist of a heat exchanger containing PCM as storage material, which during the daytime, can cool down the place. Besides, we need a system that we can activate when the indoor thermal comfort conditions are not reached by natural means.

Thus, the PCM must be in a solid state at the beginning of the day; for this reason, if the PCM is in a liquid state, solidification must take place during nighttime. The air-PCM system must maintain the comfort conditions at the outlet, regardless of the inlet conditions.

### 2.2.3 Physical phenomena involved in phase change applications for cooling and heating

In section 1.4, we presented an overview of the physical phenomena related to phase change, emphasizing the effects of the shape of the container. However, we cannot directly apply the specific knowledge highlighted in that section due to two reasons:

1. We do not know, a priori, the shape of the container; therefore we could not profoundly analyze and understand the physical phenomena since it varies from one geometry to another.
2. The system that we are designing in here is the coupling of two media: the air and the container with PCM; therefore we must think as a coupled air-PCM system rather than just a phase change problem.

Despite these two reasons, we try to keep a general analysis, regardless of the specific considerations of each container and geometry. This analysis aims to find the key parameters that play an essential role in the thermal performance, regarding the heat transfer and the energy storage/release from an air-PCM unit. These key parameters are obtained through the study of the physical laws associated with the physical phenomena existing in the air-PCM unit, providing the departure point for the design.

The unit is expected to be subjected to temperature changes, including the temperature at which the phase change occurs in the PCM. This leads to the presence of heat and mass transport making possible the sensible and latent heat storage.

If the unit is operating during daytime and nighttime modes, then it is possible that phase change occurs in the PCM if the inlet conditions of the unit allow it. Whereas, during the standby modes, the airflow inlet condition are usually outside the phase change temperature range, and therefore, if there is any heat transfer, the energy will be stored or release in its sensible form.

An appropriate way to evaluate the effect of these physical phenomena is through the use of indicators. The physical parameters that intervene in each of these indicators could be evaluated as possible key parameters for the design, depending on the effect they have on the performance of the system. For this section of the study, the most relevant dimensionless numbers, as well as specific geometric parameters, were selected for the performance evaluation.

Despite the convenience of classifying the physical phenomena according to the operation modes of the unit, in this study, we propose to divide these phenomena into a global domain (air-PCM unit) and a local domain (PCM container). This approach was selected due to the notorious differences of the physical interaction and the thermal analysis, when the exchanger is described as a whole, in comparison to the physical phenomena involved in a single container.

#### Global Phenomena

Regarding the thermal behavior of the air-PCM heat exchanger, forced convection (*FC*) governs the physical interactions. The air carries the surplus heat, and the forced convection between the air and the PCM containers allows the transfer of part of this heat. This convection mechanism depends on the airflow inlet conditions, i.e., air velocity and temperature, the container shape,

and geometric arrangement, regarding the direction of the airflow.

Dimensionless numbers usually quantify the effects of these parameters. The dimensionless numbers related to external forced convection in an air-PCM heat exchanger are the Nusselt number  $\mathcal{N}u$ , and the Reynolds number  $\mathcal{R}e$ , which were described earlier in section 1.4.1. The main mechanisms and key parameters are summarized in table 2.1.

Table 2.1 – Key parameters obtained from the physical phenomena analysis at the global domain of the air-PCM heat exchanger.

Parameter	Equation	Units	Resulting key parameters
Energy balance (inlet-outlet)	$P = \dot{m}_{air} \cdot c_{p_{air}} \cdot [T_{in} - T_{out}]$	[W]	$\dot{m}_{air}$ $T_{in} - T_{out}$
Convective heat transfer coefficient	$h_{air} = \frac{\mathcal{N}u \cdot k_{air}}{D_{hyd}}$	$[\text{W} \cdot \text{m}^{-2} \cdot \text{K}^{-1}]$	$h_{air}$ $k_{air}$ $D_{hyd}$
Nusselt	$\mathcal{N}u = \mathcal{P}r^n \cdot \mathcal{R}e^m$	[-]	
Reynolds	$\mathcal{R}e = \frac{\rho_{air} \cdot v_{air} \cdot D_{hyd}}{\mu_{air}}$	[-]	$v_{air}$

Several key performance indicators (KPI) exist in the literature for thermal energy storage systems in buildings [79]. One example of these KPI is the effectiveness of the heat exchanger  $\varepsilon_{hex}$  which is related to the maximum charge and discharge power of the unit. The effectiveness gives the ratio between the cooling power of the unit installed and the maximum cooling power that can be achieved by this unit; for air-PCM heat exchangers, the maximum effectiveness during phase change is achieved when the air temperature at the outlet is the same that the melting temperature of the exchanger. Thermal losses are usually due to the temperature difference between the unit and its surroundings, occurring mainly along the heat exchanger.

The PCM containers act opposing to the air passage within the heat exchanger, resulting in a pressure drop. When the air and the elements of the system are not in thermal equilibrium, heat transfer occurs, eventually leading to energy storage since part of the energy that was carried out by the airflow is transferred to the heat exchanger elements.

### Local Phenomena

This section aims to summarize the typical interactions between the PCM, the container, and the surrounding air, when an air-PCM heat exchanger is analyzed, regardless of any particular container shape and geometrical arrangement. Some of these phenomena were earlier mentioned in section 1.4, however in here, we extract those general criteria that we will further consider for evaluation.

Since phase change is not an instantaneous process, the PCM changes gradually from one state to another; e.g., from solid to liquid or vice versa. During this period, for some materials, a visible frontier between the liquid and the solid phase appears and its position moves. Besides, phase change itself is the natural response of the material to the heat transfer from the air and surrounding elements at a temperature near the melting point.

The PCM melting point can be a single temperature value for pure materials or a range of temperatures for alloys. If this is the case, there will be sensible and latent heat storage during

phase change. Although, the amount of sensible heat that can be stored in the PCM during phase change is usually small in comparison to the latent heat. Nevertheless, we should consider it if the material selected as storage material stores sensible heat during the designing stage, because the melting is desired to be in a small range and in between the comfort zone range for the building.

Locally, we can identify four domains during phase change within a container: air, wall, liquid PCM, and solid PCM. The heat transfer between the air and the container wall is controlled by forced convection (*FC*), and by conduction through the container wall (*Cond*). Inside the PCM, this heat transfer could be controlled either by conduction (*Cond*), by natural convection (*NC*) or both simultaneously. When the effects of natural convection are significant, buoyancy in the liquid PCM appears, leading to some currents in the molten PCM that begin to erode the solid PCM, causing some specific melting patterns. These patterns are linked to the shape of the container, the orientation regarding the gravity, and the thermal boundaries.

Stefan number *Ste*, is commonly used to define the phase change since it presents the ratio of sensible to latent heat; and the Rayleigh number *Ra*, for natural convection. The main mechanisms and key parameters are summarized in table 2.2.

Table 2.2 – Key parameters obtained from the physical phenomena analysis at the local domain of the air-PCM heat exchanger.

Parameter	Equation	Units	Resulting key parameters
Newton's law of cooling (FC)	$q = h_{air} \cdot A_{tube} \cdot [T_{air} - T_{pcm}]$	[W]	$h_{air}$ $A_{tube}$ $T_{air} - T_{pcm}$
Convective heat transfer coefficient	$h = \frac{Nu \cdot k_{air}}{D_{hyd}}$	[W·m <sup>-2</sup> ·K <sup>-1</sup> ]	$k_{air}$ $D_{hyd}$
Stefan	$Ste = \frac{c_{p_{pcm}} \cdot [T_{ow} - T_{pcm}]}{L}$	[-]	$T_{ow} - T_{pcm}$
Rayleigh	$Ra = \frac{g \cdot \rho^2 \cdot c_p \cdot \beta \cdot [T_{ow} - T_{pcm}] \cdot L_c^3}{\mu_{pcm} \cdot k_{pcm}}$	[-]	$T_{ow} - T_{pcm}$

## 2.2.4 General Analysis

### Operational Architecture (Structural Analysis)

The air conditioning system constantly interacts with its environment, and therefore the structural analysis (operational architecture) must describe these interactions. For this reason, the system is divided into three principal parts:

- the external inputs,
- the air-PCM system,
- the outlet of the system.

Figure 2.1 shows a general scheme of the system. In this scheme, the external inputs refer to the external media, all the parameters that may influence the inlet conditions, e.g., meteorological conditions and building materials. The second part, the air-PCM system, includes all the elements present on a PCM heat exchanger, e.g., the PCM, the containers, ducts, fans,



and others. At the outlet, the conditions given by the system must ensure the thermal comfort of the place. The final architecture proposed for the system must fulfill the initial objectives of the study, i.e., the air-PCM system must maintain the comfort conditions at the outlet, regardless of the inlet conditions.

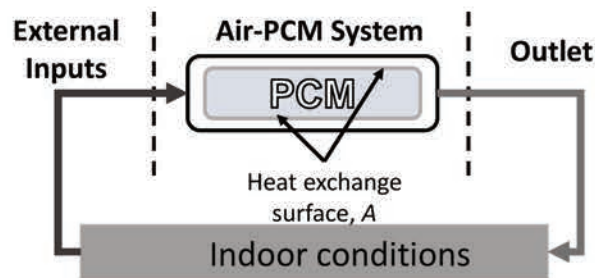


Figure 2.1 – Architectural scheme of the principal parts of an air-PCM heat exchanger for cooling applications in buildings: external inputs, air-PCM system and the outlet; and the boundaries of the system (dashed lines).

### 2.2.5 Functional Analysis

The functional analysis describes the operation modes of the system during its life (functioning) stages. For the present study, these operation modes were obtained from the system overview, the operational architecture and the review of the physical phenomena.

A group of initial constraints was defined before the development of the functional analysis. These constraints define the limits of the final product regarding the different functions that it must accomplish during its lifetime. Some of these constraints are related to the overall life (functioning) stages. For example, the system should match eco-friendly standards, so that, the final product could be considered as a sustainable solution. This constraint must be taken into account during all the life (functioning) stages of the system, i.e., the designing process, the fabrication and assemblage, the active operation periods, eventual repair, maintenance and disassemble. Other constraints are just related to a specific operation mode of the product, for example, it is desired that the system could maintain a minimum of heat losses during the standby mode.

The first two stages of the development of the product are the design and fabrication of the system. In these stages, the selection of the different materials composing the system is the primary issue since the performance will be significantly affected by them. Therefore, the materials used for the system must be easy to find and to manipulate. Since the PCM are likely to experience a volume expansion during phase transition, the material selected for the container should be capable of achieving some deformation levels, so that, the container can withstand the change of pressure. The manufacturing process should also include methodologies that consider the use of eco-friendly materials and the reduction of the amount of material used.

The manufacturing cost is usually considered as a constraint. Therefore, if possible, some optimization techniques for reducing the energy consumption and materials cost should be considered. It should also be considered the technical issues regarding the material selection, such as the thermal and mechanical properties, and how they affect the performance of the system. The assemblage and transport of the parts should be simple and easy to do. The building characteristics will restrict them, and they will undoubtedly influence the geometrical arrangement used for the containers.



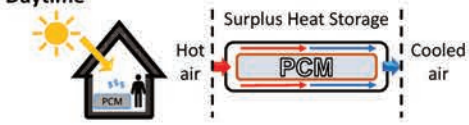
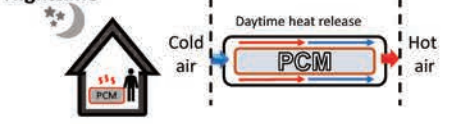
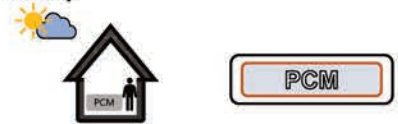
This study is mainly focused on addressing the operation modes that relate directly to the active periods of the system, i.e., the charging, discharging, and standby periods. Table 2.3 on page 50, illustrates the main physical interactions during these three operation modes, highlighting:

- the principal functions of the system during each of them (*PF*), and
- the main constraints (*CF*) associated to each of these modes.

The discharging process occurs during the daytime. In here, the principal function of the system is to cool down the building (*PF1*). For this, the hot air of the place, resulting from the high temperatures reached during the day in summertime, must pass through the system (*CF1*). Due to the temperature differences between the air and the system components, heat exchange occurs. When the air at the inlet position reaches the conditions necessary for the phase change, the PCM starts to melt, and while this happens, the surplus energy from the air is stored in the PCM in the form of latent heat. Accordingly, at the outlet, the air temperature is lowered, since part of the heat of the air has been transferred to the system. Therefore, the airflow coming out from the system could achieve the cooling objectives for the building.

During this operation mode the air passage must be ensured; otherwise, the heat transfer would not take place (*CF1*). When this process takes place, water condensation can appear as a sub-product and, if that is the case, we must recuperate this water (*CF2*).

Table 2.3 – Summary of the life stages during the active periods at the external level of the system.

Operation mode	Principal functions ( <i>PF</i> )	Constraints ( <i>C</i> )
<p><b>Daytime</b></p> 	Cool down the place ( <i>PF1</i> ).	Ensures the air passage ( <i>CF1</i> ). Recovers the condensation water ( <i>CF2</i> ).
<p><b>Nighttime</b></p> 	PCM regeneration ( <i>PF2</i> ).	Enhance the energy storage ( <i>CF3</i> ). Evacuate the hot air ( <i>CF4</i> ).
<p><b>Standby</b></p> 	Energy storage ( <i>PF3</i> ).	–

The PCM must be in a solid state at the beginning of the day. Therefore, if the PCM were used for cooling purposes during the day, they must be regenerated. During the nighttime, the ambient air temperature can achieve temperatures that could solidify the PCM. Therefore during the night, the regeneration can take place if the inlet temperature is lower than the solidification point. The principal function to be achieved in here is the solidification of the PCM (*PF2*). As a consequence of the solidification, the surplus heat that was stored during the day in the PCM is released. This process allows the PCM to store the surplus heat from the air for future use of the system.

The constraints during this process are related to the storage of “cooling potential” (*CF3*) and the evacuation of the heat that has been stored during the day (*CF4*). For this, the air passage through the system must be ensured, and the heat transfer and the energy release



should be enough for future use. Under some circumstances, this system could be used as a heating source. In this case, the heat stored during the day can be used to heat the place during the night. For this purpose, the design should meet the heating needs of the building.

In between these two processes, the system may stay in a standby period. This situation could happen in the scenario where the thermal conditions in the place are within the range of comfort, and there is no need for the system to begin its operation. Likewise, it may occur that all the PCM have been melted during the day or solidified during the night; and then, if the surrounding conditions allow it, the heat exchange would only lead to sensible heat storage or release.

An efficient system should present a minimal amount of losses during these periods. For instance, once the PCM has been solidified, all extra energy stored during this standby period results in a reduction of the heat storing potential for next use, reducing the cooling performance of the system. Thus, the main function of this operation mode is related to the energy storage (*PF3*).

The results from both, structural and functional analysis highlight two main objectives of the system: (*O1*) to transfer the heat and (*O2*) to store and release the heat. These objectives, alongside with the analysis previously done, define the system requirements. Once the systems requirements are established, then the first draft of the keyword dataset can be proposed. In this case, the physical phenomena involved were analyzed as prior knowledge.

### 2.2.6 Keywords search and analysis

In this section, we aim to present the approach followed to get the keywords dataset, based on the method developed by Valverde [114]. The resulting dataset presented in here was obtained from a tool developed by the author in Microsoft®Excel. This dataset is analyzed to further obtain design proposals. In order to build this dataset, it is necessary to start from the basic concepts that revolve around the main objectives identified early:

1. (*O1*) — To transfer the heat.
2. (*O2*) — To store and release the heat.

These concepts are the components of what we call the initial matrix or keyword dataset, who are the basis for the rest of the keywords that were found and that will be analyzed next.

Table 2.4 – Initial set of keywords for the query.

Initial set of keywords						
TRANSFER	STORAGE	ENERGY	FLUID	AIR	SYSTEM	PHASE CHANGE MATERIAL

#### Matrix Description

Regarding the visual classification, the principal words are written in CAPITALIZED letters; they result from the initial search and previous knowledge about the system. From these keywords, the matrix is expanded by semantic search. These concepts appear as lower case words in the matrix. Finally, new concepts are obtained from the iterations, the patents analysis, and further expansion of these concepts. Those keywords are written in *italic* words (see section 2.2.1).

The **Nouns** category includes the concepts related to:

- the principal objectives of the system: (i) to transfer heat, and (ii) to store and release the energy,
- the words related to the architecture of the system (devices, equipment), and
- the initial concepts related to the departure point of the search.

The second category, **verbs/adjectives/adverbs**, provides the action verbs derived from the functional analysis, e.g., to exchange, to store, to heating and to cooling.

Thirdly, **the physical phenomena/characteristics** category includes words that were the result of a prior understanding of the physical mechanisms governing the different processes involved during the system lifetime. The **technological systems** highlight the words that resulted from the patent search and iterations, while the **type (singular/plural)** category, delves into a detailed description of the system. These words are related to the possible geometries and shape parameters.

Finally, the last category, **complement**, includes the possible complements to the search, as well as the possibilities for material selection.

### Matrix Analysis

The aim of developing a complete matrix, involving a large number of keywords related to the system, was to obtain an overview of the most important aspects related to the design of the system. Some of the words obtained are familiar to every line of evolution that can be analyzed because they describe the principal functions, materials or actions that the system must undergo. Other words are more specific to a singular line, and therefore, only apply to certain outcomes. In here, we refer to the line of evolution of the opportunities of design. For example, we can say that the evolution of the shape of the container from a simple, rectangular container to a segmented, corrugated rectangular container with fins is a line of evolution.

Tables 2.5 and 2.6 on pages 53 and 54 show the keyword database. The matrix analysis consists of an evaluation of the relevance of each word regarding the objectives and requirements established at the beginning of the study. If the word follows a line of evolution that could lead in a different direction, regarding the objectives, then it is eliminated from the matrix or considered for future work.

During this analysis, the enhancement of the thermal performance of the system was used as the point of reference. Each of these keywords is analyzed; nevertheless, we only mention in here, the more relevant for our design. To help the understanding of the matrix analysis, we mention the category (first column of the matrix) and the sub-category (rows of the matrix) together.

The first thing that we can observe from this matrix are the two first concepts of the column **Noun: TRANSFER** and **STORAGE**, which correspond to the principal objectives of our systems and therefore, keywords that come from the initial matrix (see table 2.4). In this same column, we find a column presenting keywords related to the material properties named **PHASE CHANGE MATERIALS**, which describes the characteristics required from the storage materials.

Further, in this **Nouns** category it is also included a column named *MIXTURES*. The keywords in this column are related to those parameters linked to the PCM properties that could lead to an enhancement of the overall performance of the system. Even though, some options and opportunities to innovate can be imagined in this sense, and a whole search can be developed from this line of evolution, these words do not quite fit the initial objectives of the use of commercial PCM. Nevertheless, it could be considered as a later improvement, once the system

Table 2.5 – Keyword database for air-PCM heat exchangers (Part I).

	TRANSFER	STORAGE	ENERGY	FLUID	AIR	SYSTEM	PHASE CHANGE MATERIAL	SURFACE
Nouns	transference exchange transition	tank cistern container reservoir	physical phenomenon energy transfer energy storage	gas liquid substance	medim element	method structure item apparatus equipment device units module process	PCM substance	boundary bound border layer
	passage displacement conveyance	depot depository repository		fluent mobile rheological fluid matter	mixture of gasses	mechanisms modular artifact artefact	high heat of fusion latent heat storage LHS unit TES unit	
	MIXTURES assortment consolidation unification assemblage mix recombination conglomeration	VOLUME bulk mass quantity amount	TREATMENT management direction handling	ISOLATION separation discreeness discontinuity disjunction dis- association segregation	WALL partition divider fence stratum interlayer cover	FLOOR level base	PATH trajectory passage way course line	SHAPE form contour embodiment pattern morphology
Verb/ Adjective/ Adverb	MEANS substance part corpus	MAGNETS attraction attractor attractive feature magnets	CEILING upper surface cap	AREA expanse coverage limit length extent	THICKNESS dimension width			
	STOCK destocking stocking keep	REFRESH refreshment cooling	HEAT heating heat up temperature	EXCHANGE -interchange interchan- geable exchanging	INCREASE increasing change increased modify enhanced	REDUCE reducing decreased simplify reduced attenuated	FORCE forcing push pushing press	VARIATE decreasing fluctuating changing moving varying
	accumulated storing	freshen refreshen cool	change state	commute switch				
Physical Phenomena/ Characteristics	ACTIVATE activating alter modify actuate	ACT interact interacting acting move react	EFFICIENT effective efficacious operative operative efficiency	ISOLATE isolated isolating insulate set apart separate	CREATE creating make produce	SEGMENT separate divide disjoin segmenting reduce	ORIENT orientation orientating orientate position aligning	MIX mixing unify integrate desegregate combine
	CONDUCTION transmission of heat transmission	CONVECTION temperature change transfer of heat	THERMAL thermal exchange thermal conduction thermal transfer thermal conductivity	FLOW flow regime flux stream current	PHASE CHANGE state change change of state	RADIATION rays waves radioactivity	HEAT high tempera- tures high energy heat transfer	ELECTRIC electricity piezoelectric electrons
	conductivity	molecular motion natural convection forced convection	caloric temperature thermal gradient	turbulent flow laminar flow	physical change phase transition	particles energy radiated	latent heat mass heat	
Physical Phenomena/ Characteristics	MAGNETIC electro- magnetic magnetic forces magnetized attractive force magnet	MECHANIC mechanical mechanical process	CHEMICAL thermo- chemical chemical substance chemistry	GRAVITY gravitation gravitational- attraction gravitational force	SPEED velocity rate acceleration fastness	THERMO- DYNAMICS conversion of energy	CATALYSIS contact action chemical process chemical change chemical action	ABSORPTION sorption soaking up
	COMPACT- NESS concentration density denseness tightness spatial arrangement	VISCOSITY viscousness resistance of a liquid	ELASTIC DEFOR- MATION change of shape distortion modification alteration	EXPANSION COEFFICIENT expansivity thermal expansion expansion	HYDRAULIC DIAMETER hydraulic radius handling flow	MASS volumetric mass bulk volume matter		

is fully established, but for now, it will no longer be considered as a search direction.

One group of keywords obtained from the iterative process of patents search are those presented in the column called *MAGNETS*, inspiring interesting opportunities in the design. During the melting process, the cooling potential available is related to the amount of the PCM that is still in its solid state. At the beginning of the process, the solid PCM is in direct contact

Table 2.6 – Keyword database for air-PCM heat exchangers (Part II).

Technological Systems	HEAT EXCHANGERS	AIR CONDITIONING	FAN current of air movement of a surface ventilator fresh air breathing device	HEAT REGENERATOR regenerative heat exchanger regenerator	HEAT STORAGE energy storage thermal energy storage heater steam accumulator heat bank			
	transfer heat refrigeration refrigeration cycle space heating	thermal comfort A/C removing heat cooling the air removing humidity to treat air						
Type (Singular/Plural)	SPHERE	TUBE	PLATE	CORRUGATE	ROUGHNESS	SMOOTH	FINS	LAYERS
	round shape spheroid spherical surface	cylindrical shape duct pipe cylinder conduit	sheet flat solid flat artifact layer membrane panel	corrugation corugate fold furrow	raggedness smoothness not smooth texture	free form roughness smooth texture fine texture	fin vane blade flaps stabilizer	sheet flat solid structure stratum
	CONDUITS	BAGS	DIA-PRHAGMS	DOUBLE	SQUARE	RIGID	DEFOR-MABLE	DYNAMIC
	activating alter modify actuate	interact interacting actibg move react	effective eficacious operative operative efficiency	isolated isolating insulate set apart separate	creating make produce	separate divide disjoin segmenting reduce	orientation orientating orientate position aligning	mixing unify integrate desegregate combine
STATIC	OPEN	CLOSED	WAVES	ENCAP-SULATION	BLINDS			
unchanging adynamic motionless stationary stable	opnened unstoppered exposed unprotected available	close enclosed nonopening available	controls of flows pipes	micro-encapsulation macro-encapsulation capsule enclosing encapsulated	shutters shade louvre			
Complement	MATERIALS	SEGMENTED	POSITION	THICKNESS	RVTHM	HYBRID	ELEC-TRODES	BUBBLE
	aluminium steel plastics metal metallic elastomer fibers elastic materials fiber synthetic material lightweight material silvery ductile SMM shape memory elastic substance alloy polymer compound composition material composite fabric foam	segment section divide into split up segmental divided	inside outside displace spatial relation place perspective	dimension length width height	regular recurrence cyclicity periodicity recurring regular intervals	cross crossbreed inter-crossed crossed interbred	conductor electrode	globule of gas globule spherical body small globule hollow globule covering

with the container walls, but once the melting progresses, a liquid PCM layer appears, and therefore, the presence of convection as one of the main heat transfer mechanisms. In here, the magnets are proposed as a resource for enhancing the melting process, where adding some magnetic particles to the PCM and then, control them through an external magnetic mechanism could achieve better heat transfer rates.

In the category **Physical Phenomena /Characteristics** we found another source of enhancement of the thermal performance. Similarly to *MAGNETS*, *GRAVITY* proposes the idea of the use of an external force as a resource for heat transfer enhancement. In this case, this source is free, and it can be used similarly that the magnets, analyzing the container orientation where the gravity plays a major role regarding the enhancement of the heat transfer rate.

Likewise, in the **Physical Phenomena /Characteristics** category, *ELECTRIC*, *MAGNETIC*, and *MECHANIC* proposed similar keywords: external resources that can be used to enhance the system performance.

By this form of analysis, we can be inspired to perform a design that meets our requirements. In the following section, we perform a further analysis of the most pertinent keywords and categories that leads us to find the design of our air-PCM heat exchanger.

### **Selection of the line of evolution**

The analysis of the keyword database can lead to several lines of evolution that would result in a variety of final products. For instance, we could have followed the inspiration coming from the *MAGNETIC* keywords and develop a model that uses magnets to control the melting and solidification. Nevertheless, at the beginning of the search, it was established as a departure point that the line of evolution from the analysis of the keyword matrix would revolve around the concepts of thermal performance, geometry, and shape, instead of the PCM properties and features. This decision allows the use of several types of PCM, commercial types among them because the enhanced design proposed would not be a direct function of an enhancement of the PCM selected.

Our search in the keyword dataset is focused on a container shape or group of containers and their geometrical arrangement, which enhance the thermal performance of the air-PCM system. As it was mentioned earlier, relying the design decisions on indicators can be an excellent strategy to perform the evaluations of the possible solutions and to find the final solution or design.

Two thermal performance indicators allow to quantify and evaluate the selection of the container. Those indicators correspond to the two main objectives of the system: (*O1*) their heat transfer performance and (*O2*) their ability to store energy (see section 2.2.1). For this process, four typical container shapes were studied: plates, circular cylinders, spheres and rectangular cylinders (box-tube type). The decision of considering, as a departing point, only typical containers without thermal performance enhancement techniques as fins and rough surfaces, lies on the consideration of the ease of manufacturing and the adaptability to the different geometrical arrangement of these containers.

To find possible solutions for our design, we analyze together the objectives of the system, the key parameters obtained from the physical phenomena, and the keywords dataset. The physical phenomena described in section 2.2.3 were used to find the key parameters governing the performance indicators. Furthermore, the keyword dataset analysis is used as a source of opportunities for the design.

#### **(a) Analysis of the key parameters:**

In section 2.2.3, we extracted the key parameters from the global and local phenomena which we summarized on tables 2.1 and 2.2. Now we proceed to link those parameters to the objectives defined for our system.

- **Heat transfer (*O1*)**

In a single container, a high compacity (surface area to volume rate;  $A_{container}/V_{container}$ ) promotes better heat transfer rates due to the large heat transfer surface area ( $A_{container}$ ), and the reduced volume ( $V_{container}$ ), which opposes a lower thermal resistance, due to its reduced

hydraulic diameter ( $D_{hyd}$ ). From this we can conclude that we need to promote in our design maximizing the heat transfer surface area ( $A_{container}$ ), and minimizing the Volume of the container ( $V_{container}$ ).

Regarding the interactions between the air and the container, we can also increase the heat transfer rate by increasing the forced convection between them. High impact velocities ( $v_{air}$ ) between the air and the container, can result in an increase in the convective heat transfer coefficient ( $h_{air}$ ), and therefore in the heat transfer rate, which is desirable during the active operation modes of the unit.

If we now consider the whole system, globally, compact heat exchangers can result in an energy efficient solution which promotes higher rates of heat transfer and small volumes, weights and sizes. The present a high surface area to volume rate ( $A_{container}/V_{container}$ ). The major problem to overcome is the high-pressure drops that are associated with this kind of design.

- **Energy Storage (O2)**

For heat storage in a single container of PCM, the larger the volume, the greater the mass of PCM and therefore, the amount of heat that can be stored. On the other hand, a large heat transfer surface area can lead to undesirable losses when the energy is stored, decreasing the cooling potential of the PCM. From this, we can conclude that in order to promote desirable heat storage rates, we need to maximize the volume of the container ( $V_{container}$ ), and reduce the heat transfer surface area ( $A_{container}$ ).

Since we need to reduce all possible loss of energy, we need to minimize the effects of heat transfer during the storage of energy. This means that we need to keep as low as possible the convection between the air and the PCM. Therefore minimize the air velocity ( $v_{air}$ ), and the convective heat transfer coefficient ( $h_{air}$ ), are desired.

These analyses reveal what we need to do to enhance our objectives, and the results are summarized in table 2.7. Nevertheless, if we observe this table, we can see that there are physical and technical contradictions (C) between the decisions on the key parameters for both objectives; if we enhance one objective, we do it at the expense of the other objective. Therefore, before going further in the analysis of the keywords to find out which design opportunities we have, we need to identify those contradictions.

Table 2.7 – Key parameters selected from the physical phenomena analysis.

Key parameter	Description	Units	O1	O2
$A_{container}$	heat transfer surface area	[m <sup>2</sup> ]	↗	↘
$h_{air}$	convective heat transfer	[W·m <sup>-2</sup> ·K <sup>-1</sup> ]	↗	↘
$v_{air}$	air velocity	[m·s <sup>-1</sup> ]	↗	↘
$D_{hyd}$	Hydraulic diameter of the container	[m]	↘	↗
$V_{container}$	Volume of the container	[m <sup>3</sup> ]	↘	↗

(b) **Identification of the physical and technical contradictions:**

We can summarize the physical and technical contradiction as follows:

- **C1:** it is required to maximize the heat transfer surface area ( $A_{tube}$ ) to meet objective 1 (O1), and to minimize it to meet objective 2 (O2).



- **C2:** It is required to minimize the volume of storage ( $V_{tube}$ ) to meet objective 1 (**O1**), and maximize it to meet objective 2 (**O2**).
- **C3:** high rates of convection should be promoted during the active periods and avoided during the standby mode.

With the identification of the decision regarding the key parameters and the contradictions, we can now proceed to analyze the keywords dataset.

(c) **Opportunities of solution:**

At the beginning of this section, we said that, as a departure point, we were going to consider only the typical shapes of the container. From the preceding points, the keywords analysis and the identification of contradictions, we determine the behavior desired for each key parameter. We proceed now to make a further analysis of tables 2.1 and 2.2, concerning the concepts that could inspire us to find a suitable solution regarding the geometry and shape.

- *Solving the physical and technical contradictions*

To solve the physical and technical contradictions, we rely on the innovation principles related to the time and space separation. We refer to *time separation* when a characteristic is present when it is necessary, and absent or with another value within other cases. In the other hand, we refer to *space separation* when a characteristic is present in a part or section of the system, and absent or with another value within other cases.

For our case, the two objectives of the system **O1**: to transfer the heat, and **O2**: to store the heat occur in different operation modes, meaning that they happen in different times of the days. Therefore, applying time separation can be suitable as a solution technique for this matter.

Table 2.8 – Physical contradiction when comparing the objectives of the system.

Contradiction	Solution Proposed	
	<b>O1</b>	<b>O2</b>
<b>C1</b>	Large surface	Small surface
<b>C2</b>	Large Volume	Small Volume
<b>C3</b>	Dynamic fluid	Static fluid

- *Choosing a design*

We can remark from the summary presented in table 2.8 that in order to achieve a good performance of our design, we should focus on the heat transfer surface area of the container and the heat exchanger, the storage volume and the nature of the airflow.

These parameters were linked to the keyword database in tables 2.5 and 2.6 in order to search the possible techniques or methods for solutions. The most relevant keywords to this search have been shaded in cyan color for better understanding.

To understand the selection of the container, we should observe the effect of each container regarding the objectives and the surface and volume parameters. Figure 2.2 on page 58 shows the lines of evolution for the PCM container selection.



Regarding the surface, it is desired a large surface to enhance heat transfer, a characteristic that is common in plate type containers, and then, a type of container that is desired to retain. However, this large surface can become a problem during the standby periods, because it can also enhance the losses.

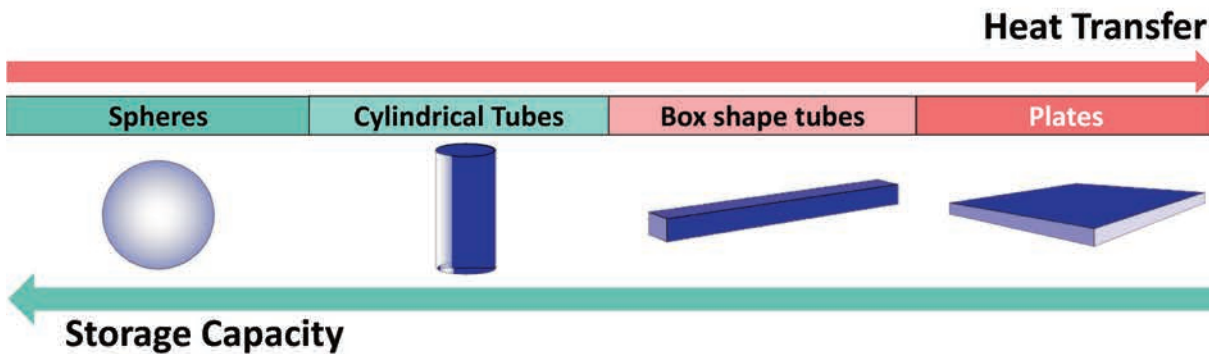


Figure 2.2 – Lines of evolution of the container shape related to the two main objectives, line 1: heat transfer and, line 2: Storage capacity.

A technique found in the keyword analysis is the segmentation of a body in multiple bodies (see the section: **Verb/Adjective/Adverb**). By segmenting a single plate, into several parallel plates, we enlarge the heat transfer surface area in contact with the airflow. Furthermore, we can also divide each of these plates into another type of container, such as small diameter cylindrical tubes, which present a good heat transfer surface area to volume. Indeed, this configuration leads to a tube bundle arrangement, which is preferred for a significant amount of industrial thermal applications due to its compactness and heat transfer rates.

This segmentation in tubes, also modify the path of the airflow (see the section: **Nouns**) and could further difficult the air passage through the system, increasing the heat convection coefficient and the turbulence associated with the  $Re$  number. By doing this during the active modes of the unit, we can achieve a dynamic fluid by promoting forced convection. The inclusion of fins, corrugated surfaces and others could also increase the heat transfer rate.

Furthermore, we can vary the rhythm of the airflow path (see the section: **Complement**), increasing the heat transfer between the air and the tubes. We can achieve that by promoting dynamic interaction from the tubes (see the section: **Type**). Then, the solution can be based on mobile tubes. This solution would also lead to the forced convection within the PCM.

On the other hand, we need the minimal exchanges during the standby periods, leaving the airflow within the exchanger as statical as possible (see the section: **Type**). This can be achieved by isolating (see the section: **Nouns**) and closing the unit, where the only interactions between the airflow and the tube, would occur by natural convection at low rates.

These decision leads to a design that accomplishes the objectives of the system and at the same time, overcomes the physical contradictions, respecting the initial constraints. One thing which has not been decided yet is the orientation of these tubes. We already mentioned that the geometrical distribution of the containers regarding the airflow path and the gravity would lead into different melting shapes and therefore different heat transfer rates.

Moreover, these tube bundle can be arranged on an in-line and staggered distribution of the horizontal and vertical position of such tubes. Staggered arrangement present better heat transfer performance since it has higher convective heat coefficient values, for similar properties, conditions, and materials. In the same way, "cross-flow arrangement" between the air and



the tube, present a more tortuous path, where the condition of each row is dependent on the previous row. This is why we decided to face our tubes vertically.

In summary, we proposed a segmentation of a single plate into a line of small diameter cylindrical vertical tubes, separating in space the initial container. The decision of vertical tubes was made to take advantage of the "cross-flow arrangement" between the air and the tube. Slender tubes of small diameter allow a larger heat transfer surface area and a low-temperature difference between the surface of the tube and the core.

Then, during the active operation modes, i.e., charging and discharging periods, where heat transfer should be maximized, forced convection between the air and the containers would be ensured by the integration of an activation system of fans, and by increasing the turbulence with a geometrical arrange of tube bundle, either in-line or in parallel.

For the standby periods, the presence of only natural convection between the air and the containers added to the compact design of the tube bundle, they would not favor heat transfer, achieving minor heat losses.

The final design proposed is a high-compactness tube bundle heat exchanger with cylindrical tubes of small diameter, using PCM as heat storage media, that allow the movement of such tubes on its own axis, as shown in figure 2.3 and 2.4.

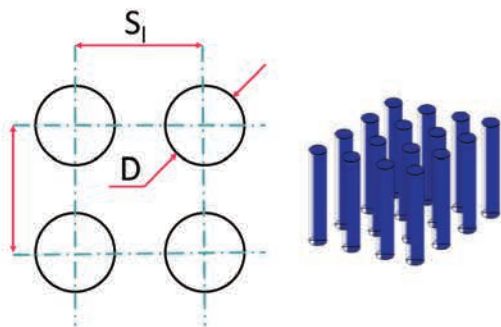


Figure 2.3 – Final design: tube bundle heat exchanger with cylindrical tubes of small diameter, using PCM as heat storage media.

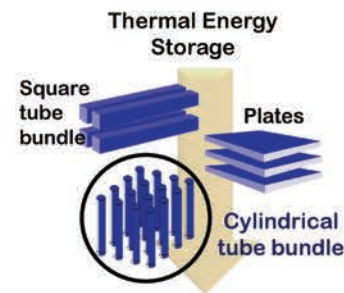


Figure 2.4 – Evolution of the air-PCM heat exchangers at the I2M laboratory.

## 2.3 Concluding remarks and perspectives

The design process of an air-PCM unit is mainly focused on the thermal application desired. Having this as a departure point, we can make the selection of the PCM, which is rather reduced, since it needs to be coupled with the melting point corresponding to such application. Geometry is what is usually subjected to a design process that leads to a system that can assure the best thermal performance. The geometry selection is commonly based on the objectives of the system, existing systems found in the literature and simulation processes and models.

In this chapter, we proposed to approach the designing of the air-PCM system as a product, following an inspiration methodology that can be subjective in some decisions, but that nevertheless seeks for optimal performance results. Regarding this design process we can gather the following remarks:

- Displaying the air-PCM system as a product, allow us to address all the life stages of this system, not only the functional ones, that are usually of interest in thermal applications.

By doing this we can assess the construction of the air-PCM system as an integral solution, carrying out an efficient disposition of its manufacture, materials, functioning and discard.

- Patent search allows exploring further possibilities for enhancing heat transfer in an air-PCM heat exchanger that may not be found in the literature review.
- The problems associated with phase change, such as physical phenomena and physical and technical contradictions, can be addressed since the designing, facilitating the implementation of these systems.
- We found that a geometrical arrangement of a tube bundle, composed of vertical slender tubes results a solution that meets the design criteria, overcoming the physical and technical contradictions by separating its functioning in time. Therefore, we have different types of functioning depending on the operation mode and the objectives. Nevertheless, the final selection of the system depends mainly on the desired applications and the expectation of the users.

In the following chapter, we explore experimentally the physical phenomena associated with the design selected during this chapter. By doing this, we can achieve a deeper understanding and get closer to our objective of finding the means of developing design tools.

An experiment is a question which science poses to Nature, and a measurement is the recording of Nature's answer.

---

Max Planck

# 3

## Experimental Approaches

### 3.1 Scope

This chapter called **Experimental Approaches** aims to develop a thoughtful study of the physical phenomena involved in an air-PCM heat exchanger. To achieve this objective, we designed a test bench where we placed an in-line tube bundle heat exchanger, based on the design obtained from Chapter 2. Then we elaborate and execute a series of experiments in which, the different conditions to which the exchanger would be submitted under real operational conditions could be tested. These experiments were carried out between 2015 and 2016, aiming to develop a better understanding of the global and local phenomena occurring inside the designed heat exchanger.

To achieve this identification, we measured air velocities and temperature measurements, together with a visual tracking of the phenomena through photographs. The main limitation of these experiments concerns the achievement of a detailed instrumentation in the local domain. Since the containers used in these experiments have a reduced size, detailed instrumentation, like those typically found in the literature, would significantly affect the normal development of the phenomena we want to observe. These experiments only show the results related to an in-line heat exchanger for a fixed geometry of containers.

## 3.2 Experimental setup and procedures

In this work we aim to provide the knowledge and the required insight for the developing of design assistance tools. Such tools could consist of models that allow the prediction of the performance of air-PCM heat exchangers. As we stated before in the introduction (see section 1), the developing of these design tools is nourished by the physical phenomena understanding and the modeling of the desired system.

To develop a deeply understanding of the physical phenomena, we proposed to rely on the the information provided by the theoretical background, the experimental results and further data processing related to these results. Since we did not found a fair amount of information concerning the type of heat exchanger that we propose to study, therefore the experiments should seek to fill in the gaps found in the literature, so that we could develop appropriate models.

The experiments carried out during these works aimed to fulfill two main objectives. The first objective is to achieve a proper understanding of the physical phenomena that could lead to the development of predictive models for the thermal performance of the air-PCM heat exchanger presented in this study. The second objective of these experiments is to validate through an energy balance of the exchanger, the models further proposed for air-PCM heat exchangers.

### 3.2.1 Design of the experiment

To design our experiments, we use as a reference the analysis of the physical phenomena developed in the literature, and the analysis carried out during the designing process. Since we are focusing on building applications, these experiments seek to recreate an air-PCM unit that aims to ensure the thermal comfort during the daytime in a building.

We focus on answering three questions:

- *Which domains are we going to study?*
- *What are we going to study?*
- *How are we going to study them?*

To answer the first question we rely on the analyze that we made during the design. In general, we can define the operations that undergo these heat exchanger into three physical domains. The first domain is the building in which we want to maintain thermal comfort. The second domain is the unit, which will allow us to ensure this thermal comfort; and finally, the third one corresponds to the PCM containers, which will store and transfer the necessary energy.

If we control the inlet conditions of the test bench directly, we can recreate, the indoor conditions of the house. Thus, for the experiments, we propose to study only the global domain and the local domain. In figure 3.1, we show the three domains related to air-PCM heat exchangers. We aim to look forward in the interaction between the local and the global domain since we follow the statement that a better understanding of the role of each container within the unit could lead to a better prediction of the thermal performance of the unit.

Now that we have selected our domains of study, we proceed to answer the second question. To do that, we focus on what we need to complete the understanding and further modeling of the physical phenomena.



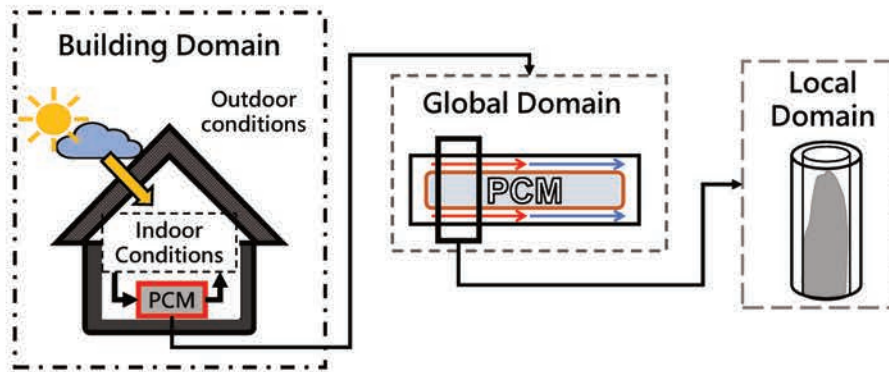


Figure 3.1 – Physical domains for experiments: the building domain, the global domain, which represents the air-PCM heat exchanger unit, and the local domain, which represents the PCM tube.

From these experiments we want to identify and evaluate the phenomena governing each domain, the interaction of such phenomena between the two domains of study and the evaluation of the performance of the process involved. Then at each domain we focus on:

- **The global domain:** in here, we focus on the global phenomena related to the unit as the energy storage and release, the heat transfer between the air and the unit components, and the global heat losses.

From these results, we can evaluate the performance of the aforementioned process. Among the evaluations that we can perform, it can be quantified the cooling/heating power  $P_{cool}$ , the operation time  $\Delta t_{op}$ , and the performance of the unit through its effectiveness  $\epsilon_{hex}$ .

- **The local domain:** in here we focus on the interactions between each container and its surrounding air. This is a domain composed of the air, the tube wall, and the PCM within a tube. The development of the phase change is one of the major analysis points because it can give us important hints about the parameters of greater importance that intervene in the phase change, and therefore that we must retain for the modeling. In this domains is important to identify how the parts interacts between them, and the phenomena governing those interactions. It is also desired to quantify the amount of energy that has been stored or released from the material and the rate of these processes.

A summary of the principal physical phenomena involved is shown in figure 3.2.

To end the design of our experiment, we need to answer the third question. From the previous analysis in the literature and during the design, we know that the interaction at each domain is related to the heat transfer processes involved. Besides in both domains, global and local, is included the interaction between the air and the PCM container. Therefore we can propose to process the process the experiments and relate these domains through the study of the convection between the air and the container, expressed in terms of the so-called Newton's law of cooling by:

$$q_{air-tube} = h_{air} \cdot A_{ow} \cdot (T_{air} - T_{pcm}) \quad (3.1)$$

where  $h_{air}$  is the convective heat transfer coefficient and,  $A_{ow}$  is the heat transfer surface area of the tube.



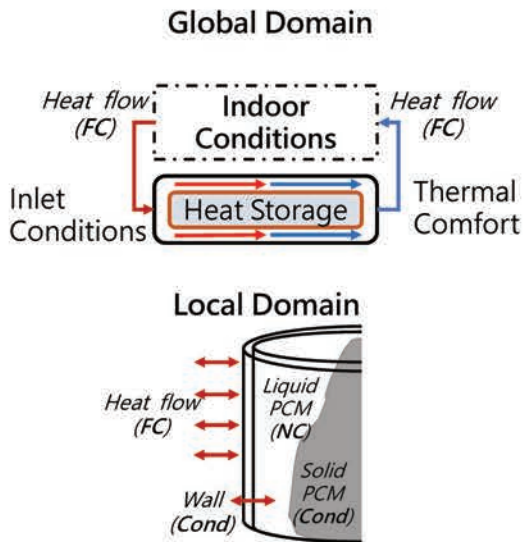


Figure 3.2 – Physical phenomena to identify through the experiments at the global and local domain. Codes: FC: forced convection, NC: natural convection, Cond: conduction.

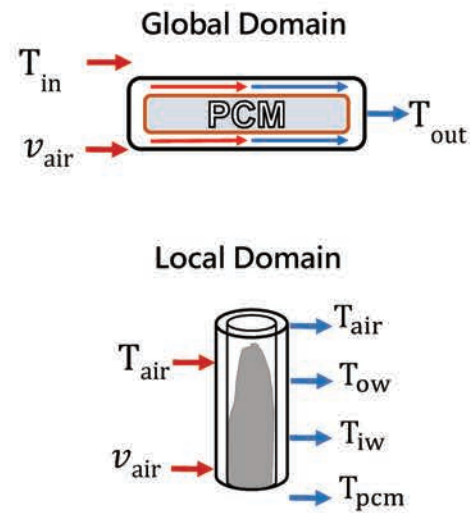


Figure 3.3 – Parameters proposed to be measured during the experiments at the global and local domain. In red are represented the input parameters of the experiments and in blue the outputs of the experiments.

If we solely focus on each domain, we can define them as control volumes, and then, the measurement need from each of these domains can be expressed in the terms of the energy balance of each of these control volumes. To complete such balances, we use temperature measurements and air velocity measurements. Using them, we can identify the phenomena by further processing of the data obtained. The proposed measurements can be seen in the figure 3.3.

Furthermore, in order to reduce the complexity of the phenomena during the experimental analysis, an initial group of assumptions was made to focus the search during the experiments. At the end of those experiments, these assumptions were proven or refuted. A complete list of these assumptions is presented in table 3.1.

### 3.2.2 Experimental setup

#### Experimental Apparatus

We propose for the experiments a test bench that allows to control and evaluate the inlet conditions; that allows to measure the global and local exchanges, and that allows us to visualize the phase change. Figure 3.4 presents a schematic diagram of the parts of the proposed test bench. It has an inlet (a) and an outlet air duct (b), through which the outdoor air passes due to the activation of a fan at the entrance of the test bench (c). This 94 W fan is the 160 L from Radiospare® is coupled with a rheostat, which allows varying the inlet airflow up to a maximum flow rate value of  $750 \text{ m}^3 \cdot \text{h}^{-1}$ .

A heating coil (d) is placed right after the fan to control the air inlet temperature. It uses a PID controller, which integrates a thermocouple ( $\pm 1,0 \text{ }^\circ\text{C}$ ) that senses the temperature at the heat exchanger inlet. Both charge and discharge cycles (corresponding to the solidification and melting cycles) take its airflow intake from the outdoor air for the experiments. If the outdoor air temperature is not low enough to ensure the solidification of the PCM in the heat exchanger,



Table 3.1 – Main Assumptions for experiments.

Physical Factors	Simplifying assumptions	Overall remarks
1. Possible gravitational, chemical, elastic, and electromagnetic effects.	Heat and mass transfer controlled mainly by conduction, others effects are neglected.	Most common case.
2. Supercooling and nucleation effects in the PCM.	Assumed not present.	Reasonable assumption in many situations.
3. Variation of the thermophysical properties.	Assume constant in each phase ( $c_{pcm_l} \neq c_{pcm_s}$ , $k_{pcm_l} \neq k_{pcm_s}$ ).	Convenience of simplicity. Reasonable for most materials under moderate temperature range variations.
4. Density changes.	Assume constant ( $\rho_{pcm_l} = \rho_{pcm_s}$ ).	Necessary assumption to avoid movement of material.
5. Surface tension and curvature effects on the interface.	These effects are neglected.	Reasonable and consistent with other assumptions.
6. Presence of sensible heat during phase change.	Only latent heat storage occurs during phase change ( $St \approx 0$ ), constant specific latent heat during the cycle and the energy storage in the container is neglected.	Reasonable if the phase change occurs in a small temperature range.
7. Local temperature and heat transfer coefficient variation along the tube.	External convective heat transfer coefficient is calculated through correlations for the tube bundle.	Results extremely difficult to measure experimentally the local temperature in each tube.
8. Local temperature and airflow variation along the inlet section on the test bench.	The temperature measurements at the centroid of the inlet section represent the overall inlet temperature.	Reasonable for the experimental cases. Convenience in temperature measurement and less intrusiveness.
9. Temperature variation in the volume of PCM	One single temperature measurement representing the behavior of the entire tube.	Convenience in temperature measurement and less intrusiveness. Reasonable if phase change occurs mainly by a radial conduction mechanism in small volumes.

then a mobile air conditioner (*e*), is used to regenerate these PCM. A galvanized steel duct, insulated with glass wool, of a diameter 0,2 m and length 1,5m, connects the fan with the rest of the test bench.

Additionally, to ensure a well-mixed airflow, a diffuser (*f*) was located at the beginning of the heat exchanger and a nozzle (*g*) at the outlet, both with an opening of 0,4 m. The original test bench was designed with a cross section that allowed the adjustment to different sizes of containers. For these experiments, the height of the container is smaller than the original cross-section; thus, to avoid a by-pass of the air and potential losses, an insulating wood slab was placed under the tubes resulting in a cross-section of (0,3 x 0,24) m<sup>2</sup>.

The heat exchanger module, (*h*), is composed by the wooden box of 2,0 m length (*i*), through which the airflow passes, and the tube bundle (*j*) which is placed within the wooden box. One of the sides of the heat exchanger consists of a Plexiglas® slab, which by being transparent, allows the visualization of the experiments and thus, the phase change tracking. The test bench leans on a metal board equipped with rollers which facilitates the transportation.

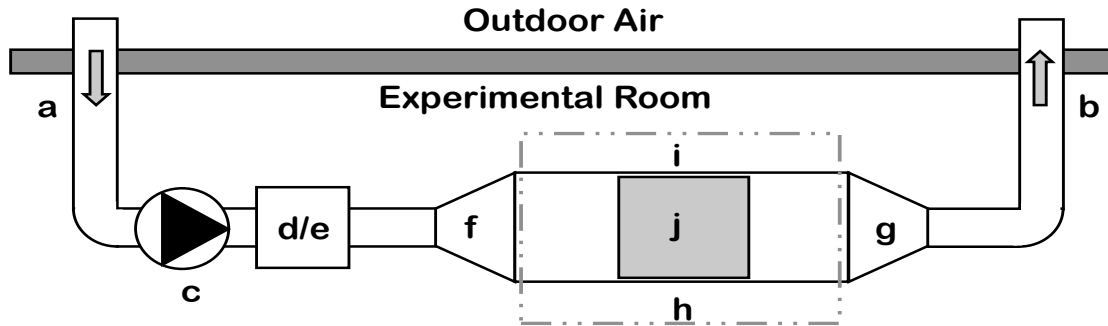


Figure 3.4 – Top view of the proposed experimental setup in the test room: a) inlet air duct b) outlet air duct, c) fan, d) air heating coil, e) mobile air conditioner, f) the diffuser, g) the nozzle, h) heat exchanger module, i) wooden box j) the tube bundle.

### Air-PCM heat exchanger

The heat exchanger module is composed of 99 tubes, distributed in an in-line arrangement of 11 rows. To optimize the thermal performance of the heat exchanger, the tube bundle must be compact, which, according to Žukauskas and Ulinskas [126], tube banks with dimensionless pitches that corresponds to  $\delta_L \times \delta_T \leq 1,25 \times 1,25$ , are considered compact. Therefore, the transversal ( $\delta_T$ ) and longitudinal ( $\delta_L$ ) pitches between the tubes were set to 0,03 m.

A schematic of the heat exchanger is shown in the sub-figure *a* of figure 3.5. For this in-line arrangement, the diagonal and transversal pitches corresponded to the same values, giving a square distribution of the tubes, that can be observed in sub-figure *b* of figure 3.5.

Glass tubes are used as PCM containers; they have been selected due to the advantages offered by this type of containers, considering that they are easily obtainable, they presented a uniform thickness, and their properties are uniform in all the geometry. Additionally, since they are transparent, the melting and solidification of the PCM can be visualized. Regarding its thermal properties, the glass presents a specific heat of  $800 \text{ J}\cdot\text{kg}^{-1}\cdot\text{K}^{-1}$  and a conductivity around  $1,2 \text{ W}\cdot\text{m}^{-1}\cdot\text{K}^{-1}$  [65], about six times larger than the PCM (see table 3.2). The major drawback of this selection is the fragility of the tubes, which leads to having extreme care when handling them.

Some techniques were tested to ensure a fixed position of each tube in the wooden box. From them, the one that best suited our needs is the use of conical screws that fixed each tube to the wood through the lid, being secured on the outside of the heat exchanger with a nut. This fixation technique can be observed in sub-figure *a* of figure 3.6. Each tube has a height of 0,24 m, of which only  $0,21 \text{ m} \pm 0,02 \text{ m}$  are in direct contact with the PCM in a solid state. This 0,03 m high air space allows the expansion of the PCM without deforming the container, besides giving enough room for the screw fixation system, as can be observed in sub-figure (*b*) of figure 3.6. These tubes have an external diameter of 0,0245 m with a wall thickness of 0,001 m.

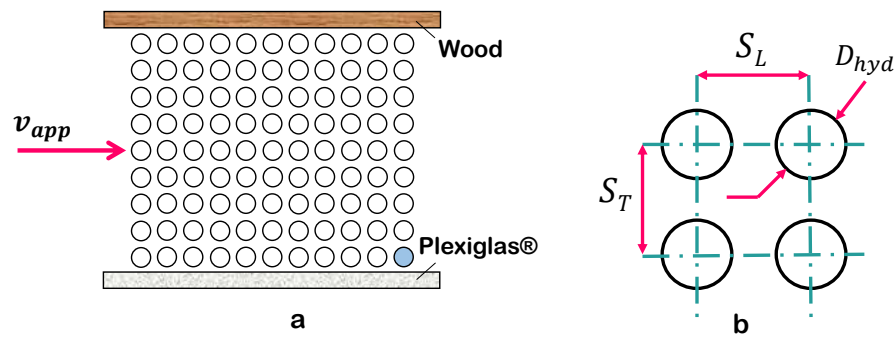


Figure 3.5 – Geometric features of the test bench: a) “In-line” arrangement of 99 tubes and b) Longitudinal pitches for the geometric arrangement of the heat exchanger.

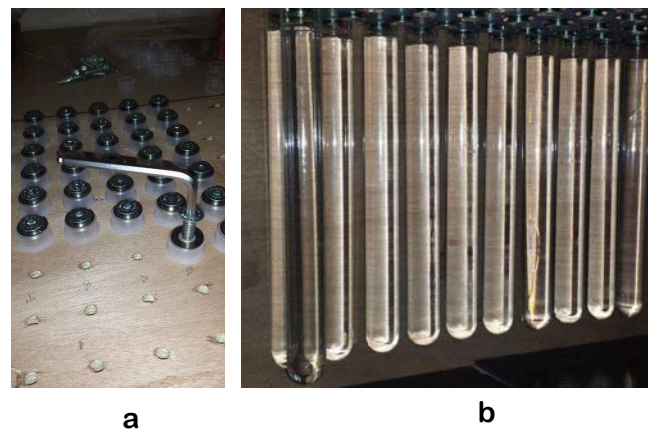


Figure 3.6 – Setting-up of the test bench: a) installment of fastening screws in the wooden structure, and b) glass tubes installment inside the test bench.

Table 3.2 – Principal thermal properties of the materials used during the experiments.

Property	Units	Glass [65]	Plywood [35]	Plexiglas [110]	PET [46]
Specific heat capacity	$[\text{J} \cdot \text{kg}^{-1} \cdot \text{K}^{-1}]$	800	1215	1470	1300
Thermal conductivity	$[\text{W} \cdot \text{m}^{-1} \cdot \text{K}^{-1}]$	1,2	0,12	0,19	0,23
Density	$[\text{kg} \cdot \text{m}^{-3}]$	2300	545	1180	1500

### PCM selection

Three different types of PCM were available in our lab for the experiments: two organic PCM, Rubitherm® RT28HC and Rubitherm® RT21, and Rubitherm® SP25E2, a mixture of organic and inorganic components. Rubitherm® RT28HC was chosen as the storage material for the experiments because it presented the most attractive features for controlled experiments. The thermal properties of this PCM were obtained from the product datasheet [25], the previous tests carried out in our lab by Rouault, [87], and from the works carried out by Soares [99], from whom we obtained complementary data.

PCM Rubitherm® RT28HC presents a melting point around 28 °C, making it suitable for

experiments that take the inlet air of the outdoors because it has solidification points that can be reached at room temperature. Another attractive feature of this PCM is that it presents a visible difference between the liquid and the solid phases. When the PCM is in a solid state, it presents a white color, whereas, when it is in the liquid state, it is transparent. This difference of colors between the phases is convenient for the visual tracking of the melting and solidification fronts during the experiments. Additionally, this product is chemically inert, so no reaction with the container material, nor the thermocouples are expected.

The DSC results of the works developed by Rouault [87] are presented in figure 3.7. A rapid characterization of this PCM was carried out by DSC with a temperature rise (magenta) and fall (lime-green) set point of  $1,5 \text{ }^\circ\text{C}\cdot\text{min}^{-1}$ . The author reported that this method induces a deviation of the estimation of the sample temperature because a too fast evolution of the setpoint does not leave the time to homogenize the temperature in the sample, thus, the conditions are non-isothermal in the sample.

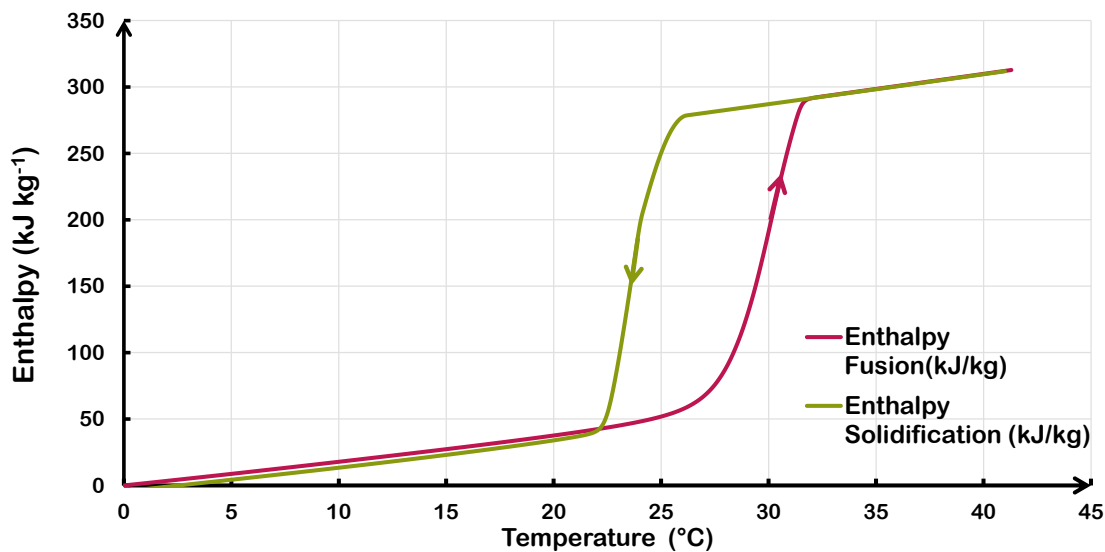


Figure 3.7 – Characterization of paraffin Rubitherm®RT28HC by DSC performed at a rate of  $1,5 \text{ }^\circ\text{C}\cdot\text{min}^{-1}$ . Color code: magenta: rise and lime-green: fall.

The thermophysical properties of PCM Rubitherm® RT28HC have been listed in Table 3.3. According to this table, melting and solidification will not occur isothermally, but in a temperature range, leading to sensible and latent heat storage or release during phase change. Although, this temperature range is not so broad that the sensible heat storage within the PCM becomes considerable, besides that the PCM selected presents a high latent heat storage capacity. A single conductivity value was found for both phases in the literature reviewed. Regarding the density of the material, we can observe a density difference between both phases which could lead to the appearance of currents in the liquid PCM.

### Metrology of the experimental setup

During the experiment design we established temperatures and air velocities measurements as the means to identify and evaluate the physical phenomena. Since the global thermal performance of the air-PCM heat exchanger can be obtained from energy balance at this control volume (between the inlet and outlet), then we must obtain the airflow rate or air velocity at the inlet; and the air temperature at the inlet and outlet position.

The local fluxes at each tube depend on the determination of the external convective heat transfer coefficient between the air surrounding the tube and the tube wall, as well as, the temperature at the frontiers between each domain: air-wall and wall-PCM. Two types of measurements are proposed: airflow measurements and temperature measurements.

(a) **Airflow rate instrumentation:**

To quantify the airflow rates and the velocity field distribution in the heat exchanger, we consider two types of instruments:

- A unidirectional hot wire anemometer (*HW*) to measure the local airflow velocity.
- A vane probe anemometer (*VP*) to measure the global airflow rate.

These airflow measurements are performed using the AMI 300 module from KIMO® Instruments [70]. The advantage of this instrument is that it consists of wireless interchangeable measurement modules, which facilitates mobility and measurements at the desired points. The hot wire anemometer allows measurements above  $0,15 \text{ m} \cdot \text{s}^{-1}$ , with an accuracy of 3% of reading  $\pm 0,03 \text{ m} \cdot \text{s}^{-1}$ , and a resolution of  $0,01 \text{ m} \cdot \text{s}^{-1}$ . The vane anemometer module presents a diameter of 100 mm, allowing measurements above  $0,25 \text{ m} \cdot \text{s}^{-1}$ , with an accuracy of 3% of reading  $\pm 0,1 \text{ m} \cdot \text{s}^{-1}$ , and a resolution of  $0,01 \text{ m} \cdot \text{s}^{-1}$ . The set of the KIMO® modules are shown in sub-figure *a* of the figure 3.9.

Table 3.3 – Thermophysical properties of PCM Rubitherm® RT28HC.

Physical Factors	Units	Rubitherm® RT28HC
Melting temperature range	[°C]	27-29 [25]
Melting-peak temperature	[°C]	$27,55 \pm 0,19$ [99]
Solidifying temperature range	[°C]	27-29 [25]
Solidifying-peak temperature	[°C]	$25,71 \pm 0,10$ [99]
Heating heat storage capacity	[kJ·Kg <sup>-1</sup> ]	$258,1 \pm 5,1$ (20°C-30°C) [99]
Cooling heat storage capacity	[kJ·kg <sup>-1</sup> ]	$251,9 \pm 6,7$ (20°C-27°C) [99]
Latent heat	[kJ·kg <sup>-1</sup> ]	245 [87]
Specific heat capacity	[J·kg <sup>-1</sup> ·K <sup>-1</sup> ]	2000 [25]
• Solid phase		$1652 \pm 105$ (0°C - 20°C) [99]
• Liquid phase		$2021 \pm 120$ (35°C - 45°C) [99]
Density	[kg·m <sup>-3</sup> ]	
• Solid phase		880 [25]
• Liquid phase		770 [25]
Volume expansion	[%]	12,5 [25]
Kinematic Viscosity	[mm <sup>2</sup> ·s <sup>-1</sup> ]	3,1 [87]
Thermal conductivity	[W·m <sup>-1</sup> ·K <sup>-1</sup> ]	0,2 [25]

(b) **Temperature instrumentation:**

Thermocouples were selected as instruments for temperature measuring because they are an instrument adaptable to the desired measurement positions and that present a good reliability-cost ratio. Two type K thermocouples are used to measure the inlet ( $T_{in}$ ) and outlet ( $T_{out}$ ) air temperatures. The thermocouple located at the inlet position was placed far from the fan (3,4 m). At this position, a well-established airflow can be expected; this thermocouple allows us to

record a better measurement of the one provided by the PID controller. The thermocouple at the outlet is located at 0,5 m after the last row of the heat exchanger.

For the local domain analysis, four thermocouples are placed in four tubes, at the height of 6 cm from the base, to measure the temperature response during the charging and discharging cycles. The thermocouples located at the local domain can be seen in figure 3.8.

The first thermocouple is located at 5 mm from the tube wall to measure the surrounding air ( $T_{air}$ ). The second thermocouple is placed at the external face of the tube wall ( $T_{ow}$ ). At the same position, but at the internal face of the tube, the third thermocouple is placed to measure the temperature at the internal side of the wall ( $T_{iw}$ ). Finally, the fourth thermocouple is located in the central axis of the tube to measure the PCM temperature ( $T_{pcm}$ ). A circular band of external diameter very slightly smaller than the inside diameter of the tube, of a thickness of 1 mm and thermal conductivity of  $0,2 \text{ W}\cdot\text{m}^{-1}\cdot\text{K}^{-1}$ , close to that of the PCM, was used to hold the thermocouples inside the tube in a fixed position.

These thermocouples were connected to a data acquisition system. We use the NI-9213 module from National Instruments® as the data acquisition system [74]. This NI-9213 module is designed with 16 channels. It presents anti-aliasing filters, open-thermocouple detection, and cold-junction compensation for high-accuracy thermocouple measurements. It presents a measurement sensitivity  $< 0,02 \text{ }^\circ\text{C}$  for type K thermocouples. This module is presented in sub-figure *b* of figure 3.9. The data collection is carried out directly through the SignalExpress software, also developed by National Instruments®. This program is advantageous to us because it displays in real time the evolution of the temperature, so that, if we observe abnormal behavior during the experiments, we can look for the source immediately.

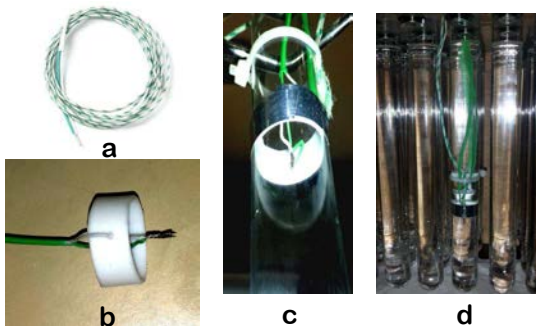


Figure 3.8 – Metrology used on the test bench for temperature measurement: a) Type K thermocouple, b) thermocouple located at the center of the tube, c) view of a tube with thermocouples, d) instrumented tube within the test bench.



Figure 3.9 – Metrology used on the test bench: a) AMI 300 KIMO® airflow measurement kit [70], and b) National Instruments® NI 9312 data acquisition for temperature measurements [74].

Figure 3.10 provides a photographic view of the final experimental setup. It is placed within an experimental room in our lab, near the windows to ease the intake of the outdoor air. These windows are coupled with external blinds (in blue in the figure 3.10), which allow controlling the direct solar radiation to the test bench.



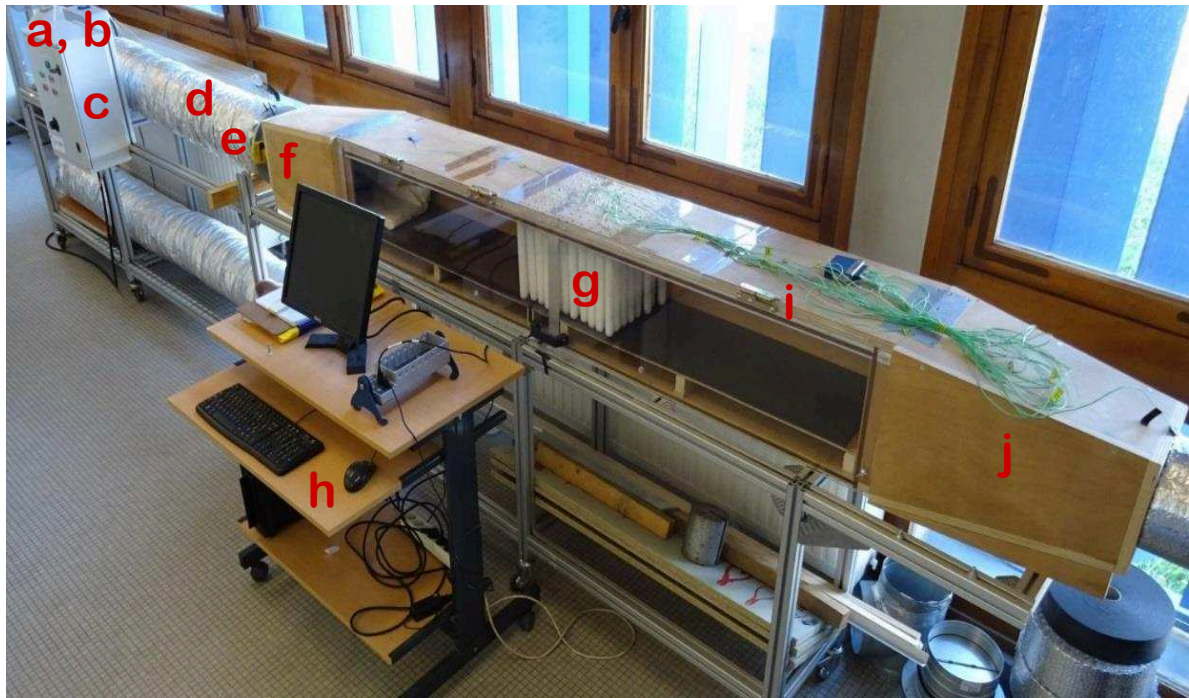


Figure 3.10 – Aerial view of the experimental setup in the test room where it can be observed: a) fan, b) air heating coil, c) airflow controller, d) an air duct, e) IRIS (pressure), f) diffuser, g) air-PCM heat exchanger, h) computer, i) data acquisition system, j) nozzle.

### 3.2.3 Experimental Procedure

#### Airflow rate measurements

Different airflow rates were proposed as inlet conditions by varying the electrical resistance of the fan, and then controlling the power of the ventilation of the fan. These values were chosen according to the maximum airflow allowed by the fan, and the ventilation values recommended within a building.

The air velocity inside rectangular conducts is not expected to be homogeneous, and a ratio between the average to the maximum velocity of  $0,67 \text{ m}\cdot\text{s}^{-1}$  has been reported in previous studies [17]. Hence, to characterize the velocity field in the upstream cross-section of the test bench, an air velocity cartography of 25 points ( $5 \times 5$ ) was made using the hot wire anemometer. A scheme of this measurement distribution can be observed in sub-figure *a* of fig. 3.11, where each blue dot represents a measurement point.

The grid consisted of a horizontal spacing every 5 cm and a vertical spacing every 4 cm. The starting reference point is located at the top of the heat exchanger, near the plexiglas® side (see figure 3.11). For example, if we refer horizontally to the second row from the Plexiglas® side and the third column from the top side, then we have the point [10,12], where 10 and 12, correspond to distance in cm from the reference point.

An average of the velocities in the cross-section has been calculated to determine the inlet airflow of the heat exchanger. Using this average velocity value and the cross-sectional area of the heat exchanger, the global airflow rate has been obtained for different rheostat positions of the fan. The airflow has also been measured with the vane probe at the end of the nozzle,



located at the outlet of the heat exchanger. This probe has a diameter of 10 cm, whereas the circular section of the nozzle has a diameter of 20 cm. Since these two do not have the same diameter, we proposed to take the average of five measurement points: four points every 90° at the circumference of the nozzle, and a single measurement at the center point of the circular section. These measurement points are represented by blue dots in sub-figure b, of figure 3.11. In the same way than with the velocities measurements, a global airflow was calculated and then compared with that at the inlet point.

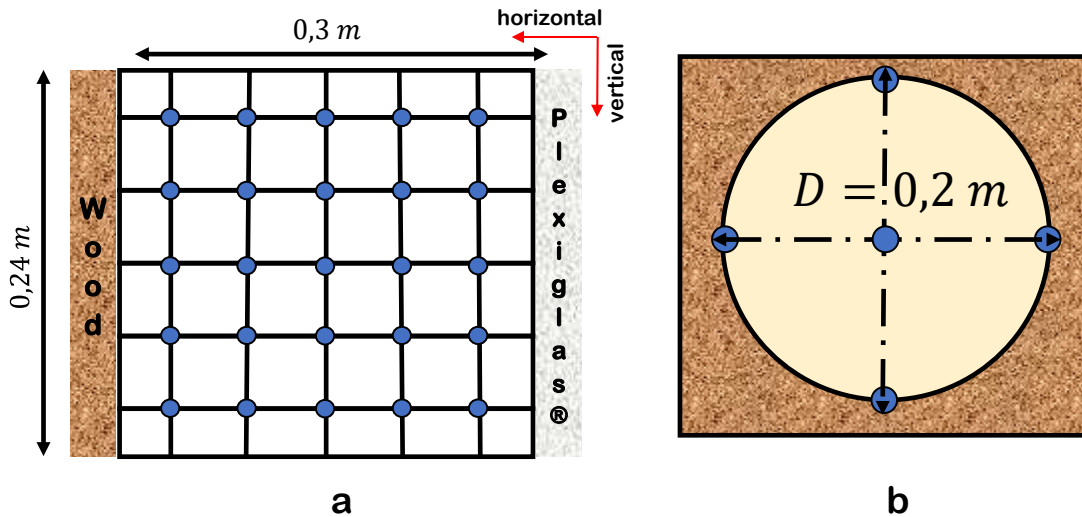


Figure 3.11 – Air velocity cartography of the heat exchanger cross-section: a) scheme of the 25 measurement points and, b) scheme of the measurement points (blue dots) at the nozzle of the test bench.

Figure 3.12 shows the results of the cartography of the velocity field  $v_{air}$  at the upstream cross-section (corresponding to the inlet air temperature measurement point). In here we can observe a variation of the velocities, where a maximum velocity of  $3,14 \text{ m}\cdot\text{s}^{-1}$  is reached in the middle point of the first row of measurements [15,4], and the minimum value of  $1,33 \text{ m}\cdot\text{s}^{-1}$ , at the point [25,12] nearby the wood side of the test bench. The average velocity corresponds to  $2,06 \text{ m}\cdot\text{s}^{-1}$ , which give us a ratio between the maximum and average velocity of  $0,65 \text{ m}\cdot\text{s}^{-1}$ , a close value to the one reported in the literature ( $0,67 \text{ m}\cdot\text{s}^{-1}$ ) by [17]. Considering the cross-section of  $0,3 \times 0,4 \text{ m}^2$  (see figure 3.11), this give us an airflow rate of  $533 \text{ m}^3\cdot\text{h}^{-1}$ . We also measured the local velocity in front of a tube (located at the fourth row of the third column), giving us a uniform velocity of  $5,4 \text{ m}\cdot\text{s}^{-1}$  along this tube.

Furthermore, we can observe that the velocity field is not uniform and that higher velocities are achieved near the Plexiglas® side. There are some reasons for this. These materials present different mechanical properties opposing different levels of friction between the air and the wall. Besides, the tubes are not evenly distributed and do not quite have the same distance to the walls in both sides.

These airflow rates characterize the heat exchanger regarding the electric power of the fan. With these results, further tests can be done without the need of measuring the air velocity at the beginning of each experiment.

Figure 3.13 presents the corresponding airflow rate for several positions of the fan rheostat, obtained by both measuring methods. Although the results of the cartography show the velocity field in a more detailed way and present a higher precision, associated to the instrument and

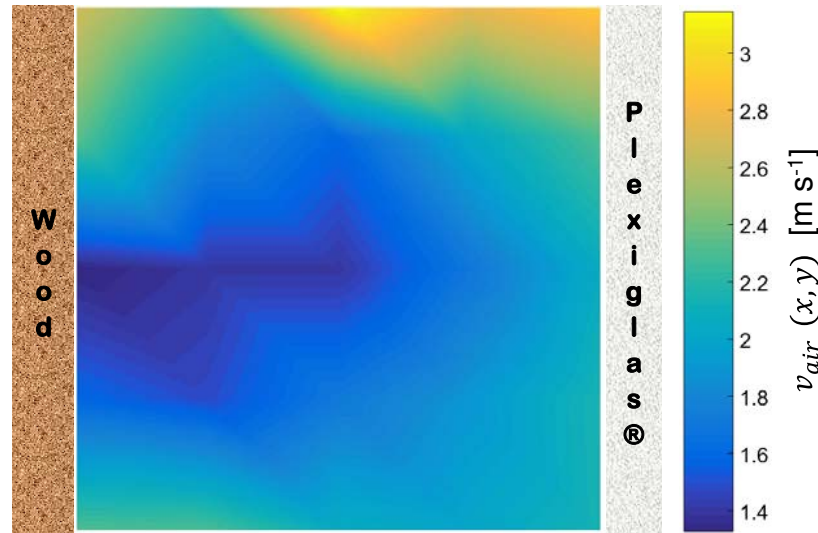


Figure 3.12 – Results of velocity field distribution  $v_{air}(x, y)$  at the upstream cross-area of the test bench ( $0,3 \times 0,4 \text{ m}^2$ ) for an airflow of  $533 \text{ m}^3 \cdot \text{h}^{-1}$  ( $T_{air} = 22^\circ\text{C}$ ).

the points of measurement, we find interesting and convenient the results obtained with the measurements of the vane probe.

We found a maximum difference between these measurements of less than 10%. The interest of this observation is the measurement time that was used for each method. The cartography was made from a three velocity measurements (with a duration of 30 s for each measurement and a data collection made every second by the instrument). The airflow measurement with the vane probe was made three times at each point with the same rate of one sample per second. Therefore, the time corresponding to the measurements (without taking into account the change of position of the instrument) is about 38 minutes for the hot-wire anemometer while it only takes 8 minutes with the vane probe. This could result conveniently if quick airflow measurements have to be performed at the beginning of a test.

Now, we proceed to estimate the overall convective heat transfer coefficient  $h_{air}$  by using two references. The first reference consists of an empirical correlation for the calculation of the convective heat transfer coefficient, developed by Zukauskas in 1972 [126]. This correlation considers the overall heat transfer coefficient of a tube bank by the analysis of experimental results together with the effect of the Reynolds number, and the influences of the pitches in the heat transfer. This study provides different correlations depending on the Reynold number (depending on the nature of the flow), and it has to be corrected if the heat exchanger has less than 16 rows of tubes.

The second method is an analytical correlation obtained by Kahn et al., [63] for tube bundles by using a boundary layer analysis method. With this method, the authors derived closed-form expressions for the calculation of average heat transfer from the tubes of a bank. This expression can be used in a wide range of parameters including longitudinal pitch, transverse pitch, Reynolds and Prandtl numbers.

To obtain these values, it is first necessary to calculate the values of Reynolds and Nusselt numbers within the heat exchanger. Their expressions were previously defined in section 1.4.1. In here, these values are calculated using the maximum velocity within the heat exchanger, which corresponds to the velocity in the minimum free cross-section; then the Reynolds number,

$Re$ , can be expressed as:

$$Re = \frac{D_{hyd} \cdot v_{max}}{\nu_{air}} \quad (3.2)$$

where  $D_{hyd}$  is the hydraulic diameter, which in this case corresponds to the tube diameter  $D$ ,  $v_{max}$  is the maximum velocity, and  $\nu_{air}$ , the dynamic viscosity. The Nusselt number is defined then by:

$$Nu = \frac{h_{air} \cdot D_{hyd}}{k_{air}} \quad (3.3)$$

where  $h_{air}$  is the overall convective heat transfer coefficient, and  $k_{air}$  is the air conductivity. This maximum air velocity  $v_{max}$  is given by:

$$v_{max} = \max\left(\frac{\mathcal{S}_L}{\mathcal{S}_L - 1} \cdot v_{app}, \frac{\mathcal{S}_L}{\mathcal{S}_D - 1} \cdot v_{app}\right) \quad (3.4)$$

where  $\mathcal{S}_L$  is the dimensionless longitudinal pitch ( $\mathcal{S}_L \equiv \frac{\delta_L}{D}$ ),  $\mathcal{S}_D$  is the dimensionless diagonal pitch, which is defined by  $\mathcal{S}_D = \sqrt{\mathcal{S}_T^2 + \frac{\mathcal{S}_L^2}{2}}$ , and  $\mathcal{S}_T$  is the transversal dimensionless pitch (see figure 3.5).

Once the  $Re$  number is obtained,  $h_{air}$  can be calculated from the empirical correlation developed by Žukauskas [126], according to the number of rows in the exchanger (for our case 11); this correlation is given by:

$$Nu = \mathcal{F} \cdot \mathcal{C} \cdot Re^n \cdot Pr^m \quad (3.5)$$

where the values of  $\mathcal{C}$ ,  $n$  and  $m$  are summarized in table 3.4.

Table 3.4 – Correlation coefficients for the expressions developed by Žukauskas [126].

Arrangement	$\mathcal{C}$	$n$	$m$	Conditions
In-line	0,90	0,40	0,36	$10 \leq Re_{max} \leq 100$
	0,52	0,50	0,36	$100 \leq Re_{max} \leq 10^3$
	0,27	0,63	0,36	$10^3 \leq Re_{max} \leq 2 \times 10^5$
	0,21	0,84	0,40	$Re_{max} \geq 2 \times 10^5$
Staggered	1,04	0,40	0,36	$10 \leq Re_{max} \leq 500$
	$0,35 \cdot [\mathcal{S}_T / \mathcal{S}_L] \exp(0,2)$	0,60	0,36	$\mathcal{S}_T / \mathcal{S}_L < 2$ $10^3 \leq Re_{max} \leq 2 \times 10^5$
	0,40	0,60	0,36	$\mathcal{S}_T / \mathcal{S}_L > 2$ $10^3 \leq Re_{max} \leq 2 \times 10^5$
	0,022	0,84	0,36	$Re_{max} \geq 2 \times 10^5$

For our case, the Reynolds results show a transition regime, then we use  $\mathcal{C}=0,27$ ,  $n=0,63$  and  $m=0,36$  for  $10^3 \leq Re_{max} \leq 2 \times 10^5$ .  $\mathcal{F}$  is a correction factor for a number of rows below 16. In this case,  $\mathcal{F}=0,985$ .

The second method developed by Kahn [63], allows to use equations instead of experimental curves, which can ease the search of the  $h_{air}$  values. The developed equation gives the  $Nu$  number for in-line arrangements, in terms of  $Re$ ,  $Pr$  and a coefficient  $\mathcal{C}_f$  as:

$$Nu = \mathcal{C}_f \cdot Re^{1/2} \cdot Pr^{1/3} \quad (3.6)$$

where,  $C_f$  is a coefficient determined from the pitches ratios for different arrangements using local and average heat transfer. This value was defined by Kahn as:

$$C_f = [0,25 + \exp(-0,55 \cdot \mathcal{S}_T)] \cdot \mathcal{S}_T^{0,285} \cdot \mathcal{S}_L^{0,212} \quad (3.7)$$

for in-line arrangement, and

$$C_f = \frac{0,61 \mathcal{S}_T^{0,091} \mathcal{S}_L^{0,053}}{1 - 2 \exp(-1,09 \mathcal{S}_L)} \quad (3.8)$$

for a staggered arrangement, given that  $\mathcal{S}_T = \mathcal{S}_L$  (cf. fig. 3.5). Finally, these results are shown in figure 3.14. We can observe from this figure that those values scatter from each other, as the airflow rate grows. However this difference is not large ( $13 \text{ W} \cdot \text{m}^{-2} \cdot \text{K}^{-1}$ ), henceforth we will use the correlation developed by Kahn since it is simpler and it can be applied to a wide range of conditions.

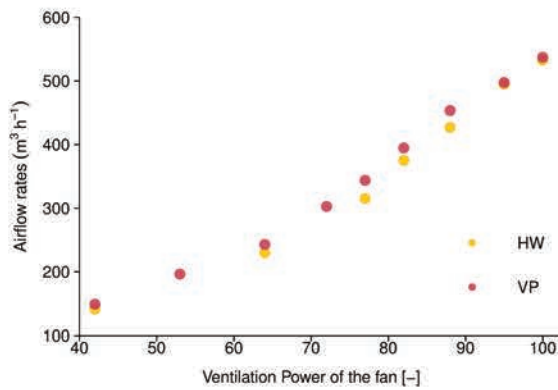


Figure 3.13 – Characterization of the airflow rates according to the position of the rheostat in the fan with: the hot wire anemometer in magenta, (HW) and the vane probe in yellow, (VP).

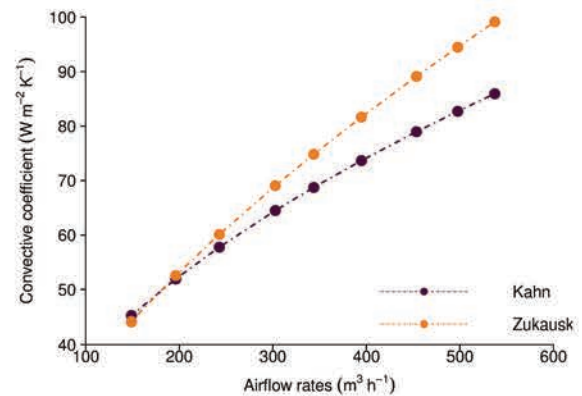


Figure 3.14 – Convective heat transfer coefficient obtained by theoretical correlation (Kahn), in purple; and by empirical correlation (Žukauskas), in mustard.

### Temperature measurements

Since the airflow conditions regarding the air velocity were collected prior to the charging-discharging cycles tests, only temperature measurements are performed during the tests. A previous calibration was performed to know the accuracy of the thermocouples used. The thermostatic water bath LAUDA ECO SILVER RE 415 G from Lauda® was used to ensure uniform temperatures during the calibration. This thermostatic bath includes a PT100 temperature sensor which ensures a stability of  $\pm 0,01 \text{ }^\circ\text{C}$ . It presents a temperature accuracy of  $\pm 0,3 \text{ }^\circ\text{C}$  and  $\pm 0,5 \text{ }^\circ\text{C}$  of the temperature displayed. It has a stability of  $\pm 0,01 \text{ }^\circ\text{C}$ . The data was acquired through the acquisition system (CompactDAQ® and SignalExpress® by National Instruments®). The thermocouples reported a maximum standard deviation of  $\pm 0,12 \text{ }^\circ\text{C}$ , with an absolute error of  $0,65 \text{ }^\circ\text{C}$  with the reference. The calibration process is detailed in the Appendix B (Calibration).

### Testing protocol

1. Begin the temperature data acquisition.



2. Set the rheostat position corresponding to the desired airflow.
3. Enter the initial temperature of the experiment in the heating coil controller.
4. Let the airflow established during 24 hours before the test.
5. Passed these 24 hours, set the inlet air temperature to the desired final temperature of the test.
6. Take photographs with an interval between them corresponding to the phenomena observed.
7. Once the final temperature is achieved by all the thermocouples, wait for all these temperatures to stabilize to complete the data acquisition.

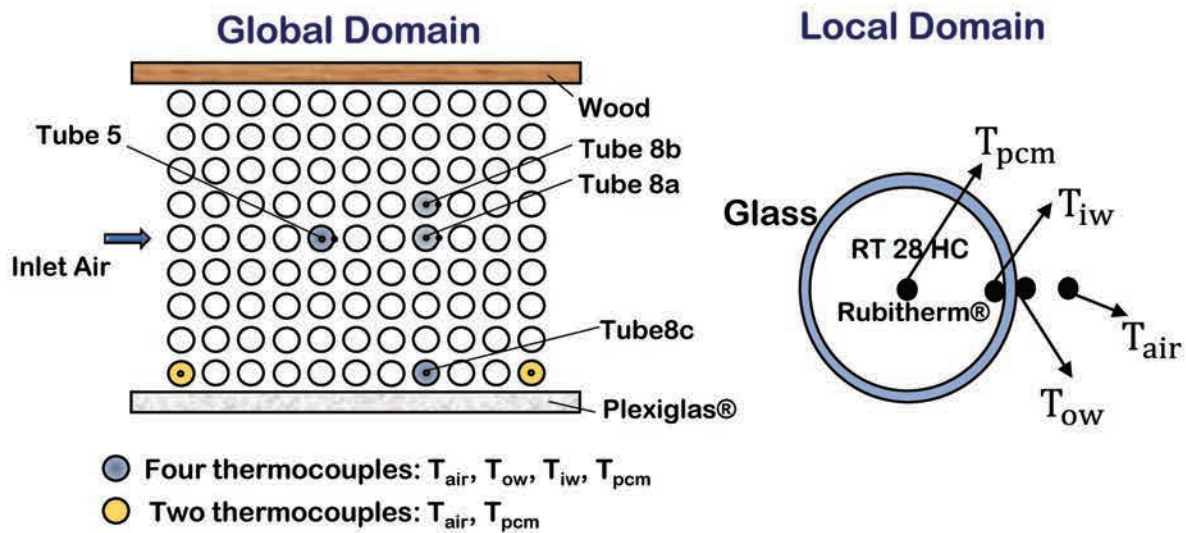


Figure 3.15 – Location of the thermocouples within the test bench. The tubes in color blue represent those to whom four thermocouples have been integrated measuring  $T_{air}$ ,  $T_{ow}$ ,  $T_{iw}$ , and  $T_{pcm}$ ; in yellow those tubes to whom two thermocouples have been integrated measuring  $T_{air}$ , and  $T_{pcm}$ .

### 3.3 Experimental results and discussion

In this section, we present the results for melting and solidification cycles using RT28HC paraffin as the storage material. For the melting cycle, the initial temperature of the experiment was set at 22 °C with an airflow rate of 193 m<sup>3</sup>·h<sup>-1</sup>. Then, the air temperature was set at the inlet of the test bench to 34 °C for the melting cycle.

For the solidification cycle, which was tested after the melting cycle, the initial temperature of the test bench was set at 34 °C, and then, the air inlet temperature for the solidification test corresponded to 22 °C. These temperatures results are complemented with photographs that were taken during the cycles.

### 3.3.1 Melting cycle results

#### Temperature measurements:

In table 3.5 are shown the principal results from the melting cycle test. To help us understand the results from the melting cycle, we have divided the results into three plots. The first one, figure 3.16, shows the results for the global and local domains. The second one, figure 3.17, shows the air distribution and stratification within the heat exchanger, and the third one, figure 3.18 shows the PCM measurements at the center of the tube distribution within the heat exchanger.

#### (a) Heat transfer during melting:

For figure 3.16, in salmon and cyan colors, we have the air inlet ( $T_{in}$ ) and outlet ( $T_{out}$ ) temperatures of the heat exchanger, respectively. The rest of the temperatures correspond to the local domain measurements. In magenta, we have the air surrounding a tube located at the eighth row of the heat exchanger ( $T_{air}$ ); in green-lime, we have the external face of the tube ( $T_{ow}$ ), while in yellow, the internal face of the same tube ( $T_{iw}$ ). Finally, in purple, we have the phase change temperature of the tube ( $T_{pcm}$ ).

We can observe that the air temperature at the inlet reached the set temperature quickly and remained constant throughout the cycle, after the first 3 minutes. The increase in the temperature of the air at the outlet is influenced and slowed by the presence of the air-PCM tube bundle and therefore, it has a lower temperature than the air at the inlet.

The rest of the temperatures reached the thermal equilibrium after 240 minutes. However, the outlet temperature did not reach this temperature. After these 240 minutes, we left this final condition of 34 °C as the set point for the PID controller for 24 hours to ensure the thermal equilibrium at the beginning of the solidification cycle. Nevertheless, the conditions of the air temperature at the exit remained constant. This behavior can be related to the losses through the heat exchanger walls to the surroundings as well as the effect of the fan (active element of the heat exchanger). This intrinsic temperature difference must be taken into account to obtain the baseline of operation of the exchanger, and thus be able to calculate the cooling or heating power correctly. note here that the temperature recorded at the inlet is lower, than the temperature shown by the PID display.

Regarding the phase change temperature  $T_{pcm}$ , the determination of the beginning of phase change needs to be addressed in more detail. We can observe a gradual change of the slope between minute 10 and minute 30, when reaches a slope that remains constant until the end of the phase change. In here, we can observe that the temperature does not remains constant during the cycle, rapidly changing of slope from around a temperature of 26,3 °C, until it reaches a constant slope around 26,8 °C.

After that, the PCM temperature continues to increase until the end of the phase change, around  $t = 190$  minutes. This temperature range indicates, *a priori*, that the mechanisms controlling heat transfer during the melting of the PCM do not remain constant during this time. We can expect that at the beginning of the melting cycle, conduction controls the heat transfer, since the PCM is mostly in a solid state; although the effect of the buoyancy forces related to the natural convection in the liquid part of the PCM could also explain this temperature range. From the observations made during these tests, we notice that when the liquid PCM reached the PCM thermocouple position, it immediately increased its temperature measurement to the inlet temperature ( $T_{in}$ ), which happened between minutes 185 and 205.



Concerning the external and internal wall faces temperatures, we can observe that the temperature gap between them remained constant for the first 90 minutes, then it slightly increased, until almost the end of the phase change, where the internal temperature of the wall presented a higher value. We could explain this temperature difference by the effect of the currents of liquid PCM at the wall, allegedly due to natural convection. During the melting cycle, the heat enters the PCM tube through the wall, then it is expected the presence of the PCM in its liquid state first in the outermost layers of the PCM tube (in the radial direction). Then, since we observed that when the liquid part of the PCM reaches the thermocouple measurement point, the PCM temperature immediately increases to the inlet conditions, we could suppose a similar phenomenon. If the temperature of the liquid PCM is at a higher value than that of the solid part, and 2-D melting occurs, the axial heat transfer from the liquid part could make an increase on the temperature of internal face of the wall. Then, this could explain this temperature difference.

**(a) Other physical phenomena interpretation: stratification within the heat exchanger**

We use figures 3.17 and 3.18 to observe further phenomena during this melting cycle. In figure 3.17 we observe the air temperatures within the heat exchanger. These measurements corresponded to the air at the inlet position, the air surrounding a tube in the first row ( $T_{air1}$ ) near the plexiglas® wall, in orange, in the middle of the fifth row ( $T_{air5}$ ), in yellow, and in the eighth row ( $T_{air8}$ ), in lime-green. The main interest of this plot is that we can extract from the information that presents, the progress of the phase change globally in the heat exchanger.

From this figure we can infer the presence of a stratification within the heat exchanger. For instance, the temperature  $T_{air1}$  presents a lower value of about 0,5 °C with  $T_{air5}$  from minute 20 until minute 140. This could be related to the axial air velocity distribution which was lower at the lowest positions of the tube (see figure 3.12).

Figure 3.18 shows the PCM temperature of six tubes within the heat exchanger. During melting the beginning of phase change for each tube corresponds to the position of the tube. For instance, we notice in the subplot of figure 3.18, that  $T_{pcm_1}$  is the first to begin phase change. Concerning the tubes in the eighth row  $T_{pcm_{8c}}$  achieve first this point, which is expected since the air velocity near the plexiglas® side of the heat exchanger is higher regarding the middle point.

Phase change takes place in a similar way for all tubes up to  $t = 170$  min, where the fifth tube  $T_{pcm_5}$  reaches the end of phase change and begins to raise its temperature until reaching the conditions at the inlet of the heat exchanger. We observe that  $T_{pcm_5}$  reaches the end of phase change first that  $T_{pcm_1}$ . This could be related to the axial position of the thermocouples, wherein the first tube is about 2 cm from the base, while in the fifth tube is about 6 cm, following the same stratification observed before for the air temperature measurements. Lastly,  $T_{pcm_{11}}$ , reaches the end of phase change an hour after the rest of the tubes.

### Image Analysis

In this section, we aim to observe and analyze the images profiles of the melting cycle of the air-PCM heat exchanger. These images, together with the temperature measurements would give us a deeper understanding of the mechanisms controlling the phase change for future data treatment and modeling. We begin this section with the images of the the whole heat exchanger shown in tables 3.6 to 3.8. For this analysis, we have selected those images where the most noticeable changes during melting are observed. The description of the images is below:

- **t = 0 min.** At the beginning of the melting cycle, the PCM is completely in its solid phase. However, it was solidified in a cycle before this test. This solidification cycle occurred uncontrolled in terms of the solidification of the material; therefore air voids formation can be present in the solid PCM, and irregular shapes at the top can be formed due to this voids, which is observed in figure 3.19.
- **t = 30 min.** At this moment we can notice the presence of bubbles in the outermost layers of the PCM (red box), this being the first visual evidence of a change between the solid and liquid phase for the PCM. Also, we can observe a small layer of liquid PCM at the top of the tubes, as observed in figure 3.20.
- **t = 60 min.** After the first hour of the melting cycle, a thicker layer of liquid PCM can be observed at the top of the tubes of the first rows. In the last rows, the tubes present a wet appearance as shown in figure 3.21.
- **t = 90 min.** After this time, a 2D melting pattern can be observed in the tubes located in the first rows (red box). We observe that the layer at the top of the tubes of the first rows continue to grow, while it begins to increase the amount of liquid PCM in the radial direction of those tubes. Meanwhile, in the last rows, the liquid can be now observable in all the tubes as shown in figure 3.22.
- **t = 120 min.** The 2D melting pattern now becomes more clear in the tubes of the first rows, where a conical form in the solid PCM begins to appear (red box). At the same time, we can still observe a 1D melting pattern in the last rows of the heat exchanger (red line) in figure 3.23.
- **t = 150 min.** The remaining solid in the tubes of the first rows have taken a sharp conic form (red box), while we can still observe an axial melting in the "z" direction (red line). We can notice in this figure 3.24, which the placement of the thermocouple in tube<sub>1</sub> has affected the radial melting of the PCM. If we compare this tube<sub>1</sub>, with the subsequent tubes, we can observe that it takes more time for this tube to melt than the following tubes, leading to a noticeable difference in the height of the solid PCM between them ( $\Delta z$ ).
- **t = 175 min.** We now observe in figure 3.25 the final stages of melting in the first rows, while a 2D conical melting is already observed in the last rows of the heat exchanger. In the first rows (with exception of the first tube, where the difference in the melting pattern it has been accentuated), the buckling of the PCM has already happened, where the melting pattern cannot be easily predicted.
- **t = 245 min.** After four hours of the cycle, almost all the PCM has already changed into the liquid phase, except for the last rows, as can be observed in figure 3.26. We can also notice that the melting has occurred more slowly in the tubes near the walls of the heat exchanger, which can be expected due to the edge effects, and the airflow pattern observed in figure 3.12.
- **t = t<sub>final</sub>.** At the end of the cycle, we can observe in figure 3.27 that all the PCM is in its liquid phase.

Table 3.6 – Visual evolution of phase change during the melting cycle.

## Global Domain

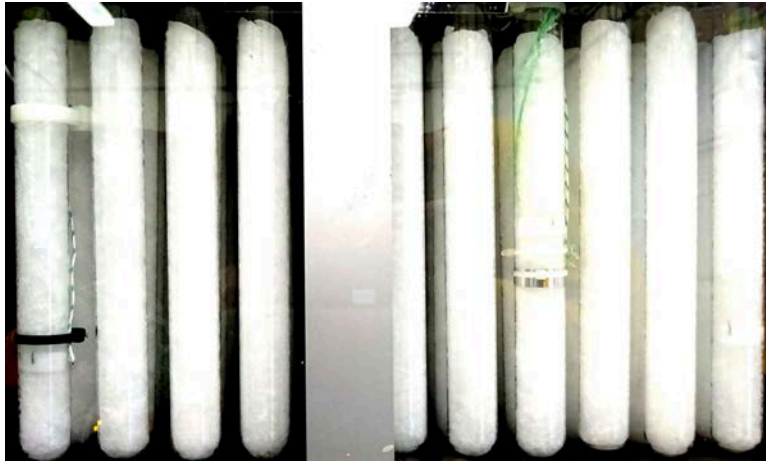
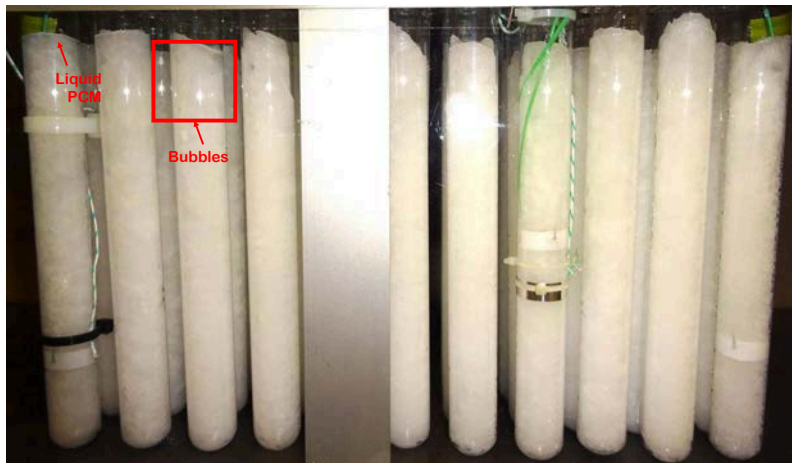
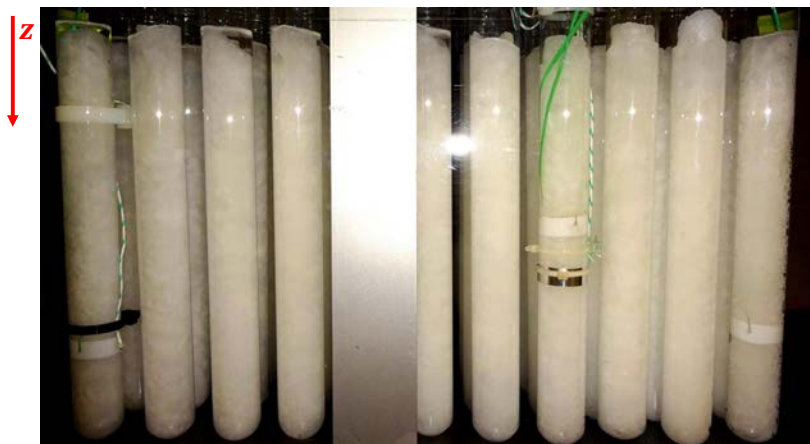
Figure 3.19 –  $t = 0$  min. All the PCM in the heat exchanger is in its solid form.Figure 3.20 –  $t = 30$  min. Strong presence of bubbles and a small thin layer of liquid PCM on the top.Figure 3.21 –  $t = 60$  min. A thicker liquid layer appears in the first rows and 1D melting pattern.

Table 3.7 – Visual evolution of phase change during the melting cycle

## Global Domain

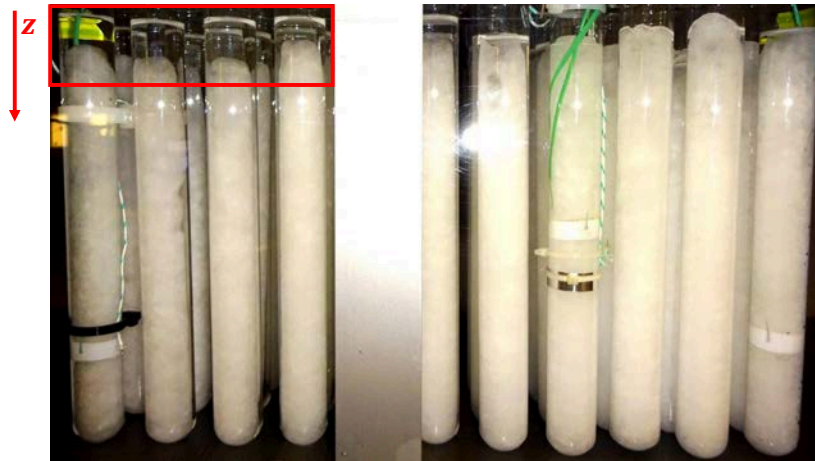


Figure 3.22 –  $t = 90$  min. Visible layer of liquid PCM on the top of the first rows. Liquid has already appeared in all the rows of the heat exchanger.

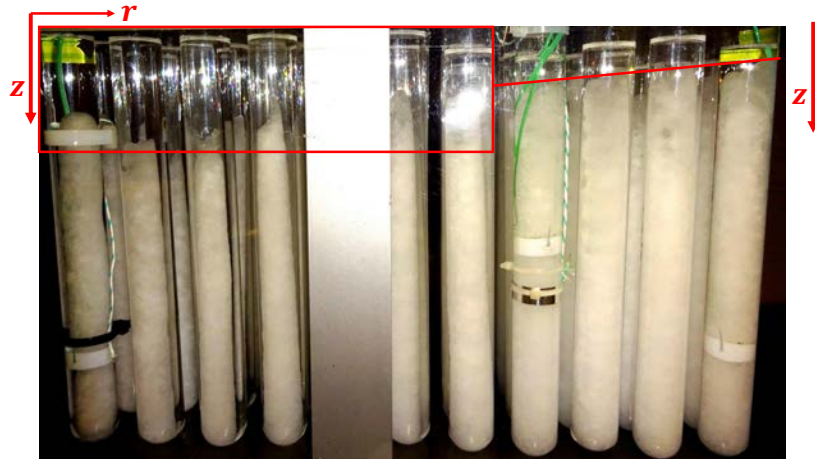


Figure 3.23 –  $t = 120$  min. Thick layer on the top of all the rows. Conic 2D pattern in the first rows (melting in the axial and radial directions).

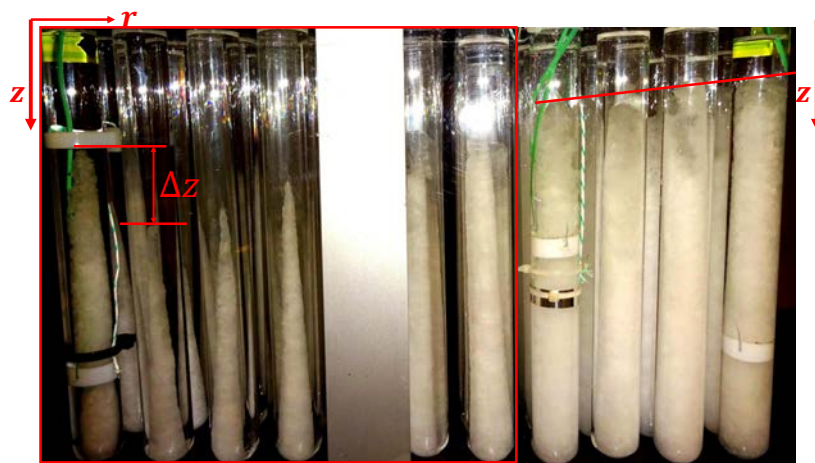


Figure 3.24 –  $t = 150$  min. Pronounced conical shape in the first rows (2D melting). 1D melting in the last rows.



Table 3.8 – Visual evolution of phase change during the melting cycle.

## Global Domain

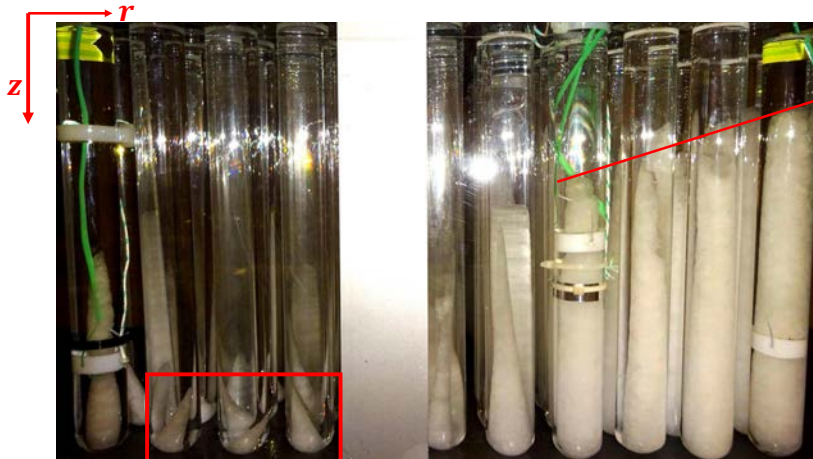


Figure 3.25 –  $t = 175$  min. Buckling of the solid PCM in the first rows (red box). Most of the PCM is still in its solid phase in the last rows.



Figure 3.26 –  $t = 245$  min. Almost all the PCM has melted, except for the last rows.

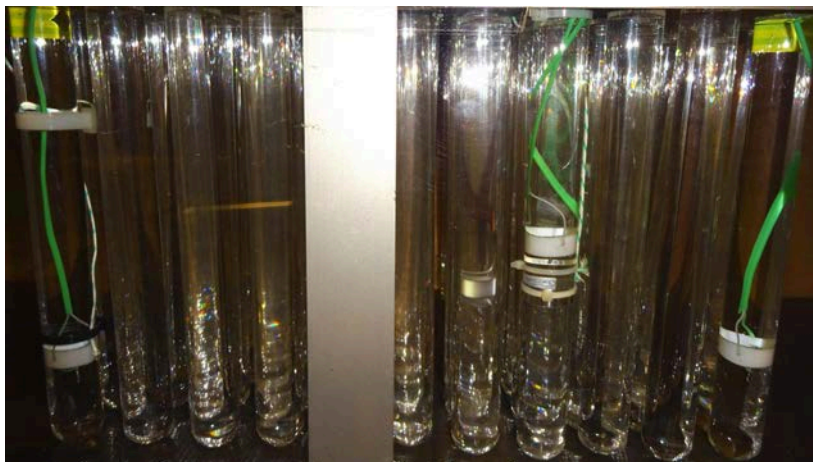


Figure 3.27 – All the PCM in liquid state.



From this global analysis of the figures obtained for the melting cycle, we can also extract further information about the phase change process. This analysis presented in the figures of tables 3.9 and 3.10 is focus on the signs of phase change: bubble formation and the evolution of the melting pattern.

Table 3.9 – Visual evolution of phase change during the melting cycle.

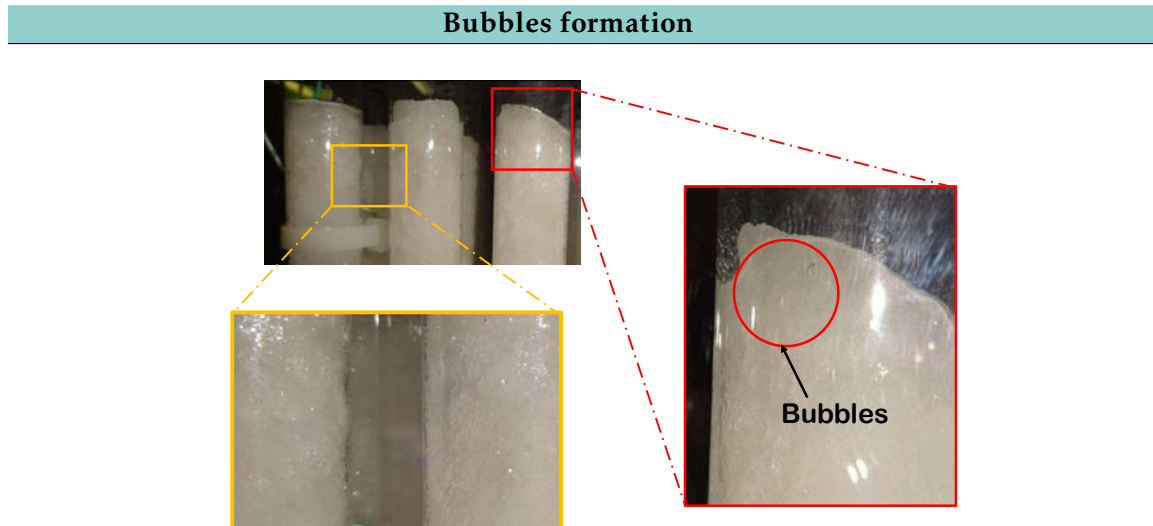


Figure 3.28 –  $t = 15$  min. The bubble formation begins in the first rows of the heat exchanger.

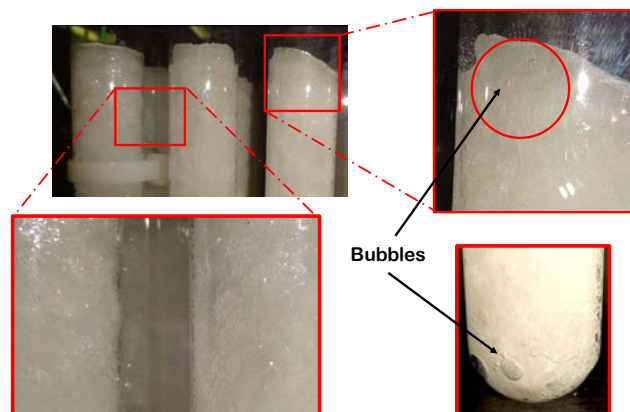


Figure 3.29 –  $t = 20 - 30$  min. There is a strong presence of bubbles and a small thin layer of liquid has formed on top.

*Note: In the figures where two images are shown, one in the left and one in the right, each one correspond respectively to the times cited in the legend of each figure.*

- Bubble formation:** The first sign of the beginning of phase change is the bubble formation, observed in figures 3.28 and 3.29. As mentioned before, after the solidification, air voids are formed within the solid PCM. Then, naturally, when the PCM is heated, this trapped air begins to be released from the solid PCM, and when the outermost layers of the PCM achieve the melting temperature, we can observe the bubble movement. These bubbles and the thin layer of liquid PCM is observed between the time  $t = 10$  min and  $t = 30$  min, in the first rows and the last rows of the heat exchanger, respectively.

- **Melting Patterns:** Different melting patterns can be spotted during the melting cycle. Those patterns are the result of the erosion caused by the liquid PCM over the solid PCM. Locally, in a single tube, we can observe three different patterns, which are explained hereunder. To do so, we will only focus on the behavior shown by the tubes in the first rows.

The first melting direction spotted is a one-dimensional melting in the axial direction of "z", which draw a cylindrical melting pattern: as the cycle progresses the remaining solid takes the form of a cylinder which maintains the original diameter but reduces its height. This pattern can be observed in figure 3.30.

Near the end of the second hour of the cycle, we can spot a two-dimensional pattern in the remaining solid in figure 3.31. Now, the melting front follows a rather conic pattern instead of the cylindrical pattern observed before. The conic shape becomes sharper as the cycle progresses, because of the amount of liquid PCM increases, provoking greater buoyancy forces that induce stronger erosion on the top of the remaining solid.

The last pattern that can be observed is when the buckling of the remaining solid PCM occurs in figure 3.32. At this moment the amount of liquid is much greater than the solid, then this solid part can no longer stand due to the forces exerted by the liquid on the solid, and then, this solid falls. During this stage, we do not observe a unique form of the solid part for all the tubes.

Furthermore, in figure 3.32 it is highlighted an observation mentioned before in section 3.3.1 related to the PCM temperature measurement variation, which increases rapidly to the inlet conditions once the thermocouple touches the liquid region. Although, it is not directly related to the spotted signs of phase change, it is related to the instrumentation. We show in this image the moments when the thermocouple within the tube<sub>1</sub> still touches the solid region of the PCM and then, when it no longer touches it, which occurs between minutes  $t = 185$  min and  $t = 193$  min, respectively. Moreover, we already stated that the placement of a thermocouple inside a tube appears to affect the melting of the PCM in the radial direction, which, in turn, affects the time it takes for an instrumented tube to completely change phase.

To relate the behavior found in these photographs, we compare them with the PCM temperature measurement of the tube<sub>1</sub>,  $T_{pcm_1}$ , shown in figure 3.33. In this figure we highlight those findings of the photographs, where each purple point represent a visual remark made during the images analysis. For instance, we can now observe that the bubble formation observed in figures 3.28 and 3.29 correspond to the period of transition between the sensible heat storage and latent heat storage. Moreover, we can now demonstrate that in fact, once the thermocouple touches the liquid region, the PCM temperature increases until it reaches the inlet conditions, relating figures 3.32 and figure 3.33.

In summary, we have found that the melting in the heat exchanger is first axial downward rather than radial. Results under controlled conditions that were already reported in the literature for tubes with small diameter ( $D \leq 2,0$  cm), has shown that melting follows a radial pattern controlled mainly by conduction [64], while for wide tubes, the melting pattern observed is rather conical, resulting in a two-dimensional melting [57]. Even though our external tube diameter is slightly bigger than the one reported in the literature ( $D_{ow} = 2,45$  cm), we were expecting a radial melting pattern, controlled by conduction.

Yet, these photos reveal otherwise three melting patterns:

1. First, a rapid downward melting of the uppermost solid PCM (in the axial direction of "z"), which form a liquid PCM layer above the solid phase.

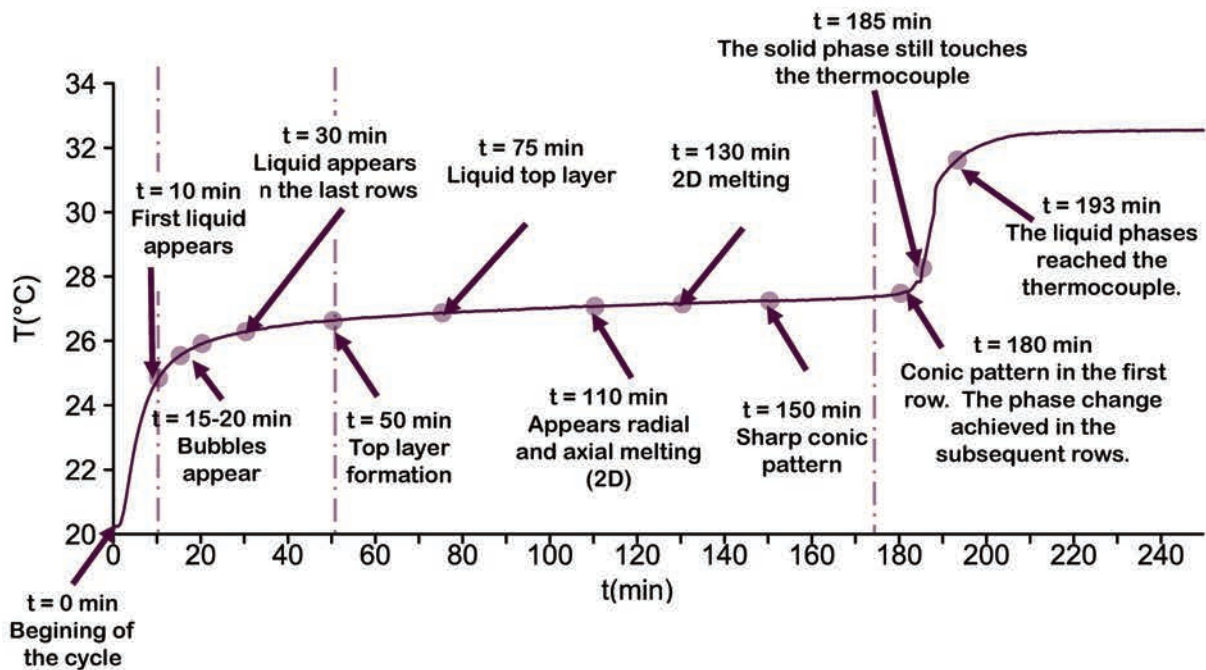


Figure 3.33 – PCM temperature measurements  $T_{pcm_1}$  for the tube<sub>1</sub> located on the first row near the plexiglas® side. Each purple point represents a visual remark during phase change.

2. Second, an radial melting (in the radial direction “ $r$ ”), due the upward motion of the melted PCM.
3. An unpredictable pattern when the amount of solid PCM is low within the tube and therefore, the buckling of the PCM occurs.

Now these patterns can help us to understand the mechanisms controlling heat transfer, and therefore the overall physical phenomena during melting.

In summary, the regimes observed during this cycle are:

- **First regime:** *Heat transfer with sensible heat storage.* The energy storage occurs in the PCM by sensible heat (due to the temperature difference) and controlled only by conduction. This regime can be observed between  $t = 0$  and  $t = 10$  min.
- **Second regime:** *Heat transfer with sensible and latent heat storage.* When the melting just begun, heat transfer occurs only by conduction between the heated wall to the PCM and the solid-liquid interface. This regime can be observed between  $t=10$  min and  $t = 50$  min.
- **Third regime:** *Heat transfer with sensible and latent heat storage.* Natural convection effects appears leading to 2D melting pattens. Heat transfer is controlled by natural convection between the liquid and solid PCM, and by conduction in the remaining solid. This regime is observed between  $t = 50$  min and  $t = 175$  min
- **Fourth regime:** *Heat transfer with sensible and latent heat storage.* The amount of solid PCM left is minimal, presenting irregular shapes. Convection controls the phase change.

### 3.3.2 Solidification cycle results:

#### Temperature measurements

In the same way than with the melting cycle, we have divided the solidification temperature measurements for better interpretation from figures 3.34 to 3.36.

Figure 3.34 shows the results for the solidification cycle. We can observe that phase change occurs isothermally (thermal arrest), where the transition between the liquid phase and the period of phase change is smoother and more defined than with the solid phase. Then following the same interpretation made with figure 3.16 during melting, we could infer that in here the mechanism controlling heat transfer remains constant.

Conduction is expected to control heat transfer during solidification. However, the thermocouple measuring the PCM temperature  $T_{pcm}$  is located at the axis of the tube. The solid phase is expected to reach lastly this point; therefore, a strong convection between the remaining liquid and the thermocouple may be present, allowing an uniform measure of the PCM temperature.

We can also observe that the transition between the phase change and solid state, occurs in accordance with the position of each tube within the heat exchanger. If we compare this observation with the results presented in melting, we can link these results to the experimental observation made earlier by Zalba et al. [121], which state that melting was dependent on the airflow, whether the solidification was not. That could explain why in here we do not observe the same effects of the heterogeneity when comparing solidification in the different tubes in figure 3.36.

In brief, we have noticed that the PCM solidification presents more constant and uniform temperature behaviors than melting, which suggest a minor effect of the presence of the convection in the liquid phase or volumetric solidification, instead of heat transfer during solidification preferred in a specific direction.

#### Image Analysis

To validate some of the observations made with the temperature results, we now proceed to evaluate the photographs and the temperatures together. From figure 3.37 to 3.41 we highlight the most significant changes observed during solidification. This joint observation will allow us to address the physical phenomena intervening and thus be able to quantify the performance of the unit and develop the prediction models.

- **t=0** At the beginning of the solidification all the PCM is in liquid state, following a melting cycle.
- **t=13 min.** After 13 minutes one can observe the dendrites formation within the tubes. As it can be detected, the formation begins at the upper section of the tube and at the outermost layers in the radial direction. As expected, the density of these dendrites decrease with the rows, with exception of the first tube.
- **t=30 min.** After 30 minutes of the cycle, we can observe a solid appearance on almost all the tubes. We can further notice the development of frozen layers at the upper section of the tube.
- **t=45 min.** After the first 45 minutes, the crystallization process (freezing) can be observed in most of the tubes.

- $t_{final}$ . At the end of the cycle all the PCM is fully crystallized.



Table 3.5 – Temperature results from the melting cycle.

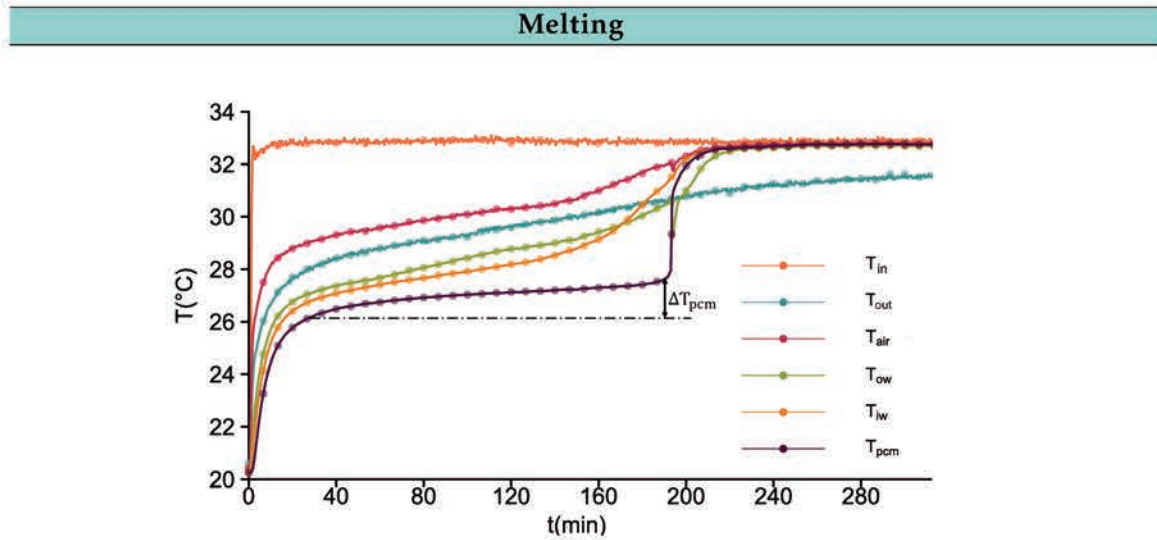


Figure 3.16 – Global (inlet-outlet) and local (tube<sub>8c</sub>) domains temperature profiles.

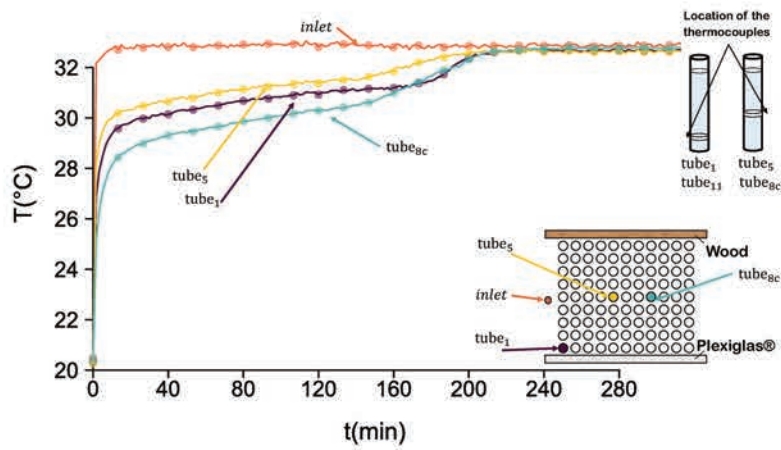


Figure 3.17 – Air temperatures vs tube position.

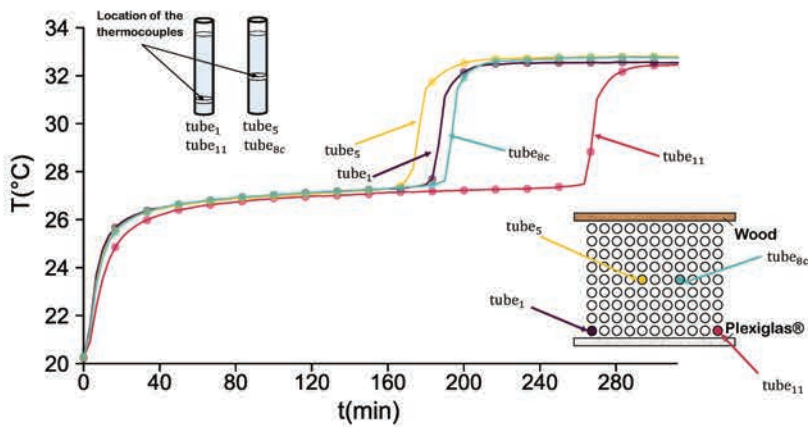


Figure 3.18 – PCM temperatures per tube position.

Table 3.10 – Visual evolution of phase change during the melting cycle.

### Melting patterns

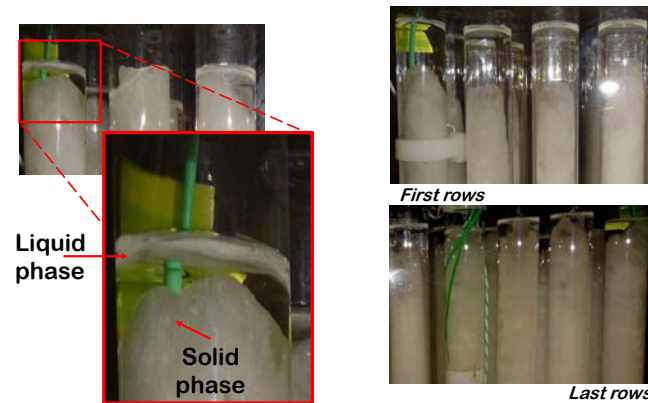


Figure 3.30 –  $t = 50 - 90$  min. Liquid layer in the top of the tube and conic pattern in the solid PCM.

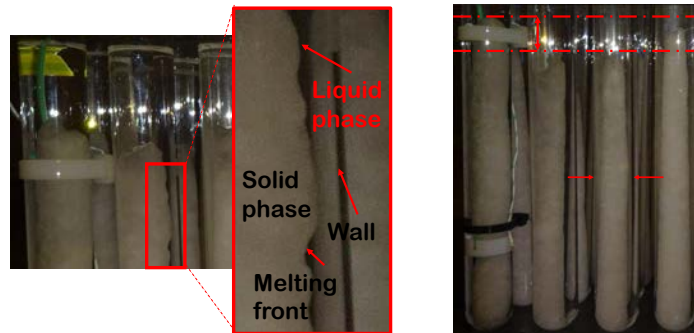


Figure 3.31 –  $t = 110 - 150$  min. Melting pattern moves along the axial and the radial directions.

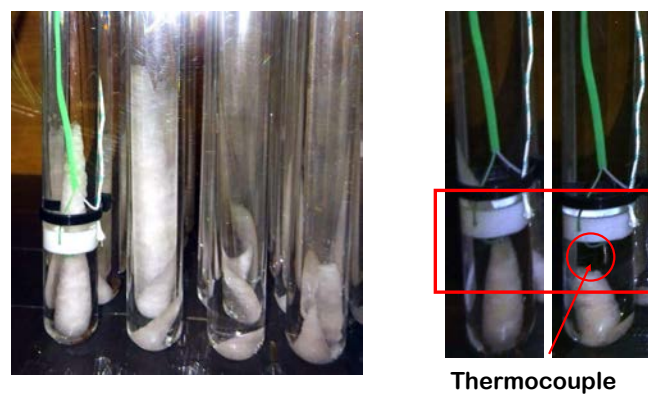


Figure 3.32 –  $t = 180 - 193$  min. Sharp conic pattern in the solid PCM before the buckling happens.

*Note: In the figures where two images are shown, one in the left and one in the right, each one correspond respectively to the times cited in the legend of each figure.*

Table 3.11 – Temperature results during the solidification cycle.

**Solidification**

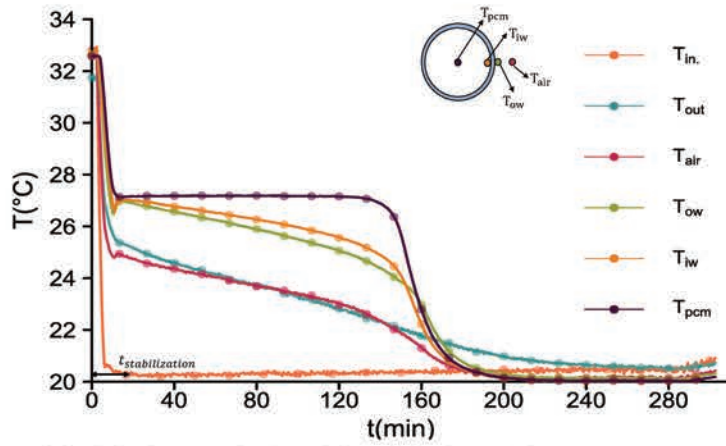


Figure 3.34 – Global (inlet-outlet) and local ( $tube_{8c}$ ) domains temperature profiles.

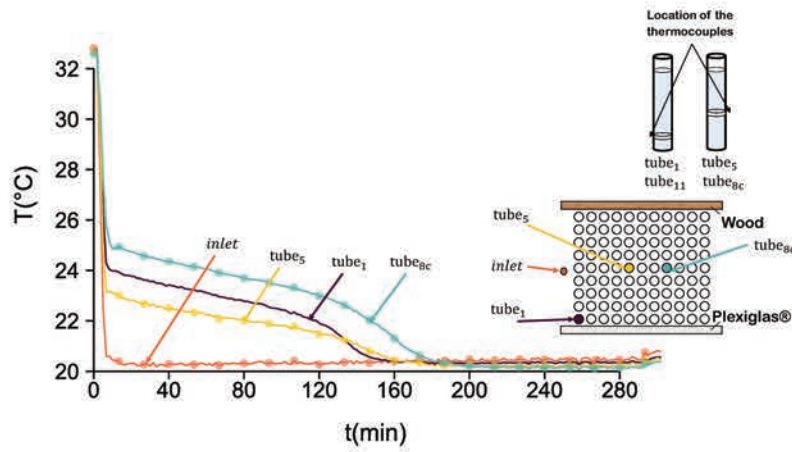


Figure 3.35 – Air temperatures vs tube position.

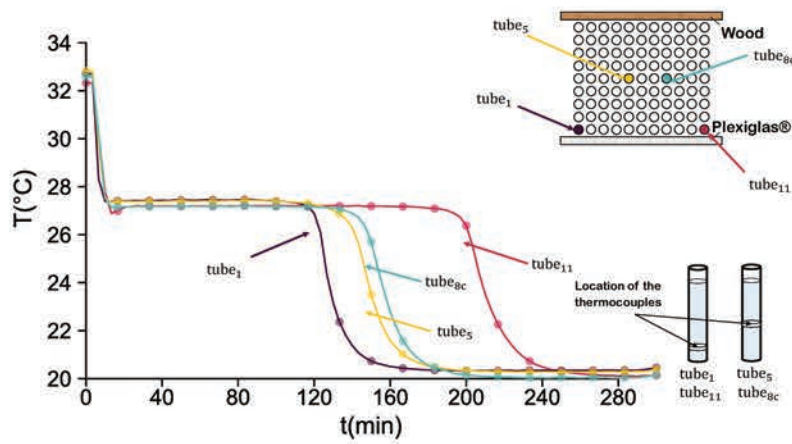


Figure 3.36 – PCM temperatures per tube position.

Table 3.12 – Visual evolution of phase change during the melting cycle.

## Melting cycle



Figure 3.37 –  $t = 0$ . At the beginning all the PCM is in liquid state, following a melting cycle.

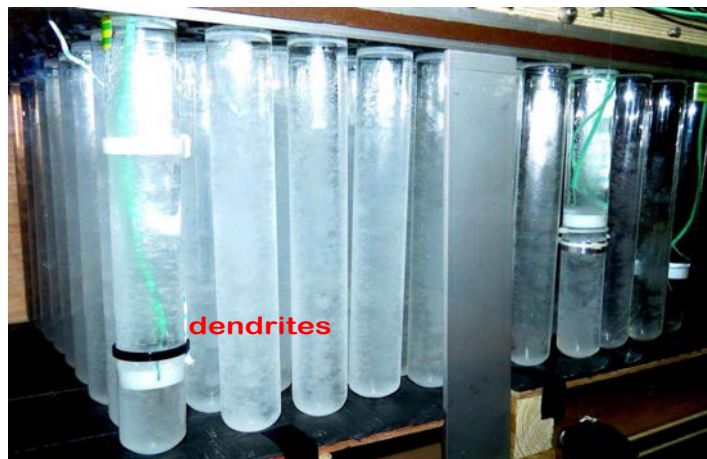


Figure 3.38 –  $t = 13$  min. At this moment we can observe the dendrites formation in the layers near the tube wall. The density of these dendrites decrease with the rows, with the exception of the first tube (instrumented with thermocouples).



Figure 3.39 –  $t = 30$  min. Once the first half hour of the cycle has passed, we can observe the crystallization starting at the top of the tubes.



Table 3.13 – Visual evolution of phase change during the melting cycle.

**Melting cycle**



Figure 3.40 –  $t = 45$  min. The crystallization process follows an axial direction along the tube, as can be observed in the last rows of the heat exchanger.



Figure 3.41 –  $t = t_{final}$  min. At the end of the cycle all the PCM is fully crystallized.



## 3.4 Thermal performance of the unit

### 3.4.1 Data processing for thermal performance evaluation

Now that we have highlighted the physical phenomena involved in an air-PCM heat exchanger through the analysis of the temperature measurement and photographs, we can proceed to quantify its thermal performance. Different types of performance indicators can be used depending on the information that we want to extract from these experiments and the domain that we are analyzing. In here, we focus on those that can quantify the two objectives established for the unit: the storage capacity and the heat transfer rate for each domain (see section 2.2.6). In the next section, we will present the different indicators selected for each physical domain.

#### Global Domain

All types of heat exchangers are usually evaluated by their heat transfer rate. This value can be expressed in terms of the cooling or heating power ( $P_{cool}$ ), depending on the applications; or as well by their effectiveness ( $\varepsilon_{hex}$ ), which evaluates the ratio between the actual heat transfer rate and the maximum possible heat transfer rate. The time of operation ( $\Delta t_{op}$ ) is another indicator of importance, especially in latent heat thermal energy storage systems: the main reason for this is the limited time of use of these systems which is associated with the amount of solid PCM remaining in the unit. Then,  $\Delta t_{op}$  is defined as the time between the initial moment and the instant at which the stabilization of the air temperature at the exit of the exchanger is reached. In these experiments, we have considered that this stabilization is reached when a difference of less than 0,1 °C between the outlet air temperature and the temperature achieved by the other components of the exchanger is observed. In the following sections, we present the models used to quantify this information.

#### (a) Cooling and heating power

For air-cooling applications, the cooling power of a heat exchanger is given by the amount of heat that can be extracted from the air, which can be quantified as a function of the air temperature difference between the inlet at the outlet as:

$$P_{cool} = \dot{V}_{air} \cdot c_{p_{air}} \cdot [T_{air_{in}} - T_{air_{out}}]. \quad (3.9)$$

The losses through the heat exchanger walls can be expressed in terms of a thermal circuit, delimiting the control-volume each wall of the unit as:

$$W_{loss} = \frac{\bar{T}_{air_{hex}} - \bar{T}_{air_{ext}}}{\frac{1}{h_{air} \cdot A} + \frac{e_{hex}}{k_{hex} \cdot A_{hex}} + \frac{1}{h_{ext} \cdot A_{hex}}} \quad (3.10)$$

where  $e_{hex}$  is the heat exchanger wall thickness and  $h_{ext}$  is the external heat transfer coefficient between the surrounding air and the heat exchanger wall.

#### (b) Effectiveness and NTU

The effectiveness-NTU method (number of transfer units) evaluates the performance of the unit from the effectiveness. The maximum effectiveness of an air-PCM heat exchanger is achieved when the outlet temperature is the same that the melting point of the PCM. This effectiveness is obtained for a constant value of  $T_{pcm}$  for any point in time by:

$$\varepsilon_{hex} = \frac{T_{in} - T_{out}}{T_{in} - \bar{T}_{pcm}} \quad (3.11)$$

where  $\bar{T}_{pcm}$  is the average temperature inside the PCM domain. This expression is only valid within the phase change temperature range and therefore the average effectiveness of the unit is calculated within this period as follows:

$$\varepsilon_{hex}^- = \frac{\int_0^1 \varepsilon_{hex}(t) \cdot dt}{t_{cycle}} \quad (3.12)$$

where  $t_{cycle}$  is the duration of the melting/solidification. This average value for the effectiveness will allow us to find the number of transfer units NTU, which defines the ratio of the overall conductance to the smaller heat capacity rate.

Regarding the NTU during a heat exchanger analysis, this value remains constant for a given mass airflow. However, for an air-PCM heat exchanger the heat transfer surface area  $A_{hex}$  and the overall heat transfer coefficient  $U_{hex}$  change with time due to phase change. Therefore the NTU can be expressed as:

$$NTU = -\ln(1 - \varepsilon_{hex}) \quad (3.13)$$

and also as:

$$NTU = \frac{U_{hex} \cdot A_{hex}}{\dot{V}_{air} \cdot c_{p_{air}}} \quad (3.14)$$

where  $U_{hex} \cdot A_{hex}$  represents the inverse of the total thermal resistance of the exchanger  $R_{th_{hex}}$ .

### Local Domain

The phenomena occurring at the local level are reflected in the global behavior of this type of heat exchangers. Given that the most attractive operation mode is when the phase change occurs because we can achieve large energy storage or release, good performance indicator should be able to quantify the potential of storing or releasing energy with a convenient heat transfer rate.

We propose then, the melting fraction  $m_f$  as the main local thermal performance indicator because it represents the amount of PCM that has already melted, and can be related with the remaining potential of cooling of the tube by latent heat. For its obtaining, we develop three types of approaches:

- (a) Thermal energy balance.
- (b) One-dimensional radial melting model approach.
- (c) Image processing.

The first approach accounts the melting fraction as the ratio of the amount of energy that is transferred by forced convection between the air and the tube wall. The second approach allows to obtain the melting front position as an equivalent radii, where the solid-liquid interface is found. The third approach measures the amount of solid and liquid PCM from the photographs obtained during the tests. These models are tested during the phase change period of the cycle; therefore, the beginning and the end of the melting should be prior determined. For the two first approach, it results useful if we define each sub-domain as a thermal circuit. In figure 3.43, we represent the local domain as a thermal circuit of resistance in series, being each resistance one of the sub-domains, where:  $R_{air}$  is the thermal resistance by convection, between the air and the wall,  $R_{wall}$  is the thermal resistance by conduction through the wall and  $R_{pcm}$  is the thermal resistance of the PCM.

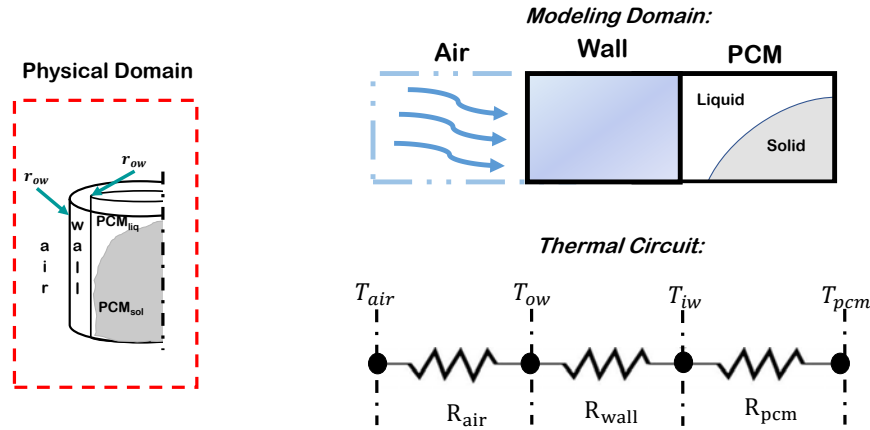


Figure 3.42 – Thermal circuit proposed for the data treatment approaches on the local domain.

(a) **Melting fraction from the thermal energy balance**

The energy transferred from the air to the tube with PCM,  $Q_{pcm}$ , is responsible for the phase change. Then if we neglect the sensible heat stored in the PCM during phase change, we can obtain the melting fraction as the ratio of the energy transferred to the PCM, to the maximum amount of energy that can be stored in the PCM by:

$$m_f = \frac{Q_{pcm}(t)}{E_L} \quad (3.15)$$

where  $E_L$  is the latent heat of the PCM, and the energy transferred  $Q_{pcm}(t)$  during phase change is given by:

$$Q_{pcm}(t) = \int_{t=0}^{t_{final}} q_{pcm}(t) \cdot dt \quad (3.16)$$

with the heat flux  $q_{pcm}(t)$ , given by:

$$q_{pcm}(t) = \frac{T_{air} - T_{iw}}{R_{air} + R_{wall}} - m_{wall} \cdot c_{p_{wall}} \cdot \frac{dT_{wall}}{dt}. \quad (3.17)$$

The wall temperature  $T_{wall}$  is an average of the temperatures of the external  $T_{ow}$  and internal  $T_{iw}$  wall faces temperatures.

The advantage of this approach is that we do not need a prior knowledge of the exact phenomena governing phase change because the energy balance is made between the air and the internal face of the wall, where the heat transfer mechanisms are known the whole time. Nevertheless, with this approach, we cannot directly know the melting front position, without implying the governing directions of the heat transfer in the PCM during the phase change. To approximate the melting front position, we propose the second approach whereby defining the directions of phase change, we can have both the melting fraction and the liquid-solid interface location.

(b) **Melting front position from an one-dimensional radial model approach**

If we now consider that axisymmetric pure conduction controls phase change in the PCM

in the radial direction, without accounting the density changes, we can locate the interface between the liquid and the solid phase.

Since the melting fraction can be expressed as:

$$m_f = \frac{L \cdot \rho_{pcm} \cdot \Delta V_{pcm_{liq}}}{L \cdot \rho_{pcm} \cdot V_{pcm}}. \quad (3.18)$$

Then, since we only consider that heat transfer occurs in the radial direction, we can write the melting fraction as:

$$m_f = \left[ 1 - \frac{r(t)}{r_{iw}} \right]^2. \quad (3.19)$$

Therefore, the radii position  $r(t)$  can be expressed as:

$$r(t) = r_{iw} \cdot [1 - m_f]^{1/2} \quad (3.20)$$

### (c) Melting fraction identification from image processing

As we observed in section 3.3.1, the image analysis resulted in a powerful tool to infer and complete the identification of the physical phenomena occurring in the PCM. However, accounting for the melting fraction directly from these images may result in a complex task, which can carry a significant amount of errors due to incorrect identification of information.

The objective of applying image processing is to obtain the what corresponds to each phase within a tube directly. To achieve this, we need to quantify what part of the image is liquid and what part is solid. Then we can no longer treat the image as the visual picture that could give us qualitative information about phase change, as we did in section 3.3.1, but as a numeric image, from which we can extract quantifiable information.

The RGB images obtained from the photographs shows a significant amount of information, some of which are not relevant for the determination of the liquid fraction. Thus, as in many cases, an image processing is used to enhance the characteristics that we want to extract from the photography and neglect those that are not important.

The test bench is mostly dark, and the paraffin RT28HC presents a white color when solid and transparent when liquid; thus the liquid phase takes the color of the background, and in this case, it presents a range of dark colors. This white and dark colors for each phase, respectively, results conveniently when processing the images because a wide dynamic range is expected between them, which makes it more easy to differentiate one phase from another.

Even though there is a noticeable difference in the original images, between one phase and the other one, each pixel of this RGB image presents three channels: red, green and blue. Each of these channels has 256 intensity values (0-255), resulting in a large range of values in each pixel, even for visually similar regions. Therefore we need to reduce the amount of information. The grayscale image still carries a large amount of information for a pixel, since each one presents 256 intensity values (0-255). This is why, we need to convert our original image, into a binary image, in this way, each pixel can only store two values: zero "0", or one "1."

We pre-selected edge detection techniques because they are the preferred techniques for these goals, since they identify the difference between two regions (edges), instead of the common properties of a region; and we try two separate two regions through their edges position. Among these, we tested several techniques such as the classic Robert, Prewitt, and Sobel filters, as well as the state of the art technique, Canny filter. The problem that we found



with these filters was that the images showed many discontinuities in the surface of the solid PCM, such as the presence of bubbles, making an erroneous detection of the edges. Thus, we finally chose to use an intensity thresholding technique because it allows us to account directly the number of pixels corresponding to each phase.

The result of the thresholding is a binary image where all the original pixels from the gray-scale image are converted to zero “0”, if the value is below the threshold, or one “1”, if not. The criterion used by thresholding can be described as:

$$BN(x, y) = \begin{cases} 1 & \text{if } I_{\text{blur}}(x, y) \geq T_h \\ 0 & \text{otherwise} \end{cases} \quad (3.21)$$

where  $T_h$  stands for the selected threshold.

With this technique, the only characteristic considered is the pixel intensity; thus we have to exclude the main sources of errors. The errors commonly associated to this technique are related to the complexity of the image, the noise, and an inappropriate illumination, which can present brighter and darker parts that not correspond to the real feature of the region. Since a clear difference between one phase and another is expected from the grayscale image, this technique could be suitable to determine the melting fraction. The threshold value can be selected manually by trial and error for simple cases. In this case, we use the *Otsu Method*, which allows performing automatic thresholding from the shape of the histogram of the image. This process is illustrated in figure 3.53.

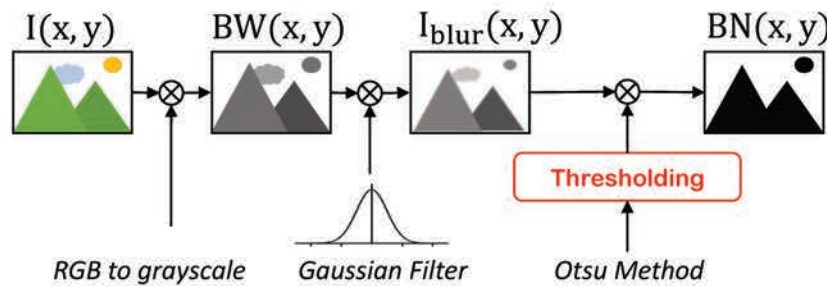


Figure 3.43 – Thermal circuit proposed for the data treatment approaches on the local domain.

Now, we proceed to obtain the number of pixels for each image. To do so, we developed the following protocol for image processing:

1. We convert the original RGB image  $I(x, y)$  into a grayscale image  $BW(x, y)$ .
2. We apply a Gaussian filter to the image to reduce the noise and to obtain a smoother image  $I_{\text{blur}}(x, y)$ .
3. We select the intensity threshold value automatically using the Otsu method. If the image presents several intensity gradients, multiple thresholds are selected. This step results in a binary image  $BN(x, y)$ . The choice of the threshold value  $T_h$  was made automatically by the Matlab<sup>®</sup> software using the *graythresh()* function.
4. We identify the main sources of noise in the image under processing, such as the thermocouple, flash effects, and reflections from the PCM of adjacent tubes.
5. We account the pixels corresponding to the noises, and we convert them to the opposite intensity value.



6. We account the number of black and white pixels, as well as the total number of pixels of the image.
7. Since the black pixels correspond to the liquid phase, and the white ones, to the solid; we proceed to obtain the ratio between the black pixels and the total number of pixels.

These images are a two-dimensional representation of the melting occurring within the tubes. Then, following the same approach that the one use to find the melting fraction in eq. 3.18, we can say that the ratio between the black pixels (liquid PCM) and the total number of pixels represents the melting fraction  $m_f$ .

In brief, we propose in here three approaches to quantify the melting fraction with the following features:

- **Melting fraction from the thermal energy balance:** It considers the heat flux entering the tube from the temperature measurements. Does not consider a governing direction of the heat transfer and does not accounts for the melting front.
- **Melting fraction from an one-dimensional radial model approach:** Considers radial as the main direction of heat transfer, and accounts the corresponding melting front for this assumption using the temperature measurements.
- **Melting fraction identification from image processing:** Considers two-dimensional melting (varying in “z” and “r”). Accounts the melting front, visually.

### 3.4.2 Results and Analysis of the thermal performance evaluation

#### Global Domain

Different airflow were tested for the heat exchanger installed in the test bench. These measurements correspond to the same set point of  $T_{air_{in}} = 34$  °C. Figure 3.44 to 3.47 presents the results for five different airflows, which remained constant during each tests. The purple line represents an airflow of  $540 \text{ m}^3 \cdot \text{h}^{-1}$ ; orange,  $453 \text{ m}^3 \cdot \text{h}^{-1}$ ; lime-green,  $344 \text{ m}^3 \cdot \text{h}^{-1}$ ; magenta,  $243 \text{ m}^3 \cdot \text{h}^{-1}$ ; and yellow,  $196 \text{ m}^3 \cdot \text{h}^{-1}$ . Between these experiments the mean air inlet temperature was  $T_{air_{in}} = 31,9 \pm 0,1$  °C, while the phase change temperature was  $T_{pcm} = 26,9 \pm 0,1$  °C for the melting cycle. During solidification, the mean air inlet temperature was  $T_{air_{in}} = 21,4 \pm 0,4$  °C, while the phase change temperature was  $T_{pcm} = 27,3 \pm 0,1$  °C.

#### (a) Melting cycle

##### (a.1) Air cooling power [ $P_{cool_{max}}$ ↙ $\dot{V}_{air}$ ↘]

In figure 3.44 is shown the results of the cooling power for five different inlet conditions. We can highlight the following: at the beginning of the melting cycle, the cooling power rises quickly, achieving the maximum power rate (between 750 W and 450 W for the airflows shown), then it decreases regularly until it reaches its minimal value at the end of the cycle.

##### (a.2) Operation time [ $\Delta t_{op}$ ↗ $\dot{V}_{air}$ ↘]

From figure 3.44 we can also extract the information about the operation time. Unsurprisingly, the operation time  $\Delta t_{op}$  increases when the airflow decreases, which can be explained by the lower heat transfer rates between the air and the PCM when the airflow rate is lower. All the airflow values assure an operation above 100 W for almost four hours.

(a.3) Effectiveness of the heat exchanger [ $\epsilon_{cool} \nearrow \dot{m}_{air} \searrow$ ]

From figure 3.45 we can observe the temporal effectiveness of the heat exchanger. Just after the cycle has begun this value is above 1, which correspond to the sensible heat storage of the heat exchanger, before phase change begins and  $T_{air_{out}}$  is lower than the melting point. After that, it decreases uniformly until it reaches its lower value. We can highlight higher effectiveness values for the lower inlet airflow rates. This could be explained by the amount of PCM of the unit of roughly 8 kg, compared to the high external forced convection generated by these airflow values on the heat exchanger.

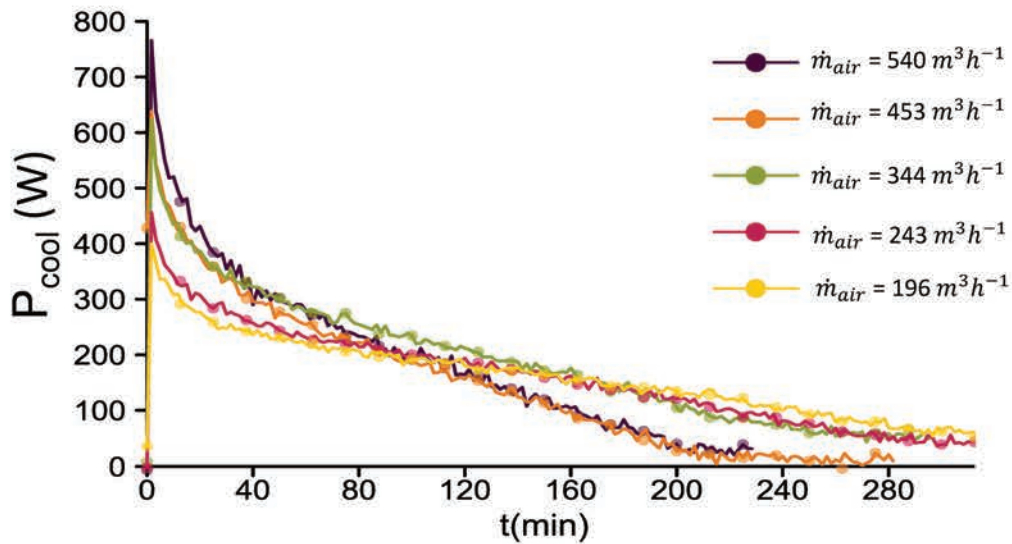


Figure 3.44 – Cooling power for different inlet airflows in the heat exchanger with  $T_{air_{in}} = 32^{\circ}\text{C}$ . Purple:  $540 \text{ m}^3\cdot\text{h}^{-1}$ , orange:  $453 \text{ m}^3\cdot\text{h}^{-1}$ , lime-green:  $344 \text{ m}^3\cdot\text{h}^{-1}$ , magenta:  $243 \text{ m}^3\cdot\text{h}^{-1}$ , and yellow:  $196 \text{ m}^3\cdot\text{h}^{-1}$ .

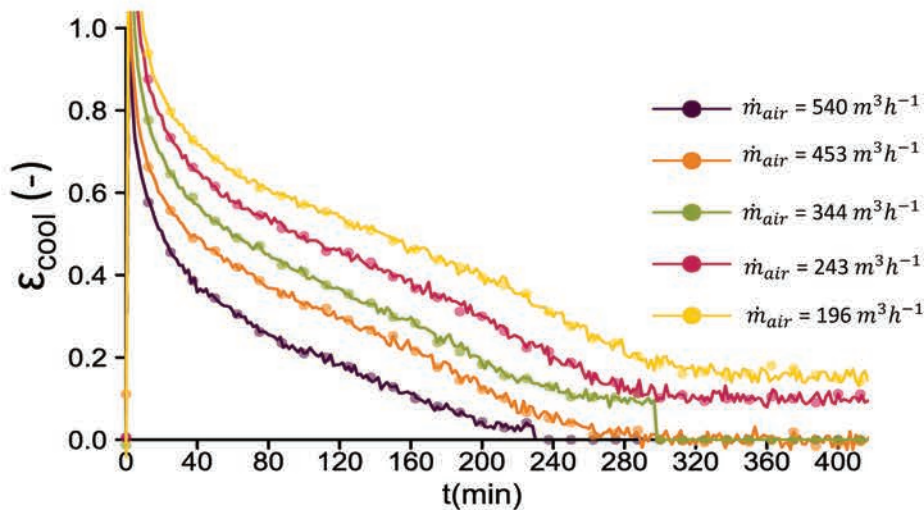


Figure 3.45 – Temporal effectiveness for different inlet airflows during a heating cycle in the heat exchanger with  $T_{air_{in}} = 22^{\circ}\text{C}$ . Purple:  $540 \text{ m}^3\cdot\text{h}^{-1}$ , orange:  $453 \text{ m}^3\cdot\text{h}^{-1}$ , lime-green:  $344 \text{ m}^3\cdot\text{h}^{-1}$ , magenta:  $243 \text{ m}^3\cdot\text{h}^{-1}$ , and yellow:  $196 \text{ m}^3\cdot\text{h}^{-1}$ .

## (b) Solidification cycle

(b.1) Air heating power during the melting of the PCM [ $P_{heat_{max}}$  ↗  $\dot{V}_{air}$  ↘]

In figure 3.46 we have the heating power during the solidification of the PCM for different inlet conditions. We can observe a quick increase in the heating power at the beginning of the cycle. After that, the decrease of the heating power occurs on a nearly constant linear slope.

(b.2) Operation time [ $\Delta t_{op}$  ↗  $\dot{V}_{air}$  ↘]

In the same figure 3.46 we can observe that as the airflow decreases, the operation time  $\Delta t_{op}$  of the PCM solidification cycles increases.

(b.3) Effectiveness of the heat exchanger [ $\varepsilon_{cool}$  ↗  $\dot{m}_{air}$  ↘]

In figure 3.47 we also observe a quick decrease in the effectiveness in the first minutes of the cycle, and then it starts to decrease uniformly until they reach  $\varepsilon = 0$ .

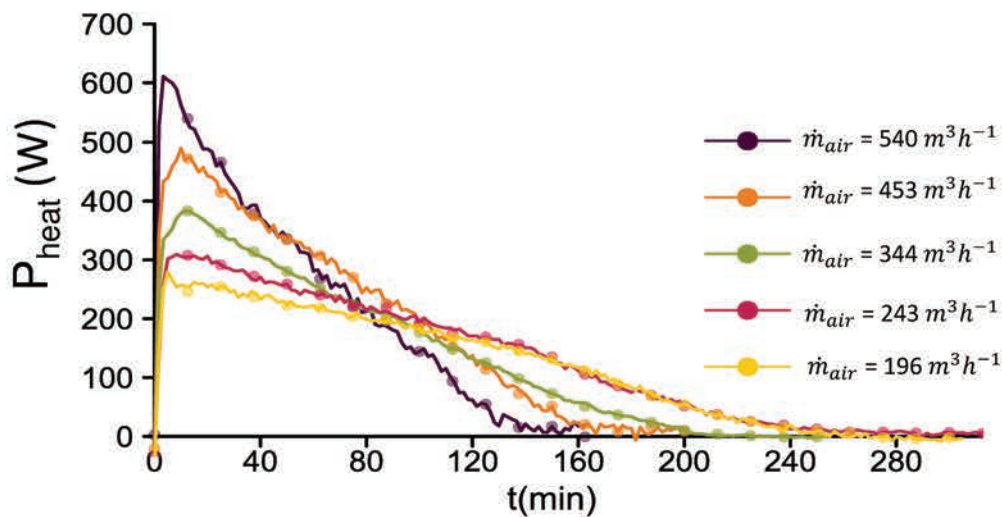


Figure 3.46 – Heating power for different inlet airflows during a cooling cycle in the heat exchanger with  $T_{air_{in}} = 22^{\circ}\text{C}$ . Purple:  $540 \text{ m}^3 \cdot \text{h}^{-1}$ , orange:  $453 \text{ m}^3 \cdot \text{h}^{-1}$ , lime-green:  $344 \text{ m}^3 \cdot \text{h}^{-1}$ , magenta:  $243 \text{ m}^3 \cdot \text{h}^{-1}$ , and yellow:  $196 \text{ m}^3 \cdot \text{h}^{-1}$ .

## (c) Comparison of melting and solidification cycles

Now comparing both cycles, we notice that the maximum value of the air cooling power  $P_{cool}$  and the maximum value corresponding to the air heating power  $P_{heat}$  do not correspond, the latter presenting lower values for the airflows tested. During the solidification cycle, the elements of the air-PCM heat exchanger achieve the inlet temperature faster, if we compare to the melting cycle. Therefore, we can observe lower values on the total operation time  $\Delta t_{op}$  during the solidification. Regarding the effectiveness of the heat exchanger  $\varepsilon_{hex}$  for both cycles we can observe lower values during the solidification cycle. This can be expected since the solidification occurs more rapidly and thus, the temperatures within the heat exchanger decrease faster.



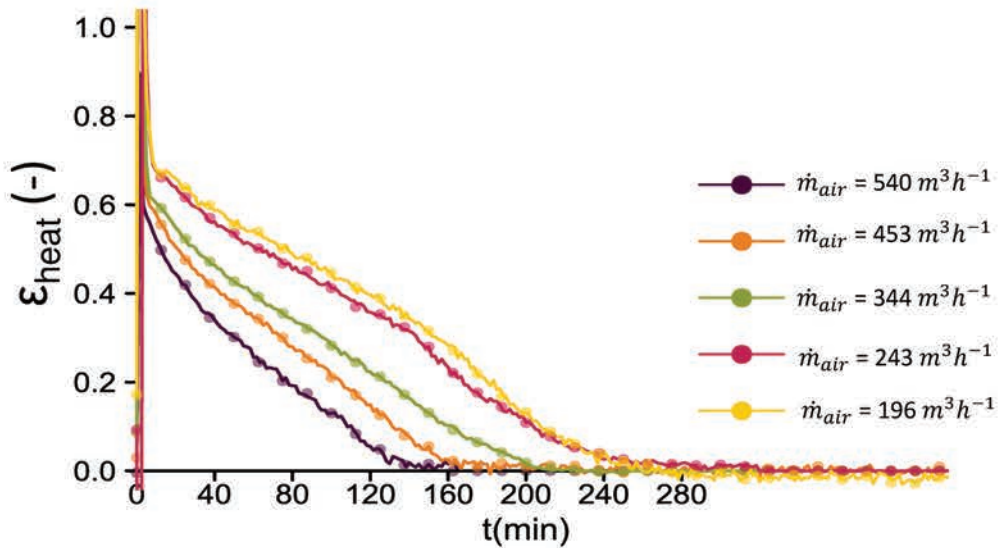


Figure 3.47 – Temporal effectiveness for different inlet airflows during a heating cycle in the heat exchanger with  $T_{air,in} = 22^{\circ}\text{C}$ . Purple:  $540 \text{ m}^3\cdot\text{h}^{-1}$ , orange:  $453 \text{ m}^3\cdot\text{h}^{-1}$ , lime-green:  $344 \text{ m}^3\cdot\text{h}^{-1}$ , magenta:  $243 \text{ m}^3\cdot\text{h}^{-1}$ , and yellow:  $196 \text{ m}^3\cdot\text{h}^{-1}$ .

A general trend that can be observed in both cycles is that the higher the airflow values, the lower the operation time of the heat exchanger. This behavior is expected since, we have a limited source heat transfer, which is related to the maximum energy storage or release capacity due to phase change. Then, in brief, we can conclude that when selection the operative parameters of the heat exchanger, namely the inlet temperature and the airflow value, we need to weigh between the duration in which we need it to work depending on the application and the cooling or heating power, needed for this application.

If we integrate the cooling  $P_{cool}$  and heating power  $P_{heat}$  over the operation time  $\Delta t_{op}$ , we can obtain the cumulative heat release or stored by the heat exchanger. These values correspond to the latent heat stored or released from the PCM due to the phase change in the PCM, as well as the sensible heat due to the temperature difference between the elements of the heat exchanger. If we consider the elements of the heat exchanger namely:

- the walls of the glass tubes containing the PCM,
- the walls of the heat exchanger (consisting of wood and plexiglas®), and
- the PCM itself,

we can quantify the potential of storing or releasing of these elements for the temperature difference during the cycle. The potential of the heat exchanger of store or release sensible energy for a temperature difference of  $\pm 10^{\circ}\text{C}$  is about  $E_S = 742 \text{ kJ}$ . According to the PCM properties (see table 3.3), the potential of storage in latent heat form for the PCM is about  $E_L = 1,9 \text{ MJ}$ .

In table 3.14, are shown the results for the cumulative heat during the cooling and heating cycles. For the cooling cycle this value corresponds to  $E_{cum_m} = 2,78 \pm 0,2 \text{ MJ}$ . Then, we have that:

- $E_{cum_{cool}} = 2,78 \pm 0,2 \text{ MJ}$
- $E_S = 0,742 \text{ MJ}$
- $E_L = 1,9 \text{ MJ}$

Leaving an amount of  $0,138 \pm 0,2 \text{ MJ}$ , which can correspond to the losses, since the temperature inside the testing room is lower than the temperature inside the heat exchanger ( $T_{room} \approx 21$

Table 3.14 – Values obtained from the data processing at the global domain.

$\dot{V}_{air}$ [m <sup>3</sup> ·h <sup>-1</sup> ]	$E_{cum_{cool}}$ [MJ]	$E_{cum_{heat}}$ [MJ]	$\varepsilon_{cool}$ [-]	$\varepsilon_{heat}$ [-]	$\Delta t_{op_{cool}}$ [min]	$\Delta t_{op_{heat}}$ [min]
540	2,75	2,25	0,172	0,12	227	165
453	2,60	2,39	0,249	0,16	275	200
344	3,18	2,16	0,334	0,20	297	250
243	2,72	2,38	0,420	0,24	350	300
196	2,64	2,18	0,520	0,34	375	288

°C); therefore the heat transfer is promoted from inside the heat exchanger to the surroundings. We can also compare these values for the solidification cycle where:

- $E_{cum_{heat}} = 2,27 \pm 0,097$  MJ
- $E_S = 0,742$  MJ
- $E_L = 1,9$  MJ

In this case the  $0,39 \pm 0,097$  MJ, could correspond to the energy gains from the testing room.

The table also shows the values for the mean effectiveness of the heat exchanger for both cycles, as well as the operating time. The low values of the mean effectiveness are expected since high heat transfer rates by forced convection are achieved, and the heat transfer surface area decreases in time.

#### (d) Empirical correlations

An empirical relation between the inlet airflow and the operation time  $\Delta t_{op}$ , corresponding to the melting and solidification cycles was obtained from these experimental results. The expressions obtained for melting and solidification are expressed as follows:

(d.1) **Melting operation time  $\Delta t_{op_m}$ :**

$$\Delta t_{op_m} = -0,4091 \cdot \dot{V}_{air} + 450,10 ; R^2 = 0,9793 \quad (3.22)$$

(d.2) **Solidification operation time  $\Delta t_{op_s}$ :**

$$\Delta t_{op_s} = -0,3945 \cdot \dot{V}_{air} + 380,72 ; R^2 = 0,9620 \quad (3.23)$$

These regressions were further used to predict other test and then compare its accuracy to the experimental  $\Delta t_{op}$  for the melting and solidification cycles. In figure 3.48 we can observe the results for five test where the regressions were applied. In here we can observe the results for the melting (dot) and solidification (asterisk) in black, and the predicted values for the melting and solidification cycles, in red and blue, respectively. The relative errors predicting the operation time  $\Delta t_{op}$  can be observed in the histograms in figure 3.49. We can notice that the regression obtained for melting presents lower error values than the one obtained for solidification. The importance on the prediction of the operation time lies on their use to adjust the inlet airflow of the unit to suit the energy needs of the building.

### Local Domain

#### (a) Thermal analysis from temperature measurements



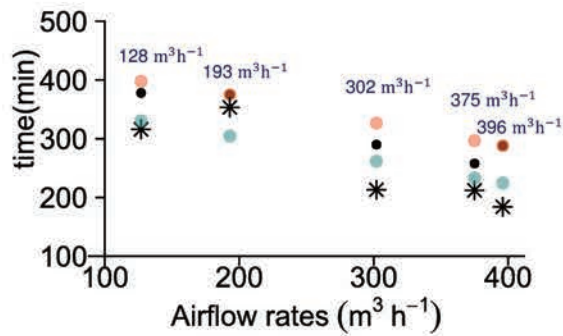


Figure 3.48 – Time operation prediction for five test carried out in the test bench. *Color code:* black point: measured  $\Delta t_{op_m}$ , black asterisk: measured  $\Delta t_{op_s}$ , red dots: predicted  $\Delta t_{op_m}$ , blue dots: predicted  $\Delta t_{op_s}$ .

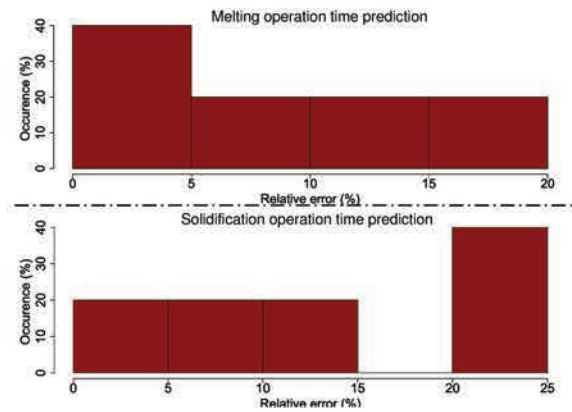


Figure 3.49 – Distribution of the errors for the linear regression obtained for  $\Delta t_{op_m}$  and measured  $\Delta t_{op_s}$ , where for melting cycle RMSE = 25,47 min and for solidification cycle RMSE = 37,46 min.

#### (a.1) Melting fraction from the thermal energy balance

Figures 3.50 and 3.51 show the heat flux and the melting fraction for four tubes obtained by thermal energy balance at the local level, between the air and the internal side of the wall, using eqs. 3.15 and 3.16, over the phase change period. The purple line corresponds to a tube located in the middle of the fifth line  $tube_5$ , the orange, to a tube in the middle of the eighth line  $tube_{8a}$ , the lime-green line, to a tube in the middle of the eighth line  $tube_{8b}$ ; and the line in magenta to a tube in the eighth line near the plexiglas® side of the heat exchanger,  $tube_{8c}$ .

We can observe that those tubes located in the same row, keep similar behavior, if we compare them to  $tube_5$ . This could be explained by the stratification along the heat exchanger, where the heat transfer profiles are not the same for the fifth and the eighth row of the heat exchanger, because that for a given time, the air temperature in the fifth row is higher to the corresponding air temperature at the eight row.

In figure 3.51 we present the melting fraction profiles for the tubes mentioned above. The first thing that we can highlight is that we can observe two different regions:

- A first region during the first three hours of the cycle, where the melting fraction increases slowly.
- A second region during the last hour of the cycle, where the melting fraction increases rapidly.

In the first region, we have that for almost two hours, the PCM remained in solid state, even though we can observe that a nearly constant heat flux entering the tube in figure 3.50. These segmented behavior on the melting fraction could be related to the following:

- The temperature measurement positions within the tube. Since the tubes are of a small diameter ( $D_{ow} = 2,45$  cm), installing several thermocouples to measure different points was not a suitable solution. Each time we place a thermocouple inside the tube, we change its heat transfer features, which move us away from knowing the behavior under real conditions, changing the operation time and the melting and solidification patterns. Thus, the temperatures were assumed constant in the axial axis (“z”), and the heat flux is calculated from those measurements made at a single height of the tube. Then, if more

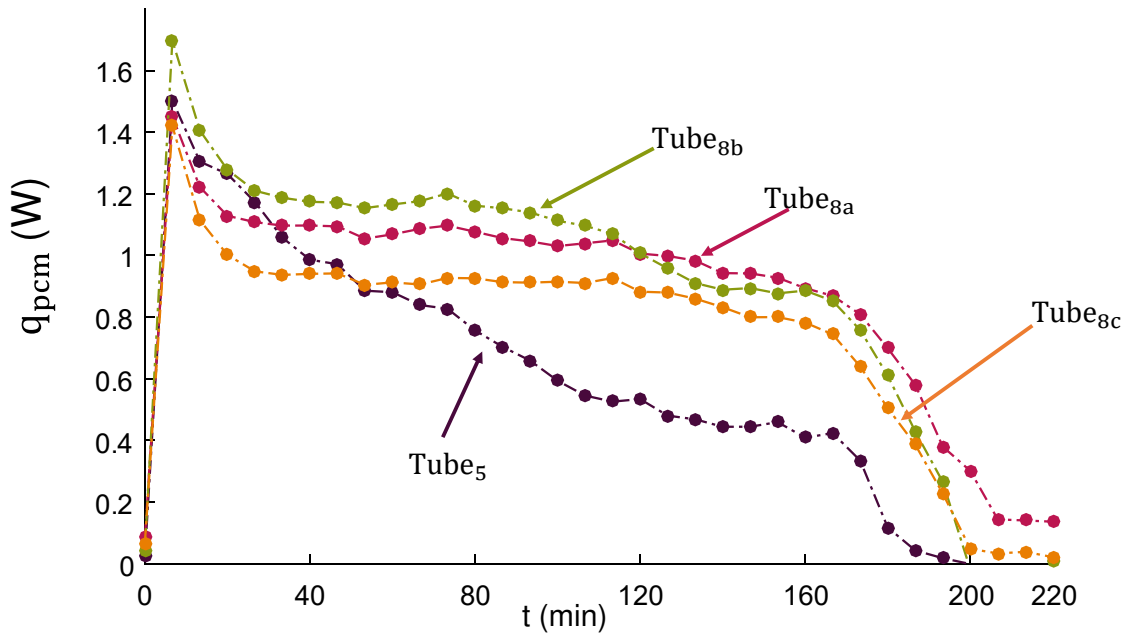


Figure 3.50 – Heat flux entering the tubes by thermal heat energy balance in the local domain for an airflow of  $\dot{V}_{air} = 193 \text{ m}^3 \cdot \text{h}^{-1}$  and a  $T_{air_{in}} = 32 \text{ }^\circ\text{C}$ . Color codes: Purple: tube in the middle of the fifth line, orange: tube in the middle of the eighth line, lime-green: tube in the middle of the eighth line, magenta: tube in the eighth line near the plexiglas® side of the heat exchanger.

complex heat flux profiles exist within the tube, it would affect the melting fraction calculation.

#### (a.2) Melting fraction from an 1D radial model approach

Figure 3.52 presents the solid-liquid interface prediction from an 1D radial model approach in the local domain (see 3.17). Axisymmetrical conditions were supposed for this analysis; therefore at the end of the cycle, this interface reaches the center of the tube. The interest of using this numerical model is to be able to predict the position of the interface between the liquid and solid PCM. Nevertheless, the biggest issue with this prediction is that we assume an ideal profile of heat transfer by pure conduction in the radial direction, and we obtain a response that we cannot verify its validity through experimental temperature measurements. However, this approach could be useful if a melting front tracking is desired.

We can highlight that it follows the same pattern observed on the melting fraction profiles. According to these results on figures 3.51 and 3.52, we can imply that the melting does not follow a constant increase with time, showing that at the beginning the change of the PCM from the solid to the liquid state occurs slowly, and once it reaches a determined value, it begins to melt quickly. To complete this analysis, we will compare these results with the image processing of the photographs of the melting cycle.

#### (b) Comparison of the results

Now we can compare these results obtained for the local domain, with those obtained for the global domain in section 3.4.2. The cumulative energy for the tubes can be calculated obtaining

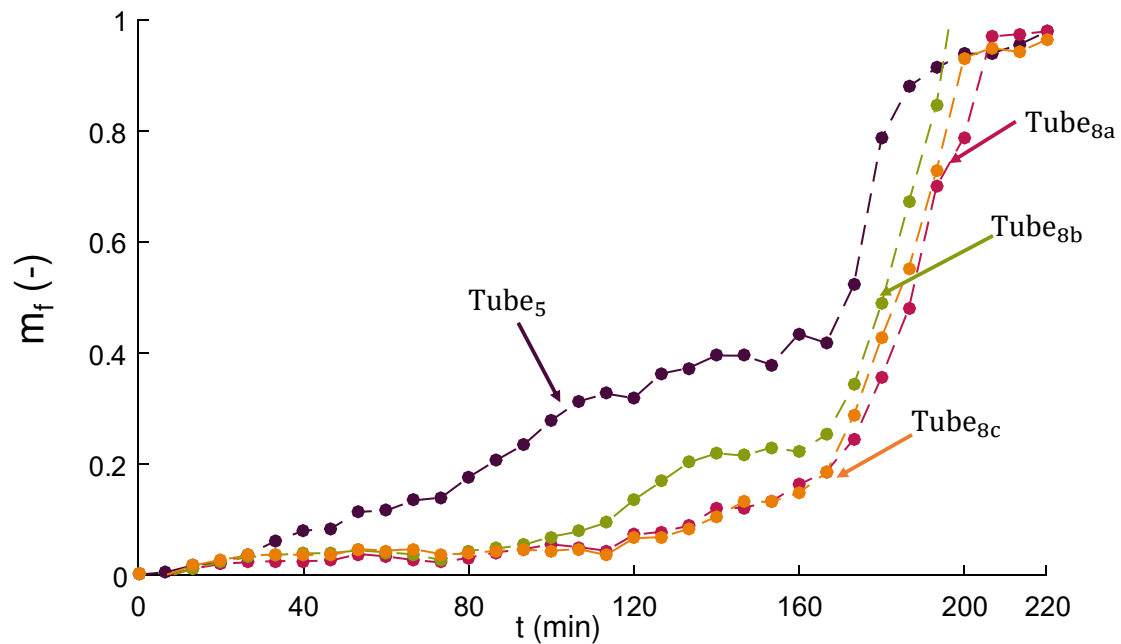


Figure 3.51 – Melting fraction by thermal heat energy balance in the local domain for an airflow of  $\dot{V}_{air} = 193 \text{ m}^3 \cdot \text{h}^{-1}$  and a  $T_{air_{in}} = 32 \text{ }^\circ\text{C}$ . Color codes: Purple: tube in the middle of the fifth line, orange: tube in the middle of the eighth line, lime-green: tube in the middle of the eighth line, magenta: tube in the eighth line near the plexiglas® side of the heat exchanger.

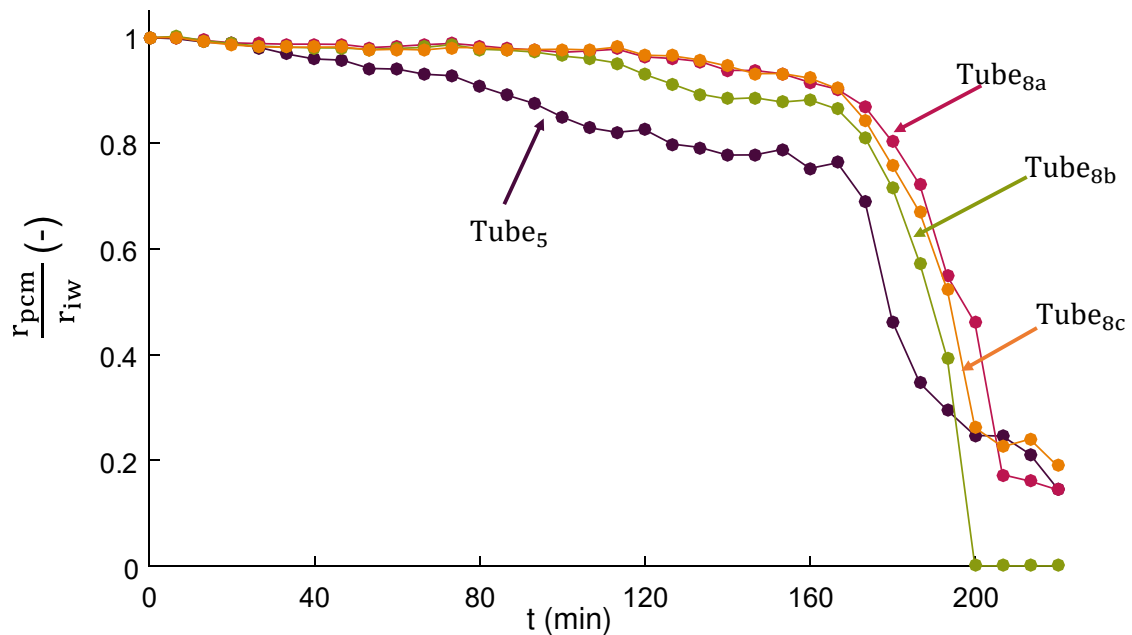


Figure 3.52 – Solid-Liquid interface position from an 1D radial model approach for a tests carried out under the following conditions:  $\dot{V}_{air} = 193 \text{ m}^3 \cdot \text{h}^{-1}$  and a  $T_{air_{in}} = 32 \text{ }^\circ\text{C}$ . Color codes: Purple: tube in the middle of the fifth line, orange: tube in the middle of the eighth line, lime-green: tube in the middle of the eighth line, magenta: tube in the eighth line near the plexiglas® side of the heat exchanger .

a mean value for the tubes in the eight row of  $E_{cum_{pcm}} = 20,7 \pm 0,05$  kJ. Having in mind that we have 99 tubes in the heat exchanger and that:

- $E_{cum_{cool}} = 2,78 \pm 0,2$  MJ
- $E_S = 0,742$  MJ

we can compare the value obtained by measurements and see if corresponded to the latent heat storage calculated from the properties of the material  $E_L = 1,9$  MJ. Then, if we account the sensible heat  $E_S = 0,742$  MJ, we can obtain that the energy stored in the heat exchanger is  $E_{cum_{cool}} = 2,7913$  MJ, which has an error of 0,4% with the value obtained from the global domain. With these results we can make the link between the global domain and the local domain.

### (c) Thermal analysis from image processing

The main objective of this section is to be able of quantify certain information of interest such as the melting fraction and the position of the melting front. From the temperature measurements from we can infer the phenomena controlling phase change, but now, with the image processing and analysis we can complete the temperature measurements and corroborate the assumptions and inferences made previously.

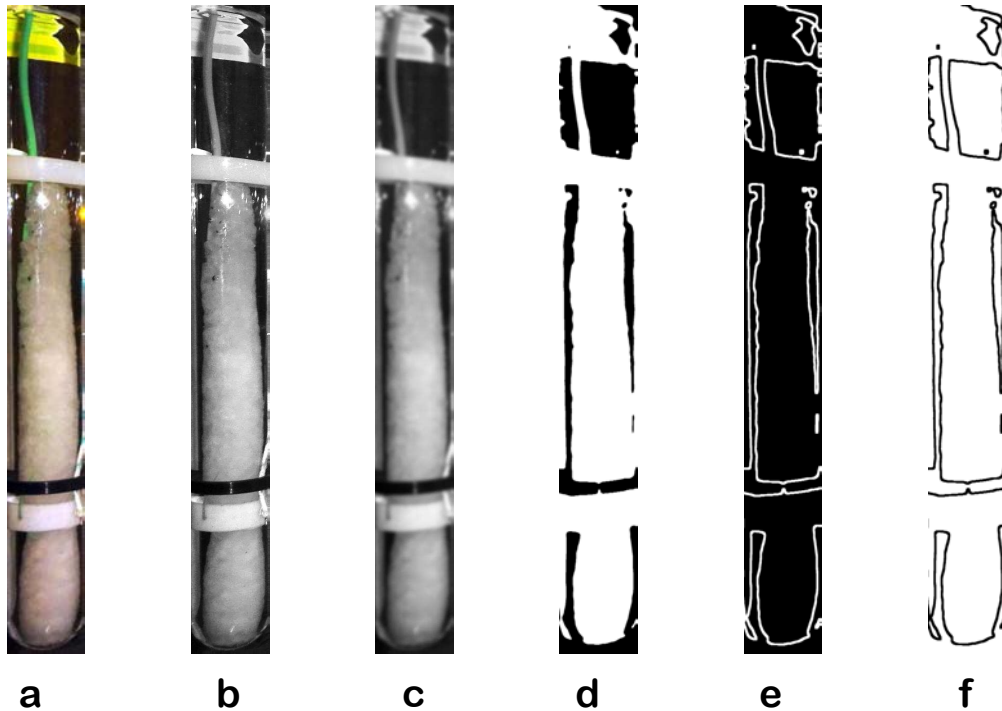


Figure 3.53 – Image processing of tube<sub>1</sub> at  $t = 144$  min from the beginning of the cycle: a) RGB image  $I(x,y)$ , b) gray-scale image  $BW(x,y)$ , c) image with Gaussian filter  $I_{blur}(x,y)$ , d) binary image after thresholding  $BN(x,y)$ , e) edge detection of the image with the Canny filter, and e) inverse image of the edge detection.

Figure 3.53 shows an overall illustrative result from the image processing of a photography of the Tube<sub>1</sub> after 144 min from the beginning of the cycle, following the methodology proposed on section (c). To select the time between the photographs we rely on the visual changes in the phenomena observed in the photographs analysis at the local domain section (3.3.1). For this purpose two tubes were processed: tube<sub>1</sub> and tube<sub>8c</sub> (see figure 3.15). The former



tube corresponds to the first row of the heat exchanger, therefore is the first to go through the changes inherent to the melting of the PCM. The latter, tube<sub>8c</sub>, is fully integrated with thermocouples; therefore we can compare the melting fraction obtained by energy balance, with the one obtained by image processing. We now detail each sub-figure of figure 3.53.

- **RGB image**  $I(x,y)$

The sub-figure *a* of figure 3.53 presents the original RGB image  $I(x,y)$ . We can notice several regions in this image: the main regions correspond to the solid PCM and the liquid surrounding the solid PCM. The rest of the regions corresponds to other elements in photography; some of them are physical elements such as the thermocouple and its support system, and others, correspond to photography effects such as the flash, and the light and dark spot regions that appear due to the difference in the lighting during the capture of the photographs. The first two, the solid and liquid PCM, are the information that we want to extract, while the others represent noises that would lead us to an erroneous calculation of the melting fraction if we do not avoid them.

- **Grayscale image**  $BW(x,y)$

Sub-figure *b*, of figure 3.53, presents the image after converting to grayscale  $BW(x,y)$ . After this conversion we can begin to enhance the image to highlight those features that we want to extract.

- **Smoothed image**  $I_{\text{blurr}}(x,y)$

The grayscale image  $BW(x,y)$  is filtered by a Gaussian Filter to smooth its edges, which facilitates finding the edges later. Now, we obtained a blurred image  $I_{\text{blurr}}(x,y)$  (sub-figure *c*), corresponding to sub-figure *c* of figure 3.53. This filter help us to reduce the noise by smoothing the image, reducing the details that could lead into false results.

- **Binary image**  $BN(x,y)$

One the image was smoothed, we proceeded to apply the thresholding following the Otsu method, finally obtaining a binary image  $BN(x,y)$  (sub-figure *d*), from which we can extract the melting fraction.

- **Edge detection using the Canny filter**

In sub-image *e* and *f* of image 3.53, we have the result of applying the Canny edge detection. From these images we can extract the information about the melting front position.

From image 3.55 to 3.58, we present the results of the image processing techniques used for our visual results, the intensity thresholding and the Canny filter. However, these binary images obtained still present some of the noises identified earlier in the original image as can be shown in sub-figure *a* of figure 3.54. We can make the image undergoes further processing, but by over-processing the image, we risk to obtain false results for the melting fraction. This is why we decided to isolate the sources of noise, and convert them manually to the opposite value, since this binary image can be represented as a matrix of ones and zeros (sub-figure *b* of 3.54). For this, we defined first the real values of this noises as presented in table 3.15.



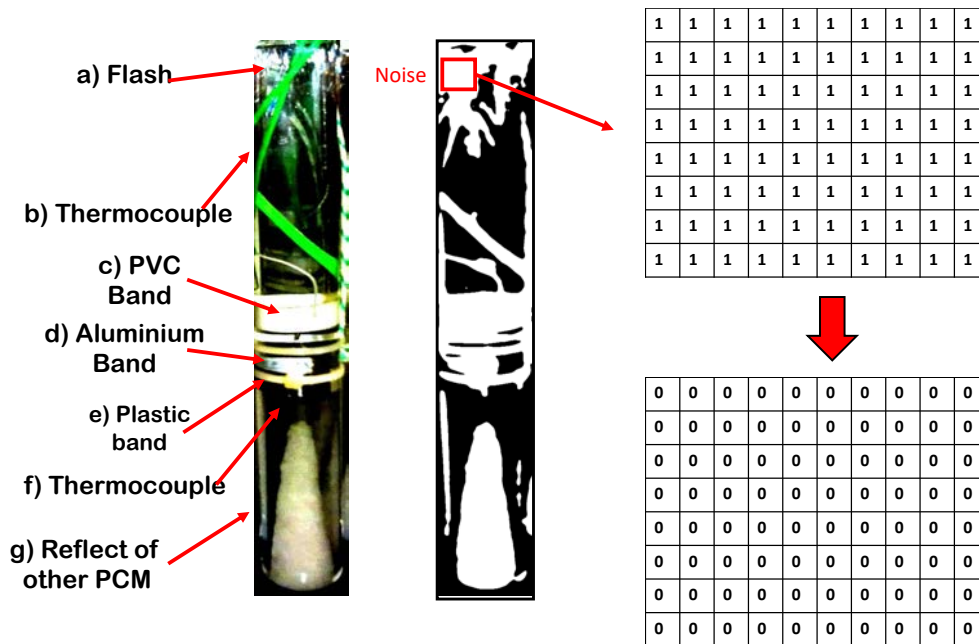


Figure 3.54 – Noise detection and correction for an image of tube<sub>8c</sub> at  $t = 214$  min from the beginning of the cycle: a) noise identification in the original image  $I(x,y)$  and after thresholding  $BN(x,y)$ ; b) representative scheme of the image mapping process: the gray colored pixels represents the noise, and after the mapping their value correspond to the opposite.

Table 3.15 – Correction of values for the sources of noise during the image processing.

Source of noise	Present value	Corrected Value
PCM meniscus	1	0
PVC band (solid)	1	1
PCV band (liquid)	1	0
Thermocouple (solid)	0	1
Thermocouple (liquid)	1	0
Aluminum band (solid)	1	1
Aluminum band (liquid)	1	0
Plastic band (solid)	0	1
Plastic band (liquid)	0	0
Scotch tape (solid)	1	1
Scotch tape (liquid)	1	0
flash (liquid)	1	0

After this process, the amount of black and white pixels can be obtained and therefore, the melting fraction. Figure 3.59 shows the melting fraction progression in time for the tube<sub>1</sub> and tube<sub>8c</sub>.

We can compare the melting fraction obtained by image processing for tube<sub>8c</sub> in magenta, and the melting fraction obtained by energy balance, in purple. In the first two hours of cycle, where the melting fraction represents less than 10% of the total amount of PCM, we observe that the energy balance and the image processing give similar results (RMSE = 0,04).

Nevertheless after the two first hours, the prediction of the melting fraction from these two methods are separated from each other, where the energy balance under predicts the melting

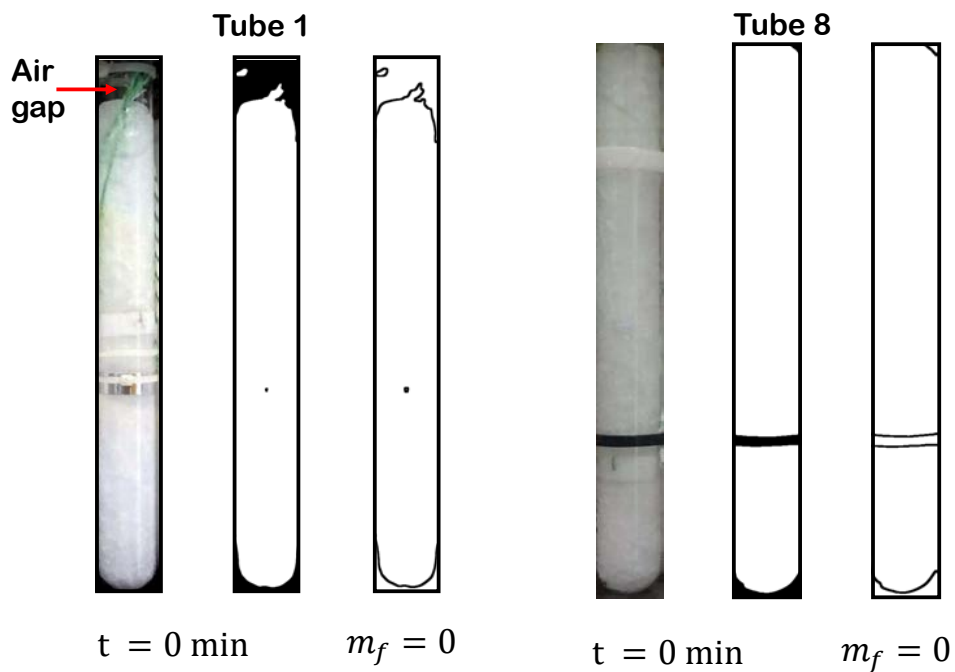


Figure 3.55 –  $t = 0$  Image processing for the tubes during the melting of PCM for a test carried out under the following conditions:  $\dot{m}_{air} = 193 \text{ m}^3 \cdot \text{h}^{-1}$  and a  $T_{air,in} = 32 \text{ }^\circ\text{C}$ . Left: Tube and right: Tube. Each figure present the original RGB image, the image processed using the threshold of intensity technique and the Canny filter technique.

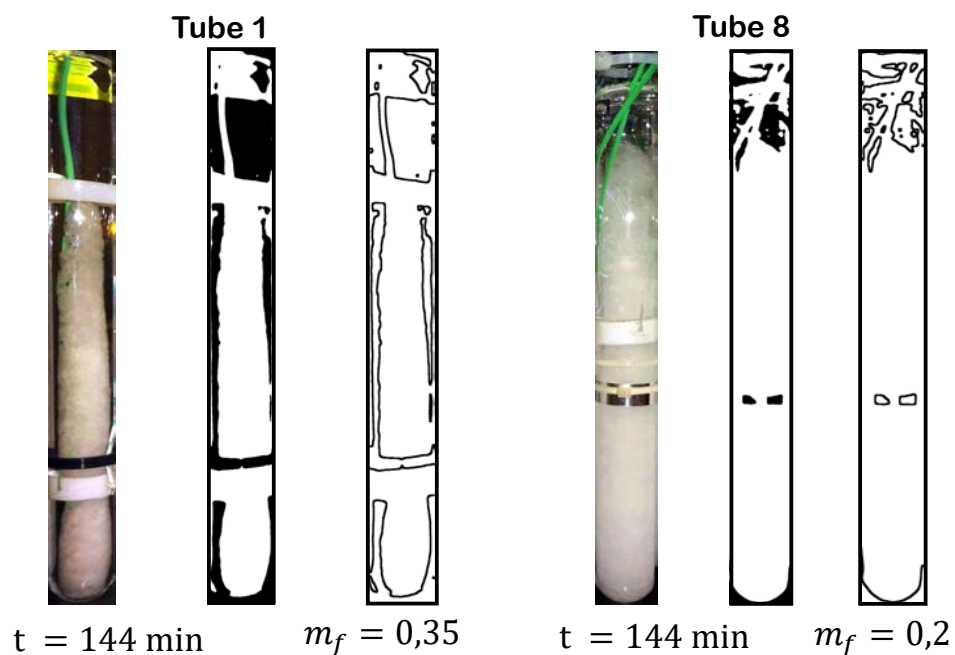


Figure 3.56 –  $t = 144 \text{ min}$ . Image processing for the tubes during the melting of PCM for a test carried out under the following conditions:  $\dot{V}_{air} = 193 \text{ m}^3 \cdot \text{h}^{-1}$  and a  $T_{air,in} = 32 \text{ }^\circ\text{C}$ . Left: Tube and right: Tube. Each figure present the original RGB image, the image processed using the threshold of intensity technique and the Canny filter technique.

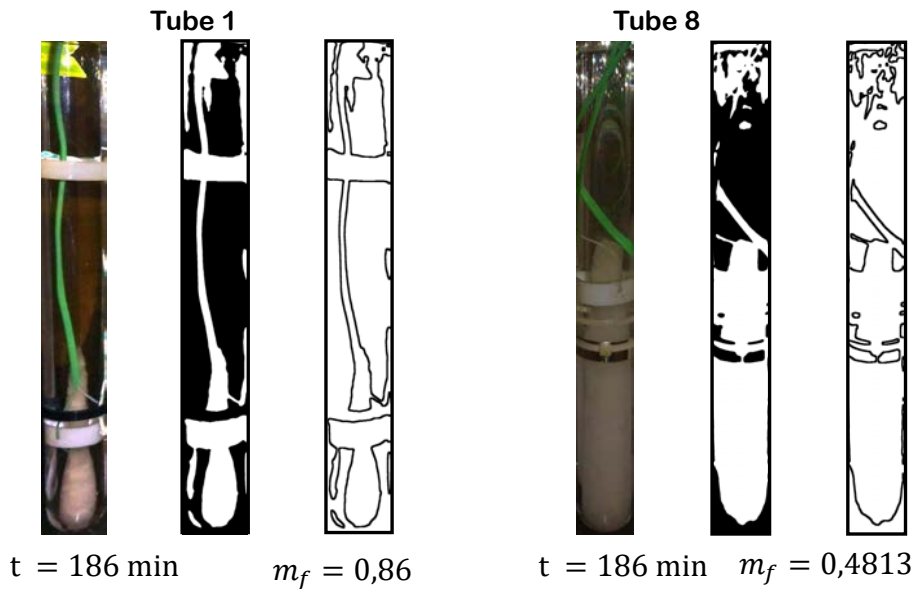


Figure 3.57 –  $t = 186$  min. Image processing for the tubes during the melting of PCM for a test carried out under the following conditions:  $\dot{V}_{air} = 193 \text{ m}^3 \cdot \text{h}^{-1}$  and a  $T_{air,in} = 32 \text{ }^\circ\text{C}$ . Left: Tube 1 and right: Tube 8. Each figure present the original RGB image, the image processed using the threshold of intensity technique and the Canny filter technique.

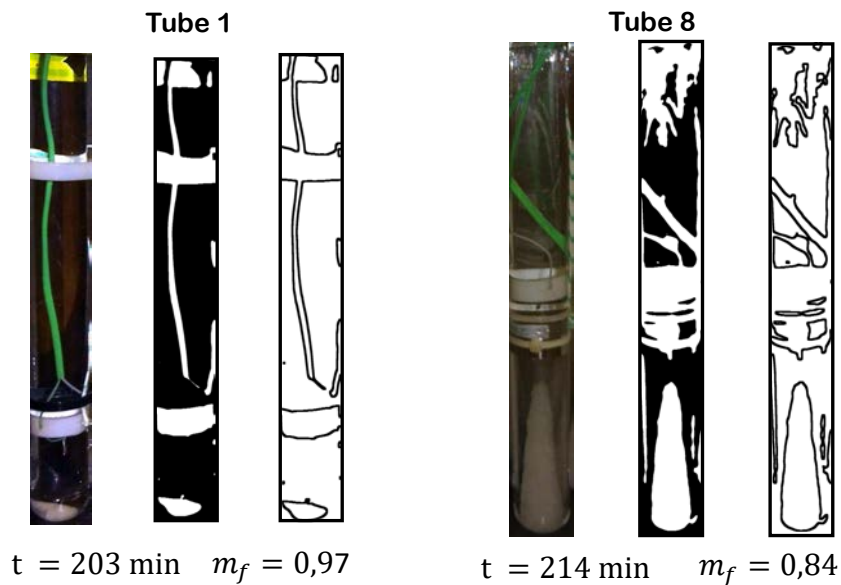


Figure 3.58 –  $t = 203$  min. Image processing for the tubes during the melting of PCM for a test carried out under the following conditions:  $\dot{V}_{air} = 193 \text{ m}^3 \cdot \text{h}^{-1}$  and a  $T_{air,in} = 32 \text{ }^\circ\text{C}$ . Left: Tube 1 and right: Tube 8. Each figure present the original RGB image, the image processed using the threshold of intensity technique and the Canny filter technique.

fraction value, if compared to the image processing results (RMSE = 0,39).

From the third hour of the cycle, the behaviors are again approaching until finally the liquid fraction predicted by the energy balance increases suddenly, and over predicts the melting fraction. This results in accordance with the behavior previously observed where the PCM temperature  $T_{pcm}$  achieve the inlet temperature once the liquid PCM reaches the thermocouple.

Therefore, it is not surprising that the melting fraction calculated by energy balance reaches its maximum value before that the one calculated by image processing.

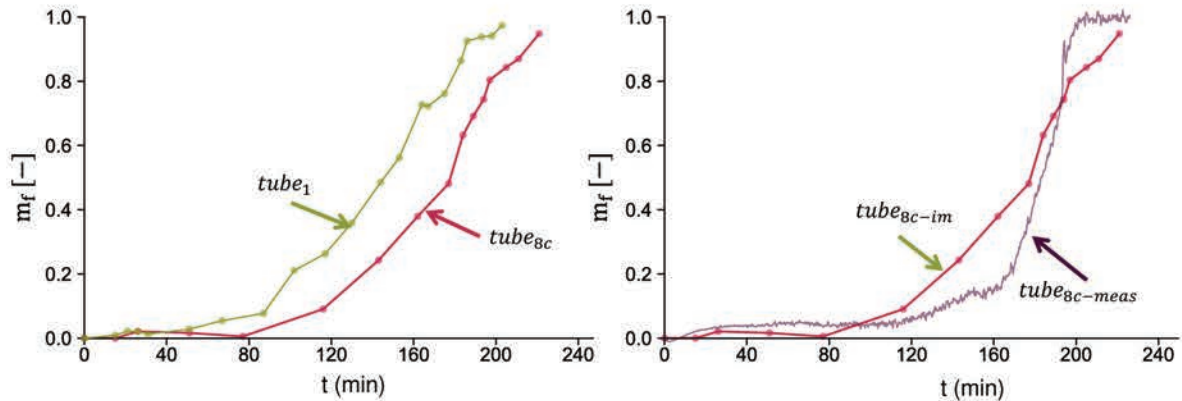


Figure 3.59 – Melting fraction within tubes with PCM. *Left*: the tube<sub>1</sub>, in lime-green; and tube<sub>8c</sub>, in magenta, obtained by image processing. *Right*: Comparison between the tube<sub>8c</sub> obtained from image processing, in lime-green, and tube<sub>8c</sub> obtained by energy balance in purple, for an inlet airflow of 193 m<sup>3</sup>·h<sup>-1</sup>.

### 3.5 Physical phenomena identification

The previous analysis allowed us to identify behaviors related to certain phenomena involved in phase change such as conduction and convection in the PCM, forced convection between the surrounding air and the tube wall, and conduction in the aforementioned wall. Nevertheless, the use of dimensionless parameters, as the dimensionless numbers, will allow us to quantify the presence and impact of these phenomena during the phase change.

In this section, we seek to determine which physical phenomena should be considered when making a model for tube bundle air-PCM heat exchangers. Besides using these dimensionless numbers can give us the range of validity of our experiments for comparison with future tests.

#### 3.5.1 Physical phenomena related to phase change

From the beginning of this work we have defined which are the most likely physical phenomena to occur within an air-PCM heat exchanger. Now, from the results obtained from the experiments, we can quantify and validate its impact in the process.

In the global domain, the central phenomena to identify is the nature of the convection between the air and the PCM containers that ensure desirable heat transfer rates.

At the local level, we assumed heat transfer controlled by conduction and convection in the three sub-domains: air, wall, and PCM. The heat exchanges between the air and the tube wall follow the same phenomena of convection in the global domain. Since the wall is a solid body, only conduction is expected as the controlling mechanism of heat transfer. Although these phenomena are necessary, the main search focuses on the sub-domain of the PCM, where it is sought if convection plays a role of consideration or not during the phase change. In the following section, we will define the dimensionless numbers associated with these physical phenomena.



### 3.5.2 Dimensionless numbers associated with an air-PCM heat exchanger

#### (a) Global Domain

At a global level when we looked for the overall convective heat transfer coefficient  $h_{air}$ , between the air and the PCM containers in section 3.2.3, we had to quantify the values of Nusselt,  $\mathcal{N}u$ , Prandtl,  $\mathcal{P}r$ , and Reynolds,  $\mathcal{R}e$ , since we used empirical and analytical correlations to find  $h_{air}$ . Now we can use these dimensionless number to quantify the nature of the external convection and heat transfer rate between the air and the PCM containers.

#### (b) Local Domain

Now, at the local domain, we mostly consider those numbers that relate to the heat transfer during phase change, namely Stefan,  $\mathcal{S}te$ , Fourier  $\mathcal{F}o$ , and, Biot  $\mathcal{B}i$  numbers.

We first consider here the Stefan number  $\mathcal{S}te$  which is associated with the phase change, it expresses the ratio between the sensible heat and latent heat available from the PCM. This Stefan number is a dimensionless form of the temperature difference between the outer surface of the tube and the PCM melting temperature defined by:

$$\mathcal{S}te = \frac{c_{p_{pcm}} \cdot [T_{ow} - T_{pcm}]}{L} \quad (3.24)$$

We also consider the Fourier number,  $\mathcal{F}o$ , as a dimensionless measure of time. It expresses the ratio between the amount of heat transmitted to the body and the sensible storage capacity of the body and it is defined by:

$$\mathcal{F}o = \frac{\alpha_{pcm} \cdot t}{L_{c_{pcm}}^2} \quad (3.25)$$

where  $\alpha_{pcm}$  is the thermal diffusivity of the PCM, and  $L_{c_{pcm}}$  is the characteristic length of the PCM, which corresponds to the length through which conduction occurs. If a 1D radial heat transfer profile is assumed, this characteristic length  $L_{c_{pcm}}$ , can be directly defined by the tube diameter  $D_{ow}$  of radius  $r_{ow}$ . However, this characteristic length can be defined, regardless the heat transfer direction, as  $\frac{V_{ow}}{A_{pcm}}$ .

The number of Fourier together with Stefan are sufficient to describe the heat transfer when the phase change is only considered by conduction [17]. For us, these numbers can be useful for determining the presence of phase change, and the heat transfer rate in the PCM during this process.

The Biot number,  $\mathcal{B}i$ , defines the ratio of the heat transfer resistances inside of and at the surface of a body. This can determine whether or not the temperatures inside a body will vary significantly in space, from a thermal gradient applied to its surface, With this number, we can define if the heat transfer across the tube wall can be considered as unidimensional conduction, and it can be defined as:

$$\mathcal{B}i = \frac{L_c \cdot h_{air}}{k_{wall}} \quad (3.26)$$

where  $L_c$  is defined as  $\frac{V_{tube}}{A_{tube}}$ .

According to this concept of  $\mathcal{B}i$  number, we can adapt an adjusted Biot number  $\mathcal{B}i'$  as the ratio of the internal thermal resistance of the PCM to its external thermal resistance as [106]:

$$\mathcal{B}i' = \frac{R_{pcm}}{R_{air} + R_{wall}} \quad (3.27)$$



This value would allow us to determine whether the heat transfer is dominated by PCM resistance or external resistance (corresponding to the air and the wall).

Finally, if we want to account the presence of natural convection during phase change, we can use the Rayleigh number  $\mathcal{Ra}$ , which defines the ratio of buoyancy forced and thermal momentum diffusivity, and it is relates to the effects of natural convection in the liquid PCM. Rayleigh number is defined as:

$$\mathcal{Ra} = \frac{g \cdot \rho^2 \cdot c_p \cdot \beta \cdot [T_{ow} - T_{pcm}] \cdot L_c^3}{\mu_{pcm} \cdot k_{pcm}}. \quad (3.28)$$

### 3.5.3 Results from the phenomena identification by dimensionless numbers

Table 3.16, presents the ranges of the dimensionless numbers values in which the experiments of the present work were carried out. From  $\mathcal{Re}$  and  $\mathcal{Nu}$ , we can verify that the heat transfer between the air and the PCM containers is controlled by convection, in this case, forced convection since the air movement is promoted by a fan. Even though we achieve high values of  $\mathcal{Re}$ , they lie below the critical value for in-line tube bundles, proposed by Žukauskas [126] as  $\mathcal{Re} > 2 \times 10^5$ , the airflow did not achieve fully developed turbulent airflows and lies within a transition zone.

From the  $\mathcal{Bi}$  values obtained for the tube wall, we can assume unidirectional (radial) heat transfer, which results in accordance with the thermal circuit proposed for data treatment in section 3.4.2.

Regarding the PCM we can analyze  $\mathcal{Fo}$ ,  $\mathcal{Ste}$  and  $\mathcal{Ra}$  numbers. The higher  $\mathcal{Fo}$  values corresponded to the lower airflows values, because it depends directly on the time and then, the longer the cycle, the higher the  $\mathcal{Fo}$  values.

Regarding the  $\mathcal{Ste}$  number, the maximum values were found at the higher airflow rates. Finally the  $\mathcal{Ra}$  values found during these experiments surpassed the critical values suggested by Chung et al. [23] for melting in cylinders with natural convection. These results are in agreement with the temperatures profiles of section 3.3.1 and the photographs analysis in section 3.3.1, where we observed melting patterns corresponding to the presence of liquid currents within the tube, and therefore, an important role of natural convection during melting.

In brief, we can establish the phenomena that we should retain for further analysis and modeling:

- Forced convection between the air and the tube wall.
- Only radial conduction heat transfer through the tube wall.
- We must account the the buoyancy effects of the natural convection.

## 3.6 Concluding remarks

The experimental tests presented in this chapter have the dual purpose to serve as a basis, both for a proper understanding of the physical phenomena involved in air-PCM heat exchangers and for the experimental validation of further modelization of such systems. From them we can conclude the following remarks:

- According to the temperature measurements, the PCM temperature is not uniform within the PCM during melting, but mostly constant during solidification. This may indicate the

Table 3.16 – Dimensionless values ranges form experiments and phenomena identification.

Dimensionless Number	Range values	Critical Value	Remarks
$Re$	$3,7 \times 10^3 < Re < 1,3 \times 10^4$	$Re > 2 \times 10^5$	Sub-critical values for $Re$ Since $Nu \gg 1$ , convection controls the heat transfer between the air and the tubes. Since $Bi < 0,1$ , we can consider unidimensional heat transfer through the wall by conduction. $Fo$ value increases when the airflow decreases, since phase change cycles are longer for lower airflows. Melting occurs when $Ste < 0,1$ Natural convection in the liquid PCM
$Nu$	$42,7 < Nu < 96$	$Nu = 1$	
$Bi$	$0,043 < Bi_{wall} < 0,082$	$Bi_{wall} < 0,1$	
$Fo$	$0 < Fo_{cycle} < 4,34/69,39$	-	
$Ste$	$Ste_{max} = 0,0314$	$Ste \leq 0,1$	
$Ra$	$7,3 \times 10^{-1} < Ra < 4,5 \times 10^8$	$Ra > 3,6 \times 10^5$	

developing of different types of phenomena within the PCM media during melting.

- Even if we are working with slender tubes, from which a melting process controlled rather by 1-D radial conduction heat transfer is expected, we find 2-D melting patterns, with a downward predominant melting direction, a product of liquid PCM streams and the erosions that these cause in the remaining solid PCM.
- The heterogeneity of the airflow affects the melting process within a tube and the heat exchanger. This could be caused by the position of the tubes, the different material for the walls of the heat exchanger and the non-centric position of the fan at the inlet. The effect of this is reflected on the non-uniform development of the heat transfer regarding the tubes, where we observed a faster development of melting in a tube located on the fifth row in comparison with the development in the first tube.
- The determination of the beginning of phase change for non-pure materials is a difficult task and a source of incertitudes. When comparing our temperature results with the images analysis, we can detect that the PCM reaches the melting temperature even when melting is not visible yet. This could be associated with a low melting rate at the beginning or a porous media behavior within the PCM.
- Only rely on temperature measurements involve interpretation of results, which in some cases could lead to a misinterpretation of the phenomena. The use of images to complete the results allows to verify the presence or not of these phenomena.
- Using the photographs obtained as a data source, through an image processing, beyond that as a support to the observation of phenomena, allows us to quantify the melting process through the determination of the liquid fraction; a parameter that allows us to determine the thermal performance.
- The approach of separating the experimental study of the air-PCM system in local and global domains is favorable because it allows us to quantify the effect that local phenomena have on the overall performance of the system. We often find studies in the literature focused only on the behavior of the PCM container alone, or on the performance of the system, but it is not common to study both parts separately.

# 4

## Modeling of a tube bundle type air-PCM unit

### 4.1 Scope

Following the experimental results, we aim now to present how can we recreate and predict the behavior observed experimentally in air-PCM heat exchangers. For this, we propose the use of empirical and numerical models, that focus on both, local and global domains. In the first part of this chapter, we present the development of an empirical model that aims to account for the local physical phenomena within a tube with PCM through the use of well known dimensionless numbers. In the second part, we present a simple numerical model that aims to recreate the behavior of an air-PCM heat exchanger and moreover, predicts its thermal performance, through some selected indicators. This model is finally validated using the experimental results shown earlier.

## 4.2 Experimental Correlations

We can obtain empirical models that associate a certain physical phenomena involved, without taking into account all the complexity associated with them. This results convenient in this particular case, where we need to associate the natural convection with other phenomena occurring during phase change. Accounting these kinetic effects of natural convection in the PCM through the modeling of the physical phenomena, involving mass transport and energy transfer, would result in expensive computation times, especially if a complete exchanger is considered. Therefore, in this section we explore the melting fraction modeling through dimensionless numbers:  $Ste$ ,  $Ra$ , and  $Fo$ , that represents the main phenomena occurring during phase change controlled by conduction and convection heat transfer mechanisms.

### 4.2.1 Previous analysis before obtaining the correlations

We propose two expressions to describe the melting fraction during the melting cycle as follows:

$$m_f = C \cdot [SteFo]^n \cdot Ra^m \quad (4.1)$$

and,

$$m_f = C \cdot Fo^x \cdot Ste^y \cdot Ra^z \quad (4.2)$$

which are in agreement with other analytical and experimental expressions previously found in the literature.

Now we use the results obtained for the melting fraction using energy balances as base for obtaining these correlations. For this, we chose the results for experimental tests carried out in the following range:  $6 \times 10^3 < Re < 1,15 \times 10^4$ , which are shown in the following figure 4.1:

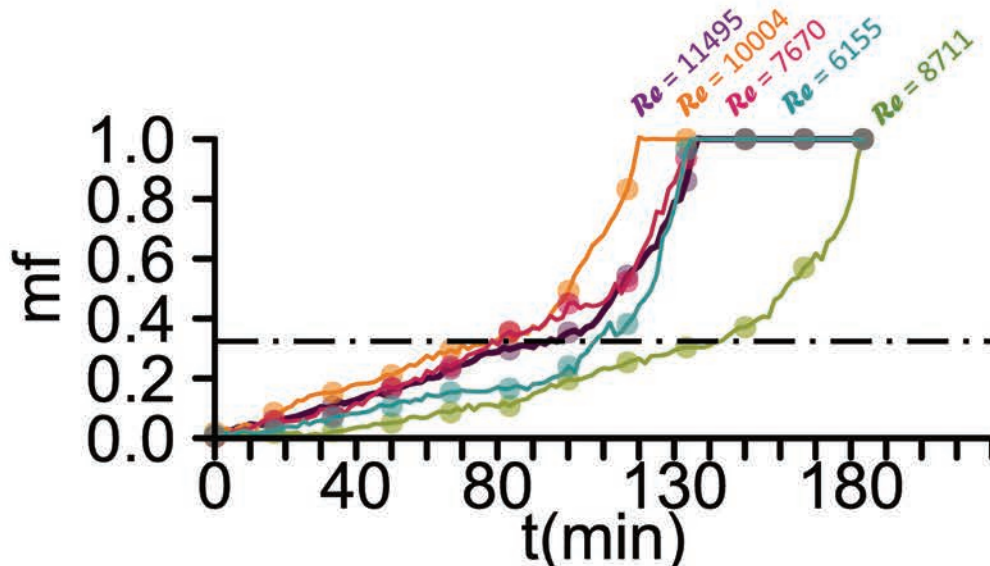


Figure 4.1 – Melting fraction profile evolution for different  $Re$  values. The dashed line highlights a sudden change in the behavior of the melting fraction.

From this figure we can observe the melting fraction profiles for the aforementioned  $Re$  range of values. The first thing that we notice is the two different regions of the melting fraction:

- During the first part of the cycle, a linear growth of the melting fraction is observed with

moderate slope. This section represents a maximum of the melting fraction in between  $m_f = 0,2$  and  $m_f = 0,4$ , for the tests analyzed (with the exception or a Reynolds of 8711, in which we observe a different behavior. This behavior can be due some problems in the experimentation).

- A sudden and non-linear rise of the melting fraction in the second part of the cycle.

Then, we can infer two different phenomena governing those two regions, *a priori*, conduction for the first region and convection for the second. We would now, then, try to fit these behavior in the form of the correlations presented in eqs. 4.1 and 4.2.

#### 4.2.2 Statistical tests to validate the multiple linear regression

These empirical correlations are obtained from experimental data. To test if the explanatory variables (independent variables) explain the dependent variable, in this case, the melting fraction  $m_f$ , we perform the statistical test to prove the validity of the regression as a function of the explanatory variables (independent variables). To help us do that, we performed a correlation chart between these variables to analyze the behavior between them. This chart allow us to perform the following statistical tests:

- **A null hypothesis test:** through the use of the  $p$ -value, we ensure that the chosen dimensionless parameters explain the phenomenon implying the melting of the MCP.
- **A linearity test:** Scatter dispersion plots between each explanatory variable and the dependent variable, to test the linearity between them.
- **A multicollinearity test:** A final test is to verify that there is no multicollinearity between the explanatory variables, using the Pearson or Spearman coefficients.

These statistical tests can be performed by using a correlation chart. For this work, we use the function `char.Correlation` of the R® software. The results are depicted in figure 4.2. This figure allows observing the results for different statistical tests at the same time such as the correlation coefficients, the scatter plots, between each of these explanatory variables and the melting fraction, and the  $p$ -value. The result from this correlation chart is as follows:

- **$p$ -value:** The values represented by the asterisks corresponding to the results of the statistical test of the  $p$ -value, where:
  - three asterisks (\*\*\*) indicate that the  $p$ -value is very close to zero,
  - two asterisks (\*\*) that are very close to 0.001,
  - one asterisk (\*) that is very close to 0.01,
  - a point (.) indicates that the  $p$ -value is very close to 0.1, and
  - nothing () indicates that is very close to 1.

For our results, a value of “ \*\*\* ” indicates a  $p$ -value zero ( $p = 0$ ), which means a rejection of the null hypothesis. Since the null hypothesis establishes that there is no direct relation between the explanatory variable and the dependent variable, a rejection of this hypothesis indicates that these variables  $\mathcal{F}o$ ,  $\mathcal{S}te$  and  $\mathcal{R}a$  are statistically relevant in the description of the melting fraction  $m_f$ .

- **A linearity test:** This figure also presents a scatter plot between all the variables, explanatory and dependent variable include, which can be observed in the lower quadrants. We can observe two linear patterns if we separate the behavior between these variables in two regions.



- **Correlation coefficients:** These correlation coefficients are desired to be lower when testing multiple variables to explain a dependent variable, as in this case. This is not the case here because the numbers of  $Ste$  and  $Ra$  are obtained from the same temperature difference measurements  $T_{ow} - T_{pcm}$ , and so, there is a strong correlation between them from a statistical point of view. Despite this, we have chosen to look for the correlation between  $m_f$  and the dimensionless numbers presented in equations 3.24, 4.30 and 4.31. Indeed, even if there is no strong statistical independence between these variables, there is, in fact, physical independence: these dimensionless parameters describe different phenomena taking place within the air-MCP exchanger, during the phase change.

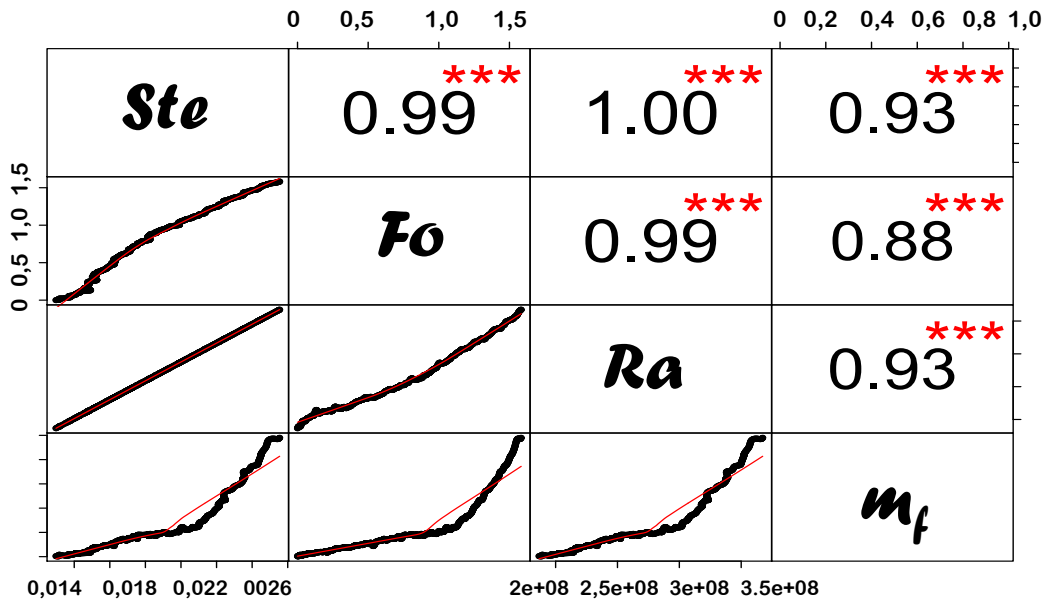


Figure 4.2 – Correlation chart between the explanatory variables  $Ste$ ,  $Ra$ , and  $Fo$ , and the melting fraction  $m_f$  resulting from the statistical tests performed prior to obtaining the correlations.

### 4.2.3 Results from the correlations for the melting fraction

To evaluate the performance of the obtained correlations we chose the following indicators:

1. Agreement between the experimental operating time  $\Delta t_{op}$  of the melting fraction with the one obtained by the correlation.
2. The RMSE between the correlation and the experimental value of the melting fraction.
3. The relative error between the correlation and the experimental value of the melting fraction.

From the previous analysis of the melting fraction we observed two different regions, therefore we would try to separate the correlation in these two regions defining a breakpoint value for the melting fraction.

#### (a) Melting fraction correlation by regions

For these types of correlations we use a manipulation methodology to find the correlation coefficients. This manipulation is made using an interactive plotting associated to the function `manipulate` of R, that also includes the results of the relative error and the RMSE.

We explore to find a single correlation and two correlations, one for each region. When we were manipulating the coefficients for both regions we realized that a better agreement between the correlation and the experiments in the second region, which is allegedly controlled by natural convection, are obtained when the melting fraction is described as a function of the separates values of  $Fo$  and  $Ste$ , and  $Ra$ .

For the first region, which is allegedly controlled by conduction we found that the better fitting of the melting fraction is as function of the combined  $FoSte$ . These results shows in agreement with previous correlations developed which established that phase change during melting only controlled by conduction can be fully explained as a function of  $FoSte$  [33].

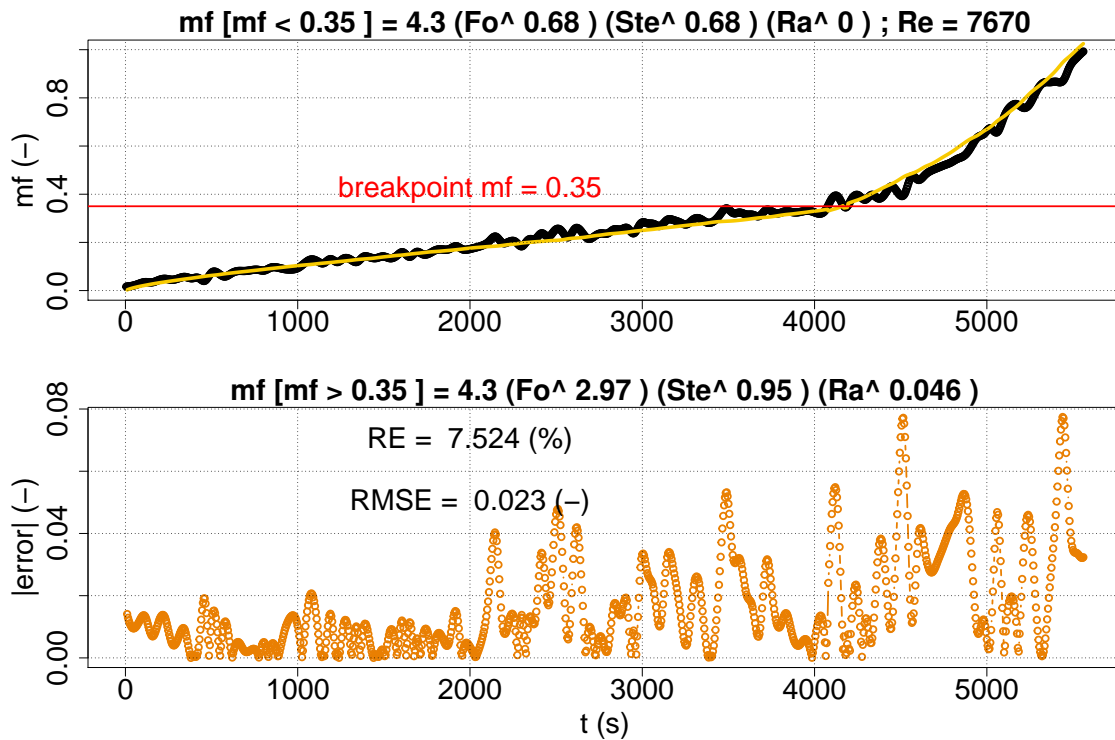


Figure 4.3 – Melting fraction correlation  $4,3 \cdot [FoSte]^{0,68}$  for the first region (conduction) and  $4,3 \cdot Fo^{2,97} \cdot Ste^{0,95} \cdot Ra^{0,046}$  for the second region (conduction and convection); for a  $Re = 7670$ .

Figure B.5 shows the result for a  $Re$  of 7670. We observe that now that we have split the correlations in two regions, we have a good performance of all the indicators proposed. We test these correlation for the experiments carried within this range and obtained the following results:

Table 4.1 – Melting fraction correlation  $C \cdot [FoSte]^{0,68}$  for the first region (conduction).

$Re$	$m_f$ breakpoint	$C$	RMSE
11496	0,36	0,89	0,025
10004	0,30	3,21	0,020
8711	0	0,46	0,037
7670	0,35	4,30	0,023
6155	0,24	2,24	0,019

Table 4.2 – Melting fraction correlation  $\mathcal{C} \cdot \mathcal{F}o^{2,97} \cdot Ste^{0,95} \cdot \mathcal{R}a^{0,046}$  for the second region (conduction).

$Re$	$m_f$ breakpoint	$\mathcal{C}$	RMSE
11496	0,36	3,04	0,025
10004	0,30	3,21	0,020
8711	0	0,46	0,037
7670	0,35	4,30	0,023
6155	0,24	2,24	0,019

In summary:

After the correlation tests we found that for a range between  $6 \times 10^3 < Re < 1,15 \times 10^4$ , the melting fraction of a container within a tube bundle air-PCM heat exchanger for 11 rows, can be expressed as:

$$m_f = \mathcal{C} \cdot [Ste\mathcal{F}o]^{0,68} \quad (4.3)$$

for melting controlled by a conductive heat transfer mechanism, and by:

$$m_f = \mathcal{C} \cdot \mathcal{F}o^{2,97} \cdot Ste^{0,95} \cdot \mathcal{R}a^{0,046} \quad (4.4)$$

for melting controlled by a convective heat transfer mechanism.

We performed this empirical methodology for obtaining the melting fraction correlations for different inlet airflow values, and we obtained the values presented in table 4.1 for the first region and in table 4.2 for the second region.

We can compare the values obtained with those presented in the literature. The expression obtained for the conductive region of the melting fraction is in agreement with the empirical correlations obtained by Ho and Viskanta [53], for *n*-octadecane within a vertical rectangular cavity, which follow similar melting patterns than tubes. Their result shows that  $V/V_0$  is proportional to  $\mathcal{F}o^{0,68} \cdot Ste^{0,68}$  which is very close to the results of the present study. A more recent study developed by Motahar et al. for rectangular containers [39], obtained the values of  $V/V_0$  proportional to  $\mathcal{F}o^{0,66} \cdot Ste^{0,76}$ . The difference lies that their prediction accounts the inclusion of dispersed titanium oxide ( $TiO_2$ ) nanoparticles into an *n*-octadecane used to enhance the thermal conductivity of the amterial.

Some remarks and interpretations can be made about these results. The first thing that we observed is that the overall behavior of the melting for the airflow values tested follows the same exponents for  $\mathcal{F}o$ ,  $Ste$  and  $\mathcal{R}a$ , which may imply similar effects of such numbers on the temporal evolution of the melting fraction. This could be understandable since the geometry and the position of the tube do not change during these tests. This can give us a hint that the constant value  $\mathcal{C}$  is related to the airflow interactions with the container.

Regarding this value, one can expect that the  $\mathcal{C}$  value would have a link with the Reynolds, which a priori expresses the nature of such airflow, but we found otherwise in our experiments. In these tables, we can observe that the values do not follow an evident pattern regarding the  $Re$  value at the inlet of the heat exchanger. One explanation for this observation could be linked to the heterogeneity that we have already detected in the experimental chapter. During these experiments, we measured the airflow values at the inlet of the heat exchanger, but for the tube, the airflow properties are calculated from these values and not directly measured, therefore, this heterogeneity could be linked to the differences noticed in the value of  $\mathcal{C}$ .

## 4.3 Thermal resistance model

### 4.3.1 Problem statement for the model

We seek to recreate the behavior of an air-PCM heat exchanger consisting of an in-line or a staggered arrangement of vertical tubes, that stores energy in the form of latent heat via phase change. The model obtained in here aims to be adaptable to integration in design tools (both heat exchangers and buildings). Then, we want to develop a model that considers:

- a) The physical phenomena controlling heat transfer and energy storage at each of the domains of the heat exchanger, as much as possible,
- b) the prediction of the selected performance indicators of the heat exchanger:
  - $P_{cool}$
  - $\Delta t_{op}$
- c) the coupling between the local and the global domain,
- d) the adaptability and variations of inputs parameters.

### 4.3.2 Resolution methodology

Throughout this work, we have described an air-PCM heat exchanger from the coupling of two domains, the global and the local domains. We could only focus on modeling the heat exchanger globally, as depicted in figure 4.4, since the performance indicators are directly related to this domain. This approach is generally used when designing and evaluating heat exchangers (for instance by  $\epsilon - NTU$  and  $LMTD$  methods). Nevertheless, if we use this approach, we would need to draw upon a *gray box approach*, because only general data of what happens inside the heat exchanger would be known, such as the properties of the PCM, number of tubes, and geometric distribution; without knowing in detail the contribution of each of these tubes to the response obtained to at the outlet of the heat exchanger.

On the contrary modeling the local domain, which is illustrated in the figure 4.5, would include as many measurable phenomena as possible. Consequently, the physical phenomena that intervene in each tube could be quantified. Therefore, by coupling these two domains, we could predict the performance of the heat exchanger by assessing the contribution of each tube to the performance of the unit.



Figure 4.4 – Global domain proposed for the modeling of an air-PCM heat exchanger. The inlet is given by the indoor conditions of the room and the outlet conditions are the air-cooling contribution of the exchanger to the room.

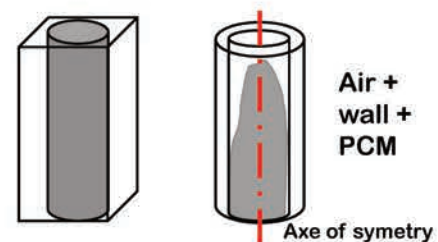


Figure 4.5 – Local discretization of an air-PCM heat exchanger. In here three media interact: the air surrounding the tube, the wall of this tube and the PCM.

To relate the behavior of the global domain, with the physical phenomena of the local

domain, a discretization of the heat exchanger by rows is proposed as presented in figure 4.6.

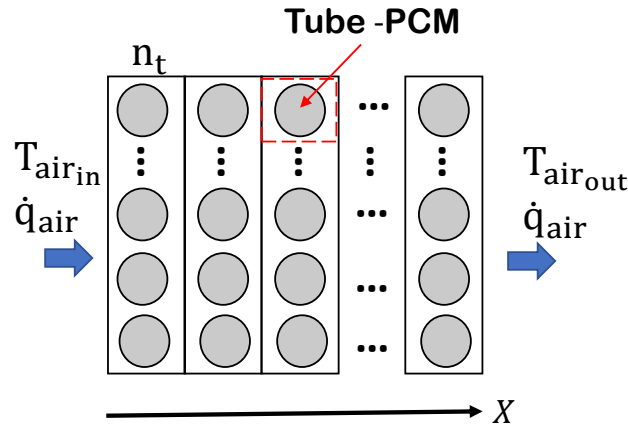


Figure 4.6 – Discretization of the global domain by a row of tubes.

The physical domain of the model can be reduced in three physical sub-domains that can explain the global-local interactions:

1. The air sub-domain, (global domain).
2. The wall sub-domain (local domain).
3. The PCM sub-domain (local domain).

Such sub-domains are, therefore, the control volumes of the model.

To account for the physical phenomena, we propose to perform energy balances in each control volume. The heat exchanges between the air and the tube (wall and PCM) are accounted by the means of the Newton's law of cooling. Before going further into the mathematical formulation of these control volumes, we need first to define the limits of our models by enlisting the assumptions considered by the model. We summarize such assumptions in the following section.

### 4.3.3 Assumptions

The assumptions made for the modeling of the air-PCM heat exchanger are summarized in the following lines:

- **Regarding the air:**
  1. The viscosity, pressure effects and external forces are neglected during the energy balance.
  2. The air is considered as an incompressible flow and with a constant heat capacity.
  3. Heat transfer only occurs in the direction of the airflow ( $X$ -axis, see figure 4.6).
- **Regarding the wall:**
  1. The energy storage in the container is neglected and conduction is considered to be uniform through the wall ( $Bi_{wall} < 1$ ).
  2. The external temperature of the wall  $T_{ow}$  is approximated to the mean temperature of the wall  $T_{wall}$  as follows:

$$T_{ow}(X, t) = T_{wall}(X, t). \quad (4.5)$$



- **Regarding the PCM:**

1. The thermophysical properties of the PCM remain constants and independent of the temperature for simplicity, except for the thermal conductivity  $k_{pcm}$ .
2. To avoid movement of the PCM, the density  $\rho_{pcm}$  is assumed to be constant.
3. Only latent heat occurs during phase change (since  $Ste \approx 0$ ), and the value of the specific latent heat is constant during the cycle and the energy storage in the container is neglected.
4. The average temperature of PCM domain can be approached by:
  - *Isothermal phase change:* In this case the temperature of the PCM during phase change is assumed constant during phase change where  $T_{pcm} = T_m$ , with  $T_m$  the melting temperature of the PCM. This supposition usually fits with PCM that present a small range of phase change temperatures.

- **Other assumptions:**

1. Losses through the wall of the heat exchanger are initially neglected.
2. Heat transfer between the tubes of the same row is neglected.

#### 4.3.4 Mathematical formulation

The definition of the energy balances proposes the mathematical formulation of each control volume following the first law of thermodynamics. This energy balance provides the solution for the temperature distribution at each domain. It follows the conventional approach to forced heat convection in ducts and in tube banks, which assumes as valid the supposition of a "pseudo steady-state" analysis. The energy balance at each domain can be written from its general form given by [17]:

$$\left\{ \begin{array}{l} \text{Rate of energy} \\ \text{accumulation} \\ \text{in the CV} \end{array} \right\}_1 = \left\{ \begin{array}{l} \text{net heat} \\ \text{transfer} \\ \text{by conduction} \end{array} \right\}_2 + \left\{ \begin{array}{l} \text{rate of} \\ \text{internal heat} \\ \text{generation} \end{array} \right\}_3 - \left\{ \begin{array}{l} \text{net work transfer} \\ \text{from the CV to} \\ \text{its environments} \end{array} \right\}_4 \quad (4.6)$$

where the third term, *the rate of internal generation* is considered in here, as the energy stored or released during phase change.

##### Air sub-domain:

The air control volume is delimited between the air surrounding a row of tubes. The energy balance within a row can be defined as:

$$\rho_{air} \cdot c_{p_{air}} \cdot A_{air} \cdot \frac{\partial T_{air}(X, t)}{\partial t} dX + \rho_{air} \cdot c_{p_{air}} \cdot v_{air} \cdot A_{air} \cdot \frac{\partial T_{air}(X, t)}{\partial X} dX = n_t \cdot h_{air} \cdot A_{ow} \cdot [T_{air}(X, t) - T_{wall}(X, t)] \quad (4.7)$$

where  $A_{air}$  is the cross-sectional surface area of the row and  $n_t$  is the number of tubes within a row.

##### Wall sub-domain:

Since we neglected the energy storage within the wall, the heat transferred to the tube (by conduction through the wall) can be expressed as:

$$h_{air} \cdot A_{ow} \cdot [T_{air}(X, t) - T_{wall}(X, t)] = \frac{T_{air}(X, t) - T_{pcm}(X, t)}{R_{air} + R_{wall} + R_{pcm}(X, t)} \quad (4.8)$$

where the heat transferred to the tube is defined as a thermal circuit of series resistances between the air and the core of the PCM.

#### PCM sub-domain:

We can write the energy balance at the PCM as:

$$L \cdot \rho \cdot \frac{dV_{pcm}(X, t)}{dt} = \frac{T_{air}(X, t) - T_{pcm}(X, t)}{R_{air} + R_{wall} + R_{pcm}(X, t)} \quad (4.9)$$

where the term on the left expresses phase change as the amount of volume of the PCM that has changed from one phase to the other.

Now, if we assume a 1-D phase change radial pattern controlled by conduction, we can rewrite 4.9 as:

$$\pi \cdot L \cdot \rho_{pcm} \cdot l_{pcm} \cdot \frac{\partial r(X, t)}{\partial t} = \frac{T_{air}(X, t) - T_{pcm}(X, t)}{R_{air} + R_{wall} + R_{pcm}(X, t)} \quad (4.10)$$

with:

$$R_{air} = \frac{1}{h_{air} \cdot A_{ow}} \quad (4.11)$$

$$R_{wall} = \frac{\ln \left| \frac{r_{ow}}{r_{iw}} \right|}{2 \cdot \pi \cdot k_{wall} \cdot l_{pcm}} \quad (4.12)$$

and,  $R_{pcm}$  for a 1-D radial approach, defined as:

$$R_{pcm} = \frac{\ln \left| \frac{r_{iw}}{r(X, t)} \right|}{2 \cdot \pi \cdot k_{pcm} \cdot l_{pcm}}. \quad (4.13)$$

Furthermore, the heat flow entering or leaving the tube can be defined as:

$$q_{pcm} = \frac{T_{air}(X, t) - T_{pcm}(X, t)}{R_{air} + R_{wall} + R_{pcm}(X, t)} \quad (4.14)$$

and the energy stored or released over time in the PCM, as follows:

$$Q_{pcm}(t) = \int_{t=0}^{t=t_{final}} q_{pcm}(t) \cdot dt \quad (4.15)$$

where  $t = 0$  refers to the beginning of phase change and  $t_{final}$  to the end of phase change.

#### 4.3.5 Initial and boundary conditions

- *Initial conditions*

$$T_{air}(X, 0) = T_{ini} \quad (4.16)$$

$$T_{wall}(X, 0) = T_{ini} \quad (4.17)$$

$$T_{pcm}(X, 0) = T_{ini} \quad (4.18)$$

$$r(X, 0) = r_{iw} \quad (4.19)$$

where  $r_{iw}$  is the internal face of the tube.

- **Boundary conditions**

The associated boundaries conditions are:

$$\frac{\partial T_{pcm}(r=0, t)}{\partial r} = 0 \quad (4.20)$$

$$k_{wall} \cdot \frac{\partial T_{wall}(r=r_{ow}, t)}{\partial r} = h_{air} \cdot [T_{air} - T_{wall}] \quad (4.21)$$

where  $r_{ow}$  is the external face of the tube wall.

### 4.3.6 Numerical Resolution

To solve this model, a mean temperature is considered at each domain. Therefore, besides the spatial discretization of the heat exchanger by rows ( $X$ ), there is no further spatial discretization in this model. At each of these domains, the air temperature  $T_{air}$  and the initial value of the radii  $r(X, t=0)$  are known. Regarding the temperature of the PCM,  $T_{pcm}$  can be known a priori, depending on the approach selected for this temperature (isothermal or non-isothermal). Then, by applying an explicit scheme, the final form of the model can be written as follows:

#### Air sub-domain

$$\dot{V}_{air} \cdot c_{p_{air}} \cdot \left[ T_{air}(X, t) - T_{air}(X+1, t) \right] = n_t \cdot h_{air} \cdot A_{ow} \cdot \left[ T_{air}(X, t) - T_{wall}(X, t) \right] \quad (4.22)$$

#### Wall sub-domain

$$h_{air} \cdot A_{ow} \cdot \left[ T_{air}(X, t) - T_{wall}(X, t) \right] = \frac{T_{air}(X, t) - T_{pcm}(X, t)}{\frac{1}{h_{air} \cdot A_{ow}} + \frac{\ln \left| \frac{r_{ow}}{r_{iw}} \right|}{2 \cdot \pi \cdot k_{wall} \cdot l_{pcm}} + \frac{\ln \left| \frac{r_{iw}}{r(X, t)} \right|}{2 \cdot \pi \cdot k_{pcm} \cdot l_{pcm}}} \quad (4.23)$$

#### PCM sub-domain

$$r(X, t+1) = r(X, t) - \left[ \frac{T_{air}(X, t) - T_{pcm}(X, t)}{\frac{1}{h_{air} \cdot A_{ow}} + \frac{\ln \left| \frac{r_{ow}}{r_{iw}} \right|}{2 \cdot \pi \cdot k_{wall} \cdot l_{pcm}} + \frac{\ln \left| \frac{r_{iw}}{r(X, t)} \right|}{2 \cdot \pi \cdot k_{pcm} \cdot l_{pcm}}} \cdot \Delta t \right]^{1/2} \quad (4.24)$$

where the parameters in magenta, represent the unknowns of the model.

The discretization by control volumes of the energy conservation equations at each volume leads to a set of differential algebraic equations. These equations can be easily solved using Matlab®. After discretization of these equations, we can obtain the melting front position, that means the boundary between the liquid and solid phase, assumed in here as only dependent of the radii.

To formulate the start of the phase change within the code, we approached the heat transfer into two heat flows:

- A parallel heat flow within a row, which assumes that all the tube change of phase at the same time.
- A sequential heat flow, in which the same volume of air comes in contact with each row sequentially; therefore, heat flow can be modeled as a series of thermal resistances.

These approaches are useful to determine how we start phase change. For the code, we

propose to start the change of phase sequentially at each row as follows:

- At  $t = 0$ , only the first tube begins with phase change. The remaining tubes stay in the initial conditions.
- At  $t = t + \Delta t$ , the first row of tubes stays in phase change (if is the case) and second row of tubes starts phase change, while the rest of rows remain in the initial conditions.

The same process of adding rows at each time step is followed until it reaches the last row. Then, at this moment, all the heat exchange is within the phase change period.

Also, include tests during different seasons of the year to observe other operations of this kind of systems. Besides, the starting setpoint of the tests could be changed to a lower temperature in order to observe the operation of the unit for a longer time.

Furthermore, we aimed for this model be developed in such a way that the user can select:

- Geometrical parameters and arrangement of the container.
- Inlet airflow rate and air temperature.
- PCM type and properties.
- Number of rows of tubes within a row.

Unknowns variables of the model for each domain:

1. **Air domain:**  $T_{air}$
2. **Wall domain:**  $T_{wall}$
3. **PCM domain:**  $r(X, t)$

Finally, we propose the algorithm of resolution of the present model as presented in figure 4.7 and the modeling domains in figure 4.8. In the latter figure, we can observe the reduction of the physical phenomena into the modeling domains: air, wall and PCM, the governing equations in each of these domains, and the inputs and outputs proposed for the model.

Figure 4.8 shows the domains of the present model:

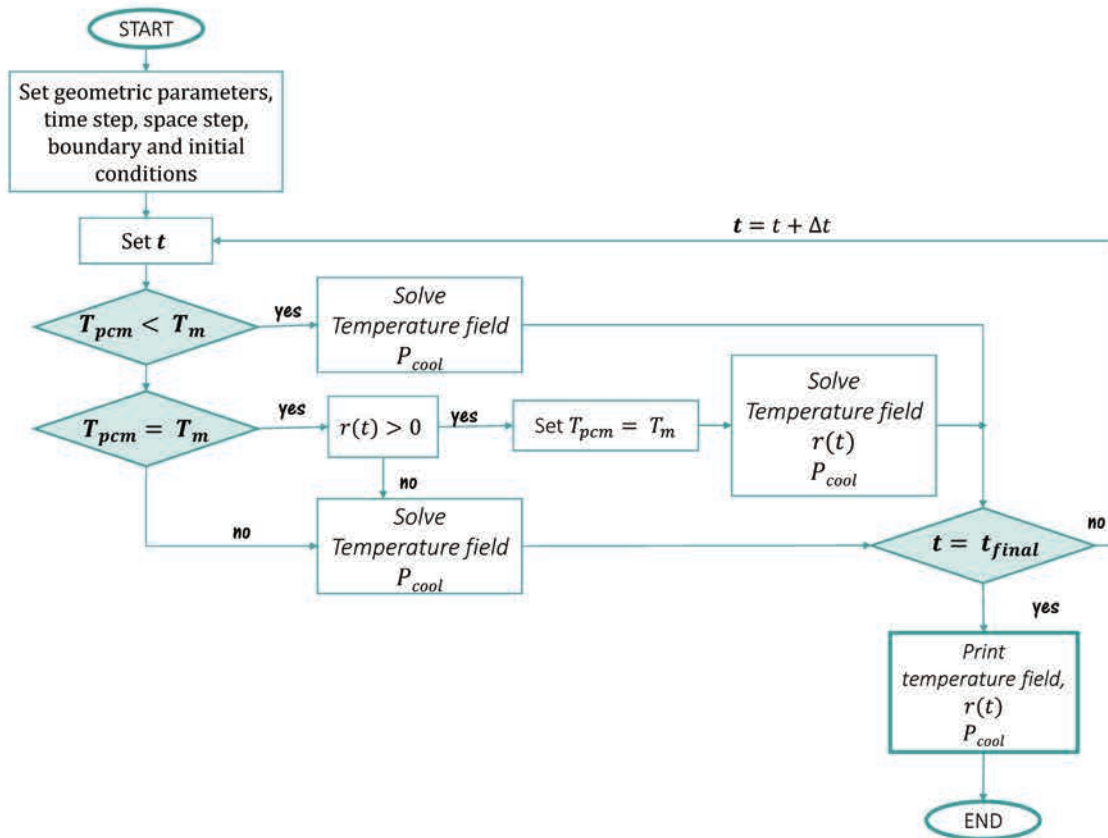


Figure 4.7 – Algorithm of the 1-D model.

#### 4.3.7 Validation of the model

To observe if there was a significant variation in the response of the model regarding the time step, we simulate the same condition for seven different time steps  $\Delta t$  between 0,01 s and 100 s. We did not observe a significant difference during most part of the cycle. Nevertheless, at the end of the cycle, we can detect some variations for the smaller time steps (0,01 s and 0,1 s) and the longest time step (100 s). The response for the smaller time steps are smoother, which is no surprise considered that in those cases, there is a finer discretization, therefore, the approximations can be more accurate. Although the computation time for those cases are much more considerable than for other cases.

To prove the validity of this model, we compare the results of the model with those obtained from the experiments: the temperature measurements and the image processing results. The experiments used for the validation of this model were carried out under the following conditions:  $\dot{V}_{air} = 193 \text{ m}^3 \cdot \text{h}^{-1}$  and a  $T_{air_{in}} = 33 \text{ }^\circ\text{C}$ . The temperature data collection was one sample each 20s giving a total of 739 temperature measurements. For the image processing, we selected 20 images of the first tube, and we selected 17 images of the eighth tube. Both, the temperature measurements and the image processing were compared to the model only during the phase change process (excluding the periods of only sensible heat storage).

As outputs of the model, we compute the temperature field of the heat exchanger at the local and global domains, we can also obtain the melting front position  $r(t)$ , and the operation time  $\Delta t_{op}$ . The further processing of the data obtained by this model, allow us to also obtain the cooling power of the heat exchanger  $P_{cool}$  and the melting fraction  $m_f$  of the PCM inside of a tube.



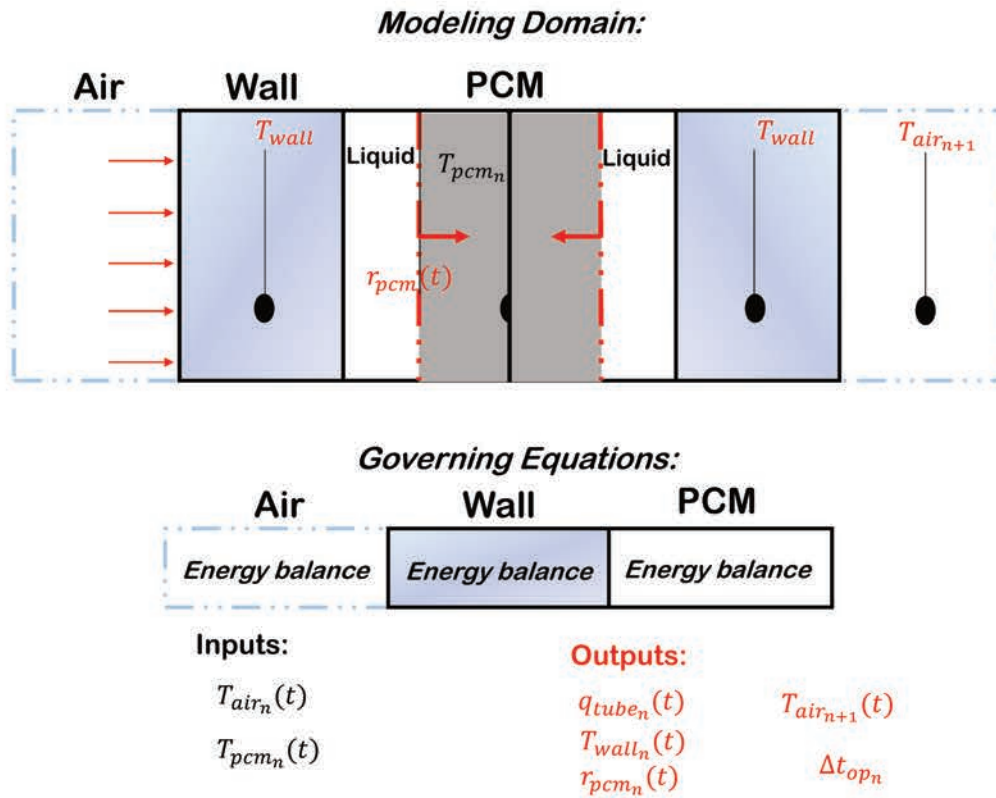


Figure 4.8 – Reduction of the physical domains into the modeling domains.

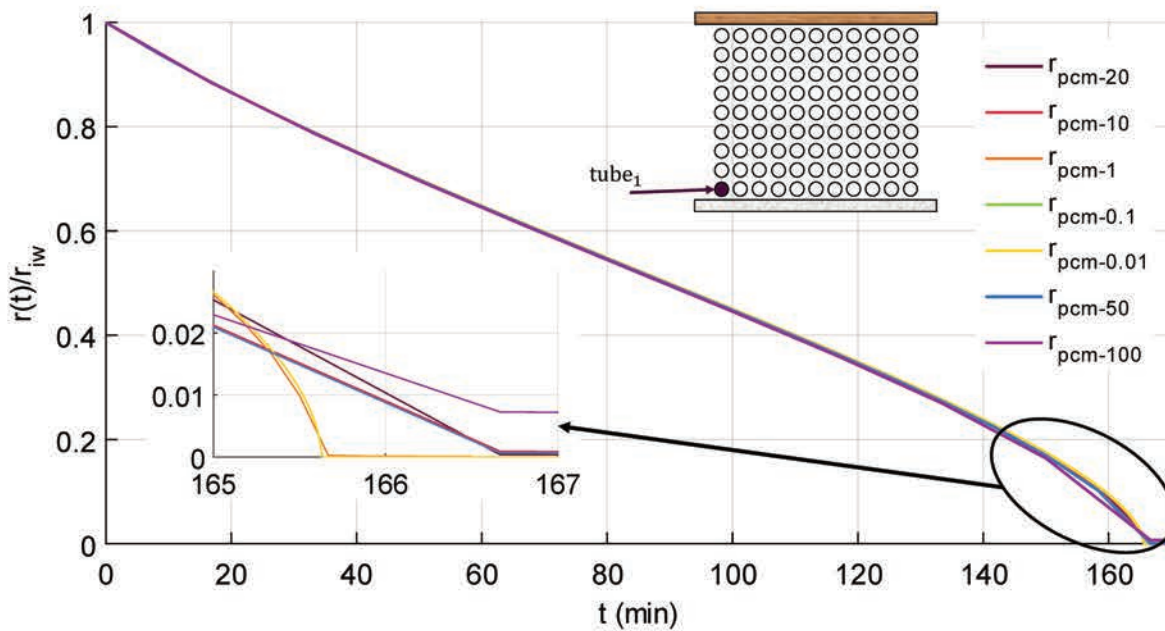


Figure 4.9 – Ratio of the melting front position to the internal radii of the tube  $r(t)/r_{iw}$  regarding the time step selection, where the number represents the time in seconds. Larger differences are observed at the end of the cycle.

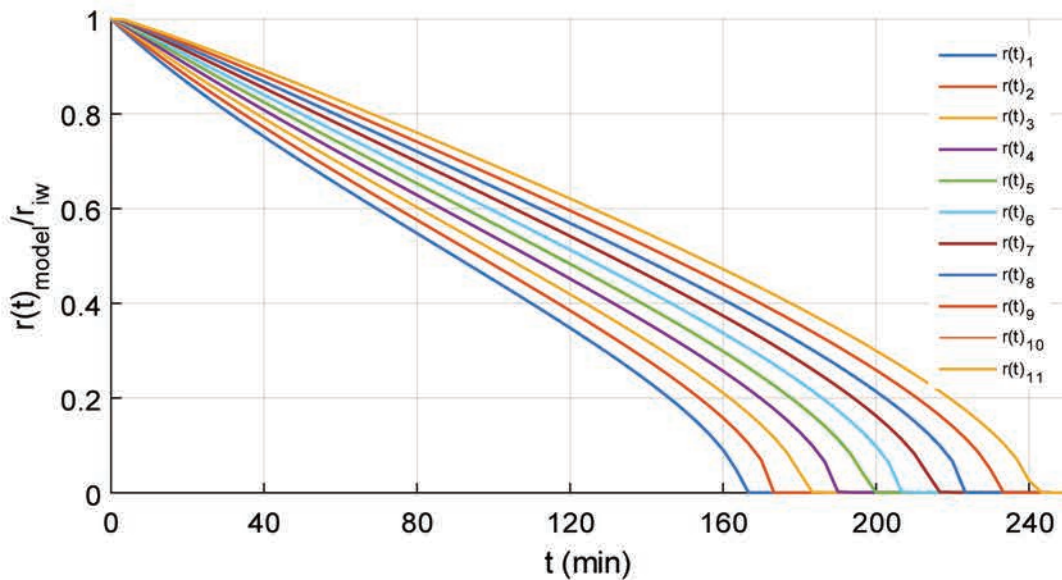


Figure 4.10 – Ratio of the melting front position to the internal radii of the tube  $r(t)/r_{iw}$  regarding the tube position, where each line represents a row of the heat exchanger.

As validation parameters and criteria, we choose those performance indicators defined at the beginning of the modeling, during the problem statement:  $P_{cool}$  and  $\Delta t_{op}$ . From the local domain, we obtain the operation time  $\Delta t_{op}$  by comparing to the image processing, and from the global domain, we obtain the cooling power  $P_{cool}$ , by further processing of the inlet  $T_{in}$  and outlet temperatures  $T_{out}$ .

#### Validations from the First tube

The first tube of the heat exchanger is submitted to the inlet conditions; therefore, the air temperature of this tube is the inlet temperature  $T_{in}$ . To validate the model results with this tube, we choose to compare the melting front position of the model given by  $r(t)$  to an equivalent of this melting front obtained from the image processing. To achieve this, we need to express the melting fraction of the experiments in the form of a 1-D melting front, assuming radial heat transfer. This experimental  $r_{exp}(t)$  does not represent the physical melting front (which from the image analysis we observed that is rather 2-D), but a 1-D equivalent of this 2-D experimental melting front. We use eq. 3.19 to obtain the equivalent value and then, be able to compare them.

The results of the validation of the first tube are shown in figure 4.11. In here we aim to validate the behavior  $r(t)$  and the operation time  $\Delta t_{op}$ , which in this case represent the total time of the melting cycle. The experimental operation time  $\Delta t_{op_{images}} = 164$  min (9840 s), while the model operation time  $\Delta t_{op_{model}} = 167$  min (10 000 s). This difference represents a relative error of about 1,62%. Now, if we compare the melting front position of the model, we can observe that the behavior obtained by the model does not quite fit the resulting melting front position obtained from image processing.

This behavior is not entirely a surprise since this model only takes into account radial conduction as heat transfer mechanism. Besides, we have already observed that the melting patterns obtained by these tubes are not radial at the beginning; instead, during the first part of the phase change, melting occurs rather downwards in the vertical direction of the tube, which is not observed until past several minutes of the cycle.

Even though we proposed to express the melting fraction obtained by image processing into

a 1-D equivalent, this may not be enough to describe the melting front. Furthermore, we also observed a constrained melting in this tube, due to the presence of a thermocouple, which resulted in a delay of the phase change, if we compared to the neighbor tubes. For now, we retain the value of operation time,  $\Delta t_{op}$ , which was the target of this analysis.

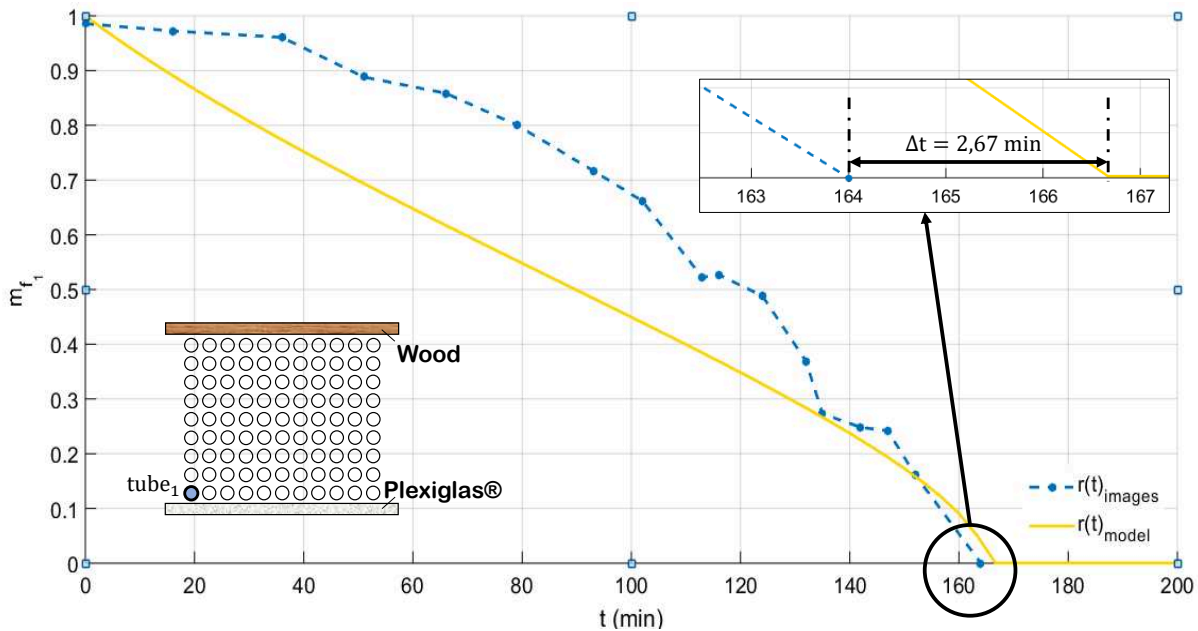


Figure 4.11 – Ratio of the melting front position to the internal radii of the tube  $r(t)/r_{iw}$  for a tube located in the first row: by the image processing (blue) and the model (yellow).

### Results from the eighth tube

The analysis of the eighth tube allows us further comparisons between the experiments and the model since on this tube, a greater amount of temperature measurements were made coupled with image processing. In this section, we present the results of the ratio of the melting front position to the internal radii of the tube  $r(t)/r_{iw}$  and the melting fraction  $m_f$  for this tube. These results are illustrated from figures 4.12 to figure 4.15.

Similar to the analysis made on figure 4.11, in figure 4.12 we present the comparison between the experimental results and the model. In here, it is shown the ratio of the melting front position to the internal radii of the tube  $r(t)/r_{iw}$  from the image processing (magenta), from experimental measurements (purple) and model (yellow). We can now observe that difference in the prediction of the operation time  $\Delta t_{op}$  increased (9,3 min), representing a 4,7% of the difference between the image processing (considered the real time) and the model.

A difference from this tube analysis with the one made for the first tube is that, since we have a fully instrumented tube, we can further obtain, from the experimental temperatures, the equivalent 1-D melting front position. These results are shown in figures 4.12 and 4.13. In the first figure, we can observe that during most of the cycle, the behavior obtained from the experiments and the model approach each other. However, when melting approaches its end, these values differ from each other, increasing the error of the model enormously. This can be observed in figure 4.13, where during most of the time the error of the model does not surpass 4%, but at the end of the cycle, this error has a sudden increase. We can further observe



that the time of ending of phase change of the model is in between the value obtained by the temperature measurements and the value obtained by image analysis. This can be linked to the results observed in Chapter 2, where we noticed that the thermocouples reached the end of melting once it touched the liquid part, even if there was still an amount of solid PCM within the tube. On the other hand, the image processing reveals a value of zero in the melting fraction, when there is no longer solid PCM within the tube. The major issue with this comparison is that both results, the experimental and the modeling results, are an equivalent of the melting front position  $r(t)$ , obtained by approaching to a 1-D melting. Thus, we rely on the image processing for operation time validation.

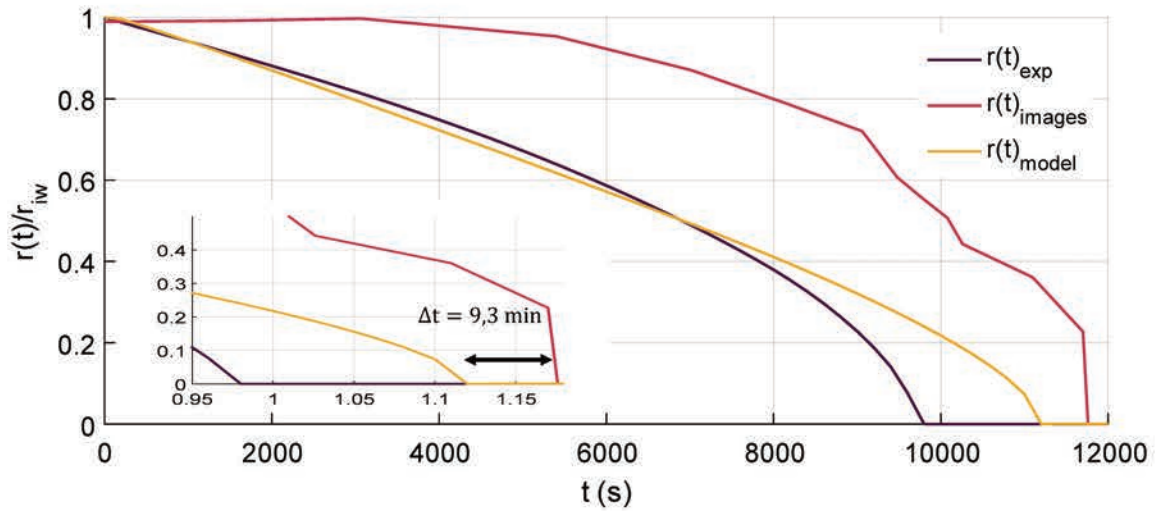


Figure 4.12 – Ratio of the melting front position to the internal radii of the tube  $r(t)/r_{iw}$  for a tube located in the eighth row: by the image processing (magenta), the experimental measurements (purple) and the model (yellow).

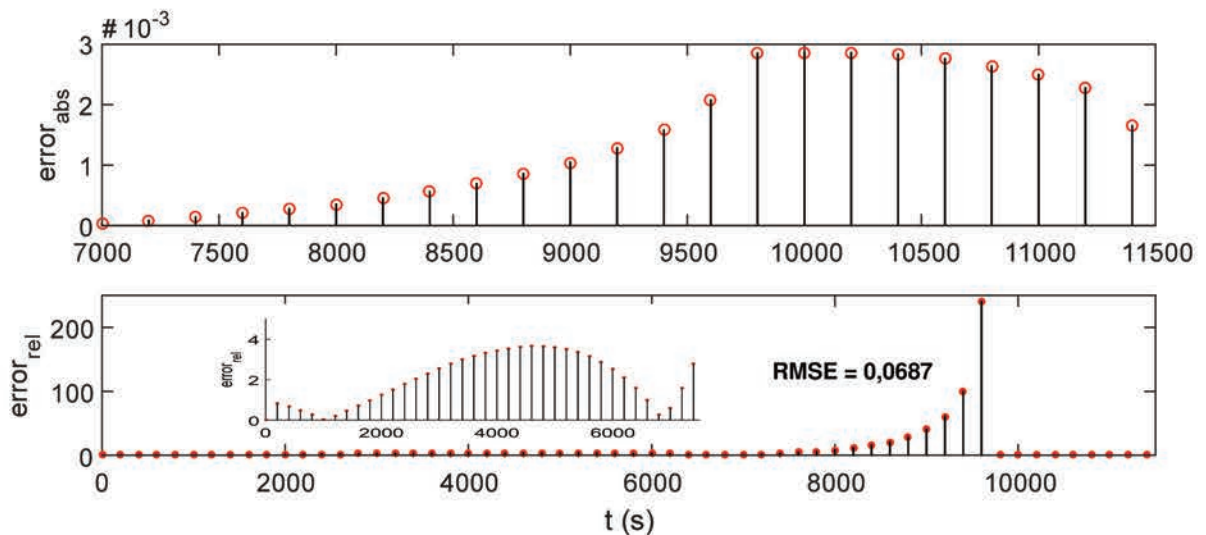


Figure 4.13 – Absolute error, relative error and RMSE between the melting front position  $r(t)_{exp}$  obtained by experiments  $m_{f-8exp}$  and the melting fraction obtained by the model  $r(t)_{model}$  for a tube located in the eighth row.

We can compare directly the values of the melting fraction  $m_f$  obtained by image processing (magenta) and experimentally (purple), with the one obtained by the model (yellow). These

result are observed in figures 4.14 and 4.15. They show similar behavior than those observed for the melting front position. The experimental melting fraction obtained from the temperature measurements, and the model, fits each other with an error of less than 10%; however, this is not the case when comparing to the results from image processing.

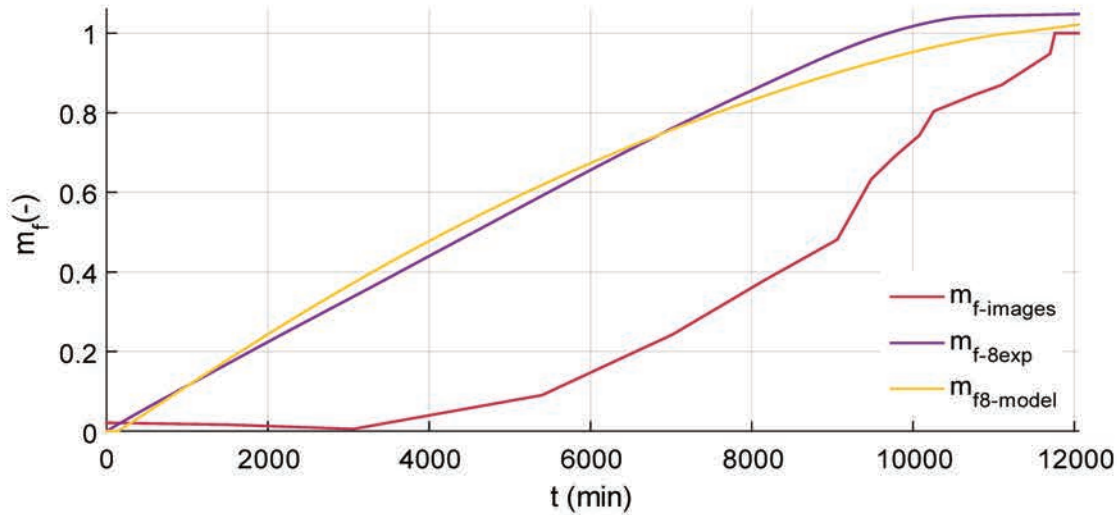


Figure 4.14 – Melting fraction obtained by the image processing (magenta), the experimental measurements (purple) and the model (yellow) for a tube located in the eighth row.

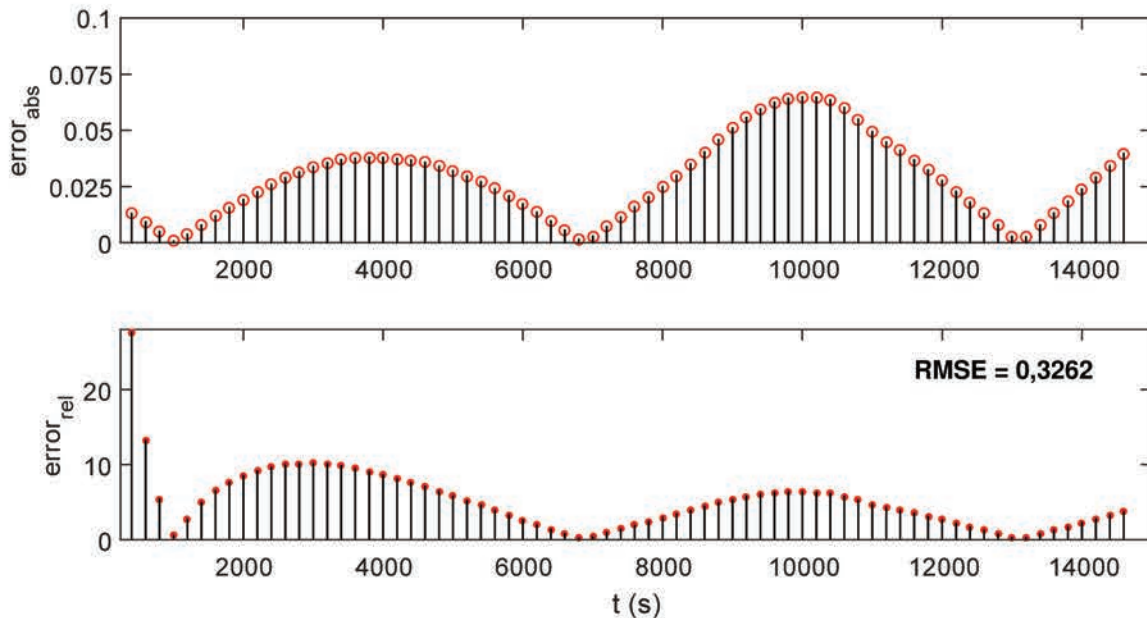


Figure 4.15 – Absolute error, relative error and RMSE between the melting fraction obtained by experiments  $m_{f-8exp}$ , and the melting fraction obtained by the model  $m_{f8-model}$  for a tube located in the eighth row.



### Global validation of the heat exchanger

From the global domain, we aim to validate the performance of the heat exchanger through the power cooling obtained from the modeling  $P_{cool,model}$ , with the power cooling obtained from further processing of experimental data  $P_{cool}$ .

This parameter can be computed through the inlet  $T_{in}$  and outlet  $T_{out}$  temperatures of the heat exchanger. The inlet  $T_{in}$  is an input of the model, whereas the outlet temperature  $T_{out}$  is a result of solving the temperature field of the heat exchanger. In figure 4.16 is shown the results of the inlet and outlet temperatures obtained from the experiments and the model.

Since the inlet temperature during the experiments is almost constant, we focus solely in the outlet temperature  $T_{out}$ . In figure 4.17 we can observe that the results from the model show a higher value than the temperature obtained by experimental measurements. This can be explained by the losses through the heat exchanger walls, that were neglected by the model, but are present in the experimental results. Furthermore, we can observe that the relative error between these two temperatures is lower than 5%, which represents an RMSE of 0,3079.

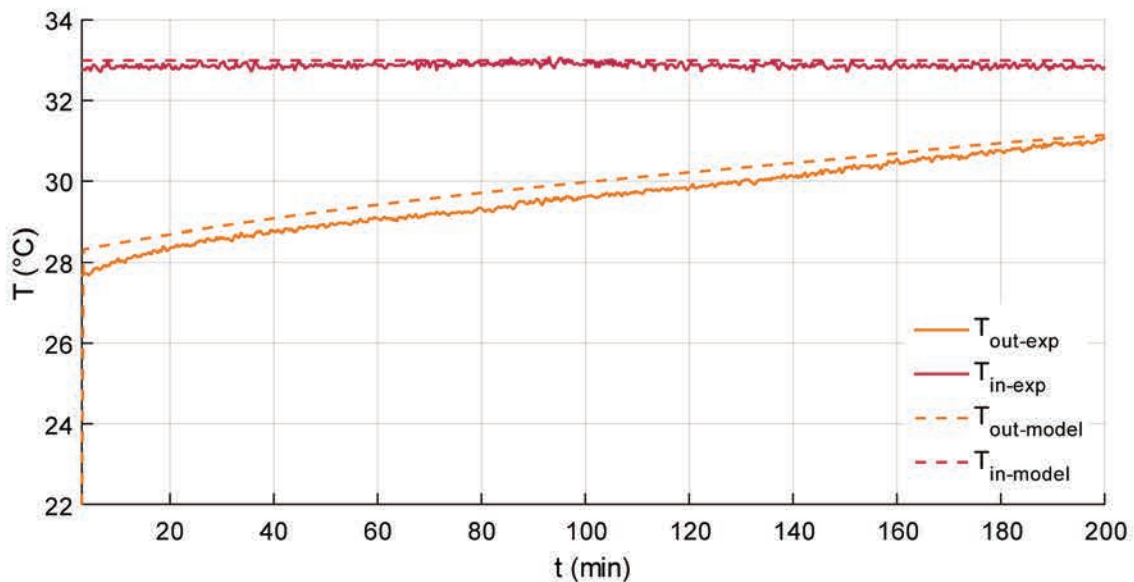


Figure 4.16 – Comparison between the experimental and modeled temperatures for the inlet and outlet positions of the heat exchanger. Inlet temperature in magenta: measurement (solid line) and model (dashed line). Outlet temperature in orange: measurement (solid line) and model (dashed line).

Since we have the inlet and outlet temperature, we can easily compute the cooling power of the heat exchanger  $P_{cool}$ . The results of this computation are observed in figure 4.18. In here we can observe that the cooling power can be predicted with a maximum error below 10% (which represent a maximum absolute error of 20 W).

From these results we observed that for this type of heat exchanger, a simple model, based solely in radial conduction, can predict the global behavior of an air-PCM heat exchanger, even if it cannot take into account all the local phenomena involved, that we stated during the experimental studies, such as natural convection, multidimensional heat transfer, and others.

Furthermore, if we want to account non-isothermal phase change, including the effects of natural convection, we can rely on the empirical correlations, obtained from the literature and the present works, together with the PCM parameters obtained from DSC analysis. A second

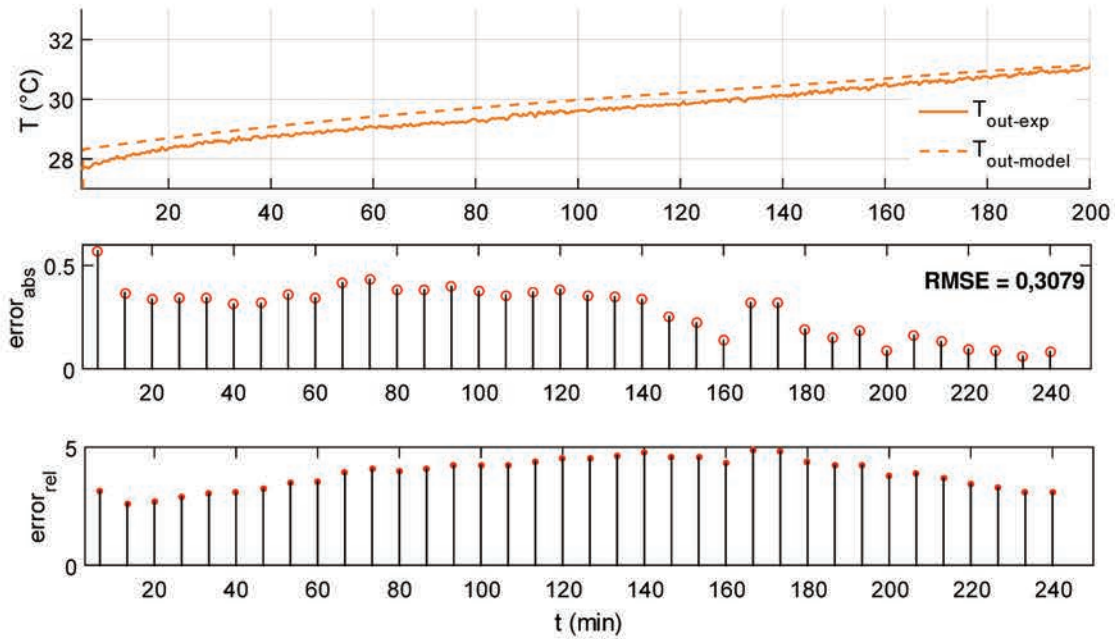


Figure 4.17 – Comparison between the experimental and modeled temperatures for the inlet and outlet positions of the heat exchanger. Inlet temperature in magenta: measurement (solid line) and model (dashed line). Outlet temperature in orange: measurement (solid line) and model (dashed line).

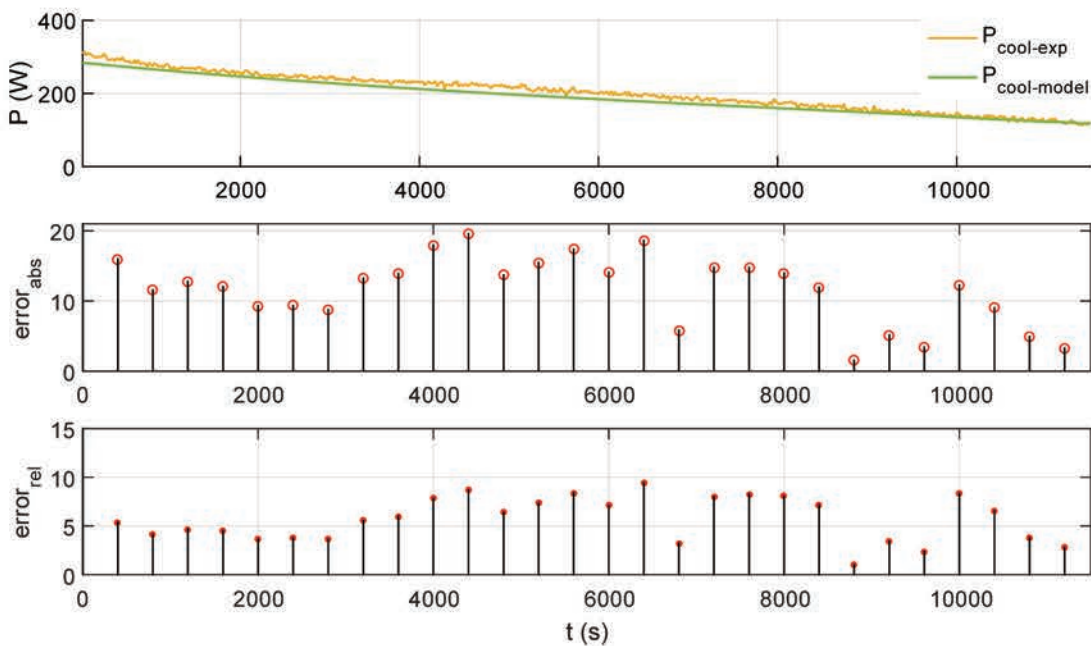


Figure 4.18 – Comparison between the experimental and modeled cooling power of the heat exchanger: experimental (yellow), and modeling (lime-green).

model is proposed for future analysis, which accounts for these subject. The mathematical formulation of the model and the main assumptions are presented in the next section.

## 4.4 Non-isothermal phase change with natural convection model

In here we propose a model to predict the behavior and performance of an air-PCM heat exchanger. For this, we reduce the global-local interactions into three sub-domains:

1. The air domain, which accounts the energy balance in a row of tubes with PCM (global domain).
2. The wall domain (local domain).
3. The PCM domain (local domain).

For the description of air and the wall sub-domain we propose to perform energy balance in each control volume, while for the PCM we propose to use the experimental correlations obtained in section 4.2. Figure 4.19 shows the approach followed for the present model:

### 4.4.1 Main assumptions for the model

The main assumptions made for the analysis can be summarized as follows:

- The radiative, gravitational, elastic and electromagnetic effects are neglected.
- The thermophysical properties of the PCM remain constants for simplicity, except for the conductivity  $k_{pcm}$ .
- Only latent heat occurs during phase change (since  $Ste \approx 0$ ), and the value of the specific latent heat is constant during the cycle and the energy storage in the container is neglected.
- An imposed convective heat flux is assumed at the frontier between the cylinder wall and the air.
- The air and the PCM during the cycle are assumed to behave as incompressible flows ( $Ma \leq 0,3$ ).
- To avoid movement of the material, the density is assumed to be constant.

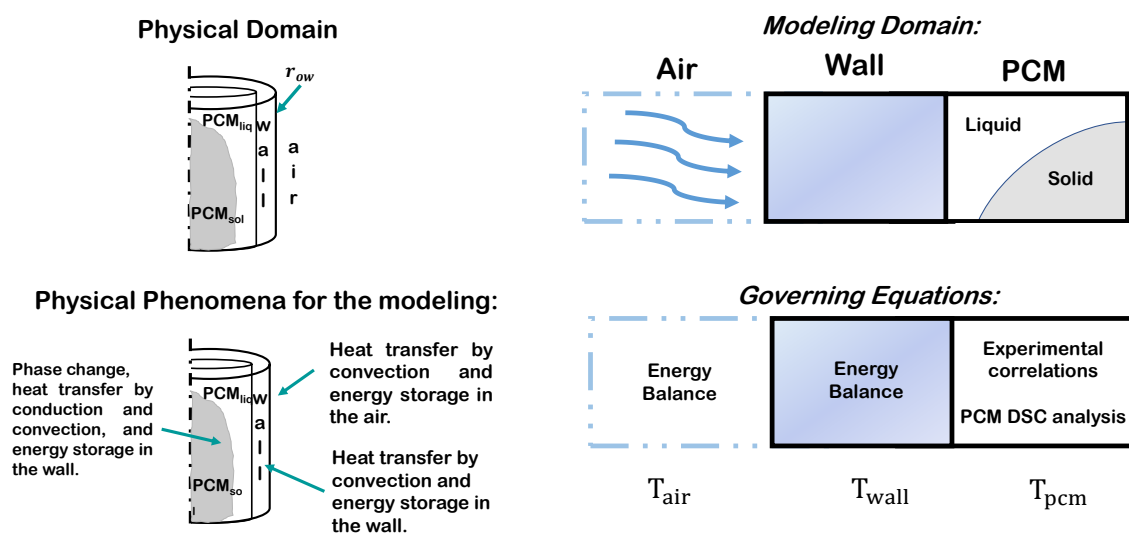


Figure 4.19 – Reduction of the physical domains into the modeling domains.

#### 4.4.2 Energy conservation in the air

The energy balance in the air sub-domain, representing a row of tubes within the air-PCM heat exchanger can be expressed as:

$$\rho_{air} \cdot c_{p_{air}} \cdot A_{air} \cdot \frac{\partial T_{air}(X, t)}{\partial t} + \rho_{air} \cdot c_{p_{air}} \cdot v_{air} \cdot A_{air} \cdot \frac{\partial T_{air}(X, t)}{\partial X} dX = n_t \cdot \frac{T_{air}(X, t) - T_{wall}(X, t)}{R_{air} + \frac{R_{wall}}{2}} \quad (4.25)$$

where  $n_t$  is the number of tubes within a row of the air-PCM heat exchanger.

#### 4.4.3 Energy conservation in the wall and PCM

The local heat exchanges in the wall of a tube can be defined by:

$$m_{wall} \cdot c_{p_{wall}} \cdot \frac{\partial T_{wall}(X, t)}{\partial t} = \frac{T_{air}(X, t) - T_{wall}(X, t)}{R_{air} + \frac{R_{wall}}{2}} - q_{pcm}(X, t) \quad (4.26)$$

where  $T_{wall} = \frac{T_{ow} + T_{iw}}{2}$ , with

$$q_{pcm}(X, t) = \frac{\partial h_{pcm}(X, t)}{\partial t} \quad (4.27)$$

which represents the heat per unit mass transferred into the PCM during melting. The enthalpy  $h_{pcm}$  is defined for all the cycle as:

$$h_{pcm}(X, t) = \begin{cases} c_p \cdot dT & \text{if } T_{pcm}(X, t) < T_{pcm_{sol}} \\ c_p \cdot dT + L \cdot \{C \cdot [Ste(X, t) \cdot Fo(t)]^n \cdot [Ra_{H_{pcm}}(X, t)]^n\} & \text{if } T_{pcm_{sol}} < T_{pcm}(X, t) < T_{pcm_{liq}} \\ c_p \cdot dT + L & \text{if } T_{pcm}(X, t) > T_{pcm_{liq}} \end{cases} \quad (4.28)$$

with

$$Ste(X, t) = \frac{c_{p_{pcm}} \cdot [T_{ow}(X, t) - T_{pcm}(X, t)]}{L} \quad (4.29)$$

$$Fo(t) = \frac{k_{pcm} \cdot t}{c_{p_{pcm}} \cdot \rho_{pcm} \cdot L_c^2} \quad (4.30)$$

$$Ra_{H_{pcm}}(X, t) = \frac{g \cdot \rho^2 \cdot c_p \cdot \beta \cdot [T_{ow}(X, t) - T_{pcm}(X, t)] \cdot L_c^3}{\mu_{pcm} \cdot k_{pcm}} \quad (4.31)$$

#### 4.4.4 Supplementary assumptions

To find the solution for this model, some supplementary assumption has to be made.

For  $Ra_{H_{pcm}}$  and  $Ste_{H_{pcm}}$ :

**Assumption 1:** We approximate the external temperature of the wall to the mean temperature of the wall as follows:

$$T_{ow}(X, t) = T_{wall}(X, t) \quad (4.32)$$

**Assumption 2:** The average temperature of PCM domain is obtained fitting the obtained from the DSC results and can be defined as a linear approximation of each region during phase



change: solid PCM, phase change region and liquid PCM by:

$$T_{pcm}(X, t) = \begin{cases} \mathcal{A}_{sol} \cdot h_{pcm}(X, t) + \mathcal{B}_{sol} & \text{if } h_{pcm}(X, t) < h_{pcm_{sol}} \\ \mathcal{A}_m \cdot h_{pcm}(X, t) + \mathcal{B}_m & \text{if } T_{pcm_{sol}} < T_{pcm}(X, t) < T_{pcm_{liq}} \\ \mathcal{A}_{liq} \cdot h_{pcm}(X, t) + \mathcal{B}_{liq} & \text{if } T_{pcm}(X, t) > T_{pcm_{liq}} \end{cases} \quad (4.33)$$

where the constant values  $\mathcal{A}$  and  $\mathcal{B}$  for each case represent the slope and the independent term, respectively.

Unknowns variables of the model for each domain:

1. **Air domain:**  $T_{air}$
2. **Wall domain:**  $T_{wall}$
3. **PCM domain:**  $T_{pcm}$

## 4.5 Concluding remarks

In this chapter, we aimed to develop models that can recreate and further predict the behavior of an air-PCM heat exchanger. The main objective of these models is to prove their usability as part of design tools. Therefore, one goal of these models is to be as simple as possible, but without getting too far away from an accurate answer. Once we develop such models we can conclude the following remarks:

*Regarding the empirical model:*

- From the empirical correlations we could observe how the heat transfer mechanism controlling melting affected the process, where we found two different melting behaviors, when melting was controlled by only conduction, and when it was controlled by both, conduction and natural convection.
- We also found further evidence on the effect of the heterogeneity of the airflow within the exchanger in the phase change process, when we compared the result of the melting fraction for different inlet airflow values.

*Regarding the numerical model:*

- A simple conduction model can be useful for assisting design tools of air-PCM heat exchangers for thermal performance prediction, whereas it could be deficient if a thorough knowledge of the local behavior of the containers of PCM is desired.
- The initialization process proposed for the heat transfer during melting could affect the validity of this model at the beginning of phase change.





# 5

## Building Applications

### 5.1 Scope

In this chapter an air-PCM unit prototype was designed and built, and tested as a cooling unit in an office of the I2M laboratory and within a plus energy house (PEH) prototype, called Sumbiosi. This studies aim to characterize the system behavior during a typical summer day in Bordeaux, France. The performance of this air-PCM unit will be evaluated through thermal performance indicators such as the temperature profiles of the unit, the operation time and the indoor air temperature of the place.

## 5.2 Mobile air-PCM unit

The results of the performance of test bench integrated with an air-PCM heat exchanger allowed us to quantify the potential of using these systems through indicators such as cooling power, effectiveness and others. However, these values resulted from tests made under controlled inlet conditions, where the phase transition was ensured to happen. Now, we propose to construct and test an air-PCM prototype unit for thermal comfort inside a house under in-situ conditions. This prototype will allow us to know the performance of the design under uncontrolled meteorological conditions, that approximate to those that the system will find in real operations.

One feature of the design of this prototype is that it has to be easy for the user to manipulate it, especially regarding transportation. This supposes a limitation to the amount of PCM and therefore, the storage capacity of the unit because its weight would be limit that could ensure the transportation by a single person. For this reason, the unit aims to supply “cold” as an auxiliary air-conditioning unit for small rooms or offices. Then, to achieve this goal, we first defined the specific requirements for a small air-PCM unit, including materials, manufacturing and assembly procedures. Most of these are detailed in the following table:

- The unit must be transported by a single person, therefore the weight must be limited to 30 kg. The inclusion of wheels is considered to facilitate transportation.
- Aluminum is considered as envelope material for the unit due to the ease of handling during manufacture and its weight. The unit must also be insulated to minimize the heat losses.
- The use of commercial paraffin due to its availability.
- The electrical consumption of the unit must be reduce to keep an attractive cost-effectiveness ratio.

These requirements serve as a starting point for the design of the unit. From them, the most important selection criterion is the unit weight, and given the physiological characteristics of the human being, the maximum weight of PCM is fixed in 22 kg. We chose a staggered distribution of the containers since its presents optimal performances regarding the geometric configurations. Now, with the selection of the storage material we will be able to calculate the maximum storage capacity of the unit. We defined two materials as possible candidates for PCM of the system: an organic paraffin RT21 and an organic-inorganic compound SP25E, both fabricated by Rubitherm® and available for use.

The architecture of the unit can be divided into three parts:

- The structure, which includes the metal casing, the insulation, the fans that control the airflow and the wheels that facilitate transport.
- The containers, in this case the tubes, where the PCM is stored.
- The PCM itself.

Once the storage material is selected, the rest of the design contemplated the choices concerning the geometric characteristics of the unit. The following sections of this chapter detail the design and construction of the first two parts of the unit architecture.

### 5.2.1 PCM containers

We looked for the design and reliable manufacturing process of containers, that could meet the initial specifications set shown in figure 5.1. These requirements sought for optimal container features, from the point of view of thermal performance, modularity/size, and pressure tightness (to address the problem of the expansion of the PCM during its melting that causes an increase of pressure in the container). To achieve this purpose, various thermoforming tests of tubes associated with a thermal welding closure were conducted; proving unsuccessful regarding the repeatability of the finished product quality.

Then, we decided to focus on thermo-blow molding processes for plating a preform in a mold. This is based on the principle of using a product already in existence, such as the PET preforms, and then, modeling it to the desired shape. This approach presents the following advantages:

- These products are used in a large number of applications as fluid containers, giving them an important presence in the market, and therefore, a very low cost (unit cost less than 4 cents of euro for the manufacture of 10000 pieces).
- Regarding the tightness of the container, they are provided with a stopper aiming and ensuring the seal under reasonable pressure, similar to a soda bottle that ensures no leakage of liquid.
- It can be guaranteed similar geometric dimensions for all manufactured containers due to its industrial process approach. For this project, the geometry was previously defined as a tube of about 2 cm in diameter, corresponding to the maximum possible thermal thickness of the PCM.

This approach was the one followed up since it was suitable for the objectives of the project. The principle of the manufacturing process is simple: the preform is preheated by radiation. Then, it is simultaneously: (i) stretched by a punch which pushes axially, inside the preform, the bottom thereof and, (ii) blown to be plated on the cylindrical mold.

The difficulty, which led to many pieces of scrap at the beginning of the manufacturing trials, is to stretch-blow without tearing, while ensuring the final shape and regularity of the inner section of the tube and the thickness of its wall. Finally, the trial-correction process led to the production of the tubes used for the applications concerned with this project in association with PDG plastics Company.

Once the manufacturing process and the PET preform were chosen, we defined the geometry of the container that we wanted to produce. Then, from a PET preform of 100 mm length, it was produced a cylindrical tube with a wall thickness of less than 1 mm, a diameter of 20 mm, and a length of about 300 mm. More details about the PET tubes can be found in appendix D.

#### Filling of the tubes with RT21

For the first experiment, the PET tubes were filled with the organic PCM RT21 [88], which has a theoretical melting range between 18 °C and 23 °C, a latent heat capacity of  $L_{pcm} = 155\,000 \text{ J}\cdot\text{kg}^{-1}$ , a heat capacity of  $c_p = 2000 \text{ J}\cdot\text{kg}^{-1}\cdot\text{K}^{-1}$ , and a thermal conductivity of  $k_{pcm} = 0,2 \text{ W}\cdot\text{m}^{-1}\cdot\text{K}^{-1}$ . We proceeded with a different approach than the one used previously for the glass tubes. We used a drying room available in our laboratory because it allowed us to set a higher temperature than the ambient temperature, that would ensure us a liquid state in the PCM. Then, we set the temperature to 32 °C and waited for the PCM to melt completely. Once it was in the liquid state, we used conventional chemical instruments for filling each tube. During this process, both temperatures, the PCM, and the room were continuously monitored.

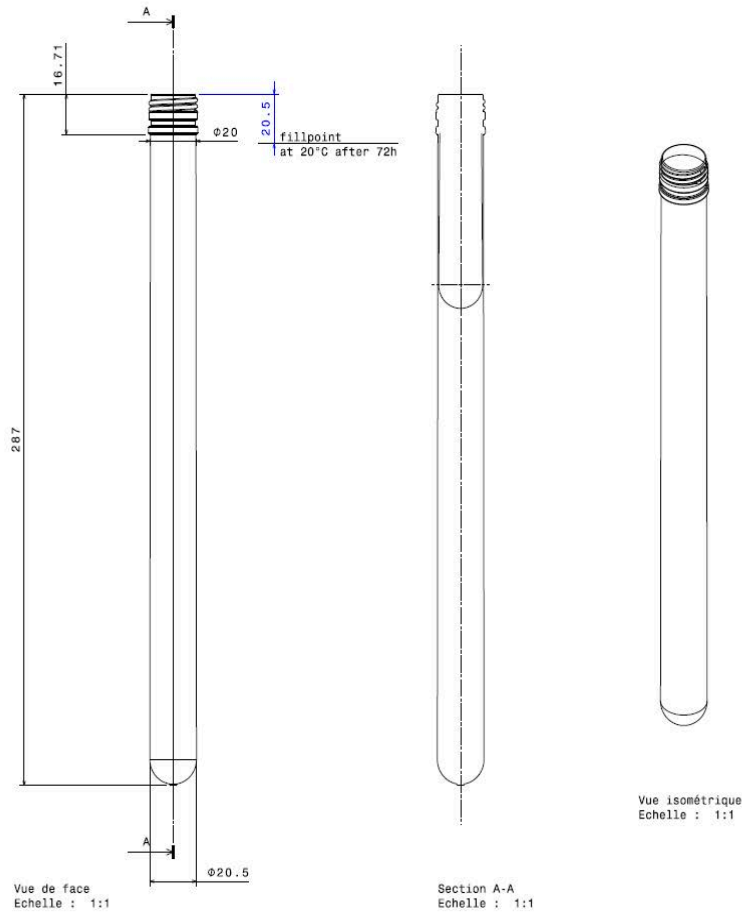


Figure 5.1 – Designs of the PET tubes proposed as PCM containers.

### Filling the tubes with SP25E

The organic-inorganic compound PCM SP25E presents different thermal characteristics than the PCM previously used. For instance, SP25E has a density around  $1\,500\text{ kg}\cdot\text{m}^{-3}$ , while RT21 and RT28HC present a density of  $770\text{ kg}\cdot\text{m}^{-3}$ , a latent heat capacity of  $L_{pcm} = 190\,000\text{ J}\cdot\text{kg}^{-1}$ , a heat capacity of  $c_p = 2000\text{ J}\cdot\text{kg}^{-1}\cdot\text{K}^{-1}$ , and a thermal conductivity of  $k_{pcm} = 0,6\text{ W}\cdot\text{m}^{-1}\cdot\text{K}^{-1}$ . Also, the viscosity of the latter is higher, making the handling of it a bit more complicated regarding the filling. Besides, SP25E is corrosive; therefore the techniques used cannot include metallic materials. We tested several techniques for this, but finally, we proceeded to heat the PCM container up to  $50\text{ }^\circ\text{C}$  with a heating belt, let it melt overnight and when it was completely melted, use conventional chemical instruments for the filling.

### 5.2.2 Unit Structure

The unit structure was at the Arts et Métiers manufacturing workshop, where we had available the machinery for the cutting, folding and assembly of the pieces. Regarding those pieces, the design was made with the least amount of mobile pieces for the case of the structure, which consisted on:

- A single piece that contained both sides and the bottom of the structure (see sub-figure a of figure 5.2).



- The detachable top piece (see sub-figure b of figure 5.2).
- The inlet with four holes where the fans are inserted (see sub-figure c of figure 5.2), and
- six plates of aluminum were made, containing 48 holes each, corresponding to the tube diameter (see sub-figure d of figure 5.2).

The drawings on Catia® and the cutting, folding and assembly of the pieces were part of a master's thesis advised during the development of this work.

Finally, the proposed design is presented in figure 5.2. One side of the unit consists of a plexiglas® plate, allowing a visual track of the melting inside the unit. The airflow across the PCM unit is ensured by four DP200A Sunon fans consisting of 22W, 44 dB, with an default airflow of 95 CFM.

The machinery used could be associated with the software Catia®, where the plans can be directly loaded, facilitating the production of each piece (see sub-figure a of figure 5.3). Besides these pieces, the fans are also considered as part of the structure. Therefore, these four fans were branched in parallel before the assembly and then inserted into the holes in the structure during the assembly. Finally, when all the aluminum pieces were bent to their actual position, they were joined together using screws, so that it could disassemble easily. With the structure ready, we proceeded to place the polystyrene insulation and the plexiglas® plate. Silicon glue was used to seal all the joints to prevent leaks (see figure 5.3).

### 5.2.3 Experimental setup and Procedure

To test the feasibility and the thermal performance, we installed the unit at one office for three persons, located in the I2M laboratory. The metrology for this setup consisted of temperature measurements and the capture of photographs. We used type T thermocouples for the temperature measurements, which were previously calibrated with a thermostatic bath Lauda® as the reference. The results from this calibration are detailed in Appendix B.

The first protocol we imagined for the tests consisted of the measuring air temperatures of two contiguous identical offices facing East. One of these offices was equipped with the air-PCM unit, while the other one, was under its usual conditions. This test was based on the assumption that both offices are subject to the same external conditions and that the heat transfer between them can be neglected. The final intent of this protocol was to compare the air temperature of both office, and then, the difference between them, would be the consequence of the use of the air-PCM unit.

Unfortunately, this protocol was not tested due to the weather conditions during the measurement campaign: the outdoor air temperature during the nights had to be lower than the solidification point of the PCM to the solidification to happen, and it was not the case during the nights of June and July. The outdoor air temperatures were higher than the PCM solidification point. In addition, the natural ventilation system of the chosen room, also did not allow the necessary air intakes. Therefore, to solidify the PCM, a portable air conditioning was added to the setup to help the regeneration during the night. The issue associated with this solution is that the surplus air stored during the night would be released to the office again during the night, and as a consequence, the initial conditions for the next day, regarding the second office, would not be the same; thus, a comparative measure between these two offices would no longer be possible.

As we expected an air temperature stratification, we measured the air temperature at three different heights: at 2,12 m, at 1,62 m and at 0,72 m, which corresponded to the height of a desk office. The sensors measuring these air temperatures can be observed in figure 5.4 at

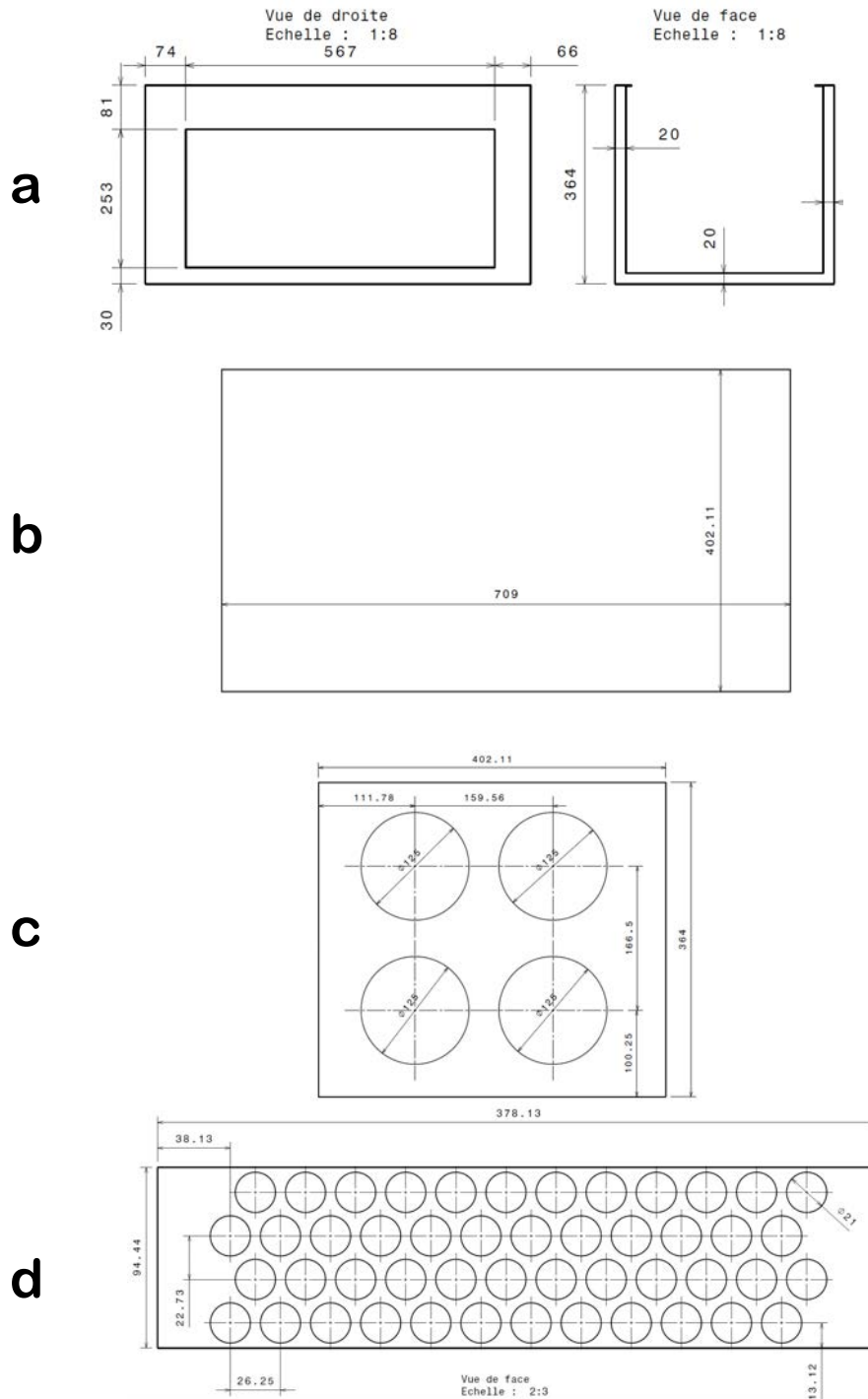


Figure 5.2 – Scheme of the plans in Catia®: a) structure of the unit, b) upper top cover of the structure c) inlet of the exchanger with holes for the fans, and d) plates for the tubes.

the locations a, b and c. From this figure, we can also observe the setup installment in the aforementioned office where d) corresponds to the portable air conditioner, e) the hot air exhaust ducting, f) the air-PCM unit, g) the data acquisition system, h and i) the photo shoot stand points, and j) the computer.

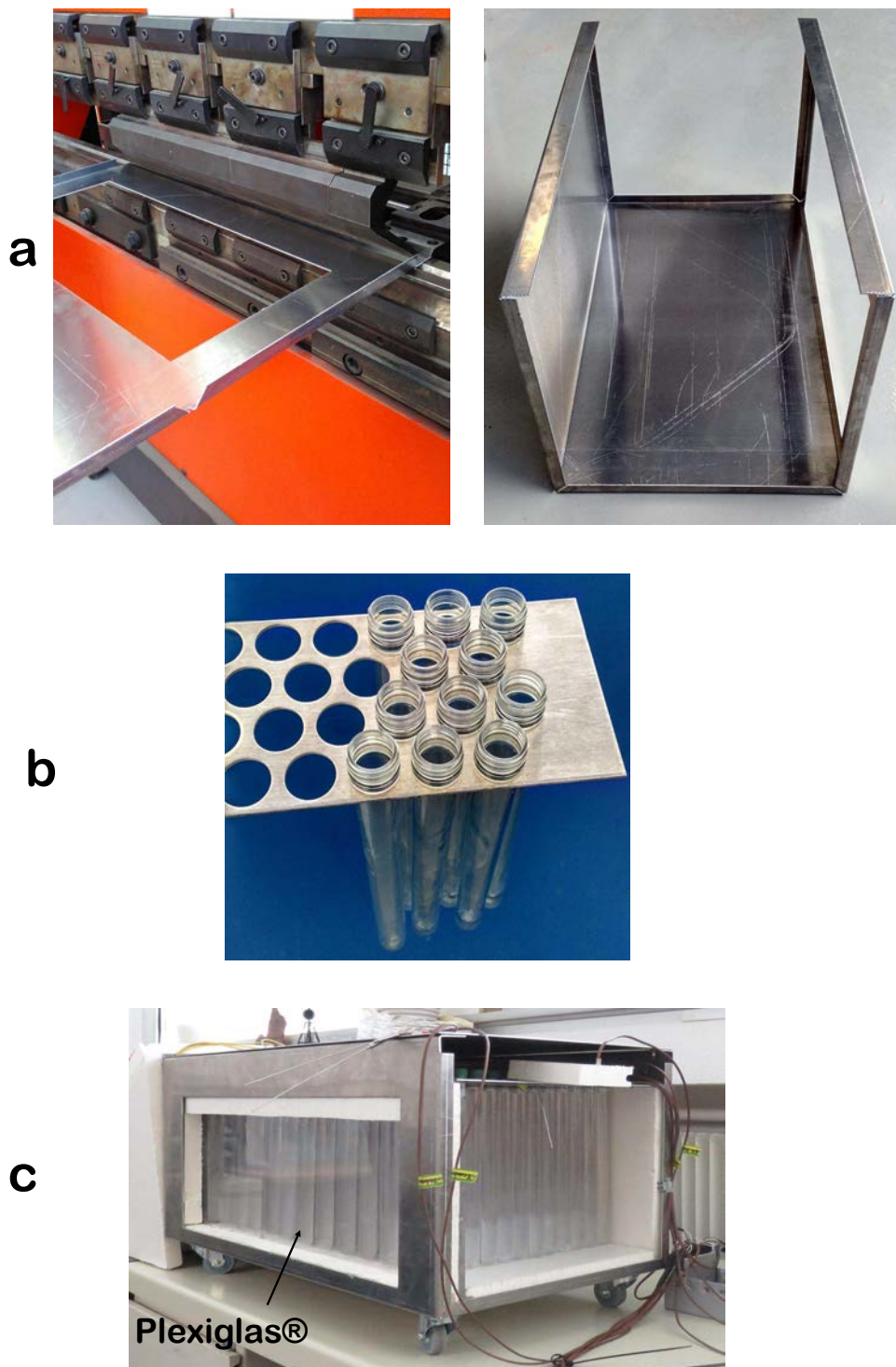


Figure 5.3 – Fabrication of the unit: a) Folding of the metallic structure. b) Principal piece of the structure, c) final air-PCM unit.

Finally, the first protocol proposed was adapted to a single office with the objective of quantify the behavior of this room under in-situ conditions. The proposed protocol to follow then, is:

1. *During daytime:* Once high indoor temperature is reached, the unit is turned on. The

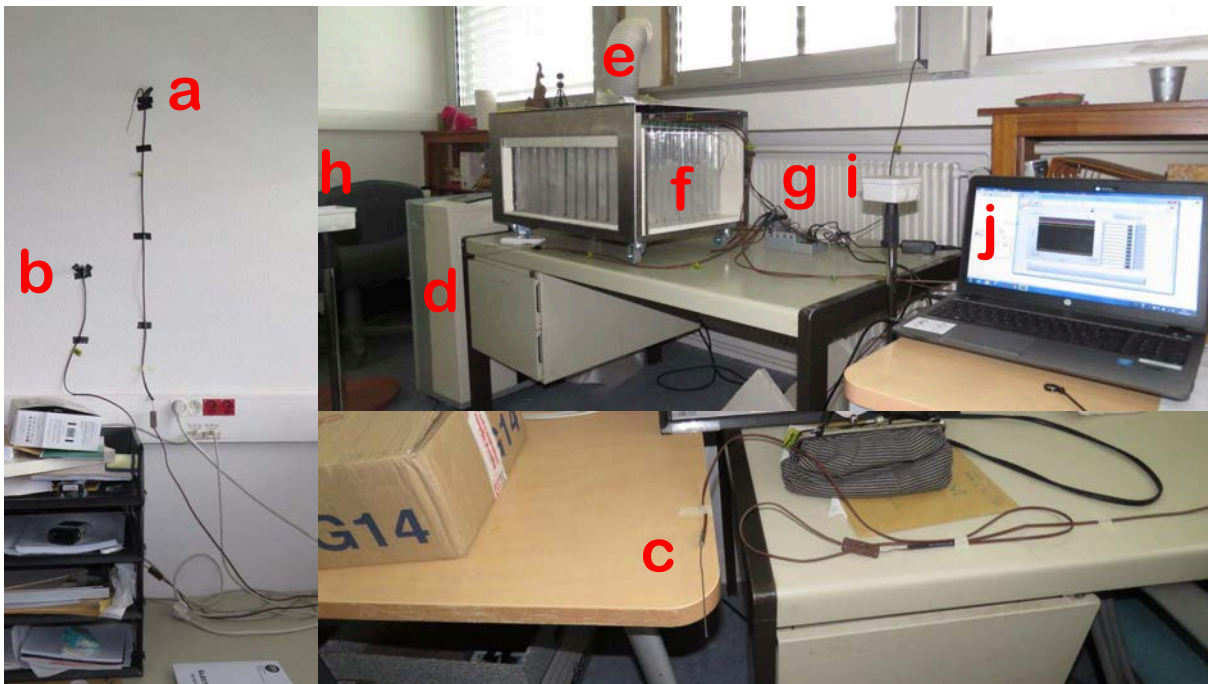


Figure 5.4 – Experimental setup installed at one I2M office: a) air temperature at 2,12 m, b) air-temperature at 1,62 m, c) air temperature at 0,72 m (height of the people sitting), d) portable air conditions, e) hot air exhaust ducting, f) air-PCM unit, g) data acquisition, h,i), photo shooting points, j) computer.

airflow rate is controlled by a voltage regulator connected to the fans.

2. *During nighttime:* For regeneration, the auxiliary portable air conditioner is used during the night. Since the laboratory is open only until 8:00 p.m., the unit is turned-off next day at 7:30 a.m. (opening time of the laboratory).
3. The rest of the day, during the standby periods, the unit remains off to ensure the least possible heat losses.

#### 5.2.4 Results under controlled conditions : Office room at I2M laboratory

##### Results and analysis

During this test, we wanted to observe and measure the temperature profiles of an air-PCM unit subjected to uncontrolled conditions, such as those presented in a building. For this we carried out a series of tests during the summer of 2016, in an office room of three people at I2M laboratory.

Figure 5.5 shows the temperature profiles during the solidification of the PCM RT21 carried between July 16<sup>th</sup>, and July 17<sup>th</sup>, 2016, at 180 V. This test was exceptionally made during the day in order to visualize the solidification and melting profiles. A portable air-conditioning unit assisted these tests to promote the regeneration of the PCM, since the natural ventilation was not enough. This air-conditioning unit is equipped with a water tank that has to be changed if it is full. During the test the occupation within the office was of one person.

The test began at 12:00 and all the temperatures achieved the inlet temperature around 16:30. We continue to solidify the PCM until next day. Around 20:00, we changed the water



tank of the auxiliary air-conditioning unit; this action disturbed the temperature measurements. From this moment, the occupation within the office was none.

In figure 5.5 we can observe two outlet air temperature profiles:  $T_{out_{low}}$  and  $T_{out}$ ; the first one corresponds to a measurement made in the lower part of the outlet of the unit, while the latter corresponds to a measurement made in the center of the outlet.

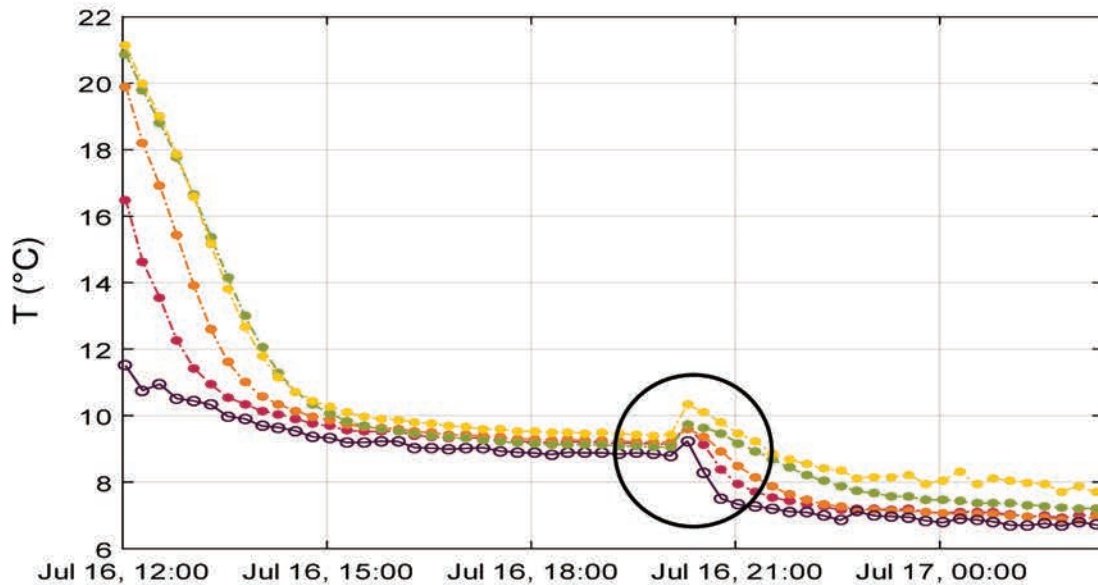


Figure 5.5 – Temperatures profile during the solidification assisted by an portable air-conditioner in July 16, 2016. *Color Code:* Purple: Indoor air temperature ( $T_{in}$ ), magenta: air temperature at the first third of the unit ( $T_{1/3}$ ), orange: air temperature at the second third of the unit ( $T_{2/3}$ ), yellow: air temperature at the outlet of the unit ( $T_{out}$ ), lime-green: air temperature at the lower part of the outlet ( $T_{out_{low}}$ ). The circled part represent the moment when we changed the water tank.

Figure 5.7 shows the air temperatures profile before the water tank change. The air inlet temperature  $T_{in}$  decreases rapidly and reaches the temperature of the auxiliary air-conditioning unit, while the other temperatures decrease slowly due to the effects of phase change in the unit. One can observe that under the inlet conditions, the regeneration of the PCM was achieved 3h30 after the beginning of the cycle. Since the inlet temperature of the unit was lower than the solidification temperature of the PCM used RT21 Rubitherm®, it has the potential for use on the next day. Figure 5.7 shows the PCM state at the beginning and at the end of the solidification cycle.

In figure 5.8 we can observe the standby period of the unit followed by a cooling cycle and the cooling cycle, where the black dashed line represent the division between these two periods. At the end of the solidification of the PCM the air temperatures within the unit  $T_{1/3}$  and  $T_{2/3}$ , were at 7°C. However, this temperature increased at the beginning of the cooling cycle, raising its value to 14°C in 5 hours, indicating a loss in temperature of the "cooling potential" of about 7°C. This loss represents a potential of storing sensible heat that cannot be further exploited, and that it should be avoided. This loss can be due to the lack of a cover in the back of the unit, as can be observed in figure 5.4.

In the same time the temperatures at the inlet  $T_{in}$  and the outlet  $T_{out}$  of the unit, which were in contact with the indoor air temperature achieved a temperature of 25°C. Nevertheless,



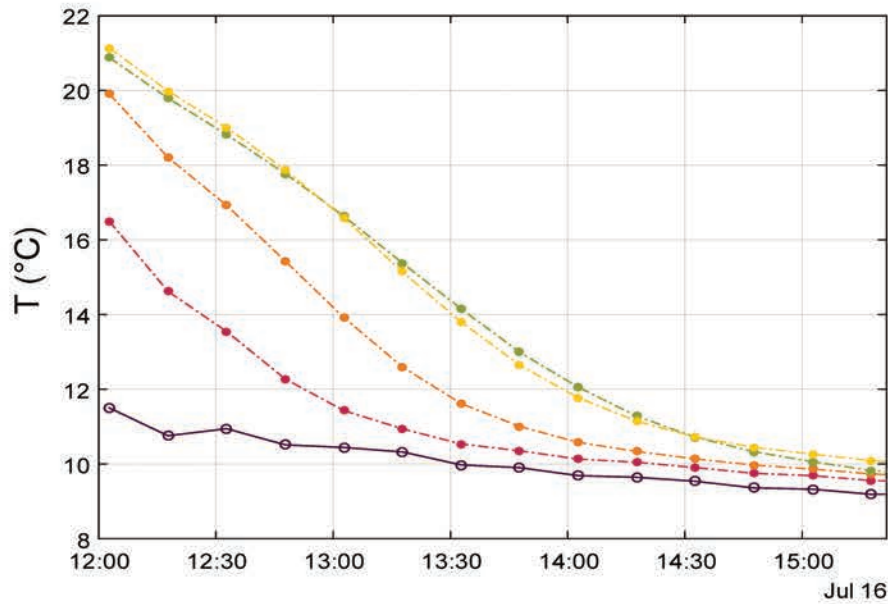


Figure 5.6 – Temperatures profile during the solidification assisted by an portable air-conditioner in July 16, 2016. *Color Code*: Purple: Indoor air temperature ( $T_{in}$ ), magenta: air temperature at the first third of the unit ( $T_{1/3}$ ), orange: air temperature at the second third of the unit ( $T_{2/3}$ ), yellow: air temperature at the outlet of the unit ( $T_{out}$ ), lime-green: air temperature at the lower part of the outlet ( $T_{out_{low}}$ ).

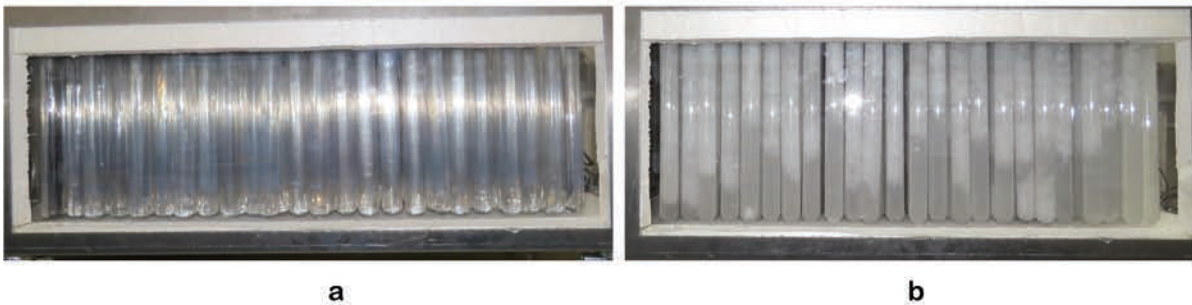


Figure 5.7 – Visual results of the solidification cycle of the PCM during a test performed at the I2M laboratory: a) at the beginning of the cycle (liquid state), and at the end of the cycle (solid state).

when the cooling cycle has begun, the air temperatures within the unit were below the melting point, indicating that the PCM were still in its solid phase, and latent heat storage could be still possible for the actual conditions of the unit.

If we now focus on the cooling cycle, which began around 15:00, we can observe a quick decrease in the outlet temperatures  $T_{out}$  and  $T_{out_{low}}$ , of 8,5 °C, and 11 °C, respectively. These sudden decrease can be explained by the forced movement of the airflow, when the unit was turned on.

At the beginning of the melting cycle, the temperature in the unit was lower than that of phase change, so during this melting cycle, it is expected the presence of sensible and latent heat storage. The range of temperature of phase change for the paraffin Rubitherm®RT21 is quite broad (between 17,25° C and 22,75 ° C), yet determining the start time of the phase change is a complicated task.

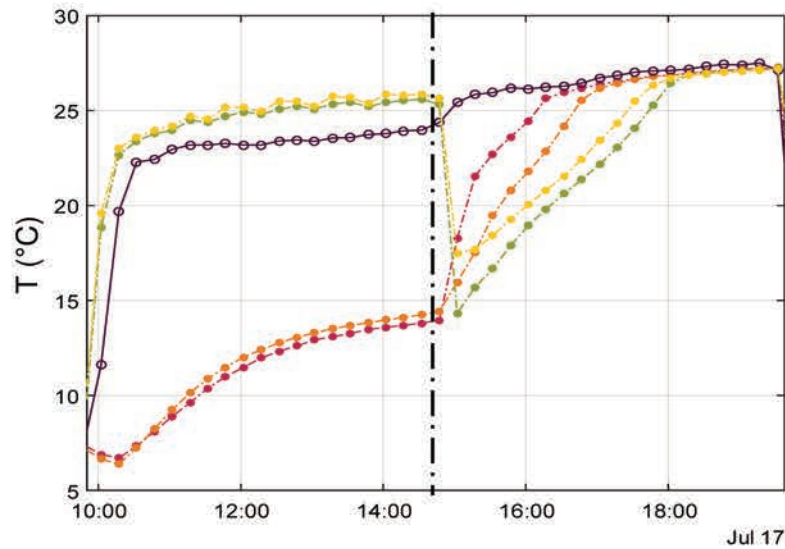


Figure 5.8 – Temperatures profile during the standby period and melting of PCM during July 17, 2016. *Color Code:* Purple: Indoor air temperature ( $T_{in}$ ), magenta: air temperature at the first third of the unit ( $T_{1/3}$ ), orange: air temperature at the second third of the unit ( $T_{2/3}$ ), yellow: air temperature at the outlet of the unit ( $T_{out}$ ), lime-green: air temperature at the lower part of the outlet ( $T_{out_{low}}$ ).

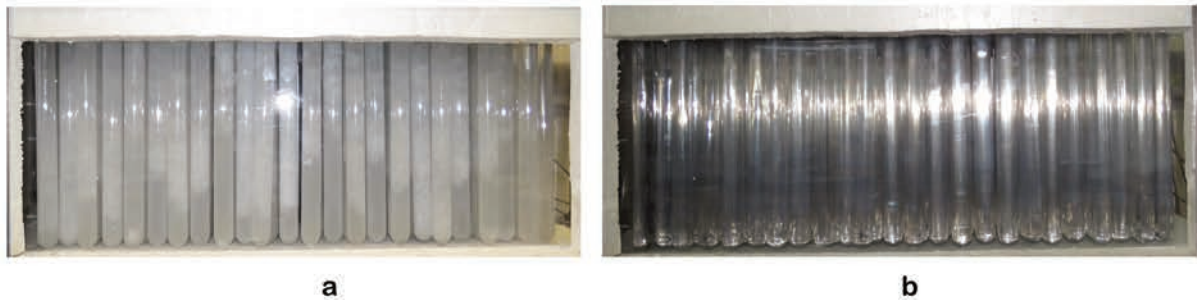


Figure 5.9 – Visual results of the melting cycle of the PCM during a test performed at the I2M laboratory: a) at the beginning of the cycle (solid state), and at the end of the cycle (liquid state).

It can be highlighted that during this cycle, the temperature profile at the outlet was not uniform, and the temperature measured presents different values, being the lower point of the outlet, the lower of both temperatures. Furthermore, the unit operated during 3,5 hours, under this airflow inlet condition.

The measurement of the airflow is not conceivable, a priori, with the original structure of the exchanger. Then, an approximate calculation using the value of theoretical latent heat and equation 3.9, described in chapter 2 for the calculation of the cooling and heating power of heat exchangers has been implemented, as follows:

$$\dot{m}_{air} = \frac{P_{cool}}{c_{p_{air}}} \cdot [T_{in} - T_{out}] \quad (5.1)$$

where  $P_{cool} = E_L / \Delta t_{op}$ .

By doing this, we can have an approximative of the airflow value of the unit during the cycle. The results obtained for the airflow during the melting cycle is about  $149 \text{ m}^3 \cdot \text{h}^{-1}$ .

From this analysis we can highlight two main aspects:

- The need of a cover at the back of the air-PCM unit for further tests, and
- The operation time of the unit, which is not that extensive.

Nevertheless, these tests allows some observations about the behavior of this unit under uncontrolled conditions. In the following section, we test this unit, at another building.

### 5.2.5 Results under real conditions : Sumbiosi PEH

#### Platform overview

A PEH prototype located in Gradignan, Bordeaux, at the South of France, was used as an experimental platform for the present study during the summer of 2017. This house was designed and constructed for the Europe Solar Decathlon 2012 competition, later becoming an experimental platform for thermal behavior and performance in buildings. A schematic of this PEH experimental platform is presented in the figure 5.10.

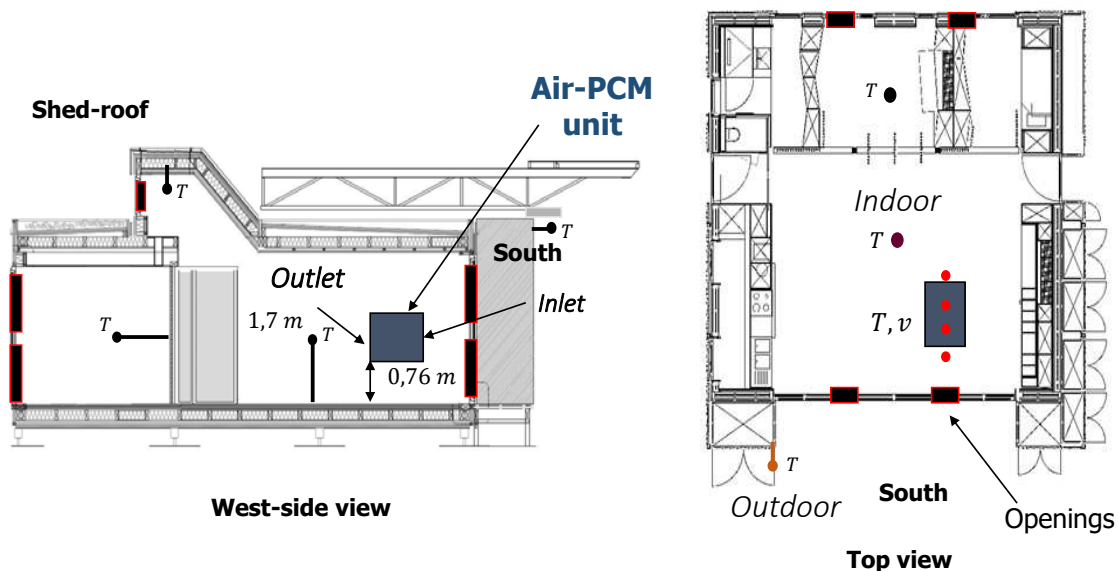


Figure 5.10 – Experimental platform schematic. Left: West-side view of the house showing the location of the unit inside the house and sensors distribution. Right: Top view of the house. The colored dots symbolize the position of the temperature and velocity sensors.

The house envelope consists of a wooden façade, made out of maritime pine, with thermal insulation of 32 cm at the floor, ceiling and North façade, and the same insulation in addition to outdoor cabinets at the East and West façades; the South façade contains large double-glazed windows. The thermally heavier-weighted of the house envelope is located on the floor due to the presence of a concrete slab within it. Moreover, the house also has ten bottom-hung openings that promote the establishment of different natural ventilation strategies by choosing a suitable opening-closing configuration. These openings are distributed as follows: four on the South façade, four on the North façade and two at the shed-roof. Each window disposes of blinds to limit the entry of solar radiation to the house.

This PEH house uses natural ventilation as passive cooling method during summertime. During these tests, we use an strategy of natural ventilation to enhance the PCM performance ensuring a complete solid state of the material before its use. Studies on the behavior of natural



ventilation in this house have been developed prior to these tests, which allowed us to choose the natural ventilation strategy during the nights [36]. In figure 5.11 is depicted the natural ventilation strategies for this house.

In fact, this platform was chosen for these tests, because it has been fully instrumented and characterized as a part of a Ph.D. thesis work. Then, by applying the modelings for predicting the performance of the house, we can further extract the effect of the unit within the house. Since these works are currently on development, we will show in here, the thermal performance of the house through global indicators, but as future work, the results obtained will be compared with the modeling of the house, and then obtain the actual effect of the unit.

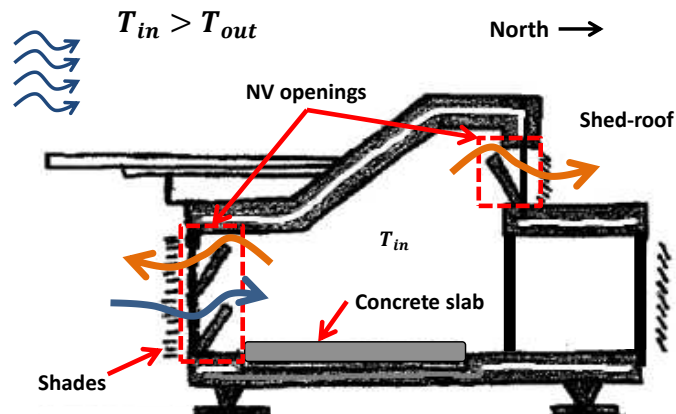


Figure 5.11 – Natural ventilation strategies apply to the PEH Sumbiosi.

### Metrology of the platform

To describe the physical phenomena and the thermal behavior of both systems, the house, and the air-PCM heat exchanger, temperature, velocity and heat flux sensors were placed in different locations within the house. Figure 5.10 illustrates the location of the air-PCM unit within the house. The unit was placed near the openings located at the South facade, at the height of 0,76 m. The indoor temperature was measured at the height of 1,70 m, as shown in figure 5.10.

Figure 5.12 shows, the position of the air-PCM unit within the house along with the following elements: (a) the openings, to allow the passage of the outdoor air during the operation of the night natural ventilation strategy. (b) The rheostat, to control the airflow rate in the unit, which is connected to the four fans at the inlet of the exchanger; (c) the inlet of the exchanger; (d) one of the locations of a couple of black and shiny heat flux meters to measure the heat losses. (e) The air temperature measurement at the exchanger outlet, and (f) the airspeed measurements. During the standby periods, an insulating polystyrene plate is placed at the outlet to avoid losses through it.

Type T thermocouples were installed to measure the outdoor ( $T_{outdoor}$ ) and indoor air temperatures, as well as, the inlet ( $T_{in}$ ) and outlet ( $T_{out}$ ) air temperatures in the PCM unit. The location of these thermocouples can be observed in colored dots in figure 5.10 and moreover in figure 5.13.

In order to know the PCM's state during the cycle, two thermocouples were placed inside two tubes: one tube was in the second third of the heat exchanger ( $T_{pcm_1}$ ), and the other one, on the last row of the exchanger ( $T_{pcm_2}$ ). To complement two measurements of air temperature

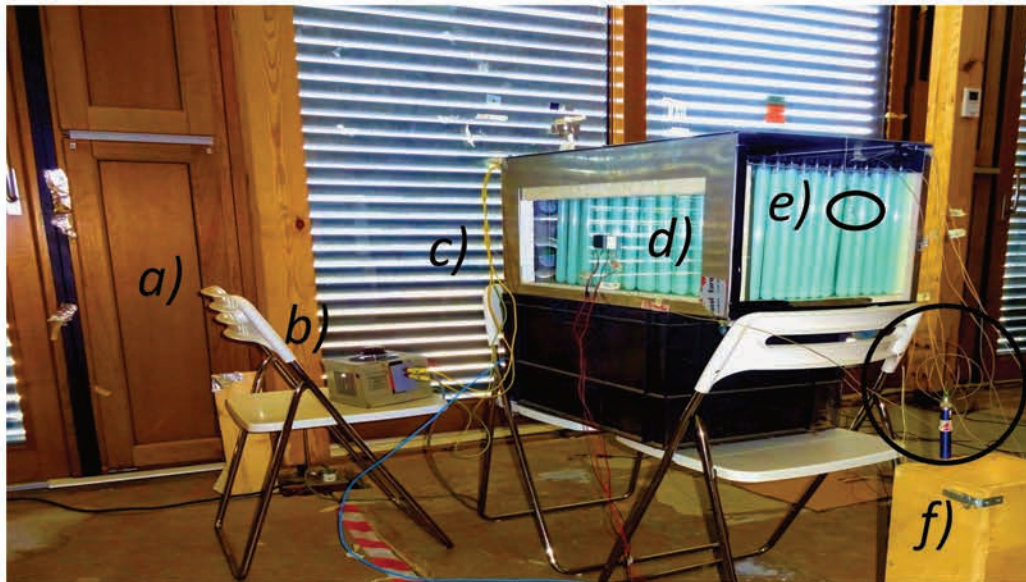


Figure 5.12 – Air-PCM unit located near the south façade of at 0,7 m high from the floor: a) openings, b) power source, c) inlet, d) heat flux meters at the plexiglas® side, e) outlet temperature measurement, and f) airspeed measurement at the outlet.

were made to one and two-thirds of the exchanger ( $T_{1/3}$  and  $T_{2/3}$ , respectively).

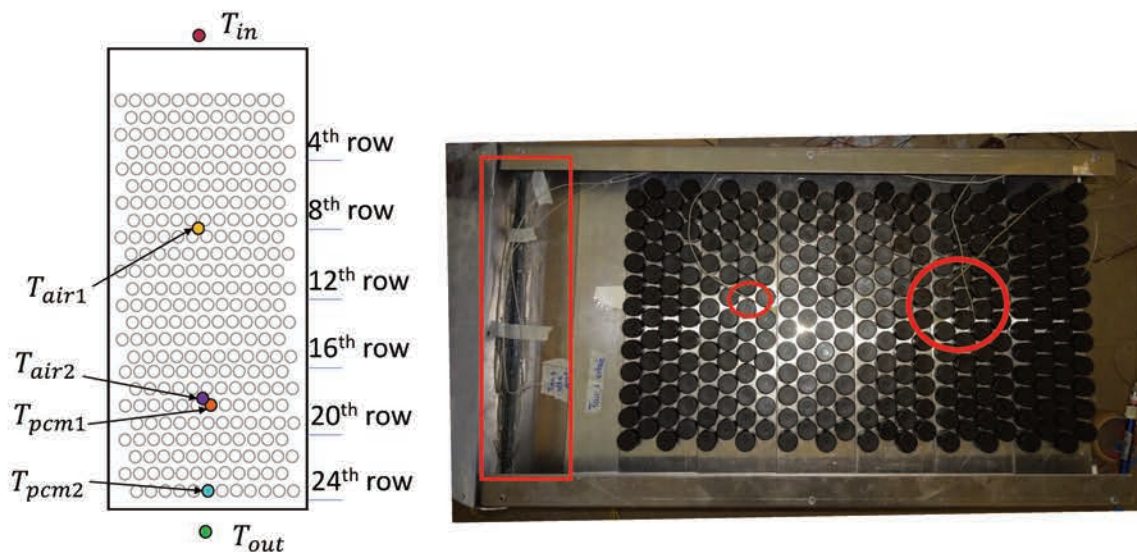


Figure 5.13 – Location of the thermocouples within the air-PCM unit: a) view of the plane of the unit. b) real location within the unit.

## Results and analysis

Weather forecasts were used to ensure suitable conditions for the operation of the system. We used them to evaluate in which days the predicted outdoor air temperature was sufficiently low to guarantee the solidification of the PCM and the system operation during the next selected day. We consulted the weather forecast for August 14th, 2017 and for the next 13 days, for Gradignan in France. We found that for that day the prediction for the outdoor air temperature of August



22<sup>nd</sup> was of 31°C. Besides, during the nighttime of the previous days, the temperatures were expected to be low enough which could ensure a total solidification of the PCM (15°C). These observations are shown in figure 5.14.



Figure 5.14 – Weather forecast for Gradignan, France (consulted on August 14th, 2017).

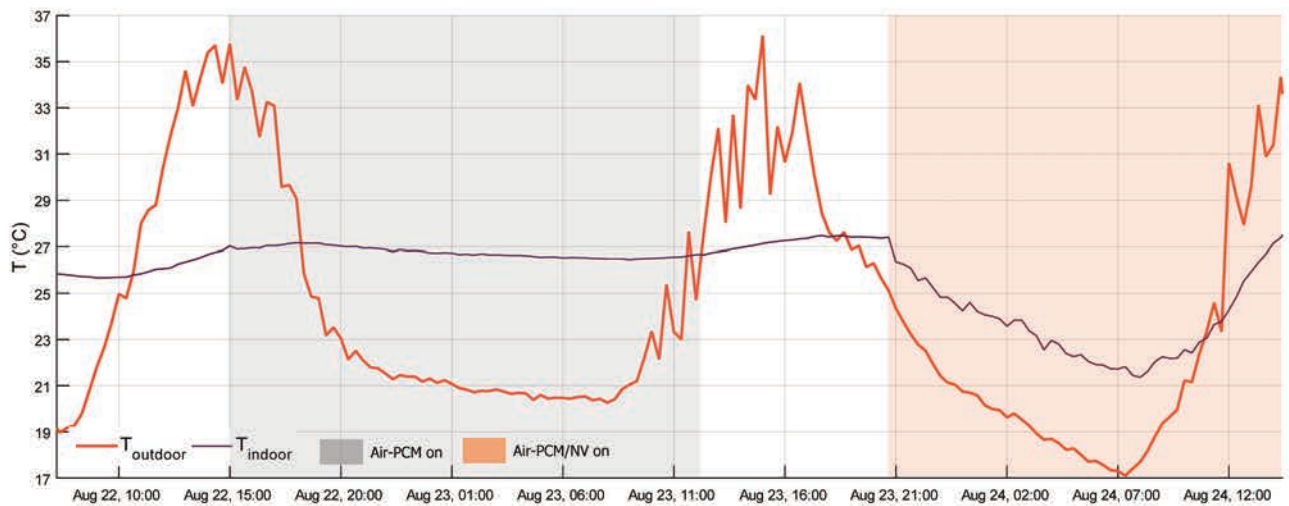


Figure 5.15 – Indoor and outdoor temperatures profile from August 22<sup>nd</sup> to August 24<sup>th</sup>, 2017. The gray area represents the period when the air-PCM unit was on, and the orange area, when the coupled natural ventilation-air-PCM strategy was on.

It can be observed in figure 6 that even if the outdoor air temperature ( $T_{outdoor}$ ) reached high values (36°C), the indoor air ( $T_{indoor}$ ) remained within the thermal comfort range established. Around 3:00 p.m. August 22<sup>nd</sup>, the air-PCM system was activated, once  $T_{indoor}$  reached 27°C, the openings and doors remaining closed. At this time, the outdoor air temperature reached its maximum value for the day.

The use of this air-PCM unit helped to maintain the indoor air temperature (from 3:00 p.m. to 6:00 p.m., when  $T_{outdoor} > T_{indoor}$ ), or act to diminish this indoor air temperature (from 6:00 p.m. to 11:00 a.m. the day after when  $T_{outdoor} < T_{indoor}$ ). Note that the maximum value of the outdoor air temperature predicted by the weather forecast during August 22<sup>nd</sup> day (31°C in fig. 5.14) was smaller than the temperature recorded (36°C in fig. 5.15); that is why we did not initially plan a PCM regeneration operation during the night between August 22<sup>nd</sup> and August 23<sup>rd</sup>.

Since we did not regenerate the PCM after using the air-PCM unit during the daytime of August 22<sup>nd</sup>, thus the unit was not able to maintain the indoor air temperature during



August 23<sup>rd</sup> daytime, and this indoor air temperature value overpassed the 27°C temperature corresponding to the set value. Then, during the night between August 23<sup>rd</sup> and August 24<sup>th</sup>, in order to refresh the experimental house platform and regenerate the PCM, a nocturnal natural ventilation strategy was carried out; the indoor air was able to regenerate the PCM about 2:00 a.m. on August 24<sup>th</sup>, when indoor air temperature value passed under 24°C.

In figure 5.16 is shown the air-PCM unit temperatures. In here, we can observe that the indoor air temperature decreased after the activation of the unit during more than half an hour and then increased again, but slower, if it is compared to the slope before the air-PCM unit activation. The temperature increasing slope changed from a 0,005°C·min<sup>-1</sup> before 3:00 p.m. to an average value of 0,001°C·min<sup>-1</sup> value after 3:30 p.m. This thermal behavior (regarding the indoor air temperature) suggests that, even if the PCM unit is a small one, compared to the house volume (136 m<sup>2</sup>), presents a positive effect on the indoor thermal comfort.

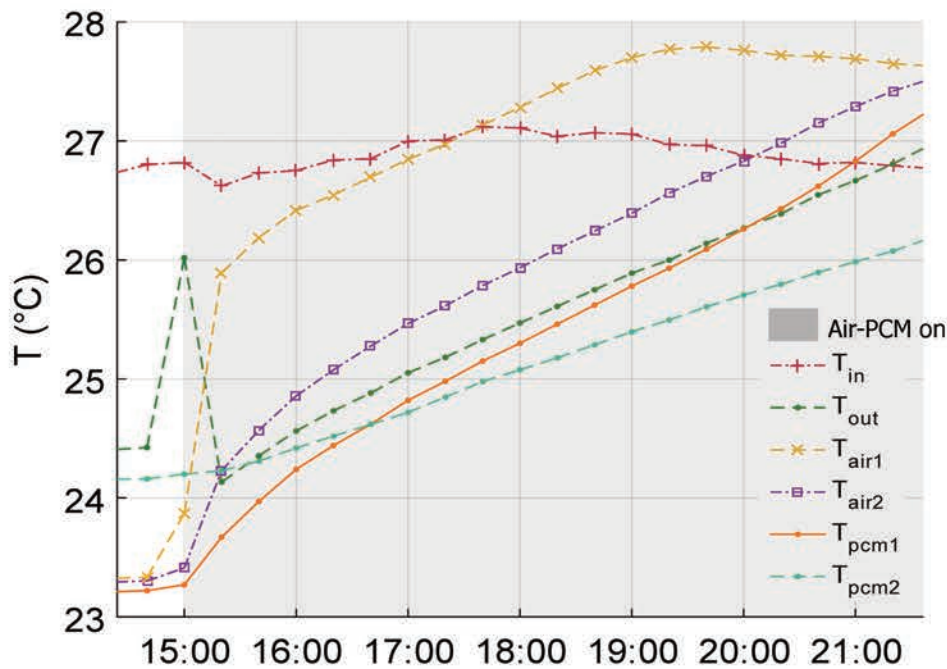


Figure 5.16 – Temperatures profile for the air-PCM heat exchanger, including the PCM temperatures, during August 22<sup>nd</sup>, 2017.

Furthermore, the isolation at the outlet allowed maintaining an almost constant value in the temperatures of the PCM before the activation of the unit, which was also reflected in the outlet temperature. This is convenient regarding heat losses during periods of standby of the unit.

Regarding the PCM behavior, it can also be observed that the unit outlet air temperature,  $T_{out}$ , is governed by the PCM temperature ( $T_{pcm1}$  and  $T_{pcm2}$ ), showing a difference between them of about 0,5 °C. Besides according to the PCM temperature measurements, a sensible storage component is shown for this material, which is in agreement with the data provided by the PCM manufacturer. Moreover, the operating time of the unit,  $\Delta t_{op}$ , is approximately 8 hours (from 3:00 p.m. to 11:00 p.m.), observed in the figure within the gray zone.

Moreover, a temperature stratification within the house was observed: when the unit was not in service, the air temperature value at 0,7 m from the floor was smaller than the one at 1,7 m ( $T_{in} < T_{indoor}$ ). This air stratification of around 0,8 °C·min<sup>-1</sup>, may suggest that placing the unit in a higher position, improve airflow distribution. During the unit operation time, the air-PCM



unit ensured satisfactory thermal conditions; this means, indoor air temperature around or less the temperature comfort condition established at the beginning of the experiment. Although considering the thermal inertia of the building, this unit should have been activated before the indoor air temperature value reached the 27 °C set value.

Figure 5.17 shows the temperature profiles during the PCM regeneration process. Once the night natural ventilation strategy was activated (around 9:00 p.m.), the temperature within the unit began to decrease. This natural ventilation strategy consisted on the opening of the windows facing South.

We can observe that the outlet air and the PCM temperatures decrease until about 4:00 a.m. when the PCM reached a temperature of 23°C. This behavior is also in agreement with the data provided by the manufacturer.

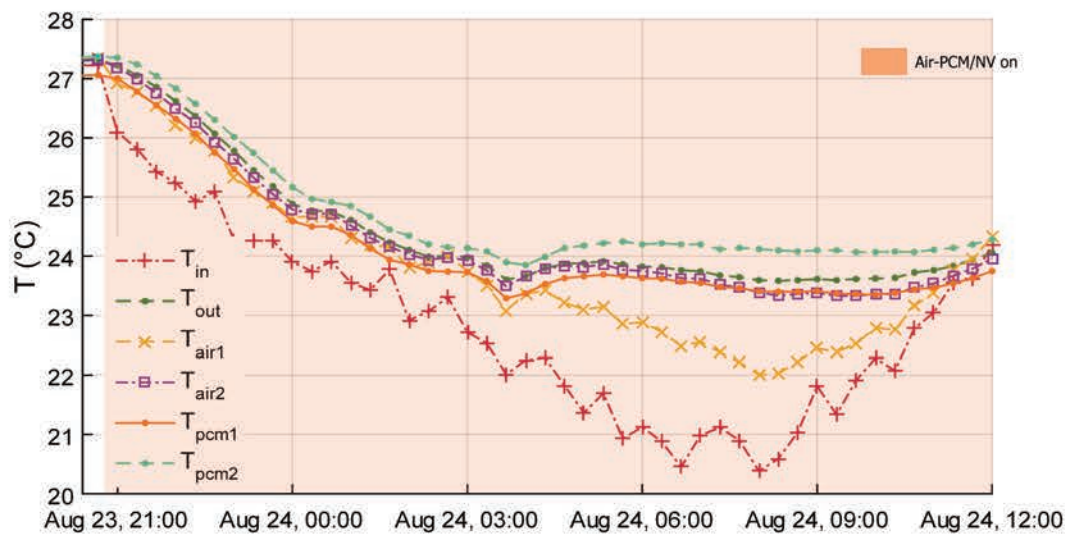


Figure 5.17 – Temperatures profile for the air-PCM heat exchanger, including the PCM temperatures, during August 24<sup>th</sup>, 2017.

### 5.3 Concluding Remarks

This chapter presents two studies that were carried out with the aim of achieving an understanding of a PCM unit behavior under real conditions inside a house. Some remarks that we can retain from these studies are the following:

- The results suggest that the air-PCM unit limits the indoor temperature rise during the unit operating time, keeping a temperature value around the upper thermal comfort limit.
- The operation time of the unit was greater than the minimum required to maintain the thermal comfort conditions in the house. However, when we tested in the I2M office, the operation was limited to 3 hours. This gives us an understanding of how well through the use of this kind of systems should always be relating the desired time of use with the airflow intake of the unit.
- These experiments also points out that the vertical position of this unit regarding the floor of the house may influence the minimization of the temperature stratification.

- As an overall conclusion, we observe that these systems' performance as active PCM units can be well adapted for an auxiliary system for a house, helping to reduce the air temperature and maintaining the thermal comfort, but it needs to be well controlled if we want a satisfactory performance. For this reason, this can be a well-adapted solution for PEH with integrated home automation that allows the optimized use of air-PCM systems.

# General Conclusions

The present work aimed to overcome the complexities related to integrating an air-PCM system, in specific, for building applications by achieving a deep comprehension of the physical phenomena associated with them. To reach this goal, two axes of research were jointly developed: a scientific axis and an axis of application. The first axis intended to cover the phenomenology, physical laws, and different research approaches to achieve the desired understanding of the kinds of systems. This axis of research is covered in chapter 1 through the theoretical background and literature review, in chapter 3, where we presented the experimental approaches, and in chapter 4 of this thesis, where we presented the modeling approaches. The second axis, aimed for the design, construction, and testing of an air-PCM heat unit for building applications. The development of this axis of application is detailed in chapter 1; in chapter 2, where we chose the design of the air-PCM system, subject of study of this work and, in chapter 5, where we designed, constructed and tested an air-PCM prototype unit under real conditions within a building.

This work began with the literature review, which is the base for both axes presented before. From this review, we realized that addressing the potential use of PCM in a specific application requires a focused search because it is a vast topic. General knowledge of phase change is quite available; nevertheless, when addressing a particular solution, one can notice that there are gaps in the knowledge which represent opportunities for further study. This is the case with the air-PCM system developed during this work. The container shape selected has been covered experimental and numerically in the literature, but only a few studies have addressed similar systems, and all of them, only focusing on the global behavior of the system and not in the local physical phenomena.

Regarding the thermal application, in here we focused on an air-PCM unit for thermal comfort within a building, and we addressed the design of such unit in chapter 2. Designing an air-PCM unit is mostly related to the desired application, and in general, is addressed as a sizing problem, where the design process is about selecting parameters that allow meeting the energy targets, such as charge and discharge rates and operation times. In this work, we presented a methodology that aimed to find a geometry that ensures an advantageous thermal performance, and that can be adapted after to fit in with the energy targets of the building. The final design obtained, using vertical tubes within a tube bundle, agrees with heat exchange geometries uses for other thermal applications, but moreover, is a design that can be easily adaptable to active and passive applications of macro-encapsulated systems in buildings.

The experimental approaches that were developed during the chapter 3 received considerable attention. They were key for further developing of this thesis and most of the understanding of the physical phenomena, a central objective of the thesis, was achieved through the development of these experiments. For instance, the phenomena surveyed during the literature review for single containers did not wholly match the results of our experiments for a system of such containers. Both conduction and convection play a significant role during different stages of the



melting cycle of the PCM, which have been found in this study by temperature and air velocity measurements, by visual analysis, and by the dimensionless numbers applying to further data processing.

The experimental approaches in PCM systems are usually based on temperature measurements, because obtaining the temperature values of key domains allows further processing of the experimental data, and therefore, completing energy balances in such volumes. Coupling those approaches with visual information obtained from photographs represents an improvement on the interpretation and analysis of the results obtained.

In chapter 4, we aimed to develop models that can recreate the behavior found during the experiments, for that purpose, we propose an empirical model expressed by melting fraction correlations, based on dimensionless numbers, to include both the conductive and convective effects during melting. Besides, we proposed two numerical models to recreate the thermal behavior of an air-PCM heat exchanger: a 1-D conductive model based on thermal resistance, and a 1-D model coupling the melting fraction correlations with thermal resistances. The first model was tested and validated using the experimental results obtained during chapter 3.

The results obtained by this model shows that a simple model based on a 1-D conductive approach based on thermal resistances can explain the overall performance of an air-PCM heat exchanger. However, it could be insufficient for describing the local behavior within a container. We consider this one of the major findings of the present works, because it reveals to us, that for sizing, or designing tools it can be sufficient to simplify the local phenomena, even though if there is the presence of complex mechanisms, such as natural convection. This 1-D approach allows the easier development of design assistance tools, one of the targets of the works developed in here.

Finally, we developed a prototype of the air-PCM system developed during this thesis. These works are presented in chapter 5. The main goal of this prototype was to test the feasibility of this system under real conditions. We found in here that they present the potential for further developing since they can help to maintain the thermal comfort during the desired period.

## **Limitation of the Research**

In this work, we achieved a deeper understanding of the physical phenomena related to a tube bundle type air-PCM unit. However, after summarizing the main conclusions and enlisting the main contributions of this work, we can acknowledge the research limitations as follows:

### **Regarding the design**

- The methodology does not take into account the PCM properties, leaving out of the design process the enhancement of the material and therefore, the thermal performance of the system.
- The methodology proposed here could have been further analyzed to find not only a customizable solution, but also an innovative solution.

### **Regarding the experimental approaches**

- A detailed instrumentation within a system is hard to implement because it can greatly disturb the results. Therefore, it results in an inconvenient when trying to couple the

global and local domain, since it cannot be easily achieved a detailed instrumentation as such implemented when analyzing a single container. In this work, the temperatures were measured at a single point, assuming that all the media was at the same temperature, regardless of the direction. This can be an oversimplification of the actual measurements.

- Even if the image analysis and further processing reveal data that enrich the temperature measurements, it stills reduce a 3-D problem into a 2-D approach, where the variations of the melting pattern with the angle (in the  $\phi$  direction) are neglected. Furthermore, the optical effects were neglected in the present work.

### **Regarding the modeling approaches**

- The empirical correlations carry the simplifications and assumptions made during the experimental approaches. Moreover, they result from tests made under the same temperature ranges, limiting the ranges of application of such correlations.
- The validated 1-D conductive model based on thermal resistance does not fully describe the local phenomena since it does not account for the convective effects. Besides, we did not test the validity of the coupled model, that includes the effects of natural convection.

### **Regarding the building application**

- The air-PCM unit constructed during this work was not extensively tested, and these tests were performed during a limited period and conditions.

## **Perspectives and future research**

Acknowledging the limitations of this present work allows us to draw the lines for future research. We highlight an overview of them in the following section:

### **Regarding the design**

1. Explore other opportunities revealed by the keyword search, such as improving the containers by not only using typical shapes. One example of this is the integration of fins to enhance heat transfer. This section can be improved by a pre-testing of the performance of the heat exchanger during the designing process.

### **Regarding the experimental approaches**

1. The developing of more controlled and detailed instrumentation within a tube, using adaptable heat fluxmeters, could be proposed as a following step regarding the local measurements. Besides placing air velocity sensors that can acquire the data at the same time of the process, can enhance the determination of the global convective heat transfer coefficient, and a better estimation of the results can be obtained by doing this, which it may reduce the effects of air circulation and velocity heterogeneities observed during this works.

2. Further studies of a single container, with enhanced instrumentation and more controlled inlet conditions, to develop correlations in terms of the melting fraction and the effective thermal conductivity of the PCM.
3. A more exhaustive PCM characterization through DSC analysis performed at a finer rate.

### **Regarding the modeling approaches**

1. The validation of the coupling of the model with the correlations obtained for melting fraction values. Furthermore, this model can explore the spatial discretization of the PCM domain in finite volumes to enhance the numerical resolution. A conductive model, using finite volumes as the spatial discretization is proposed in the appendices of this present work.

### **Regarding the building application**

1. Further test, under different conditions of the prototype unit constructed during these works. These tests can be performed in other seasons to test the feasibility. Concerning this point, it has been already planned a test to measure the performance of the unit within different climatic conditions in Mexico, comparing the performance of two similarly stressed rooms.

# Bibliography

- [1] “A finite volume method for cylindrical heat conduction problems based on local analytical solution”. In: *International Journal of Heat and Mass Transfer* 55. (2012), pp. 5570–5582. issn: 0017-9310/. doi: <http://dx.doi.org/10.1016/j.ijheatmasstransfer.2012.05.043>.
- [2] R.M. Abdel-Wahed, J.W. Ramsey, and E.M. Sparrow. “Photographic study of melting about an embedded horizontal heating cylinder”. In: *International Journal of Heat and Mass Transfer* 22.1 (1979), pp. 171–173. issn: 0017-9310. doi: [https://doi.org/10.1016/0017-9310\(79\)90110-8](https://doi.org/10.1016/0017-9310(79)90110-8). url: <http://www.sciencedirect.com/science/article/pii/0017931079901108>.
- [3] A. Abhat. “Low temperature latent heat thermal energy storage: Heat storage materials”. In: *Solar Energy* 30.4 (1983), pp. 313–332. issn: 0038-092X. doi: [https://doi.org/10.1016/0038-092X\(83\)90186-X](https://doi.org/10.1016/0038-092X(83)90186-X). url: <http://www.sciencedirect.com/science/article/pii/0038092X8390186X>.
- [4] A.D.Solomon. “Melt time and heat flux for a simple PCM body”. In: *Solar Energy* 22.3 (1979), pp. 251–257. issn: doi: [https://doi.org/10.1016/0038-092X\(79\)90140-3](https://doi.org/10.1016/0038-092X(79)90140-3). url: <https://www.sciencedirect.com/science/article/pii/0038092X79901403>.
- [5] *Advances in Heat Transfer*. Academic press, 1998.
- [6] International Energy Agency. *Picture of World Energy Outlook 2016 World Energy Outlook 2016*. Tech. rep. 2019.
- [7] Francis Agyenim et al. “A review of materials, heat transfer and phase change problem formulation for latent heat thermal energy storage systems (LHTESS)”. In: *Renewable and Sustainable Energy Reviews* 14.2 (2010), pp. 615–628. url: <https://EconPapers.repec.org/RePEc:eee:rensus:v:14:y:2010:i:2:p:615-628>.
- [8] Sarı Ahmet, Karaipekli Ali, and Kaygusuz Kamil. “Capric acid and stearic acid mixture impregnated with gypsum wallboard for low-temperature latent heat thermal energy storage”. In: *International Journal of Energy Research* 32.2 (), pp. 154–160. doi: 10.1002/er.1352. eprint: <https://onlinelibrary.wiley.com/doi/pdf/10.1002/er.1352>. url: <https://onlinelibrary.wiley.com/doi/abs/10.1002/er.1352>.
- [9] Hussein Akeiber et al. “A review on phase change material (PCM) for sustainable passive cooling in building envelopes”. In: *Renewable and Sustainable Energy Reviews* 60.C (2016), pp. 1470–1497. doi: 10.1016/j.rser.2016.03.02. url: <https://ideas.repec.org/a/eee/rensus/v60y2016icp1470-1497.html>.
- [10] Vasilios Alexiades and Alan D. Solomon. *MATHEMATICAL MODELING OF MELTING AND FREEZING PROCESSES*. Taylor and Francis, 1993, pp. isbn: 1-56032-125-3.
- [11] “Analyse des conditions de confort d’un bâtiment solaire à énergie positive : la maison ‘Napevomo’ au Solar Decathlon Europe 2010”. In: *1ère Conférence Franco-Syrienne sur les énergies renouvelables*. 2010.

- [12] Pablo Arce et al. "Use of microencapsulated PCM in buildings and the effect of adding awnings". In: *Energy and Buildings* 44 (2012), pp. 88–93. issn: 0378-7788. doi: <https://doi.org/10.1016/j.enbuild.2011.10.028>. url: <http://www.sciencedirect.com/science/article/pii/S0378778811004737>.
- [13] Fabrizio Ascione. "Energy conservation and renewable technologies for buildings to face the impact of the climate change and minimize the use of cooling". In: *Solar Energy* 154 (2017). Solar Thermal Heating and Cooling, pp. 34–100. issn: 0038-092X. doi: <https://doi.org/10.1016/j.solener.2017.01.022>. url: <http://www.sciencedirect.com/science/article/pii/S0038092X17300427>.
- [14] E. Assis et al. "Numerical and experimental study of melting in a spherical shell". In: *International Journal of Heat and Mass Transfer* 50.9 (2007), pp. 1790–1804. issn: 0017-9310. doi: <https://doi.org/10.1016/j.ijheatmasstransfer.2006.10.007>. url: <http://www.sciencedirect.com/science/article/pii/S0017931006005503>.
- [15] M. Bareiss and H. Beer. "An analytical solution of the heat transfer process during melting of an unfixed solid phase change material inside a horizontal tube". In: *International Journal of Heat and Mass Transfer* 27.5 (1984), pp. 739–746. issn: 0017-9310. doi: [https://doi.org/10.1016/0017-9310\(84\)90143-1](https://doi.org/10.1016/0017-9310(84)90143-1). url: <http://www.sciencedirect.com/science/article/pii/0017931084901431>.
- [16] Mohammad A. Bashar. "Experimental Investigation of the Melting Behavior and the Transient Heat Transfer in a Phase Change Material (PCM)". The University of Western Ontario. PhD thesis. 2016, pp.
- [17] Adrian Bejan. *Convection Heat Transfer*. John Wiley Sons, Inc, 2013, pp. xxxiii, 658. isbn: 9780470900376.
- [18] Maitine Bergounioux. *Introduction au traitement mathématique des images - méthodes déterministes*. Springer-Verlag Berlin Heidelberg, 2013, pp. isbn: 978-3-662-46538-7. doi: ~.
- [19] Elizabeth Burleson. "Paris Agreement and Consensus to Address Climate Challenge". In: *ASIL Insights* 20.8 (). url: <https://www.asil.org/insights/volume/20/issue/8/paris-agreement-and-consensus-address-climate-challenge>.
- [20] Castellón C. et al. "Compatibility of plastic with phase change materials (PCM)". In: *International Journal of Energy Research* 35.9 (), pp. 765–771. doi: 10.1002/er.1723. eprint: <https://onlinelibrary.wiley.com/doi/pdf/10.1002/er.1723>. url: <https://onlinelibrary.wiley.com/doi/abs/10.1002/er.1723>.
- [21] H. S. Carslaw and J. C. Jaeger. *Conduction of Heat in Solids*. Oxford University Press, London, 1959, pp. isbn:
- [22] Zhi Chen et al. "Synthesis and Characterization of Microencapsulated Paraffin Microcapsules as Shape-Stabilized Thermal Energy Storage Materials". In: *Nanoscale and Microscale Thermophysical Engineering* 17.2 (2013), pp. 112–123. doi: 10.1080/15567265.2012.761305. eprint: <https://doi.org/10.1080/15567265.2012.761305>. url: <https://doi.org/10.1080/15567265.2012.761305>.
- [23] Jae Dong Chung, Joon Sik Lee, and Hoseon Yoo. "Thermal instability during the melting process in an isothermally heated horizontal cylinder". In: *International Journal of Heat and Mass Transfer* 40.16 (1997), pp. 3899–3907. issn: 0017-9310. doi: [https://doi.org/10.1016/S0017-9310\(97\)00037-9](https://doi.org/10.1016/S0017-9310(97)00037-9). url: <http://www.sciencedirect.com/science/article/pii/S0017931097000379>.



- [24] M. Costa, D. Buddhi, and A. Oliva. "Numerical simulation of a latent heat thermal energy storage system with enhanced heat conduction". In: *Energy Conversion and Management* 39.3 (1998), pp. 319–330. issn: 0196-8904. doi: [https://doi.org/10.1016/S0196-8904\(96\)00193-8](https://doi.org/10.1016/S0196-8904(96)00193-8). url: <http://www.sciencedirect.com/science/article/pii/S0196890496001938>.
- [25] *Data sheet RT28HC Rubitherm*. en. url: [https://www.rubitherm.eu/media/products/datasheets/Techdata\\_-RT28HC\\_EN\\_31052016.PDF](https://www.rubitherm.eu/media/products/datasheets/Techdata_-RT28HC_EN_31052016.PDF) (visited on 07/04/2018).
- [26] "Design and optimization of PCM-air heat exchangers". In: *Virtual Concept Workshop 2016: Major Trends in product design*. 2016.
- [27] Nabeel S. Dhaidan and J.M. Khodadadi. "Melting and convection of phase change materials in different shape containers: A review". In: *Renewable and Sustainable Energy Reviews* 43 (2015), pp. 449–477. issn: 1364-0321. doi: <https://doi.org/10.1016/j.rser.2014.11.017>. url: <http://www.sciencedirect.com/science/article/pii/S1364032114009484>.
- [28] Jens H. Dieckmann. *Latent heat storage in concrete*. Eurosolar, 20006.
- [29] G.Poots D.S.Riley F.T.Smith. "The inward solidification of spheres and circular cylinders". In: *International Journal of Heat and Mass Transfer* 17.12 (1974), pp. 1507–1516. issn: doi: [https://doi.org/10.1016/0017-9310\(74\)90061-1](https://doi.org/10.1016/0017-9310(74)90061-1). url: ~.
- [30] Vadim Dubovsky, Gennady Ziskind, and Ruth Letan. "Analytical model of a PCM-air heat exchanger". In: *Applied Thermal Engineering* 31.16 (2011), pp. 3453–3462. issn: 1359-4311. doi: <https://doi.org/10.1016/j.applthermaleng.2011.06.031>. url: <http://www.sciencedirect.com/science/article/pii/S1359431111003413>.
- [31] Yvan Dutil et al. "A review on phase-change materials: Mathematical modeling and simulations". In: *Renewable and Sustainable Energy Reviews* 15.1 (2011), pp. 112–130. issn: 1364-0321. doi: <https://doi.org/10.1016/j.rser.2010.06.011>. url: <http://www.sciencedirect.com/science/article/pii/S1364032110001589>.
- [32] G. Ziskind E. Assis and R. Letan. "Numerical and Experimental Study of Solidification in a Spherical Shell". In: *J. Heat Transfer* 131.2 (2000), 5 pages. issn: 0021-9991. doi: <https://doi.org/10.1115/1.2993543>. url: <http://heattransfer.asmedigitalcollection.asme.org/article.aspx?articleid=1475014>.
- [33] T. A. Myrum E. M. Sparrow G. A. Gurtcheff. "Correlation of Melting Results for Both Pure Substances and Impure Substances". In: *Journal of Heat Transfer* 108. (), pp. 649–653. doi: ~. url: ~.
- [34] Hisham Ettouney, Hisham El-Dessouky, and Eman Al-Kandari. "Heat Transfer Characteristics during Melting and Solidification of Phase Change Energy Storage Process". In: *Industrial & Engineering Chemistry Research* 43.17 (2004), pp. 5350–5357. doi: 10.1021/ie030495b. eprint: <https://doi.org/10.1021/ie030495b>. url: <https://doi.org/10.1021/ie030495b>.
- [35] *European wood*. en. url: <http://www.europeanwood.org.cn/en/thermal-properties> (visited on 07/04/2018).
- [36] "Evaluation experimentale d'une strategie domotique de pilotage des elements mobiles : vers un controle semi-passif simple du confort d'ete en BEPos". In: *SFT 2018 Congres Francais de Thermique*. 2018.
- [37] "Experimental and computational study of constrained melting of phase change materials (PCM) inside a spherical capsule". In: *International Journal of Heat and Mass Transfer* 52. (2009), pp. 3464–3472. issn: 0017-9310. doi: 10.1016/j.ijheatmasstransfer.2009.02.043. url: ~.

- [38] “Experimental and numerical investigation of the cross-flow PCM heat exchanger for the energy saving of building HVAC Patcharapit”. In: *Energy and Buildings* 138. (), pp. 468–478. doi: <http://dx.doi.org/10.1016/j.enbuild.2016.12.043>. url: ~.
- [39] “Experimental investigation on heat transfer characteristics during melting of a phase change material with dispersed TiO<sub>2</sub> nanoparticles in a rectangular enclosure”. In: *J. Heat Transfer* 109 (2017), pp. 134–146. doi: <http://dx.doi.org/10.1016/j.jheatmasstransfer.2017.01.109>.
- [40] Mustapha Faraji and Hamid El Qarnia. “Numerical study of melting in an enclosure with discrete protruding heat sources”. In: *Applied Mathematical Modelling* 34.5 (May 2010), pp. 1258–1275. doi: <https://doi.org/10.1016/j.apm.2009.08.012>. url: <https://www.sciencedirect.com/science/article/pii/S0307904X09002431>.
- [41] M.M. FARID and A.K. MOHAMED. “EFFECT OF NATURAL CONVECTION ON THE PROCESS OF MELTING AND SOLIDIFICATION OF PARAFFIN WAX”. In: *Chemical Engineering Communications* 57.1-6 (1987), pp. 297–316. doi: 10.1080/00986448708960492. eprint: <https://doi.org/10.1080/00986448708960492>. url: <https://doi.org/10.1080/00986448708960492>.
- [42] Mohammed M. Farid and Rafah M. Husian. “An electrical storage heater using the phase-change method of heat storage”. In: *Energy Conversion and Management* 30.3 (1990), pp. 219–230. issn: 0196-8904. doi: [https://doi.org/10.1016/0196-8904\(90\)90003-H](https://doi.org/10.1016/0196-8904(90)90003-H). url: <http://www.sciencedirect.com/science/article/pii/019689049090003H>.
- [43] MOHAMMED FARID et al. “THE ROLE OF NATURAL CONVECTION DURING MELTING AND SOLIDIFICATION OF PCM IN A VERTICAL CYLINDER”. In: *Chemical Engineering Communications* 84.1 (1989), pp. 43–60. doi: 10.1080/00986448908940334. eprint: <https://doi.org/10.1080/00986448908940334>. url: <https://doi.org/10.1080/00986448908940334>.
- [44] Amy S. Fleischer. *Thermal Energy Storage Using Phase Change Materials*. Springer International Publishing, 2015, pp. X, 94. isbn: 978-3-319-20922-7. doi: 10.1007/978-3-319-20922-7.
- [45] Natesan Geetha and R. Velraj. “Passive cooling methods for energy efficient buildings with and without thermal energy storage – A review”. In: 2012.
- [46] Goodfellow *All the materials you need for Scientific and Industrial Research and Manufacturing*. en. url: <http://www.goodfellow.com/E/Polyethylene-terephthalate.html> (visited on 07/04/2018).
- [47] H. M. Ettouney H. T. El-Dessouky W. S. Bouhamra and M. Akbar. “Heat Transfer in Vertically Aligned Phase Change Energy Storage Systems”. In: *Journal of Solar Energy Engineering* (1999). issn: doi: <https://doi.org/10.1115/1.2888158>. url: <http://solarenergyengineering.asmedigitalcollection.asme.org/article.aspx?articleid=1455908&journalid=132>.
- [48] Afif Hasan. “Phase change material energy storage system employing palmitic acid”. In: *Solar Energy* 52.2 (1994), pp. 143–154. issn: doi: [https://doi.org/10.1016/0038-092X\(94\)90064-7](https://doi.org/10.1016/0038-092X(94)90064-7). url: <https://www.sciencedirect.com/science/article/pii/0038092X94900647>.
- [49] Afif Hasan. “Thermal energy storage system with stearic acid as phase change material”. In: *Solar Energy* 35.10 (1994), pp. 843–856. issn: doi: [https://doi.org/10.1016/0196-8904\(94\)90034-5](https://doi.org/10.1016/0196-8904(94)90034-5). url: <https://www.sciencedirect.com/science/article/pii/0196890494900345>.

- [50] D.W. Hawes, D. Feldman, and D. Banu. "Latent heat storage in building materials". In: *Energy and Buildings* 20.1 (1993), pp. 77–86. issn: 0378-7788. doi: [https://doi.org/10.1016/0378-7788\(93\)90040-2](https://doi.org/10.1016/0378-7788(93)90040-2). url: <http://www.sciencedirect.com/science/article/pii/0378778893900402>.
- [51] "Heat Transfer Characteristics during Melting and Solidification of Phase Change Energy Storage Process". In: *Ind. Eng. Chem.* 43.17 (2004), pp. 5350–5357. issn: 0360-5442. doi: ~. url: ~.
- [52] "Heat transfer during melting of graphene-based composite phase change materials heated from below". In: *International Journal of Heat and Mass Transfer* 79. (2014), pp. 94–104. issn: 0017-9310. doi: <http://dx.doi.org/10.1016/j.ijheatmasstransfer.2014.08.001>. url: ~.
- [53] C.-J. Ho and R. Viskanta. "Heat Transfer During Melting From an Isothermal Vertical Wall". In: *J. Heat Transfer* 106.1 (1984), 8 pages. issn: 0017-9310. doi: 10.1115/1.3246624. url: <http://heattransfer.asmedigitalcollection.asme.org/article.aspx?articleid=1438214>.
- [54] Henry Hu and Stavros A Argyropoulos. "Mathematical modelling of solidification and melting: a review". In: *Modelling and Simulation in Materials Science and Engineering* 4.4 (1996), p. 371. url: <http://stacks.iop.org/0965-0393/4/i=4/a=004>.
- [55] Thomas H. Sherer II and Yogendra Joshi. "NUMERICAL AND EXPERIMENTAL INVESTIGATION OF SHELL-AND-TUBE PHASE CHANGE MATERIAL THERMAL STORAGE UNIT". In: *Proceedings of the ASME 2015 International Technical Conference and Exhibition on Packaging and Integration of Electronic and Photonic Microsystems*. 20166. doi: 10.1115/1.4034101.
- [56] Peter Jany and Adrian Bejan. "Scaling theory of melting with natural convection in an enclosure". In: *International Journal of Heat and Mass Transfer* 31.6 (1988), pp. 1221–1235. issn: 0017-9310. doi: [https://doi.org/10.1016/0017-9310\(88\)90065-8](https://doi.org/10.1016/0017-9310(88)90065-8). url: <http://www.sciencedirect.com/science/article/pii/0017931088900658>.
- [57] Benjamin J. Jones et al. "Experimental and numerical study of melting in a cylinder". In: *International Journal of Heat and Mass Transfer* 49.15 (2006), pp. 2724–2738. issn: 0017-9310. doi: <https://doi.org/10.1016/j.ijheatmasstransfer.2006.01.006>. url: <http://www.sciencedirect.com/science/article/pii/S0017931006000573>.
- [58] Done Kim Jong Chan Choi Sang. "HEAT-TRANSFER CHARACTERISTICS OF A LATENT HEAT STORAGE SYSTEM USING  $MgCl_2 \cdot 6H_2O$ ". In: *Energy* 17 (1992), pp. 1153–1164. issn: 0360-5442. doi: [https://doi.org/10.1016/0360-5442\(92\)90004-J](https://doi.org/10.1016/0360-5442(92)90004-J). url: <https://www.sciencedirect.com/science/article/pii/036054429290004J>.
- [59] Simen Edsjø Kalnæs and Bjørn Petter Jelle. "Phase change materials and products for building applications: A state-of-the-art review and future research opportunities". In: *Energy and Buildings* 94 (2015), pp. 150–176. issn: 0378-7788. doi: <https://doi.org/10.1016/j.enbuild.2015.02.023>. url: <http://www.sciencedirect.com/science/article/pii/S0378778815001188>.
- [60] Maria das Graças E. da Silva Kamal A.R.Ismail. "Melting of PCM around a horizontal cylinder with constant surface temperature". In: *International Journal of Thermal Sciences* 42.12 (2003), pp. 1145–1152. issn: doi: [https://doi.org/10.1016/S1290-0729\(03\)00093-0](https://doi.org/10.1016/S1290-0729(03)00093-0). url: <https://www.sciencedirect.com/science/article/pii/S1290072903000930>.

- [61] Alibakhsh Kasaeian et al. "Experimental studies on the applications of PCMs and nano-PCMs in buildings: A critical review". In: *Energy and Buildings* 154 (2017), pp. 96–112. issn: 0378-7788. doi: <https://doi.org/10.1016/j.enbuild.2017.08.037>. url: <http://www.sciencedirect.com/science/article/pii/S0378778817321564>.
- [62] Wu Yong Ke and Lacroix Marcel. "Melting of a PCM inside a vertical cylindrical capsule". In: *International Journal for Numerical Methods in Fluids* 20.6 (), pp. 559–572. doi: 10.1002/flid.1650200610. eprint: <https://onlinelibrary.wiley.com/doi/pdf/10.1002/flid.1650200610>. url: <https://onlinelibrary.wiley.com/doi/abs/10.1002/flid.1650200610>.
- [63] W.A. Khan, J.R. Culham, and M.M. Yovanovich. "Convection heat transfer from tube banks in crossflow: Analytical approach". In: *International Journal of Heat and Mass Transfer* 49.25 (2006), pp. 4831–4838. issn: 0017-9310. doi: <https://doi.org/10.1016/j.ijheatmasstransfer.2006.05.042>. url: <http://www.sciencedirect.com/science/article/pii/S0017931006003796>.
- [64] G. Ziskind L. Katsman V. Dubovsky and R. Letan. "Experimental Investigation of Solid-Liquid Phase Change in Cylindrical Geometry". In: *ASME/JSME 2007 Thermal Engineering Heat Transfer Summer Conference collocated with the ASME 2007 InterPACK Conference*. 2007. doi: 10.1115/HT2007-32354.
- [65] *LAS PROPIEDADES DEL VIDRIO DE BOROSILICATO*. Spanish. url: <https://www.dedietrich.com/es/soluciones-y-productos/esmalte-vidrio-de-borosilicato/las-propiiedades-del-vidrio-de-borosilicato> (visited on 07/04/2018).
- [66] Martin Longeon et al. "Experimental and numerical study of annular PCM storage in the presence of natural convection". In: *Applied Energy* 112 (2013), pp. 175–184. issn: 0306-2619. doi: <https://doi.org/10.1016/j.apenergy.2013.06.007>. url: <http://www.sciencedirect.com/science/article/pii/S030626191300514X>.
- [67] Covadonga Loredó. "Conception, fabrication, mise à place et essais avec un prototype d'échangeur stockeur à base de MCP". Arts et Métiers ParisTech. MA thesis. 2014, pp.
- [68] J.A. Mackenzie and M.L. Robertson. "The Numerical Solution of One-Dimensional Phase Change Problems Using an Adaptive Moving Mesh Method". In: *Journal of Computational Physics* 161.2 (2000), pp. 537–557. issn: 0021-9991. doi: <https://doi.org/10.1006/jcph.2000.6511>. url: <http://www.sciencedirect.com/science/article/pii/S0021999100965112>.
- [69] Fariborz Haghghata Mahmood Mastani Joybari and Saeid Seddeghb. "Natural convection characterization during melting of phase change materials: Development of a simplified front tracking method". In: *Solar Energy* 158. (2017), pp. 711–720. issn: 0038-092X. doi: <http://dx.doi.org/10.1016/j.solener.2017.10.031>. url: <https://www.sciencedirect.com/science/article/pii/S0038092X17309015>.
- [70] *MANUAL DE USO MULTIFUNCIÓN AMI300*. Spanish. url: [https://www.midebien.com/\\_literature\\_127470/Multifunci%C3%B3n\\_AMI\\_300](https://www.midebien.com/_literature_127470/Multifunci%C3%B3n_AMI_300). (visited on 07/04/2018).
- [71] M. Mbaye and E. Bilgen. "Phase change process by natural convection–diffusion in rectangular enclosures". In: *Heat and Mass Transfer* 37.1 (Jan. 2001), pp. 35–42. issn: 1432-1181. doi: 10.1007/s002310000095. url: <https://doi.org/10.1007/s002310000095>.
- [72] *Meison Napevomo house*. en. url: <http://www.meison.fr/historique/> (visited on 08/10/2018).

- [73] A.H. Mosaffa et al. "Analytical modeling of PCM solidification in a shell and tube finned thermal storage for air conditioning systems". In: *Energy and Buildings* 49 (2012), pp. 356–361. issn: 0378-7788. doi: <https://doi.org/10.1016/j.enbuild.2012.02.053>. url: <http://www.sciencedirect.com/science/article/pii/S0378778812001478>.
- [74] *NI-9213 C Series Temperature Input Module*. en. url: <http://www.ni.com/en-us/support/model.ni-9213.html> (visited on 07/04/2018).
- [75] "Numerical investigation on the heat transfer enhancement of a latent heat thermal energy storage system with bundled tube structures". In: *Applied Thermal Engineering* 112. (2017), pp. 820–831. issn: 1359-4311. doi: <http://dx.doi.org/10.1016/j.ijheatmasstransfer.2012.05.043>. url: ~.
- [76] E. Osterman et al. "Review of PCM based cooling technologies for buildings". In: *Energy and Buildings* 49 (2012), pp. 37–49. issn: 0378-7788. doi: <https://doi.org/10.1016/j.enbuild.2012.03.022>. url: <http://www.sciencedirect.com/science/article/pii/S0378778812001703>.
- [77] M. Necati Ozisik. *Heat Conduction*. John Wiley and Sons, Inc, 1993, pp. isbn: 0-471-53256-8.
- [78] Suhas Patankar. *Numerical Heat Transfer and Fluid Flow*. CRC Press Taylor and Francis Group, 1980, 214 Pages. isbn: 9780891165224.
- [79] Claudio Del Pero et al. "Energy storage Key Performance Indicators for building application". In: *Sustainable Cities and Society* (2018). issn: 2210-6707. doi: <https://doi.org/10.1016/j.scs.2018.01.052>. url: <http://www.sciencedirect.com/science/article/pii/S2210670717313227>.
- [80] Maria Petrou and Costas Petrou. *Image Processing: The Fundamentals*. John Wiley and Sons, 2010, pp. isbn: 978-0-470-74586-1. doi: ~.
- [81] Patcharapit Promoppatum et al. "Experimental and numerical investigation of the cross-flow PCM heat exchanger for the energy saving of building HVAC". In: *Energy and Buildings* 138 (2017), pp. 468–478. issn: 0378-7788. doi: <https://doi.org/10.1016/j.enbuild.2016.12.043>. url: <http://www.sciencedirect.com/science/article/pii/S037877881631876X>.
- [82] "Proposed Modifications for Models of Heat Transfer Problems Involving Partially Melted Phase Change Processes". In: *Renewable and Sustainable Energy Reviews* 6 (2009), pp. 1–20. issn: 1546-962X. doi: <https://doi.org/10.1520/JAI102059>. url: [https://www.astm.org/DIGITAL\\_LIBRARY/JOURNALS/JAI/PAGES/JAI102059.htm](https://www.astm.org/DIGITAL_LIBRARY/JOURNALS/JAI/PAGES/JAI102059.htm).
- [83] M. Paolini R. H. Nochetto and C. Verdi. "An Adaptive Finite Element Method for Two-Phase Stefan Problems in Two Space Dimensions. II: Implementation and Numerical Experiments". In: *SIAM J. Sci. and Stat. Comput* 12.5 (1991), pp. 1207–1244. issn: 0196-5204. doi: <https://doi.org/10.1137/0912065>. url: <https://epubs.siam.org/doi/abs/10.1137/0912065>.
- [84] Banerjee Jyotirmay Rathod Manish K. "Development of correlation for melting time of phase change material in latent heat storage unit". In: *The 7th International Conference on Applied Energy – ICAE2015*. 2015. doi: ~.
- [85] A. Felix Regin, S.C. Solanki, and J.S. Saini. "Heat transfer characteristics of thermal energy storage system using PCM capsules: A review". In: *Renewable and Sustainable Energy Reviews* 12.9 (2008), pp. 2438–2458. issn: 1364-0321. doi: <https://doi.org/10.1016/j.rser.2007.06.009>. url: <http://www.sciencedirect.com/science/article/pii/S1364032107001001>.



- [86] Fabien Rouault. "Contribution to the thermal energy storage in building: development of an active system with materials with change of phase." PhD thesis. Arts et Métiers ParisTech, 2011.
- [87] Fabien Rouault. "Système intégré de rafraîchissement d'air pour le bâtiment à base de matériaux à changement de phase". PhD thesis. Arts et Métiers ParisTech, 2014.
- [88] *RT 21 HC*. en. url: [https://www.rubitherm.eu/media/products/datasheets/Techdata\\_RT21HC\\_EN\\_29062016.PDF](https://www.rubitherm.eu/media/products/datasheets/Techdata_RT21HC_EN_29062016.PDF) (visited on 08/10/2018).
- [89] *RT 28 HC*. en. url: [https://www.rubitherm.eu/media/products/datasheets/Techdata\\_RT28HC\\_EN\\_31052016.PDF](https://www.rubitherm.eu/media/products/datasheets/Techdata_RT28HC_EN_31052016.PDF) (visited on 08/10/2018).
- [90] M.C. Ruzicka. "On dimensionless numbers". In: *Chemical Engineering Research and Design* 86.8 (2008), pp. 835–868. issn: 0263-8762. doi: <https://doi.org/10.1016/j.cherd.2008.03.007>. url: <http://www.sciencedirect.com/science/article/pii/S0263876208000725>.
- [91] Menon A. S., Weber M. E., and Mujumdar A. S. "The dynamics of energy storage for paraffin wax in cylindrical containers". In: *The Canadian Journal of Chemical Engineering* 61.5 (), pp. 647–653. doi: 10.1002/cjce.5450610505. eprint: <https://onlinelibrary.wiley.com/doi/pdf/10.1002/cjce.5450610505>. url: <https://onlinelibrary.wiley.com/doi/abs/10.1002/cjce.5450610505>.
- [92] Saleh Nasser AL-Saadi and Zhiqiang (John) Zhai. "Modeling phase change materials embedded in building enclosure: A review". In: *Renewable and Sustainable Energy Reviews* 21 (2013), pp. 659–673. issn: 1364-0321. doi: <https://doi.org/10.1016/j.rser.2013.01.024>. url: <http://www.sciencedirect.com/science/article/pii/S1364032113000555>.
- [93] Andrew P. Sage and William B. Rouse. *Handbook of systems engineering and management*. John Wiley Sons, Inc, 2009, pp. xix, 1236. isbn: 0-471-15405-9.
- [94] Pramod B. Salunkhe and Prashant S. Shembekar. "A review on effect of phase change material encapsulation on the thermal performance of a system". In: *Renewable and Sustainable Energy Reviews* 16.8 (2012), pp. 5603–5616. doi: 10.1016/j.rser.2012.06.02. url: <https://ideas.repec.org/a/eee/rensus/v16y2012i8p5603-5616.html>.
- [95] Randall Schumacker and Sara Tomek. *Understanding Statistics Using R*. Springer-Verlag New York, 2013, pp. XVI, 292. isbn: 978-1-4614-6226-2. doi: 10.1007/978-1-4614-6227-9.
- [96] Paul-Antoine SERRAULT. *Intégration et Pilotage d'un système de refroidissement d'air à Matériaux à Changement de Phase dans un bâtiment à énergie positive : le cas de SUMBIOSI*. Arts et Métiers ParisTech, 2014.
- [97] Atul Sharma et al. "Review on thermal energy storage with phase change materials and applications". In: *Renewable and Sustainable Energy Reviews* 13.2 (2009), pp. 318–345. issn: 1364-0321. doi: <https://doi.org/10.1016/j.rser.2007.10.005>. url: <http://www.sciencedirect.com/science/article/pii/S1364032107001402>.
- [98] R. Letan Shmueli G. Ziskind. "Melting in a vertical cylindrical tube: Numerical investigation and comparison with experiments". In: *International Journal of Heat and Mass Transfer* 53. (), pp. 4082–4091. doi: ~. url: ~.
- [99] Nelson Soares. "Thermal energy storage with phase change materials (PCMs) for the improvement of the energy performance of buildings". Universidade de Coimbra. PhD thesis. 2015, 1 vol. (217 p.)

- [100] *Solar-Decathlon-2012-Casa-Sumbiosi-de-abc-Francia*. sp. url: <http://blog.is-arquitectura.es/2012/08/29/solar-decathlon-2012-casa-sumbiosi-de-abc-francia/> (visited on 08/10/2018).
- [101] Chris Solomon and Toby Breckon. *Fundamentals of Digital Image Processing: A Practical Approach with Examples in Matlab*. John Wiley and Sons, 2010. isbn: 978-0-470-84472-4.
- [102] Mengjie Song et al. “Review on building energy performance improvement using phase change materials”. In: *Energy and Buildings* 158 (2018), pp. 776–793. issn: 0378-7788. doi: <https://doi.org/10.1016/j.enbuild.2017.10.066>. url: <http://www.sciencedirect.com/science/article/pii/S037877881732916X>.
- [103] Farah Souayfane, Farouk Fardoun, and Pascal-Henry Biwole. “Phase change materials (PCM) for cooling applications in buildings: A review”. In: *Energy and Buildings* 129 (2016), pp. 396–431. issn: 0378-7788. doi: <https://doi.org/10.1016/j.enbuild.2016.04.006>. url: <http://www.sciencedirect.com/science/article/pii/S0378778816302419>.
- [104] E. M. Sparrow and J. A. Broadbent. “Inward Melting in a Vertical Tube Which Allows Free Expansion of the Phase-Change Medium”. In: *Journal of Heat Transfer* (1982). issn: doi: <https://doi.org/10.1115/1.3245089>. url: <http://heattransfer.asmedigitalcollection.asme.org/article.aspx?articleid=1437692>.
- [105] Uroš Stritih. “An experimental study of enhanced heat transfer in rectangular PCM thermal storage”. In: *International Journal of Heat and Mass Transfer* 47.12 (2004), pp. 2841–2847. issn: 0017-9310. doi: <https://doi.org/10.1016/j.ijheatmasstransfer.2004.02.001>. url: <http://www.sciencedirect.com/science/article/pii/S0017931004000365>.
- [106] Weiguang Su, Jo Darkwa, and Georgios Kokogiannakis. “Review of solid–liquid phase change materials and their encapsulation technologies”. In: *Renewable and Sustainable Energy Reviews* 48 (2015), pp. 373–391. issn: 1364-0321. doi: <https://doi.org/10.1016/j.rser.2015.04.044>. url: <http://www.sciencedirect.com/science/article/pii/S1364032115003147>.
- [107] G Sun and Z Zhang. “Mechanical strength of microcapsules made of different wall materials”. In: *International Journal of Pharmaceutics* 242.1 (2002), pp. 307–311. issn: 0378-5173. doi: [https://doi.org/10.1016/S0378-5173\(02\)00193-X](https://doi.org/10.1016/S0378-5173(02)00193-X). url: <http://www.sciencedirect.com/science/article/pii/S037851730200193X>.
- [108] N. H. S. Tay. “Numerical modeling of inward and outward melting of high temperature PCM in a vertical cylinder”. In: *AIP Conference Proceedings*. 2016. doi: 10.1063/1.4949137.
- [109] N.H.S. Tay, F. Bruno, and M. Belusko. “Experimental validation of a CFD and an  $\epsilon$ -NTU model for a large tube-in-tank PCM system”. In: *International Journal of Heat and Mass Transfer* 55.21 (2012), pp. 5931–5940. issn: 0017-9310. doi: <https://doi.org/10.1016/j.ijheatmasstransfer.2012.06.004>. url: <http://www.sciencedirect.com/science/article/pii/S0017931012004243>.
- [110] *Technical Information PLEXIGLAS*. en. url: <https://www.plexiglas.net/sites/lists/pm/documentsap/211-1-plexiglas-gs-xt-en.pdf> (visited on 07/05/2018).
- [111] S. Saeed Mostafavi Tehrani et al. “An Improved, Generalized Effective Thermal Conductivity Method for Rapid Design of High Temperature Shell-and-Tube Latent Heat Thermal Energy Storage Systems”. In: *Renewable Energy* (2018). issn: 0960-1481. doi: <https://doi.org/10.1016/j.renene.2018.08.038>. url: <http://www.sciencedirect.com/science/article/pii/S0960148118309881>.

- [112] “The calculation of variable heat flow in solids”. In: *Philosophical Transactions of the Royal Society of London A: Mathematical, Physical and Engineering Sciences* 240.813 (1946), pp. 1–57. issn: 0080-4614. doi: 10.1098/rsta.1946.0002. eprint: <http://rsta.royalsocietypublishing.org/content/240/813/1.full.pdf>. url: <http://rsta.royalsocietypublishing.org/content/240/813/1>.
- [113] Anica Trp. “An experimental and numerical investigation of heat transfer during technical grade paraffin melting and solidification in a shell-and-tube latent thermal energy storage unit”. In: *Solar Energy* 79.6 (2005). Polymeric Materials for Solar Energy Applications, pp. 648–660. issn: 0038-092X. doi: <https://doi.org/10.1016/j.solener.2005.03.006>. url: <http://www.sciencedirect.com/science/article/pii/S0038092X05001337>.
- [114] Ulises Valverde. “Méthodologie d’aide à l’innovation par l’exploitation des brevets et des phénomènes physiques impliqués”. Arts et Métiers ParisTech. PhD thesis. 2015, 1 vol. (184 p.)
- [115] Conrad Voelker, Oliver Kornadt, and Milan Ostry. “Temperature reduction due to the application of phase change materials”. In: *Energy and Buildings* 40.5 (2008), pp. 937–944. issn: 0378-7788. doi: <https://doi.org/10.1016/j.enbuild.2007.07.008>. url: <http://www.sciencedirect.com/science/article/pii/S0378778807002034>.
- [116] V. R. Voller. “FAST IMPLICIT FINITE-DIFFERENCE METHOD FOR THE ANALYSIS OF PHASE CHANGE PROBLEMS”. In: *Numerical Heat Transfer, Part B: Fundamentals* 17.2 (1990), pp. 155–169. doi: 10.1080/10407799008961737. eprint: <https://doi.org/10.1080/10407799008961737>. url: <https://doi.org/10.1080/10407799008961737>.
- [117] E.M. Sparrow W. Minkowycz. *Advances In Numerical Heat Transfer*. Taylor and Francis Group, 1997, pp. isbn: 1-56032-441-4.
- [118] Adeel Waqas and Zia Ud Din. “Phase change material (PCM) storage for free cooling of buildings—A review”. In: *Renewable and Sustainable Energy Reviews* 18 (2013), pp. 607–625. issn: 1364-0321. doi: <https://doi.org/10.1016/j.rser.2012.10.034>. url: <http://www.sciencedirect.com/science/article/pii/S136403211200576X>.
- [119] R. Werner. “Compatibility of organic latent heat storage materials and plastic container materials”. In: *Heat Recovery Systems and CHP* 7.4 (1987), pp. 383–388. issn: 0890-4332. doi: [https://doi.org/10.1016/0890-4332\(87\)90101-3](https://doi.org/10.1016/0890-4332(87)90101-3). url: <http://www.sciencedirect.com/science/article/pii/0890433287901013>.
- [120] K. Vafai Y. Wang A. Amiri. “An experimental investigation of the melting process in a rectangular enclosure”. In: *International Journal of Thermal Sciences* 42. (2003), pp. 3659–3672. issn: doi: ~. url: ~.
- [121] Belén Zalba et al. “Free-cooling of buildings with phase change materials”. In: *International Journal of Refrigeration* 27.8 (2004), pp. 839–849. issn: 0140-7007. doi: <https://doi.org/10.1016/j.ijrefrig.2004.03.015>. url: <http://www.sciencedirect.com/science/article/pii/S0140700704000623>.
- [122] Rami Zeinelabdein, Siddig Omer, and Guohui Gan. “Critical review of latent heat storage systems for free cooling in buildings”. In: *Renewable and Sustainable Energy Reviews* 82 (2018), pp. 2843–2868. issn: 1364-0321. doi: <https://doi.org/10.1016/j.rser.2017.10.046>. url: <http://www.sciencedirect.com/science/article/pii/S1364032117314223>.

- [123] Yuwen Zhang et al. "Melting in an enclosure with discrete heating at a constant rate". In: *Experimental Thermal and Fluid Science* 6.2 (1993), pp. 196–201. issn: 0894-1777. doi: [https://doi.org/10.1016/0894-1777\(93\)90029-I](https://doi.org/10.1016/0894-1777(93)90029-I). url: <http://www.sciencedirect.com/science/article/pii/089417779390029I>.
- [124] G. Ziskind. "12 - Modelling of heat transfer in phase change materials (PCMs) for thermal energy storage systems". In: *Advances in Thermal Energy Storage Systems*. Ed. by Luisa F. Cabeza. Woodhead Publishing Series in Energy. Woodhead Publishing, 2015, pp. 307–324. isbn: 978-1-78242-088-0. doi: <https://doi.org/10.1533/9781782420965.2.307>. url: <http://www.sciencedirect.com/science/article/pii/B9781782420880500122>.
- [125] B. Zivkovic and I. Fujii. "An analysis of isothermal phase change of phase change material within rectangular and cylindrical containers". In: *Solar Energy* 70.1 (2001), pp. 51–61. issn: 0038-092X. doi: [https://doi.org/10.1016/S0038-092X\(00\)00112-2](https://doi.org/10.1016/S0038-092X(00)00112-2). url: <http://www.sciencedirect.com/science/article/pii/S0038092X00001122>.
- [126] A. Žukauskas. "Heat Transfer from Tubes in Crossflow". In: ed. by James P. Hartnett and Thomas F. Irvine. Vol. 8. *Advances in Heat Transfer*. Elsevier, 1972, pp. 93–160. doi: [https://doi.org/10.1016/S0065-2717\(08\)70038-8](https://doi.org/10.1016/S0065-2717(08)70038-8). url: <http://www.sciencedirect.com/science/article/pii/S0065271708700388>.





# List of Tables

1.1	Overview of the advantages and disadvantages of each PCM group of materials (developed by Kalnæs and Jelle). . . . .	21
1.2	Summary of developed correlations for melting and solidification for PCM. . .	34
2.1	Key parameters obtained from the physical phenomena analysis at the global domain of the air-PCM heat exchanger. . . . .	47
2.2	Key parameters obtained from the physical phenomena analysis at the local domain of the air-PCM heat exchanger. . . . .	48
2.3	Summary of the life stages during the active periods at the external level of the system. . . . .	50
2.4	Initial set of keywords for the query. . . . .	51
2.5	Keyword database for air-PCM heat exchangers (Part I). . . . .	53
2.6	Keyword database for air-PCM heat exchangers (Part II). . . . .	54
2.7	Key parameters selected from the physical phenomena analysis. . . . .	56
2.8	Physical contradiction when comparing the objectives of the system. . . . .	57
3.1	Main Assumptions for experiments. . . . .	65
3.2	Principal thermal properties of the materials used during the experiments. . .	67
3.3	Thermophysical properties of PCM Rubitherm®RT28HC. . . . .	69
3.4	Correlation coefficients for the expressions developed by Žukauskas [126]. . .	74
3.6	Visual evolution of phase change during the melting cycle. . . . .	80
3.7	Visual evolution of phase change during the melting cycle . . . . .	81
3.8	Visual evolution of phase change during the melting cycle. . . . .	82
3.9	Visual evolution of phase change during the melting cycle. . . . .	83
3.5	Temperature results from the melting cycle. . . . .	88
3.10	Visual evolution of phase change during the melting cycle. . . . .	89
3.11	Temperature results during the solidification cycle. . . . .	90
3.12	Visual evolution of phase change during the melting cycle. . . . .	91
3.13	Visual evolution of phase change during the melting cycle. . . . .	92
3.14	Values obtained from the data processing at the global domain. . . . .	102

---

3.15	Correction of values for the sources of noise during the image processing. . . .	108
3.16	Dimensionless values ranges form experiments and phenomena identification.	114
4.1	Melting fraction correlation $\mathcal{C} \cdot [\mathcal{F}oSte]^{0,68}$ for the first region (conduction). . .	119
4.2	Melting fraction correlation $\mathcal{C} \cdot \mathcal{F}o^{2,97} \cdot Ste^{0,95} \cdot Ra^{0,046}$ for the second region (conduction). . . . .	120
D.1	Short-term mass degradation (during 6 month) . . . . .	203

# List of Figures

r.i	Analyse fonctionnelle du système. . . . .	xxvi
r.ii	Analyse des phénomènes physiques en deux domaines : global et local. . . . .	xxvi
r.iii	Contradictions physiques associés à la conception. . . . .	xxvi
r.iv	Synthèse de résultats des expériences a l'échelle a) Globale et b) Locale. . . . .	xxviii
r.v	Synthèse de résultats des expériences à l'échelle a) Globale et b) Locale. . . . .	xxix
r.vi	Synthèse de résultats de la modélisation à l'échelle a) Locale et b) Globale. . . . .	xxx
r.vii	Test en application « maison » avec les résultats pour la journée du 22 août 2017. . . . .	xxx
i.8	World overview of the total final consumption by sector. The residential sector ranked third in 2015 (22%). . . . .	7
i.9	World CO <sub>2</sub> emissions from fuel combustion by sector, 2015. . . . .	7
i.10	Comparison of the heat storage capacity between construction materials and some commercial PCM. . . . .	8
i.11	Potential peak load shifting and energy savings due to the use of PCM in building applications. . . . .	8
i.12	Napevomo house at the Solar Decathlon competition. . . . .	10
i.13	Principle of operation of the air cooling system using PCM at the Napevomo house. . . . .	10
i.14	One box shape tube bundle containing the PCM. . . . .	11
i.15	The view of an open heat exchanger and a closed heat exchanger connected to an air network. . . . .	11
i.16	Sumbiosi house at the Solar Decathlon Europe 2012. . . . .	11
i.17	LHTES test bench used in the Sumbiosi house. . . . .	11
i.18	Operation principle of the Sumbiosi House during the Solar Decathlon 2012. . . . .	12
i.19	PCM system embeded in the Sumbiosi house wall at the IUT campus in Bordeaux. . . . .	12
i.20	Plastic bags used as PCM containers [67]. . . . .	13
i.21	Evolution line of the LHTES systems developed by the I2M laboratory [26]. . . . .	13
i.22	Axes of research and thesis structure. . . . .	14
i.23	Scientific approaches for the development of the present work. . . . .	15

1.1	Classification of latent heat storage materials. . . . .	19
1.2	Different types of PCM according to their melting temperature and enthalpy. . . . .	20
1.3	Thermal conductivity distribution for different types of PCM. . . . .	20
1.4	A typical control volume grid for finite difference methods [125]. . . . .	30
1.5	A typical control volume grid for finite volume methods [92]. . . . .	30
1.6	Photographic study on melting about an embedded horizontal heating cylinder performed by Wahed. . . . .	35
1.7	Representation of the melting shapes and time history performed by Sparrow et al. . . . .	35
1.8	Instantaneous photographs of the melting of paraffin wax inside a horizontal cylindrical capsule performed by Regin et al. . . . .	35
1.9	Photographs taken during the melting of wax within the cylindrical enclosure for a wall temperature at four different times performed by Jones et al. . . . .	36
1.10	Typical melting patterns in a narrow tube found by Katsman. . . . .	36
1.11	Instantaneous photographs of the melting of PCM inside the spherical capsule performed by Tan et al. . . . .	36
1.12	Simulated density distributions and vector maps vs. experimental images performed by Shmueli et al. . . . .	37
1.13	Colormaps of the temperature field and image of the melting of PCM performed by Bashar. . . . .	37
1.14	Experimental system for validation of the modeling developed by Sherer. . . . .	37
1.15	Real scale prototype of the phase change material heat exchanger used by Promapatum. . . . .	37
1.16	Intensity image and Canny segmentation filter by Bergounioux. . . . .	39
1.17	Simple thresholding versus hysteresis thresholding by Petrou and Petrou. . . . .	39
2.1	Architectural scheme of the principal parts of an air-PCM heat exchanger for cooling applications in buildings: external inputs, air-PCM system and the outlet; and the boundaries of the system (dashed lines). . . . .	49
2.2	Lines of evolution of the container shape related to the two main objectives, line 1: heat transfer and, line 2: Storage capacity. . . . .	58
2.3	Final design: tube bundle heat exchanger with cylindrical tubes of small diameter, using PCM as heat storage media. . . . .	59
2.4	Evolution of the air-PCM heat exchangers at the I2M laboratory. . . . .	59
3.1	Physical domains for experiments: the building domain, the global domain, which represents the air-PCM heat exchanger unit, and the local domain, which represents the PCM tube. . . . .	63
3.2	Physical phenomena to identify through the experiments at the global and local domain. Codes: <i>FC</i> : forced convection, <i>NC</i> : natural convection, <i>Cond</i> : conduction. . . . .	64

3.3	Parameters proposed to be measured during the experiments at the global and local domain. In red are represented the input parameters of the experiments and in blue the outputs of the experiments. . . . .	64
3.4	Top view of the proposed experimental setup in the test room: a) inlet air duct b) outlet air duct, c) fan, d) air heating coil, e) mobile air conditioner, f) the diffuser, g) the nozzle, h) heat exchanger module, i) wooden box j) the tube bundle. . .	66
3.5	Geometric features of the test bench: a) “In-line” arrangement of 99 tubes and b) Longitudinal pitches for the geometric arrangement of the heat exchanger. . .	67
3.6	Setting-up of the test bench: a) installment of fastening screws in the wooden structure, and b) glass tubes installment inside the test bench. . . . .	67
3.7	Characterization of paraffin Rubitherm®RT28HC by DSC performed at a rate of $1,5\text{ }^{\circ}\text{C}\cdot\text{min}^{-1}$ . Color code: magenta: rise and lime-green: fall. . . . .	68
3.8	Metrology used on the test bench for temperature measurement: a) Type K thermocouple, b) thermocouple located at the center of the tube, c) view of a tube with thermocouples, d) instrumented tube within the test bench. . . . .	70
3.9	Metrology used on the test bench: a)AMI 300 KIMO ®airflow measurement kit [70], and b) National Instruments ®NI 9312 data acquisition for temperature measurements [74]. . . . .	70
3.10	Aerial view of the experimental setup in the test room where it can be observed: a) fan, b) air heating coil, c) airflow controller, d) an air duct, e) IRIS (pressure), f) diffuser, g) air-PCM heat exchanger, h) computer, i) data acquisition system, j) nozzle. . . . .	71
3.11	Air velocity cartography of the heat exchanger cross-section: a) scheme of the 25 measurement points and, b) scheme of the measurement points (blue dots) at the nozzle of the test bench. . . . .	72
3.12	Results of velocity field distribution $v_{air}(x,y)$ at the upstream cross-area of the test bench ( $0,3\times 0,4\text{ m}^2$ ) for an airflow of $533\text{ m}^3\cdot\text{h}^{-1}$ ( $T_{air}=22^{\circ}\text{C}$ ). . . . .	73
3.13	Characterization of the airflow rates according to the position of the rheostat in the fan with: the hot wire anemometer in magenta, ( <i>HW</i> ) and the vane probe in yellow, ( <i>VP</i> ). . . . .	75
3.14	Convective heat transfer coefficient obtained by theoretical correlation ( <i>Kahn</i> ), in purple; and by empirical correlation ( <i>Žukauskas</i> ), in mustard. . . . .	75
3.15	Location of the thermocouples within the test bench. The tubes in color blue represent those to whom four thermocouples have been integrated measuring $T_{air}$ , $T_{ow}$ , $T_{iw}$ , and $T_{pcm}$ ; in yellow those tubes to whom two thermocouples have been integrated measuring $T_{air}$ , and $T_{pcm}$ . . . . .	76
3.19	$t = 0\text{ min}$ . . . . .	80
3.20	$t = 30\text{ min}$ . . . . .	80
3.21	$t = 60\text{ min}$ . . . . .	80
3.22	$t = 90\text{ min}$ . . . . .	81
3.23	$t = 120\text{ min}$ . . . . .	81
3.24	$t = 150\text{ min}$ . . . . .	81
3.25	$t = 175\text{ min}$ . . . . .	82



3.26 $t = 245$ min . . . . .	82
3.27 $t_{final}$ . . . . .	82
3.28 $t = 15$ min . . . . .	83
3.29 $t = 20 - 30$ min . . . . .	83
3.33 PCM temperature measurements $T_{pcm_1}$ for the tube <sub>1</sub> located on the first row near the plexiglas®side. Each purple point represents a visual remark during phase change. . . . .	85
3.16 Global (inlet-outlet) and local (tube8 <sub>c</sub> ) domains temperature profiles. . . . .	88
3.17 Air temperatures vs tube position . . . . .	88
3.18 PCM temperature . . . . .	88
3.30 $t = 50 - 90$ min. . . . .	89
3.31 $t = 110 - 150$ min. . . . .	89
3.32 $t = 180 - 193$ min. . . . .	89
3.34 Global (inlet-outlet) and local (tube8 <sub>c</sub> ) domains temperature profiles. . . . .	90
3.35 Air temperatures vs tube position. . . . .	90
3.36 PCM temperatures per tube position. . . . .	90
3.37 $t = 0$ . . . . .	91
3.38 $t = 13$ min . . . . .	91
3.39 $t = 110 - 150$ min. . . . .	91
3.40 $t = 45$ min. . . . .	92
3.41 $t = t_{final}$ . . . . .	92
3.42 Thermal circuit proposed for the data treatment approaches on the local domain. . . . .	95
3.43 Thermal circuit proposed for the data treatment approaches on the local domain. . . . .	97
3.44 Cooling power for different inlet airflows in the heat exchanger with $T_{air_{in}} = 32^\circ\text{C}$ . Purple: $540 \text{ m}^3 \cdot \text{h}^{-1}$ , orange: $453 \text{ m}^3 \cdot \text{h}^{-1}$ , lime-green: $344 \text{ m}^3 \cdot \text{h}^{-1}$ , magenta: $243 \text{ m}^3 \cdot \text{h}^{-1}$ , and yellow: $196 \text{ m}^3 \cdot \text{h}^{-1}$ . . . . .	99
3.45 Temporal effectiveness for different inlet airflows during a heating cycle in the heat exchanger with $T_{air_{in}} = 22^\circ\text{C}$ . Purple: $540 \text{ m}^3 \cdot \text{h}^{-1}$ , orange: $453 \text{ m}^3 \cdot \text{h}^{-1}$ , lime-green: $344 \text{ m}^3 \cdot \text{h}^{-1}$ , magenta: $243 \text{ m}^3 \cdot \text{h}^{-1}$ , and yellow: $196 \text{ m}^3 \cdot \text{h}^{-1}$ . . . . .	99
3.46 Heating power for different inlet airflows during a cooling cycle in the heat exchanger with $T_{air_{in}} = 22^\circ\text{C}$ . Purple: $540 \text{ m}^3 \cdot \text{h}^{-1}$ , orange: $453 \text{ m}^3 \cdot \text{h}^{-1}$ , lime-green: $344 \text{ m}^3 \cdot \text{h}^{-1}$ , magenta: $243 \text{ m}^3 \cdot \text{h}^{-1}$ , and yellow: $196 \text{ m}^3 \cdot \text{h}^{-1}$ . . . . .	100
3.47 Temporal effectivenessr for different inlet airflows during a heating cycle in the heat exchanger with $T_{air_{in}} = 22^\circ\text{C}$ . Purple: $540 \text{ m}^3 \cdot \text{h}^{-1}$ , orange: $453 \text{ m}^3 \cdot \text{h}^{-1}$ , lime-green: $344 \text{ m}^3 \cdot \text{h}^{-1}$ , magenta: $243 \text{ m}^3 \cdot \text{h}^{-1}$ , and yellow: $196 \text{ m}^3 \cdot \text{h}^{-1}$ . . . . .	101
3.48 Time operation prediction for five test carried out in the test bench. <i>Color code</i> : black point: measured $\Delta t_{op_m}$ , black asterisk: measured $\Delta t_{op_s}$ , red dots: predicted $\Delta t_{op_m}$ , blue dots: predicted $\Delta t_{op_m}$ . . . . .	103

3.49	Distribution of the errors for the linear regression obtained for $\Delta t_{op_m}$ and measured $\Delta t_{op_s}$ , where for melting cycle RMSE = 25,47 min and for solidification cycle RMSE = 37,46 min. . . . .	103
3.50	Heat flux entering the tubes by thermal heat energy balance in the local domain for an airflow of $\dot{V}_{air} = 193 \text{ m}^3 \cdot \text{h}^{-1}$ and a $T_{air_{in}} = 32 \text{ }^\circ\text{C}$ . <i>Color codes:</i> Purple: tube in the middle of the fifth line, orange: tube in the middle of the eighth line, lime-green: tube in the middle of the eighth line, magenta: tube in the eighth line near the plexiglas®side of the heat exchanger. . . . .	104
3.51	Melting fraction by thermal heat energy balance in the local domain for an airflow of $\dot{V}_{air} = 193 \text{ m}^3 \cdot \text{h}^{-1}$ and a $T_{air_{in}} = 32 \text{ }^\circ\text{C}$ . <i>Color codes:</i> Purple: tube in the middle of the fifth line, orange: tube in the middle of the eighth line, lime-green: tube in the middle of the eighth line, magenta: tube in the eighth line near the plexiglas®side of the heat exchanger. . . . .	105
3.52	Solid-Liquid interface position from an 1D radial model approach for a tests carried out under the following conditions: $\dot{V}_{air} = 193 \text{ m}^3 \cdot \text{h}^{-1}$ and a $T_{air_{in}} = 32 \text{ }^\circ\text{C}$ . <i>Color codes:</i> Purple: tube in the middle of the fifth line, orange: tube in the middle of the eighth line, lime-green: tube in the middle of the eighth line, magenta: tube in the eighth line near the plexiglas®side of the heat exchanger . . . . .	105
3.53	Image processing of tube <sub>1</sub> at $t = 144$ min from the beginning of the cycle: a) RGB image $I(x, y)$ , b) gray-scale image $BW(x, y)$ , c) image with Gaussian filter $I_{blur}(x, y)$ , d) binary image after thresholding $BN(x, y)$ , e) edge detection of the image with the Canny filter, and e) inverse image of the edge detection. . . . .	106
3.54	Noise detection and correction for an image of tube <sub>8c</sub> at $t = 214$ min from the beginning of the cycle: a) noise identification in the original image $I(x, y)$ and after thresholding $BN(x, y)$ ; b) representative scheme of the image mapping process: the gray colored pixels represents the noise, and after the mapping their value correspond to the opposite. . . . .	108
3.55	$t = 0$ Image processing for the tubes during the melting of PCM for a test carried out under the following conditions: $\dot{m}_{air} = 193 \text{ m}^3 \cdot \text{h}^{-1}$ and a $T_{air_{in}} = 32 \text{ }^\circ\text{C}$ . Left: Tube and right: Tube. Each figure present the original RGB image, the image processed using the threshold of intensity technique and the Canny filter technique. . . . .	109
3.56	$t = 144$ min. Image processing for the tubes during the melting of PCM for a test carried out under the following conditions: $\dot{V}_{air} = 193 \text{ m}^3 \cdot \text{h}^{-1}$ and a $T_{air_{in}} = 32 \text{ }^\circ\text{C}$ . Left: Tube and right: Tube. Each figure present the original RGB image, the image processed using the threshold of intensity technique and the Canny filter technique. . . . .	109
3.57	$t = 186$ min. Image processing for the tubes during the melting of PCM for a test carried out under the following conditions: $\dot{V}_{air} = 193 \text{ m}^3 \cdot \text{h}^{-1}$ and a $T_{air_{in}} = 32 \text{ }^\circ\text{C}$ . Left: Tube and right: Tube. Each figure present the original RGB image, the image processed using the threshold of intensity technique and the Canny filter technique. . . . .	110
3.58	$t = 203$ min. Image processing for the tubes during the melting of PCM for a test carried out under the following conditions: $\dot{V}_{air} = 193 \text{ m}^3 \cdot \text{h}^{-1}$ and a $T_{air_{in}} = 32 \text{ }^\circ\text{C}$ . Left: Tube and right: Tube. Each figure present the original RGB image, the image processed using the threshold of intensity technique and the Canny filter technique. . . . .	110

3.59	Melting fraction within tubes with PCM. <i>Left</i> : the tube <sub>1</sub> , in lime-green; and tube <sub>8c</sub> , in magenta, obtained by image processing. <i>Right</i> : Comparison between the tube <sub>8c</sub> obtained from image processing, in lime-green, and tube <sub>8c</sub> obtained by energy balance in purple, for an inlet airflow of 193 m <sup>3</sup> ·h <sup>-1</sup> . . . . .	111
4.1	Melting fraction profile evolution for different $Re$ values. The dashed line highlights a sudden change in the behavior of the melting fraction. . . . .	116
4.2	Correlation chart between the explanatory variables $Ste$ , $Ra$ , and $Fo$ , and the melting fraction $m_f$ resulting from the statistical tests performed prior to obtaining the correlations. . . . .	118
4.3	Melting fraction correlation $4,3 \cdot [FoSte]^{0,68}$ for the first region (conduction) and $4,3 \cdot Fo^{2,97} \cdot Ste^{0,95} \cdot Ra^{0,046}$ for the second region (conduction and convection); for a $Re = 7670$ . . . . .	119
4.4	Global domain proposed for the modeling of an air-PCM heat exchanger. The inlet is given by the indoor conditions of the room and the outlet conditions are the air-cooling contribution of the exchanger to the room. . . . .	121
4.5	Local discretization of an air-PCM heat exchanger. In here three media interact: the air surrounding the tube, the wall of this tube and the PCM. . . . .	121
4.6	Discretization of the global domain by a row of tubes. . . . .	122
4.7	Algorithm of the 1-D model. . . . .	127
4.8	Reduction of the physical domains into the modeling domains. . . . .	128
4.9	Ratio of the melting front position to the internal radii of the tube $r(t)/r_{iw}$ regarding the time step selection, where the number represents the time in seconds. Larger differences are observed at the end of the cycle. . . . .	128
4.10	Ratio of the melting front position to the internal radii of the tube $r(t)/r_{iw}$ regarding the tube position, where each line represents a row of the heat exchanger. . . . .	129
4.11	Ratio of the melting front position to the internal radii of the tube $r(t)/r_{iw}$ for a tube located in the first row: by the image processing (blue) and the model (yellow). . . . .	130
4.12	Ratio of the melting front position to the internal radii of the tube $r(t)/r_{iw}$ for a tube located in the eighth row: by the image processing (magenta), the experimental measurements (purple) and the model (yellow). . . . .	131
4.13	Absolute error, relative error and RMSE between the melting front position $r(t)_{exp}$ obtained by experiments $m_{f-8exp}$ , and the melting fraction obtained by the model $r(t)_{model}$ for a tube located in the eighth row. . . . .	131
4.14	Melting fraction obtained by the image processing (magenta), the experimental measurements (purple) and the model (yellow) for a tube located in the eighth row. . . . .	132
4.15	Absolute error, relative error and RMSE between the melting fraction obtained by experiments $m_{f-8exp}$ , and the melting fraction obtained by the model $m_{f8-model}$ for a tube located in the eighth row. . . . .	132

4.16	Comparison between the experimental and modeled temperatures for the inlet and outlet positions of the heat exchanger. Inlet temperature in magenta: measurement (solid line) and model (dashed line). Outlet temperature in orange: measurement (solid line) and model(dashed line). . . . .	133
4.17	Comparison between the experimental and modeled temperatures for the inlet and outlet positions of the heat exchanger. Inlet temperature in magenta: measurement (solid line) and model (dashed line). Outlet temperature in orange: measurement (solid line) and model(dashed line). . . . .	134
4.18	Comparison between the experimental and modeled cooling power of the heat exchanger: experimental (yellow), and modeling (lime-green). . . . .	134
4.19	Reduction of the physical domains into the modeling domains. . . . .	135
5.1	Designs of the PET tubes proposed as PCM containers. . . . .	142
5.2	Scheme of the plans in Catia®: a) structure of the unit, b)upper top cover of the structure c) inlet of the exchanger with holes for the fans, and d) plates for the tubes. . . . .	144
5.3	Fabrication of the unit: a) Folding of the metallic structure. b) Principal piece of the structure, c) final air-PCM unit. . . . .	145
5.4	Experimental setup installed at one I2M office: a) air temperature at 2,12 m, b) air-temperature at 1,62 m, c) air temperature at 0,72 m (height of the people sitting), d) portable air conditions, e) hot air exhaust ducting, f) air-PCM unit, g) data acquisition, h,i), photo shooting points, j) computer. . . . .	146
5.5	Temperatures profile during the solidification assisted by an portable air-conditioner in July 16, 2016. <i>Color Code</i> : Purple: Indoor air temperature ( $T_{in}$ ), magenta: air temperature at the first third of the unit ( $T_{1/3}$ ), orange: air temperature at the second third of the unit ( $T_{2/3}$ ), yellow: air temperature at the outlet of the unit ( $T_{out}$ ), lime-green: air temperature at the lower part of the outlet ( $T_{out_{low}}$ ). The circled part represent the moment when we changed the water tank. . . . .	147
5.6	Temperatures profile during the solidification assisted by an portable air-conditioner in July 16, 2016. <i>Color Code</i> : Purple: Indoor air temperature ( $T_{in}$ ), magenta: air temperature at the first third of the unit ( $T_{1/3}$ ), orange: air temperature at the second third of the unit ( $T_{2/3}$ ), yellow: air temperature at the outlet of the unit ( $T_{out}$ ), lime-green: air temperature at the lower part of the outlet ( $T_{out_{low}}$ ). . . . .	148
5.7	Visual results of the solidification cycle of the PCM during a test performed at the I2M laboratory: a) at the beginning of the cycle (liquid state), and at the end of the cycle (solid state). . . . .	148
5.8	Temperatures profile during the standby period an melting of PCM during July 17, 2016. <i>Color Code</i> : Purple: Indoor air temperature ( $T_{in}$ ), magenta: air temperature at the first third of the unit ( $T_{1/3}$ ), orange: air temperature at the second third of the unit ( $T_{2/3}$ ), yellow: air temperature at the outlet of the unit ( $T_{out}$ ), lime-green: air temperature at the lower part of the outlet ( $T_{out_{low}}$ ). . . . .	149
5.9	Visual results of the melting cycle of the PCM during a test performed at the I2M laboratory: a) at the beginning of the cycle (solid state), and at the end of the cycle (liquid state). . . . .	149

5.10	Experimental platform schematic. Left: West-side view of the house showing the location of the unit inside the house and sensors distribution. Right: Top view of the house. The colored dots symbolize the position of the temperature and velocity sensors. . . . .	150
5.11	Natural ventilation strategies apply to the PEH Sumbiosi. . . . .	151
5.12	Air-PCM unit located near the south façade of at 0,7 m high from the floor: a) openings, b) power source, c) inlet, d) heat flux meters at the plexiglas® side, e) outlet temperature measurement, and f) airspeed measurement at the outlet. . . . .	152
5.13	Location of the thermocouples within the air-PCM unit: a) view of the plane of the unit. b) real location within the unit. . . . .	152
5.14	Weather forecast for Gradignan, France (consulted on August 14th, 2017). . . . .	153
5.15	Indoor and outdoor temperatures profile from August 22 <sup>nd</sup> to August 24 <sup>th</sup> , 2017. The gray area represent the period when the air-PCM unit was on, and the orange area, when the coupled natural ventilation- air-PCM strategy was on. . . . .	153
5.16	Temperatures profile for the air-PCM heat exchanger, including the PCM temperatures, during August 22 <sup>nd</sup> , 2017. . . . .	154
5.17	Temperatures profile for the air-PCM heat exchanger, including the PCM temperatures, during August 24 <sup>th</sup> , 2017. . . . .	155
A.1	Calibration process of the thermocouples. <i>Left</i> : thermocouples inside the thermostatic water bath LAUDA ECO SILVER RE 415 G . <i>Right</i> : display of the data acquisition with LabVIEW SignalExpress software from National Instruments®. . . . .	186
A.2	Statistical Dispersion on Thermocouples. . . . .	186
A.3	Statistical Dispersion on Thermocouples for the air-PCM unit tests. . . . .	187
A.4	Air velocity measured with the vane probe for the heat exchanger without tubes. . . . .	187
A.5	Airflow values obtained from the hot wire anemometer and the vane probe for the heat exchanger with tubes. . . . .	188
A.6	Comparison between the airflow values obtained from the hot wire anemometer and the vane probe for the heat exchanger with tubes. . . . .	188
B.1	Algorithm proposed to find the melting correlation using the function manipulate of R. . . . .	189
B.2	Melting fraction correlation $3,04 \cdot [FoSte]^{0,68}$ for the first region (conduction) and $0,89 \cdot Fo^{2,97} \cdot Ste^{0,95} \cdot Ra^{0,046}$ for the second region (conduction and convection); for a $Re = 11496$ . . . . .	190
B.3	Melting fraction correlation $3,21 \cdot [FoSte]^{0,68}$ for the first region (conduction) and $3,21 \cdot Fo^{2,97} \cdot Ste^{0,95} \cdot Ra^{0,046}$ for the second region (conduction and convection); for a $Re = 10004$ . . . . .	190
B.4	Melting fraction correlation $0,46 \cdot [FoSte]^{0,68}$ for the first region (conduction) and $0,46 \cdot Fo^{2,97} \cdot Ste^{0,95} \cdot Ra^{0,046}$ for the second region (conduction and convection); for a $Re = 8711$ . . . . .	191
B.5	Melting fraction correlation $4,3 \cdot [FoSte]^{0,68}$ for the first region (conduction) and $4,3 \cdot Fo^{2,97} \cdot Ste^{0,95} \cdot Ra^{0,046}$ for the second region (conduction and convection); for a $Re = 7670$ . . . . .	191



B.6	Melting fraction correlation $2,24 \cdot [FoSte]^{0,68}$ for the first region (conduction) and $2,24 \cdot Fo^{2,97} \cdot Ste^{0,95} \cdot Ra^{0,046}$ for the second region (conduction and convection); for a $Re = 6155$ . . . . .	192
B.7	Temperature results of the model for the outlet temperature of the heat exchanger $T_{out}$ for a $Re = 11496$ . . . . .	192
B.8	Temperature results of the model for the outlet temperature of the heat exchanger $T_{out}$ for a $Re = 10004$ . . . . .	193
B.9	Temperature results of the model for the outlet temperature of the heat exchanger $T_{out}$ for a $Re = 8711$ . . . . .	193
B.10	Temperature results of the model for the outlet temperature of the heat exchanger $T_{out}$ for a $Re = 6155$ . . . . .	194
C.1	Volumes de contrôle dans un échangeur air-PCM : (1)lignes de tubes et (2) tubes avec MCP. . . . .	198
C.2	Discrétisation d'un volume de contrôle Tube - MCP par la méthode de volumes finis . . . . .	198
C.3	Architectural scheme of the principal parts of an air-PCM heat exchanger for cooling applications in buildings: external inputs, air-PCM system and the outlet; and the boundaries of the system (dashed lines). . . . .	199
D.1	Experimental platform schematic. Left: West-side view of the house showing the location of the unit inside the house and sensors distribution. Right: Top view of the house. The colored dots symbolize the position of the temperature and velocity sensors. . . . .	201
D.2	Experimental test for tube degradation and leakage using RT21 PCM and water contained inside the PET tubes . . . . .	202
D.3	Tubes support plate. . . . .	203
D.4	Principal structure of the air-PCM unit. . . . .	204
D.5	Isolating plate. . . . .	205
D.6	Visual tracking of the solidification during the test performed on July 16 <sup>th</sup> , 2016 at I2M. After 15 minutes of the solidification cycle, the PCM have started to solidify. . . . .	206
D.7	Visual tracking of the solidification during the test performed on July 16 <sup>th</sup> , 2016 at I2M. We can see that an increase of the density (of solid PCM) starts at the upper part of the tubes. . . . .	206
D.8	Visual tracking of the solidification during the test performed on July 16 <sup>th</sup> , 2016 at I2M. We can clearly see that the solidification front moves downward in the axial direction of the tube. . . . .	207
D.9	Visual tracking of the solidification during the test performed on July 16 <sup>th</sup> , 2016 at I2M. In this figure, we can visualize that a complete solidification was only reached in the upper side of the tube. . . . .	207

D.10 Visual tracking of the solidification during the test performed on July 16 <sup>th</sup> , 2016 at I2M. After three hours of the solidification cycle, we can observe that the temperatures reached a constant value; although the PCM within tubes are not entirely solid. . . . .	208
D.11 Visual tracking of the solidification during the test performed on July 16 <sup>th</sup> , 2016 at I2M. We left the mobile air-conditioner over the night to see if the solidification front moves forward in the axial direction. Even though the air conditioning was left for almost 18 hours, it did not completely solidify. . . . .	208
D.12 Visual tracking of the melting during the test performed on July 17 <sup>th</sup> , 2016 at I2M. After 15 minutes of the solidification cycle, the PCM have started to solidify. . . . .	209
D.13 Visual tracking of the melting during the test performed on July 17 <sup>th</sup> , 2016 at I2M. After 40 minutes from the beginning of the cycle, we start to observe the melting of the PCM. The melting front moves downward in the axial direction of the tube, beginning with the upper part. . . . .	210
D.14 Visual tracking of the melting during the test performed on July 17 <sup>th</sup> , 2016 at I2M. After an hour of the cycle, the melting front moves forward through the rows of the unit, keeping the downward movement in the axial direction of the tube, beginning with the upper part. . . . .	210
D.15 Visual tracking of the melting during the test performed on July 17 <sup>th</sup> , 2016 at I2M. After an hour and a half of the cycle, the melting front have move forward through the rows of the unit, reaching the temperature measurement point located at one-third of the unit. In this figure, we can observe that at this moment the air temperature reaches the inlet conditions. . . . .	211
D.16 Visual tracking of the melting during the test performed on July 17 <sup>th</sup> , 2016 at I2M. After two hour of the cycle, we can observe that almost all the PCM have been solidified. . . . .	211

# Calibration

## A.1 Temperature calibrations

The thermocouples were calibrated in order to know the error value of each one for the experiments. To perform this essay, we used as reference a thermostatic water bath LAUDA ECO SILVER RE 415 G, which accept as input a set point to regulate and maintain the water temperature. During the calibration, the thermocouples were in contact with this water. At the same time, we acquired the temperature data of each one of these thermocouples through the CompactDAQ from NI<sup>®</sup>.

The calibration process was as follows: The K type and type T thermocouples were introduced into the water bath; these thermocouples have different coating materials: Teflon and fiberglass. Since the bath maintains the water at the same temperature, it was possible to have a constant measure as a reference.

The test was carried out at different temperatures: 14°C, 24°C, 28°C, 32°C, and 40°C. These temperatures were selected because they were higher and lower value than the melting point of the selected PCM Rubitherm<sup>®</sup> RT28HC. To display the data acquired, we used LabVIEW SignalExpress software from National Instruments<sup>®</sup>. We also include during this calibration the PID controller thermocouple to observe its deviation.

To know the uncertainties of the measure of each thermocouple, a recapitulation table is presented in figures [A.2](#) and [A.3](#), with the mean value of the measures, the standard deviation, and the absolute and relative error has been made. Figure [A.2](#) presents the results for the type K thermocouples used in the test bench, whereas figure [A.3](#) shows the results for the type T thermocouples used in the air-PCM unit.

## A.2 Velocity and airflow calibrations

Furthermore, the test bench airflow velocities were calibrated using the KIMO<sup>®</sup> instruments, already detailed in Chapter 3. In here, we present further results of this calibration from figure [A.4](#) to [A.6](#).

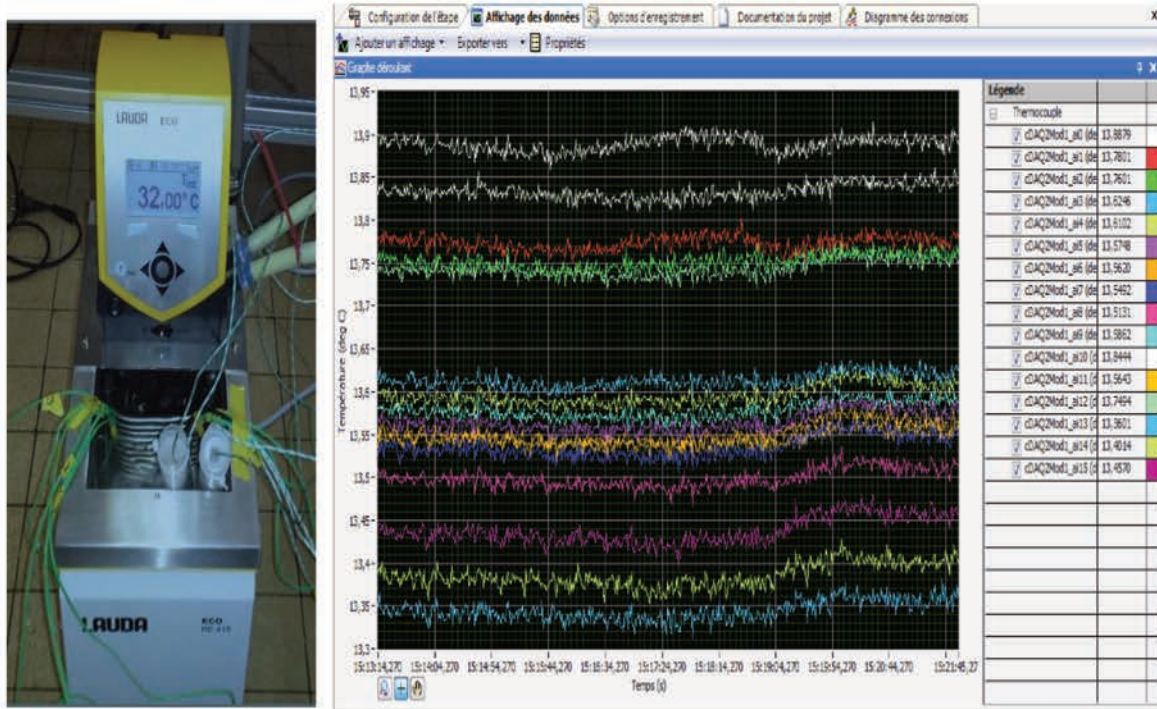


Figure A.1 – Calibration process of the thermocouples. *Left*: thermocouples inside the thermostatic water bath LAUDA ECO SILVER RE 415 G. *Right*: display of the data acquisition with LabVIEW SignalExpress software from National Instruments®.

	Description	Standard Deviation	Mean	Absolute Error (ref. Mean)
<b>Thermocouples</b>	$T_{in}$	0.01	13.54	0.46
	$T_{out}$	0.01	13.62	0.38
	$T_{air\_8a}$	0.01	13.44	0.56
	$T_{ow\_8a}$	0.01	13.78	0.22
	$T_{iw\_8a}$	0.01	13.39	0.61
	$T_{pcm\_8a}$	0.01	13.57	0.43
	$T_{air\_8b}$	0.17	14.00	0.00
	$T_{ow\_8b}$	0.01	13.76	0.24
	$T_{iw\_8b}$	0.01	13.56	0.44
	$T_{pcm\_8b}$	0.01	13.35	0.65
	$T_{air\_8c}$	0.04	13.59	0.41
	$T_{ow\_8c}$	0.01	13.90	0.1
	$T_{iw\_8c}$	0.01	13.61	0.39
	$T_{pcm\_8c}$	0.01	13.51	0.49
	$T_{air\_5}$	0.05	13.62	0.38
$T_{ow\_5}$	0.12	13.88	0.12	

Figure A.2 – Statistical Dispersion on Thermocouples.

Thermocouple	Calibration Function
T0	1,0261T -0,5915
T1	0,9973T+0,2257
T2	1,0215T-0,4521
T3	1,0226T-0,4562
T4	1,0228T-0,455
T5	0,9738T+0,5062
T6	1,0212T-0,3162
T7	1,0194T-0,1979
T8	1,0205T-0,2108
T9	1,0249T-0,2522

Figure A.3 – Statistical Dispersion on Thermocouples for the air-PCM unit tests.

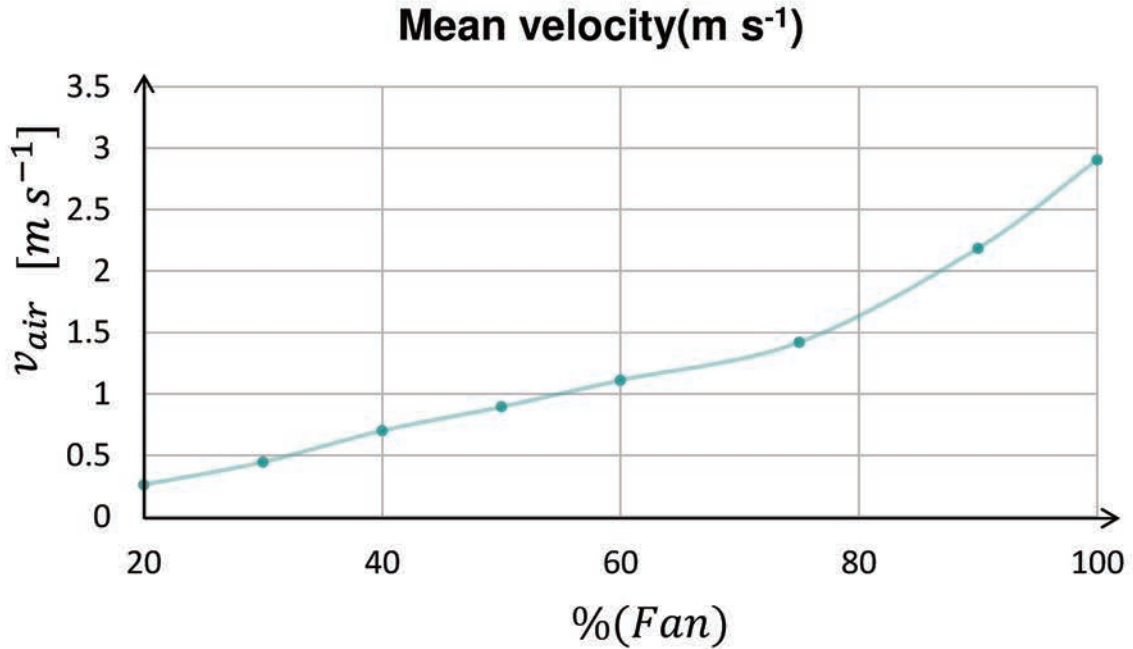


Figure A.4 – Air velocity measured with the vane probe for the heat exchanger without tubes.



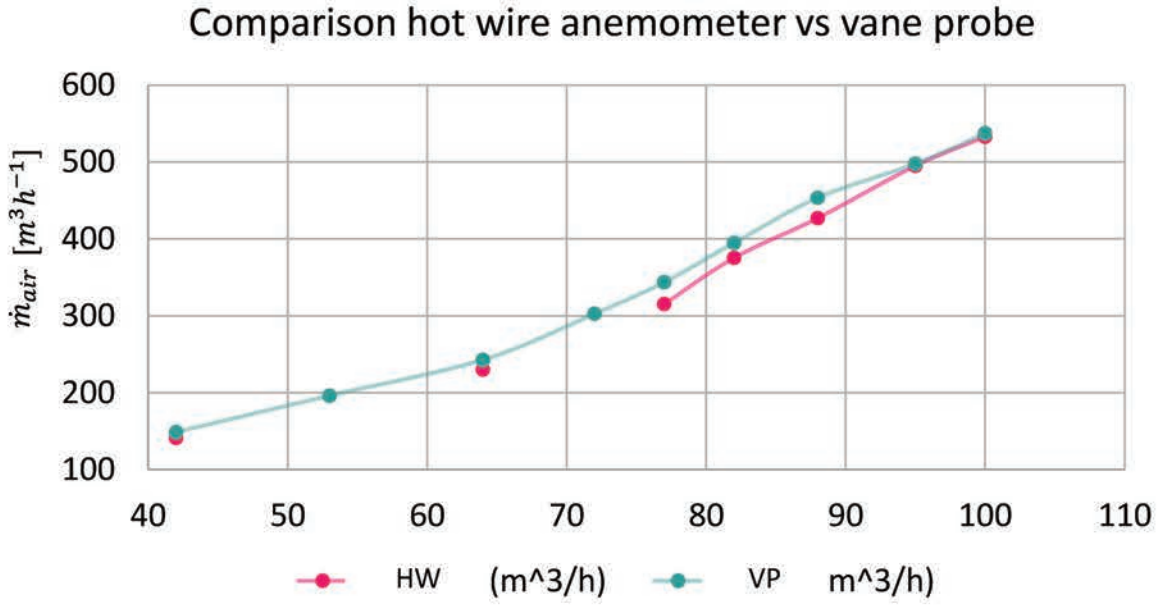


Figure A.5 – Airflow values obtained from the hot wire anemometer and the vane probe for the heat exchanger with tubes.

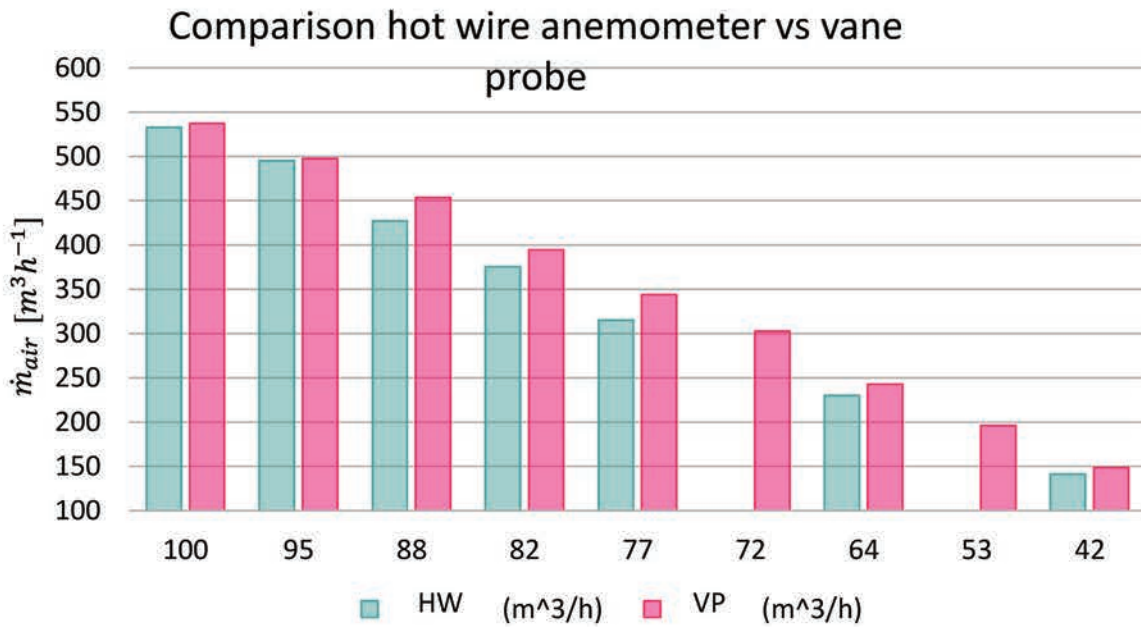


Figure A.6 – Comparison between the airflow values obtained from the hot wire anemometer and the vane probe for the heat exchanger with tubes.

## Modeling Results

### B.1 Melting correlations results

In this section we aim to present further results of the correlations obtaining for the melting fraction within a cylindrical tube, inside an air-PCM heat exchanger. To achieve these correlations we used the `manipulate` of R, since it permits the manual setting of the input coefficients. The algorithm followed is presented in figure B.1 This tools was used because an automatic response of the correlation coefficient through regression lead to unrealistic physical parameters.

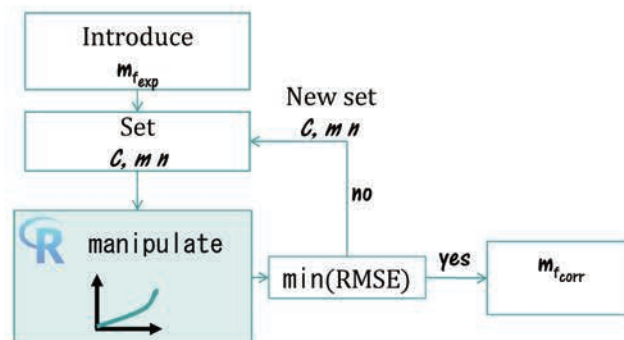


Figure B.1 – Algorithm proposed to find the melting correlation using the function `manipulate` of R.

These algorithm was tested at different inlet airflow values. The results of these correlations are presented from figure B.2 to figure B.6.

### B.2 1-D thermal resistance modeling results

Further results for the air temperature at the outlet of the heat exchanger  $T_{out}$  are presented in this section. In these plots from figures B.7 to figure B.10, we compare the experimental results, in solid orange lines, with the model results in orange dashed line.

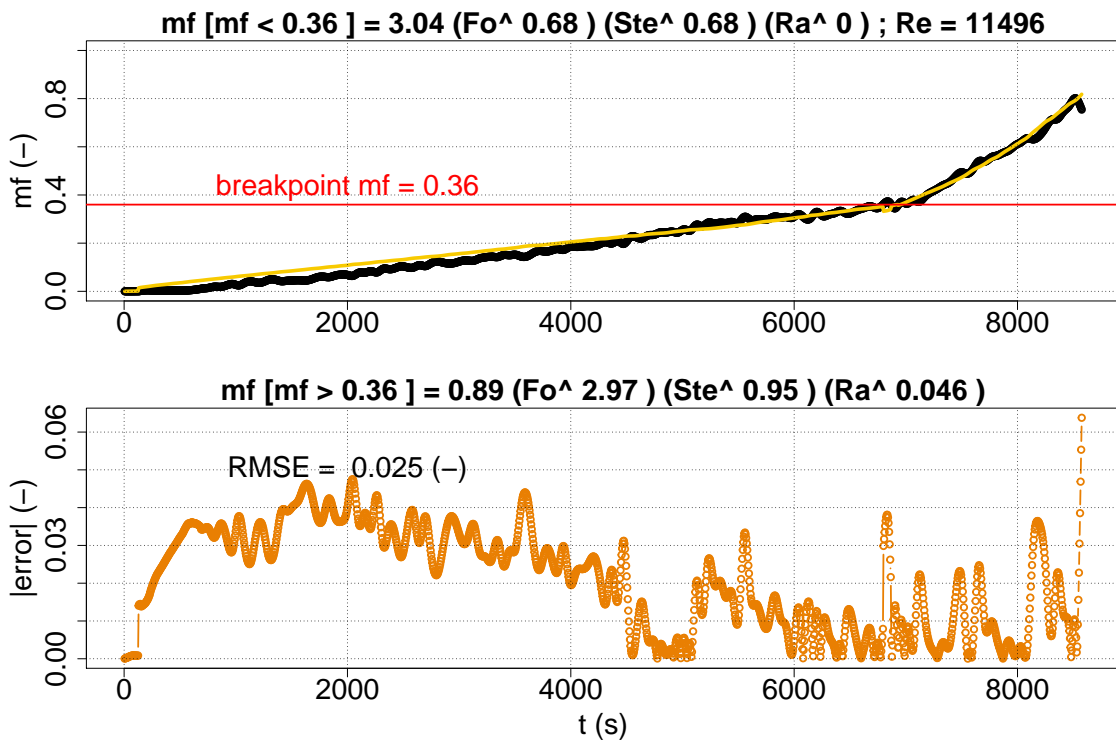


Figure B.2 – Melting fraction correlation  $3,04 \cdot [FoSte]^{0,68}$  for the first region (conduction) and  $0,89 \cdot Fo^{2,97} \cdot Ste^{0,95} \cdot Ra^{0,046}$  for the second region (conduction and convection); for a  $Re = 11496$ .

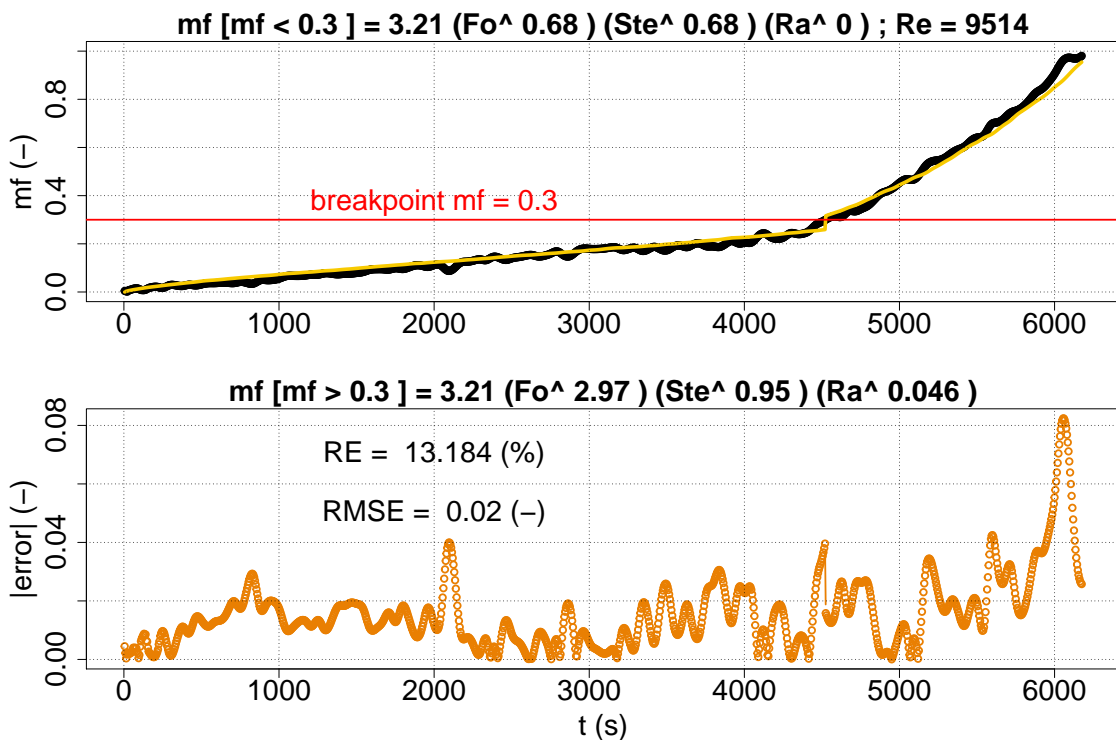


Figure B.3 – Melting fraction correlation  $3,21 \cdot [FoSte]^{0,68}$  for the first region (conduction) and  $3,21 \cdot Fo^{2,97} \cdot Ste^{0,95} \cdot Ra^{0,046}$  for the second region (conduction and convection); for a  $Re = 10004$ .

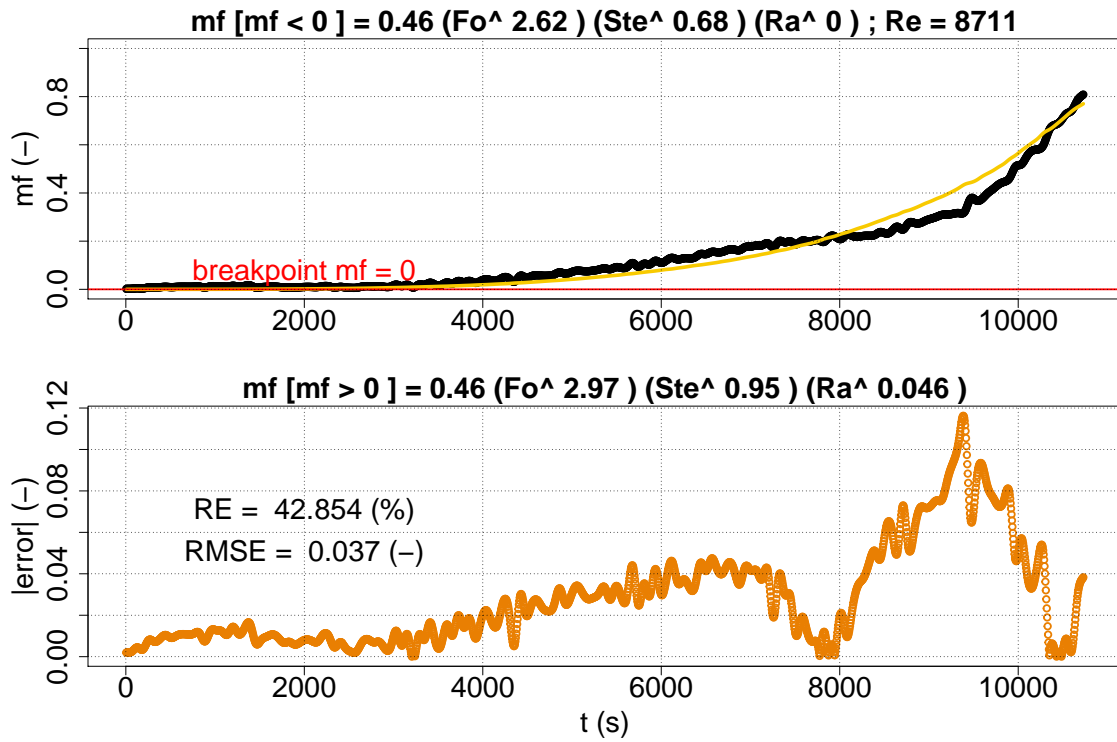


Figure B.4 – Melting fraction correlation  $0,46 \cdot [FoSte]^{0,68}$  for the first region (conduction) and  $0,46 \cdot Fo^{2,97} \cdot Ste^{0,95} \cdot Ra^{0,046}$  for the second region (conduction and convection); for a  $Re = 8711$ .

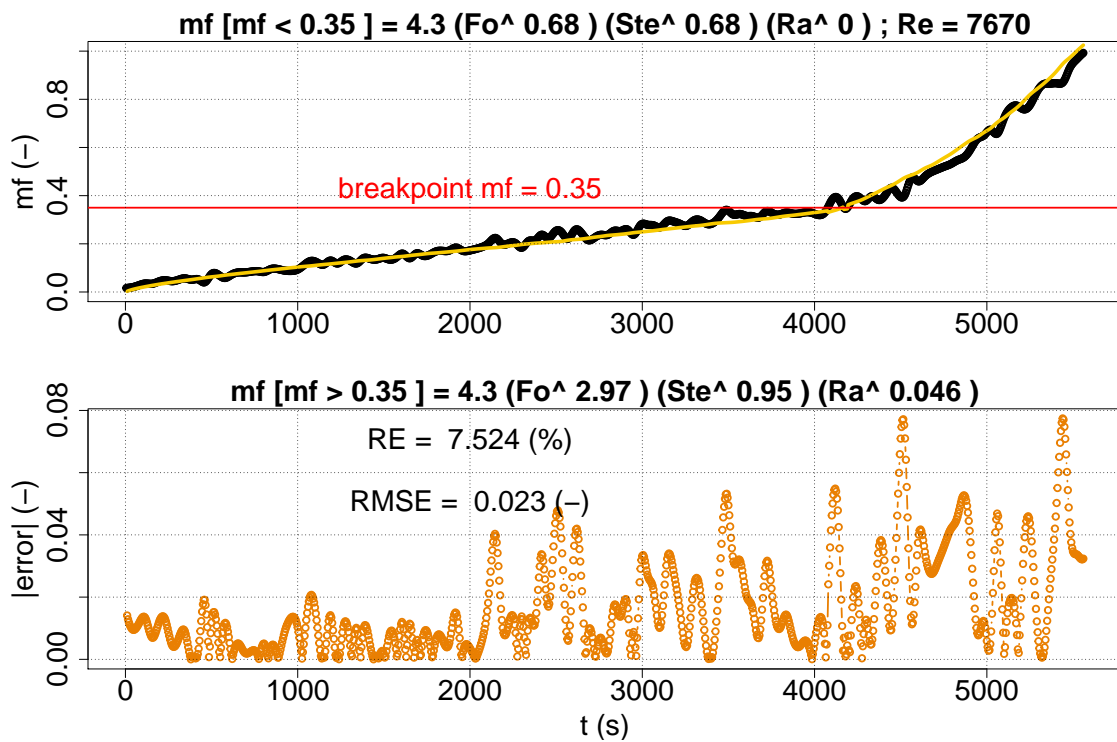


Figure B.5 – Melting fraction correlation  $4,3 \cdot [FoSte]^{0,68}$  for the first region (conduction) and  $4,3 \cdot Fo^{2,97} \cdot Ste^{0,95} \cdot Ra^{0,046}$  for the second region (conduction and convection); for a  $Re = 7670$ .

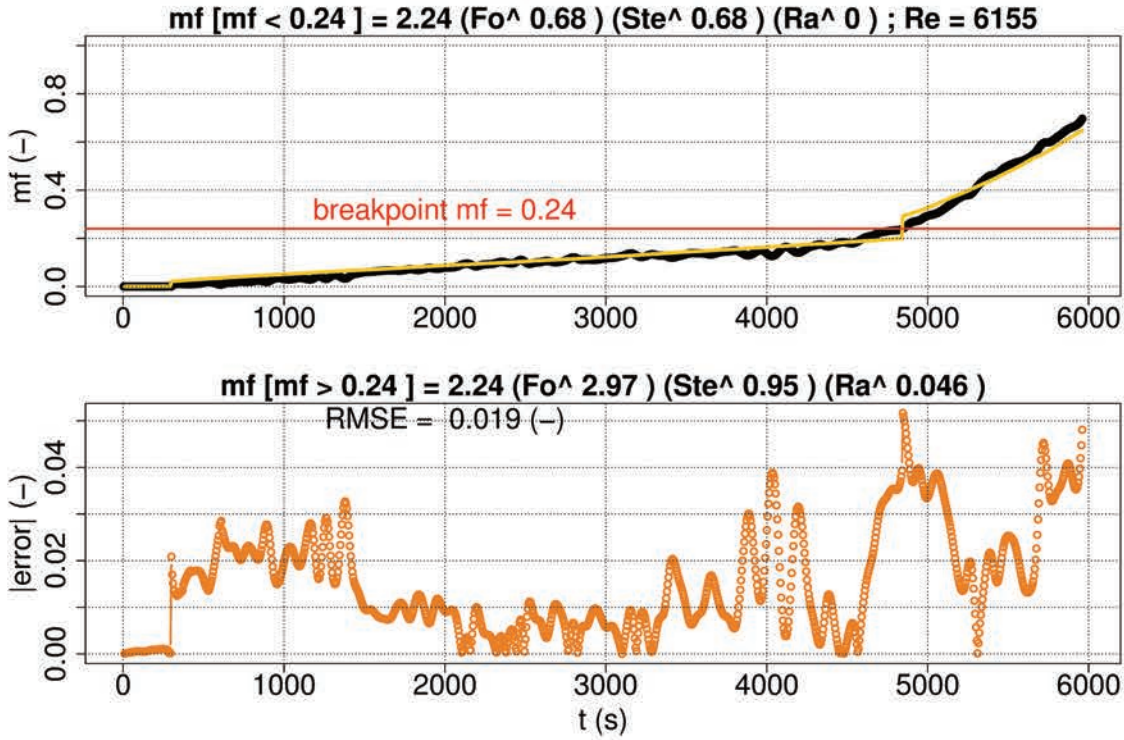


Figure B.6 – Melting fraction correlation  $2,24 \cdot [FoSte]^{0,68}$  for the first region (conduction) and  $2,24 \cdot Fo^{2,97} \cdot Ste^{0,95} \cdot Ra^{0,046}$  for the second region (conduction and convection); for a  $Re = 6155$ .

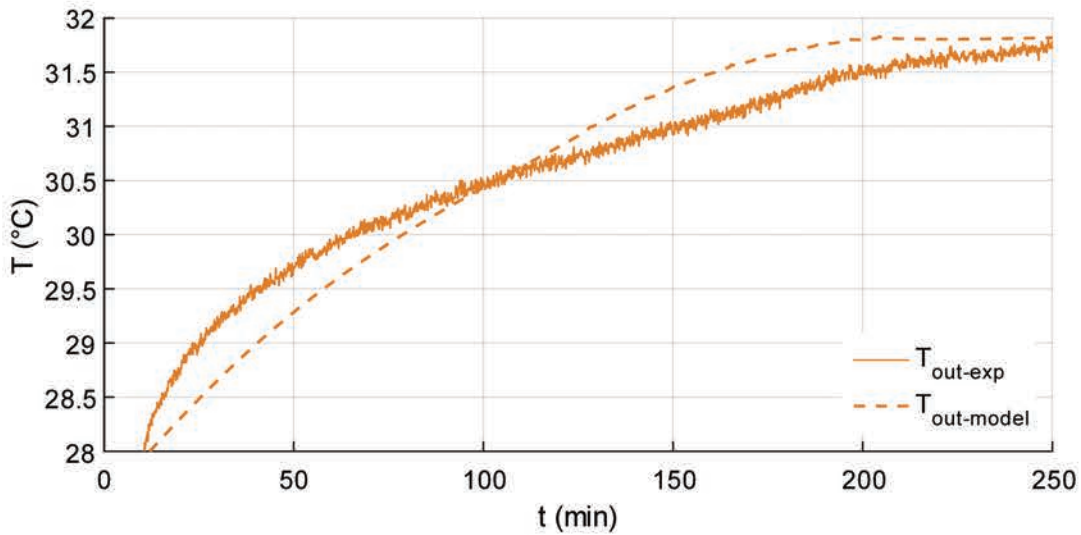


Figure B.7 – Temperature results of the model for the outlet temperature of the heat exchanger  $T_{out}$  for a  $Re = 11496$ .



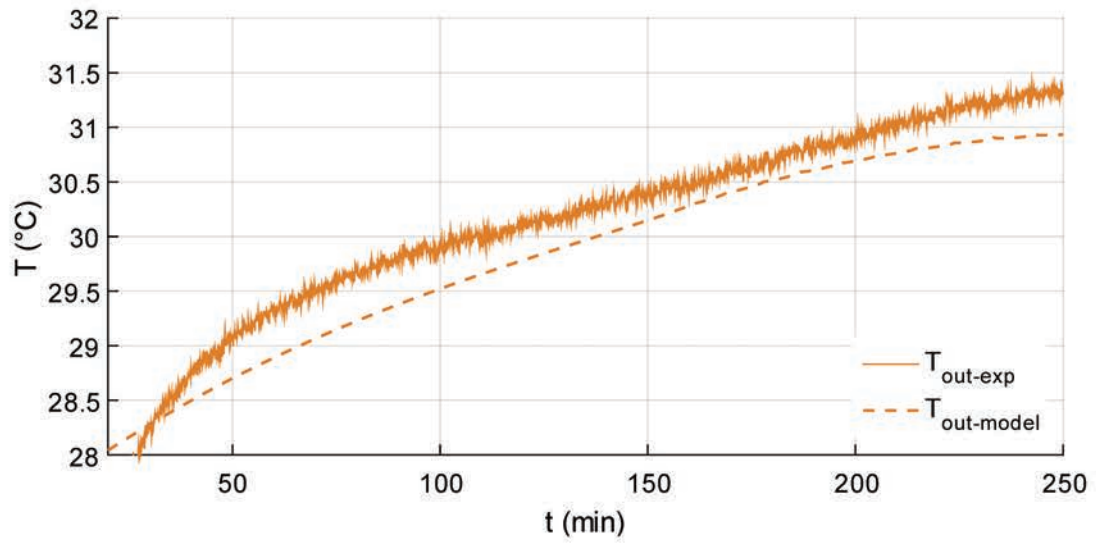


Figure B.8 – Temperature results of the model for the outlet temperature of the heat exchanger  $T_{out}$  for a  $Re = 10004$ .

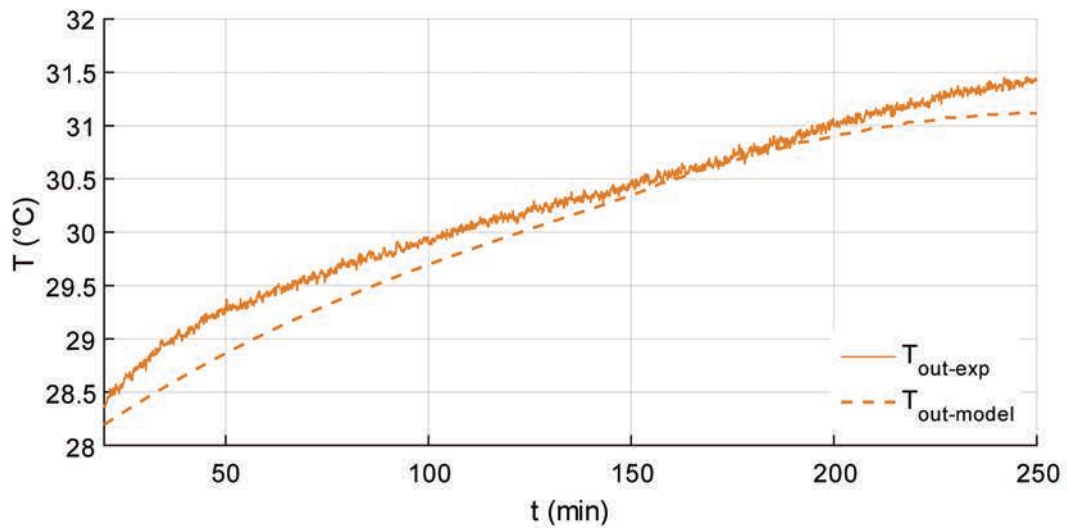


Figure B.9 – Temperature results of the model for the outlet temperature of the heat exchanger  $T_{out}$  for a  $Re = 8711$ .

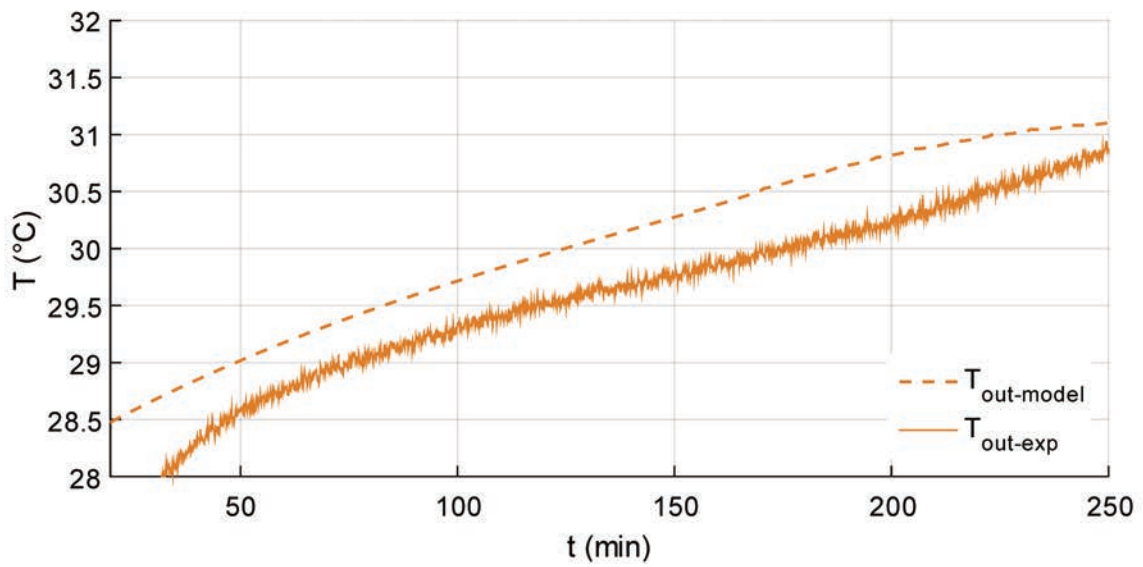


Figure B.10 – Temperature results of the model for the outlet temperature of the heat exchanger  $T_{out}$  for a  $Re = 6155$ .

# Pure conduction enthalpy method modeling

## C.1 Enthalpy method modeling

In this section we present the proposition for a conductive modeling of the PCM. In here, it is assumed a non-uniform heat transfer within the PCM. To solve phase change we propose the use of the so-called enthalpy method. The discretization is proposed using finite volume method. This method is a variation of the one proposed by [55].

### C.1.1 Mathematical formulation

The governing equation phase change in terms of total volumetric enthalpy  $H(T)$  can be written as:

$$\rho \frac{\partial H}{\partial t} = \nabla \cdot (k \nabla T) \quad (\text{C.1})$$

where,  $k$  is the thermal conductivity of the PCM. The total volumetric enthalpy can be expressed as the sum of sensible  $h(T)$ , and latent heat,  $L$

$$H(T) = h(T) + m_l \cdot L \quad (\text{C.2})$$

where

$$h(T) = \int_{T_m}^T c_p dt \quad (\text{C.3})$$

and,  $m_f$  is the melting fraction of the PCM. The melting fraction for isothermal phase change can be evaluated after a relationship with the phase change temperature  $T_m$  presented by Swaminathan and Voller [Swaminathan et Voller]:

$$m_f(T) = \begin{cases} 0, & \text{if } T_{pcm} < T_m \\ 0 < m_f < 1, & \text{if } T_{pcm} = T_m \\ 1, & \text{if } T_{pcm} > T_m \end{cases} \quad (\text{C.4})$$

Following the eq. C.1 to eq.C.3, the relationships between the node temperature and the total mass enthalpy, H-T, are given by:

$$H(T) = \begin{cases} \int_{T_m}^T c_{p_s} dt & \text{if } T < T_m \\ Lf_l & \text{if } T = T_m \\ \int_{T_m}^T c_{p_s} dt + L & \text{if } T > T_m \end{cases} \quad (\text{C.5})$$

For one-dimensional radial heat transfer, C.1 becomes:

$$\rho c_p \frac{\partial T}{\partial t} = \frac{1}{r} \frac{\partial}{\partial r} \left( rk \frac{\partial T}{\partial r} \right) - \rho \cdot L \frac{\partial m_f}{\partial t}. \quad (\text{C.6})$$

By separating the total volumetric enthalpy in terms of sensible and latent heat, it allows to isolate the nonlinear behavior associated with phase change into a source term.

The initial temperature is described as:

$$T(r, 0) = T_{in} \quad (\text{C.7})$$

And the associated boundaries conditions are:

$$k_{pcm} \frac{\partial T(r=0, t)}{\partial r} = 0 \quad (\text{C.8})$$

$$k_{wall} \nabla T = k_{wall} \frac{\partial T(r=r_o, t)}{\partial r} = h \cdot (T_{air} - T_{ow}) \quad (\text{C.9})$$

### C.1.2 Numerical Solution

Here, we propose a spatial discretization of the local domain, based on the finite volume method proposed by Patankar, and a time discretization by the finite difference method, with an implicit resolution scheme. For this case, we consider a domain mesh consisting of small volumes equal to  $rdrd\phi dz$ , in which the heat propagates radially, remaining constant in the axial,  $z$ ; and angular,  $\phi$ , directions (see Figure 2). To facilitate the calculations, the  $\phi$  and  $z$  coordinates are defined as  $\Delta\phi = \Delta z = 1$ . A piecewise profile assumption over the integration in the control volumes was made, where linear interpolation functions are used between the grid points.

The discretization was derived by integration over the control volume and over the time interval from  $t$  to  $t+\Delta t$ . Thus:

$$\int_t^{t+\Delta t} \int_w^e r \rho c_p \frac{\partial T}{\partial t} dr dt = \int_t^{t+\Delta t} \int_w^e \frac{1}{r} \frac{\partial}{\partial r} \left( rk \frac{\partial T}{\partial r} \right) r dr dt - \int_t^{t+\Delta t} \int_w^e r \rho L \frac{\partial m_f}{\partial t} dr dt \quad (\text{C.10})$$

The term on the left hand of the C.10 represents the amount of sensible heat that is needed to raise the temperature of the control volume over a time step. After integration this term can be written as follows:

$$\int_t^{t+\Delta t} \int_w^e r \rho c_p \frac{\partial T}{\partial t} dr dt = \frac{r_e^2 - r_w^2}{2} \cdot \rho c_p \cdot T_P - T_P^0 \quad (\text{C.11})$$

The first term on the right hand of eq. C.10 represents the heat transfer from the neighboring volumes. After discretization they can be expressed as:

$$\int_t^{t+\Delta t} \int_w^e \frac{1}{r} \frac{\partial}{\partial r} \left( r k \frac{\partial T}{\partial t} \right) r dr dt = r_e \cdot k_e \frac{T_E - T_P}{r_e - r_p} \Delta t - r_w \cdot k_w \frac{T_P - T_W}{r_p - r_w} \Delta t \quad (\text{C.12})$$

And the last term on the right hand of eq. C.10 can be expressed as:

$$\int_t^{t+\Delta t} \int_w^e r \rho L \frac{\partial f_l}{\partial t} dr dt = + \frac{r_e^2 - r_w^2}{2} \rho L (m_f^0 - m_f^k) \quad (\text{C.13})$$

Finally, eq.C.10 becomes

$$\frac{r_e^2 - r_w^2}{2} \cdot \rho c_p \cdot \frac{T_P - T_P^0}{\Delta t} = r_e k_e \frac{T_E - T_P}{r_e - r_p} - r_w k_w \frac{T_P - T_W}{r_p - r_w} + \frac{r_e^2 - r_w^2}{2 \Delta t} \rho L (m_f^0 - m_f^k) \quad (\text{C.14})$$

To solve eq.C.14 it can be written in the algebraic form

$$a_P T_P = a_E T_E + a_W T_W + b \quad (\text{C.15})$$

where the temperature fields are solved at the present iteration level  $k$ . The melting fraction field and the temperatures related to the old time iteration are grouped as the source term  $b$ . with:

$$a_P = \frac{r_e^2 - r_w^2}{2} \rho c_p + a_E + a_W \quad (\text{C.16})$$

$$a_E = \frac{r_e k_e}{r_e - r_p} \quad (\text{C.17})$$

$$a_W = \frac{r_w k_w}{r_p - r_w} \quad (\text{C.18})$$

$$b = \frac{r_e^2 - r_w^2}{2 \Delta t} \cdot \rho c_p \cdot T_P^0 + \frac{r_e^2 - r_w^2}{2 \Delta t} \rho L (m_f^0 - m_f^k) \quad (\text{C.19})$$

### Melting fraction update

The update of the melting fraction in a node is obtained according to the method developed by Voller as follows:

1. Set the time and space values, the boundary and the initial conditions.
2. At the start of the time step, the initial iterative fields of Temperature  $T_P^0$  and melting fraction  $m_f^0$  are set to the previous time step values.
3. Calculate the temperature fields from:

$$a_P T_P = a_E T_E + a_W T_W + \frac{r_e^2 - r_w^2}{2 \Delta t} \cdot \rho c_p \cdot T_P^0 + \frac{r_e^2 - r_w^2}{2 \Delta t} \rho L (m_f^0 - m_f^k) \quad (\text{C.20})$$

This step ensures that the the update of the liquid fraction is made due to the effect of the temperature field associated to the sensible enthalpy. For this equation,  $m_f^0$  and  $m_f^{k-1}$  take the same value, since the superscript "0" refers to the old field value and " $k-1$ " corresponds to the field value from the previous iteration. Therefore the term including the melting fraction value is equal to zero.



4. If  $T_p$  in the present node is equal to the melting temperature  $T_m$ , then the melting fraction is calculated from the following equation:

$$f_{l_p}^{k+1} = f_{l_p}^k + \frac{a_p T_p - a_E T_E - a_W T_W - \rho c_p \cdot r_p T_p^0}{\rho L \cdot r_p} \quad (\text{C.21})$$

La présence de changement de phase dans un nœud est estimée à partir de l'équation (3). Voller propose que si le changement de phase a lieu dans le nœud  $\mathcal{P}$ , alors il est attribué une grande valeur à  $a_p$ ,  $BIG = 10^{15}$ . Les itérations auront lieu jusqu'à ce que l'état actuel de la fraction liquide change, ou que la convergence est achevée.

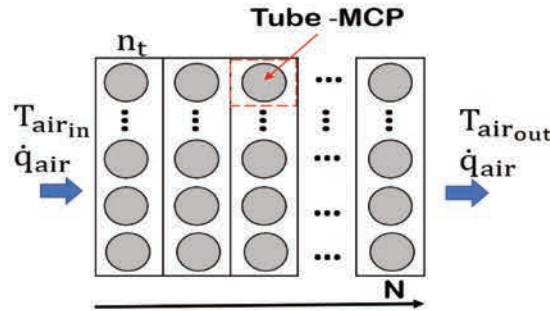


Figure C.1 – Volumes de contrôle dans un échangeur air-PCM : (1) lignes de tubes et (2) tubes avec MCP.

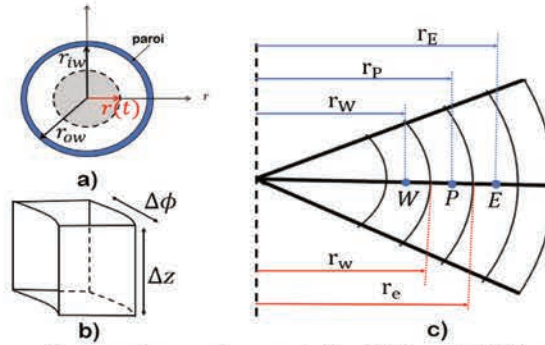


Figure C.2 – Discretisation d'un volume de contrôle Tube - MCP par la méthode de volumes finis

### Discretization in each finite-volume : Temperature field

1. Temperature field for the first volume at  $i = 1$ , corresponding to the tube wall:

$$a_p T_p = a_w T_W + h_{air} \cdot r_{ow} T_{air} + \frac{r_e^2 - r_w^2}{2\Delta t} \cdot \rho c_p \cdot T_p^0 \quad (\text{C.22})$$

where for this case a "ghost volume" at the left neighbor  $\mathcal{W}$  corresponds to the convection between the air surrounding the tube and the tube wall and therefore the coefficient  $a_w = 2r_p h_{air}$ . In the same way for this finite-volume the material properties such as the specific heat capacity  $c_p$  and the density  $\rho$  correspond to the wall tube material. As phase change does not occur in this finite-volume, the source term does not include the latent heat.

2. Temperature field for the second volume at  $i = 2$ , corresponding to the first volume of PCM:

$$a_P T_P = a_E T_E + a_W T_W + \frac{r_e^2 - r_w^2}{2\Delta t} \cdot \rho c_p \cdot T_P^0 + \frac{r_e^2 - r_w^2}{2\Delta t} \rho L (m_f^0 - m_f^k) \quad (C.23)$$

For this finite-volume the values of the coefficients  $a_P$ ,  $a_E$ , and  $a_W$  correspond to those defined from eq.C.16 to C.19. Although, the west volume  $\mathcal{W}$  thermal conductivity  $k_w$  correspond to the wall conductivity.

3. Temperature field from the third volume until the node  $n - 1$ :

$$a_P T_P = a_E T_E + a_W T_W + \frac{r_e^2 - r_w^2}{2\Delta t} \cdot \rho c_p \cdot T_P^0 + \frac{r_e^2 - r_w^2}{2\Delta t} \rho L (m_f^0 - m_f^k) \quad (C.24)$$

For this finite-volume the values of the coefficients  $a_P$ ,  $a_E$ , and  $a_W$  correspond to those defined from eq.C.16 to C.19.

4. Temperature field from the last finite-volume  $n$ :

$$a_P T_P = a_E T_E + \frac{r_e^2 - r_w^2}{2\Delta t} \cdot \rho c_p \cdot T_P^0 + \frac{r_e^2 - r_w^2}{2\Delta t} \rho L (m_f^0 - m_f^k) \quad (C.25)$$

This is the last finite-volume located right before the center of the tube at  $r = 0$ . To ensure the axisymmetry of the heat transfer in the tube a condition of  $\frac{dT}{dr} = 0$  is set for this volume.

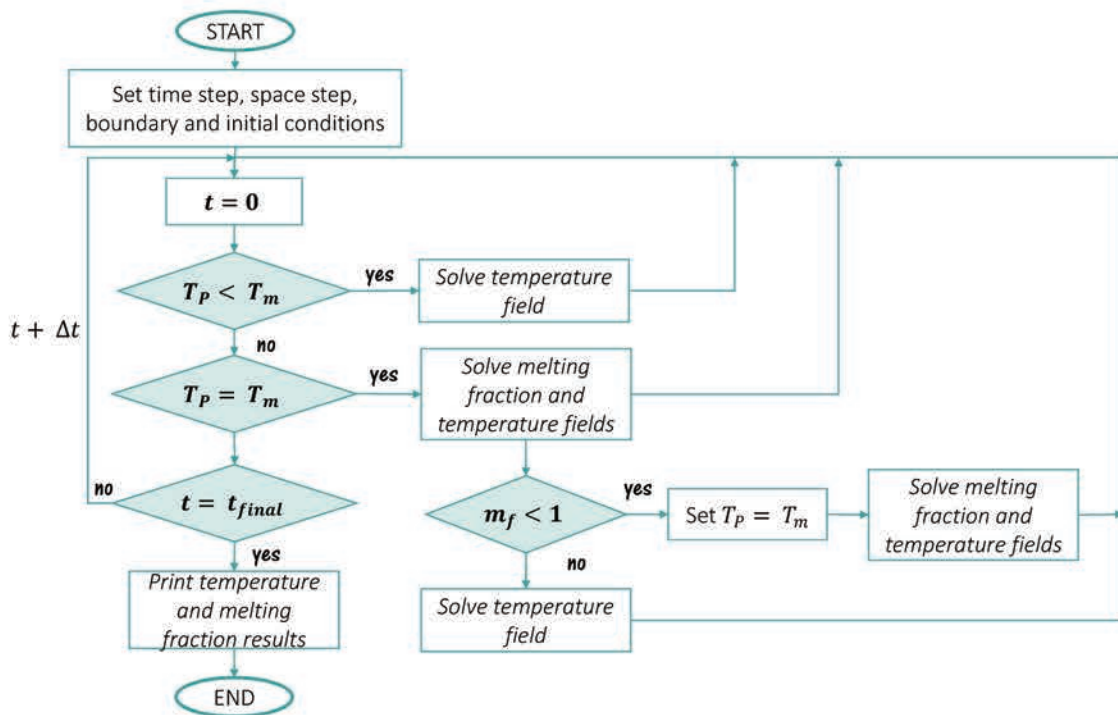


Figure C.3 – Architectural scheme of the principal parts of an air-PCM heat exchanger for cooling applications in buildings: external inputs, air-PCM system and the outlet; and the boundaries of the system (dashed lines).

### Discretization in each finite-volume : melting fraction field

1. Melting fraction field for the volumes from  $i = 2$  to  $i = n - 1$ :

$$m_f^k = m_f^0 + \frac{a_E T_E + a_W T_W - \left( \frac{r_e^2 - r_w^2}{2\Delta t} \cdot \rho c_p \cdot + a_E + a_W \right) T_P + \frac{r_e^2 - r_w^2}{2\Delta t} \cdot \rho c_p \cdot T_P^0}{\frac{r_e^2 - r_w^2}{2\Delta t} \cdot \rho L} \quad (\text{C.26})$$

This equation update the melting fraction field within the finite-volume that is undergoing a phase change. If at the  $k$ th iteration melting fraction started at least one iteration ago and phase change occurs isothermally, then  $T_P^k = T_P^0 = T_m$ , where  $T_m$  is the melting temperature. This condition reduce eq.C.27 to:

$$m_f^k = m_f^0 + \frac{a_E T_E + a_W T_W}{\frac{r_e^2 - r_w^2}{2\Delta t} \cdot \rho L} \quad (\text{C.27})$$

As sensible heat does not exists while phase change occurs in the control-volume, all the heat supplied is used for changing the amount of latent heat content of that control volume.

### C.1.3 Conductivity value

Basic Approximations for the value of k:

1. The arithmetic mean :

$$k_e = \frac{k_P + k_E}{2} \quad (\text{C.28})$$

with similar expressions for the other interface conductivities, and

2. The harmonic mean:

$$k_e = \frac{2k_P \cdot k_E}{k_P + k_E} \quad (\text{C.29})$$

The Kirchhoff Approximation:

Presented by Patankar and Voller in 1993 where a central difference approximation of the terms lead to the following expression for the interface of conductivities:

$$\nabla \phi = k \nabla T \quad (\text{C.30})$$

$$\nabla \cdot (k \nabla T) = \nabla^2 \phi \quad (\text{C.31})$$

$$k_e = \text{frac} \phi_E - \phi_P T_E - T_P \quad (\text{C.32})$$

$$k_w = \text{frac} \phi_W - \phi_P T_W - T_P \quad (\text{C.33})$$

They proposed this arrangement as a convenient and accurate mean of dealing with discontinuities in thermal conductivity in a fixed-grid control-volume solution a phase-change problem.

# Mobile air-PCM unit

## D.1 Selection of the PET tubes

The design of this tubes responds to the search of a container that allows to obtain a good performance of the unit during all its operation modes. Cylindrical tubes allow a slender shape, which is favorable in terms of heat transfer due to its large surface area. Previous and parallel works to the development of this thesis, set the basis and requirements for the geometry of these containers, which are detailed in the figures 5.1 and D.1

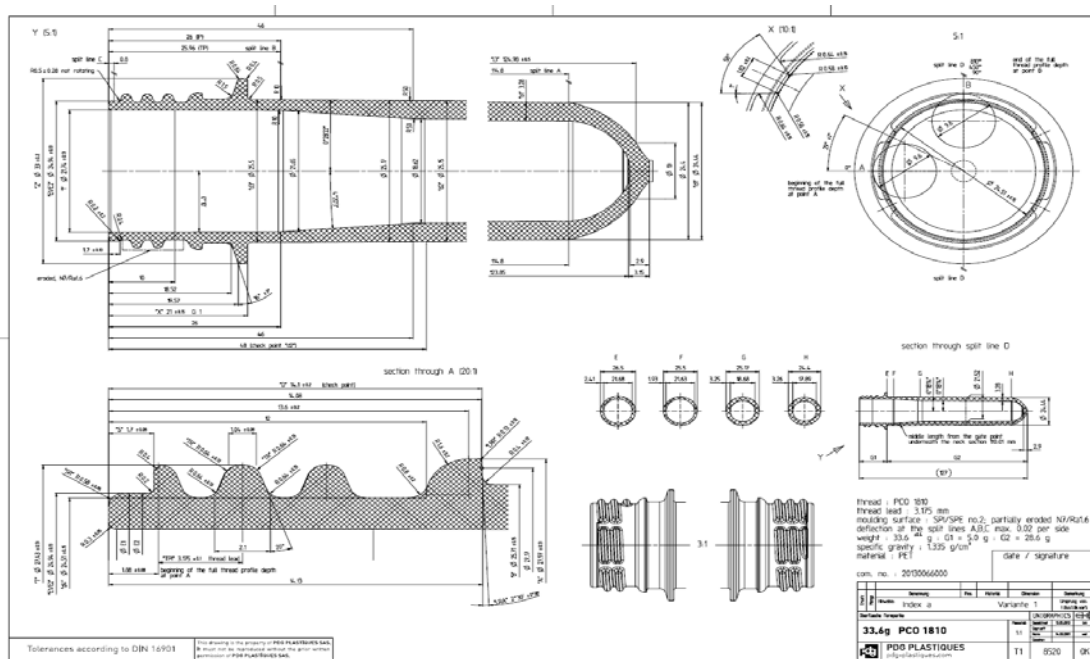


Figure D.1 – Experimental platform schematic. Left: West-side view of the house showing the location of the unit inside the house and sensors distribution. Right: Top view of the house. The colored dots symbolize the position of the temperature and velocity sensors.

### D.1.1 Partnership for manufacturing

MCPFlex project decided to work on the development of this product with a big national SME which is independent of the big global groups of manufacturing of PET food containers: the company PDG-Plastiques (Malesherbes, France).

In here, the manufacturing costs included the desired mold, the men's times of the engineer of the preliminary manufacturing tests. It should be noted on this one, that the cost of the tube is not that of a normal manufacture: it integrates the development and especially a part of the time of not use in production of the production line used.

### D.1.2 Short-term reliability test

For 6 months, we tested the tightness of PET tubes with MCP. For this, five test tubes were filled with RT21®, and placed head up, head down and horizontally and then cycled in temperature. The tubes were weighed before and after this experiment to detect any presence of leakage. The condition of the capsules was checked to determine if the materials had not degraded in contact with the paraffins used. Figure ?? shows the test tubes while table D.1 shows the the loss of mass for six months for these tubes.

We also tested the resistance of the tubes to the stresses caused by the liquid-solid volume change of the paraffin. A first test tube was filled with liquid PCM at 50°C to the brim. The second was filled leaving a dead zone of about 1cm. The tubes were then cycled in temperature. No particular degradation was observed over the 6 months of testing.



Figure D.2 – Experimental test for tube degradation and leakage using RT21 PCM and water contained inside the PET tubes



Table D.1 – Short-term mass degradation (during 6 month)

Description	Initial Mass (g)	Final Mass (g)
RT21 vertical position	77,5	77,4
RT21 inverse vertical position	78,0	77,9
RT 21 horizontal position	77,2	77,2
Water inverse vertical position	95,8	95,8
RT21 50°C (with air gap)	77,3	77,2
RT21 50°C (without air gap)	80,9	80,9

## D.2 Air-PCM unit Plans

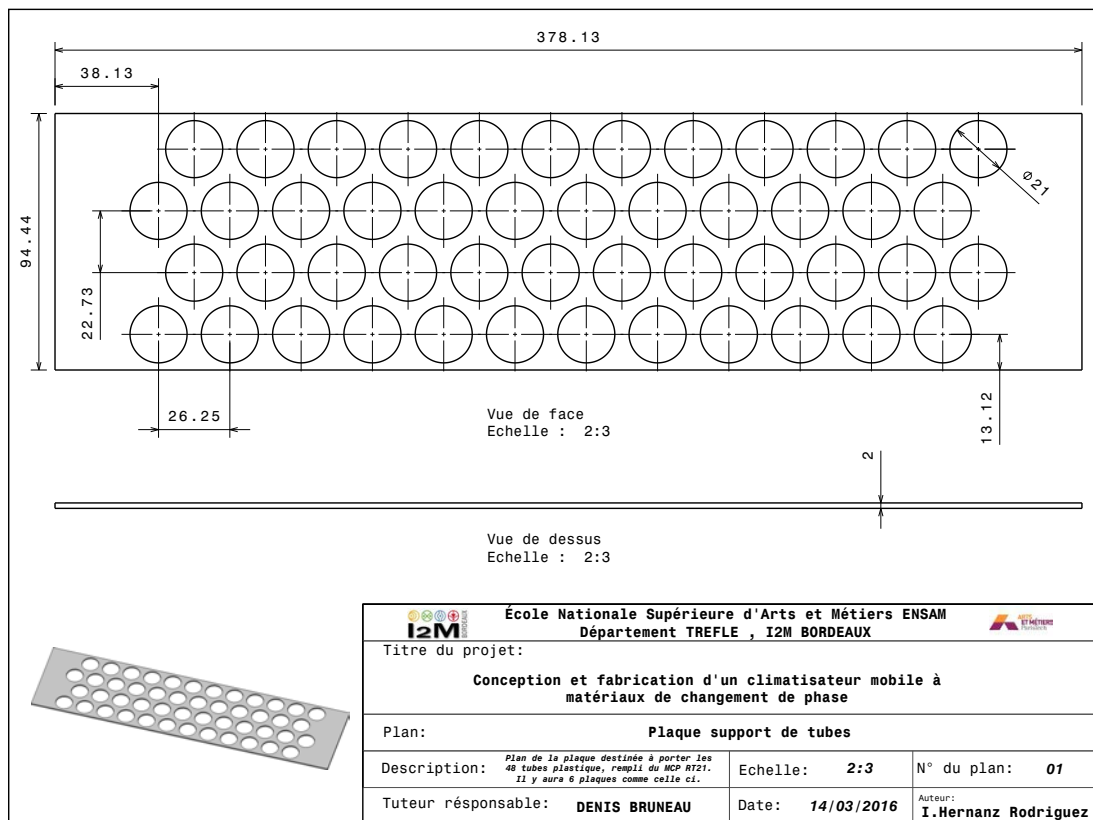


Figure D.3 – Tubes support plate.

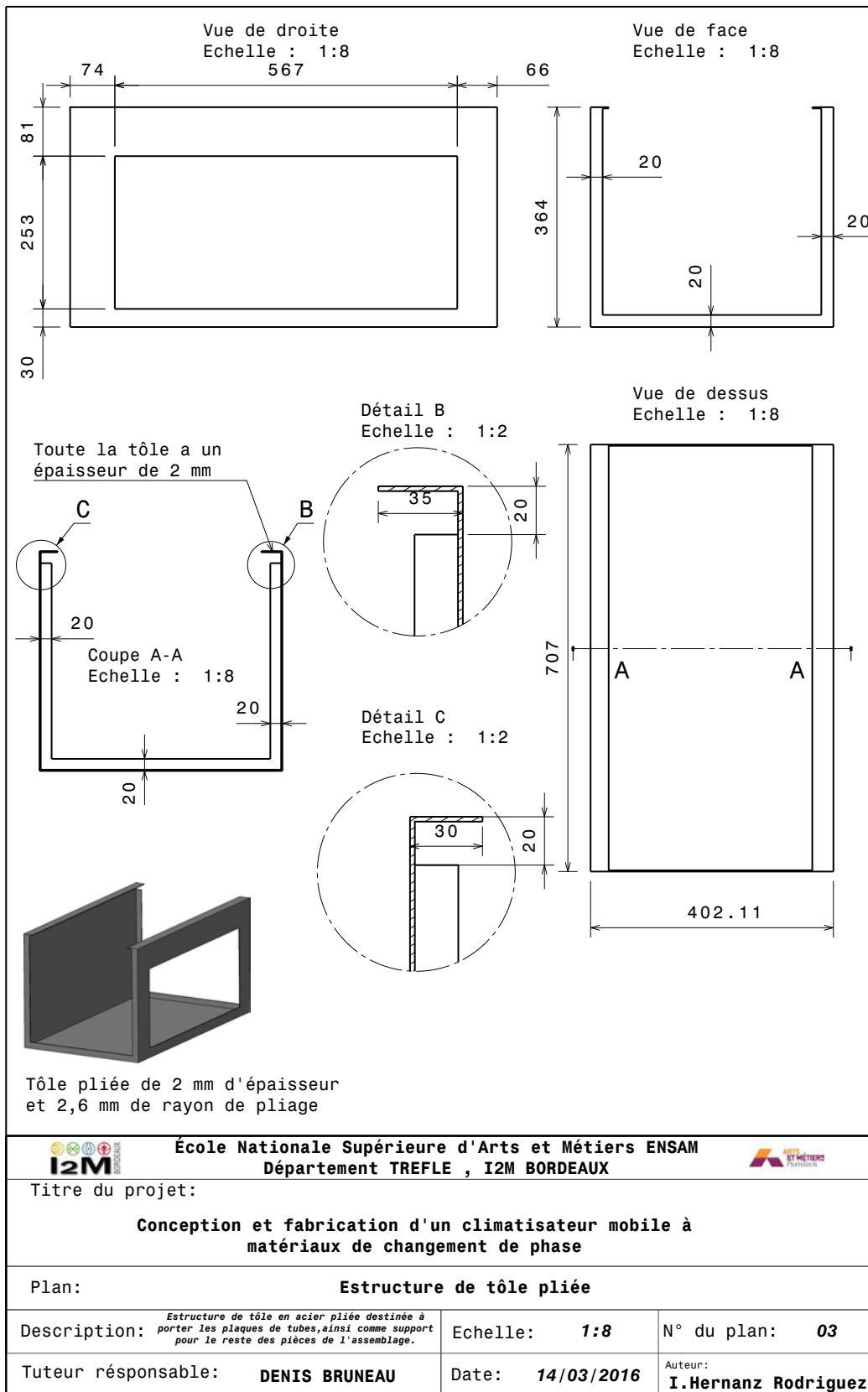


Figure D.4 – Principal structure of the air-PCM unit.

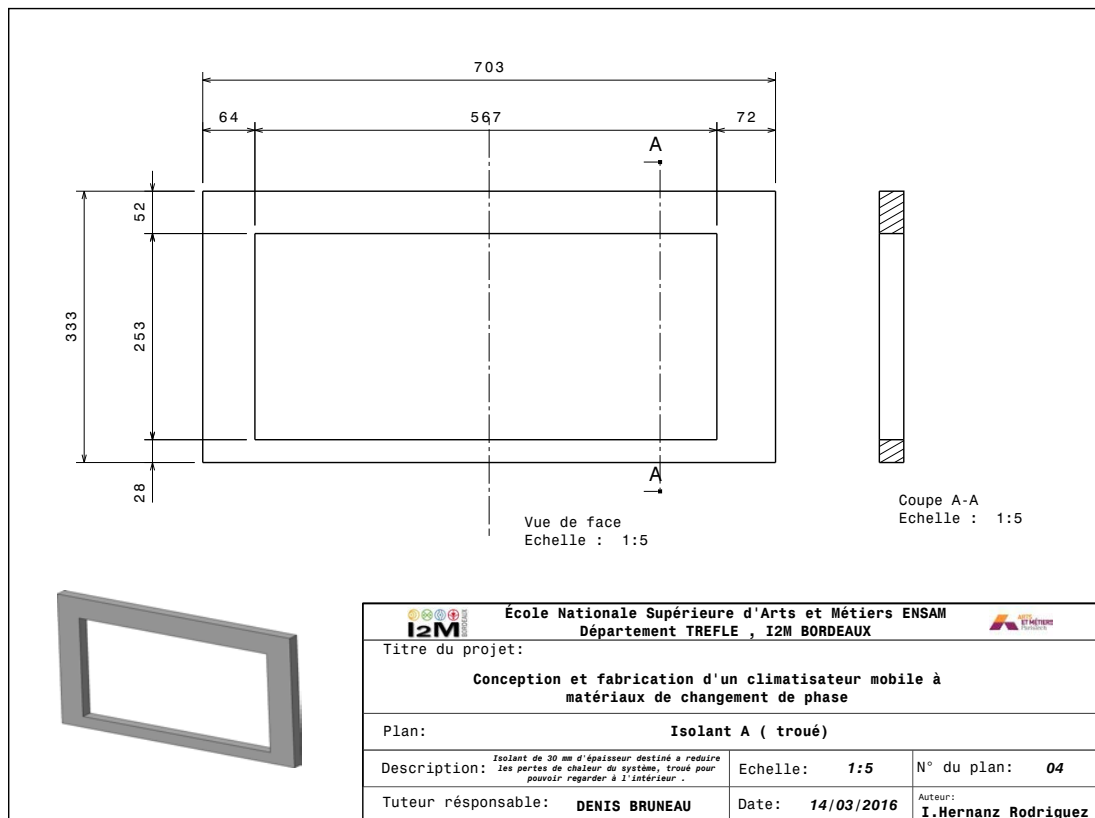


Figure D.5 – Isolating plate.

### D.3 Visual tracking of phase change for the air-PCM unit

During the tests developed at the I2M laboratory, using RT21 Rubitherm® paraffin as storage material, we conducted a visual tracking of the PCM.

#### D.3.1 Solidification cycle

From figures D.6 to D.11, we can observe the results of the solidification cycle within the air-PCM unit. For this test an portable air-conditioner was used, since the nocturnal natural ventilation was not enough for achieving the total regeneration of the PCM.

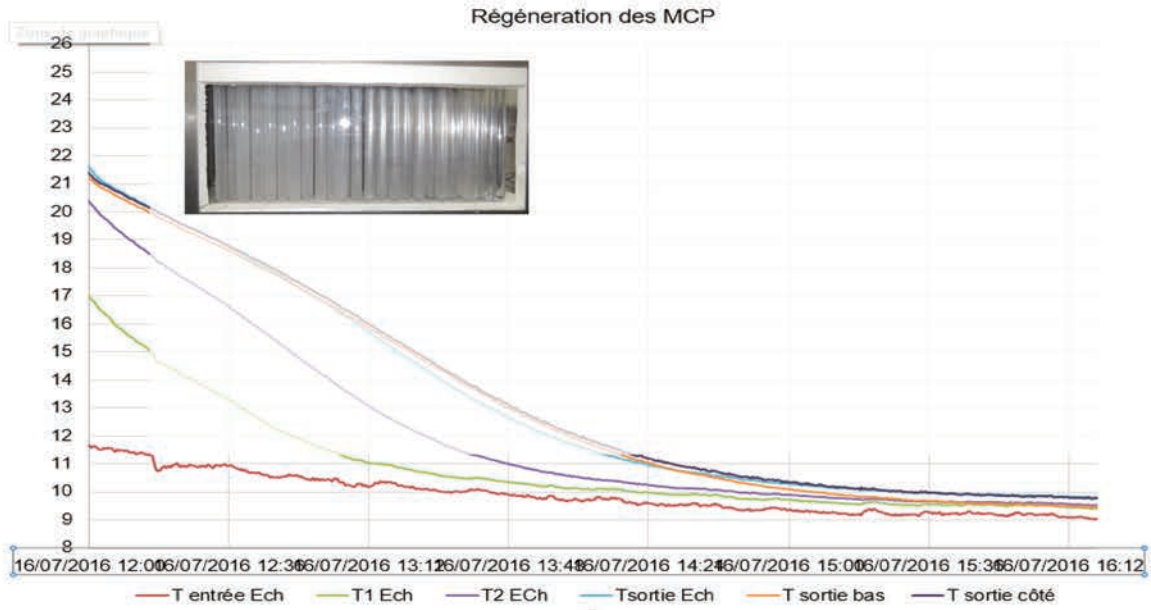


Figure D.6 – Visual tracking of the solidification during the test performed on July 16<sup>th</sup>, 2016 at I2M. After 15 minutes of the solidification cycle, the PCM have started to solidify.

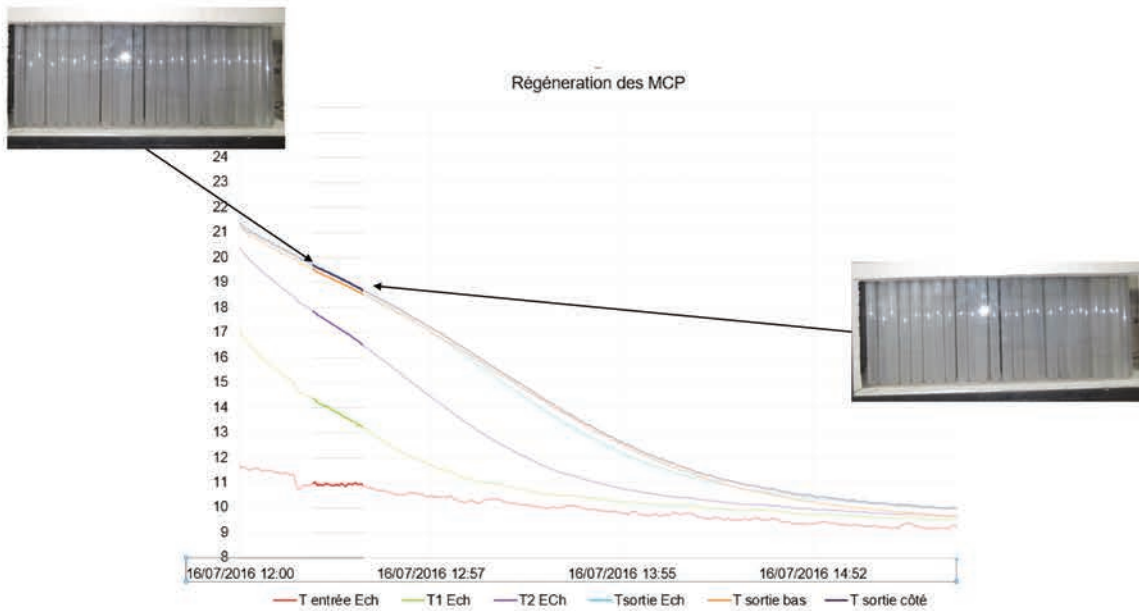


Figure D.7 – Visual tracking of the solidification during the test performed on July 16<sup>th</sup>, 2016 at I2M. We can see that an increase of the density (of solid PCM) starts at the upper part of the tubes.

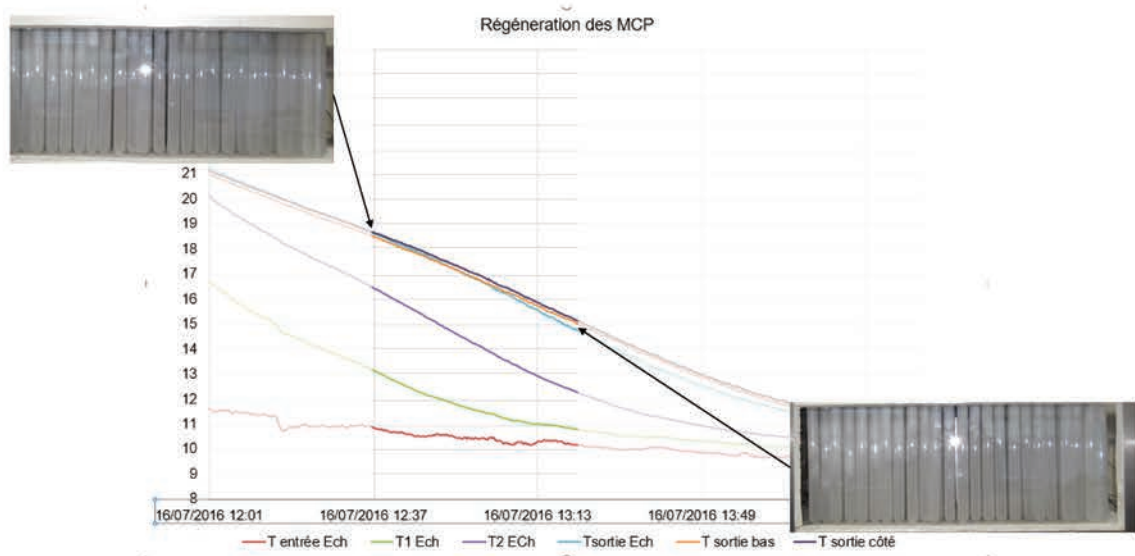


Figure D.8 – Visual tracking of the solidification during the test performed on July 16<sup>th</sup>, 2016 at I2M. We can clearly see that the solidification front moves downward in the axial direction of the tube.

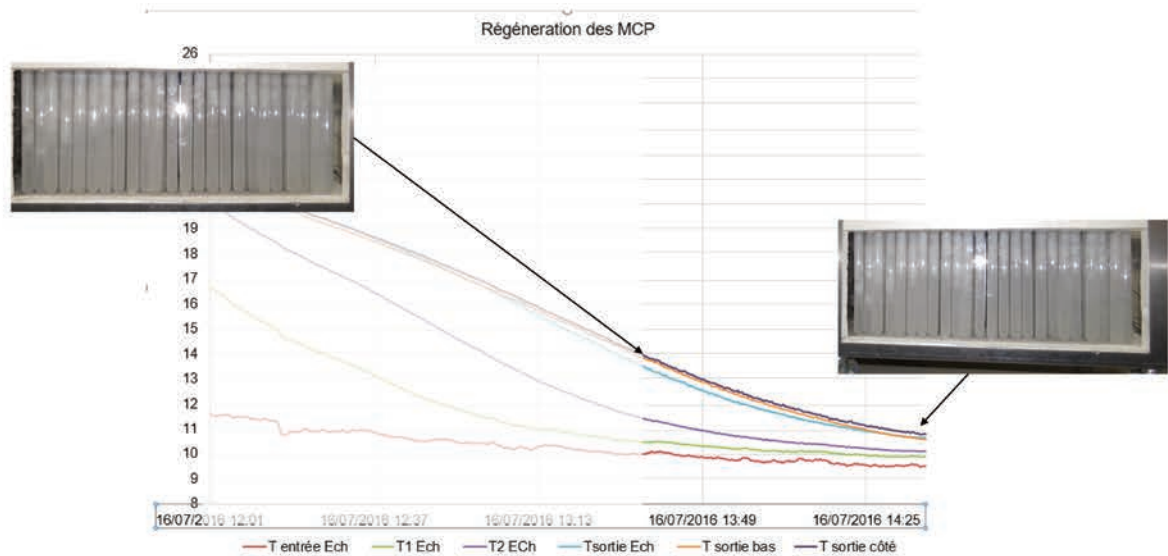


Figure D.9 – Visual tracking of the solidification during the test performed on July 16<sup>th</sup>, 2016 at I2M. In this figure, we can visualize that a complete solidification was only reached in the upper side of the tube.



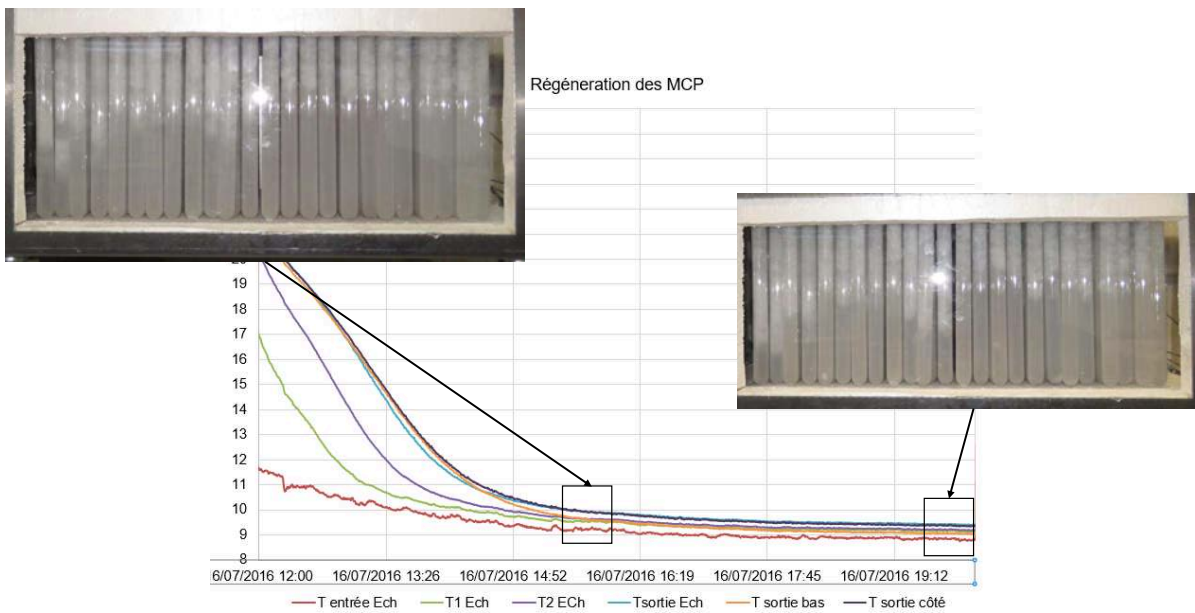


Figure D.10 – Visual tracking of the solidification during the test performed on July 16<sup>th</sup>, 2016 at I2M. After three hours of the solidification cycle, we can observe that the temperatures reached a constant value; although the PCM within tubes are not entirely solid.

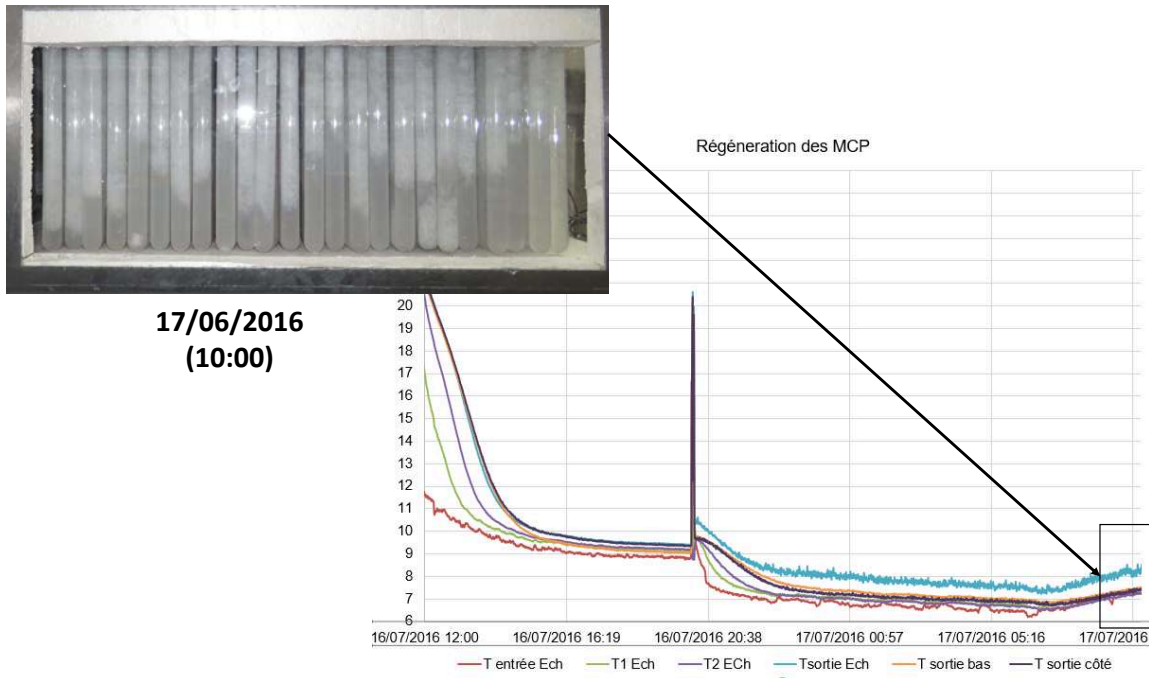


Figure D.11 – Visual tracking of the solidification during the test performed on July 16<sup>th</sup>, 2016 at I2M. We left the mobile air-conditioner over the night to see if the solidification front moves forward in the axial direction. Even though the air conditioning was left for almost 18 hours, it did not completely solidify.

### D.3.2 Melting cycle

From figures D.12 to D.16 we present the visual tracking of melting during a test carried out on July 17<sup>th</sup>, 2016 at I2M. This test comes after the regeneration of the PCM made on July 16<sup>th</sup>. We can observe that the melting front moves downward instead of in the radial direction, as was reported for single tubes of external diameters of less than 2cm by Ziskind et al. [124]. Besides, this downward pattern keeps the same direction during solidification and melting for this air-PCM unit.

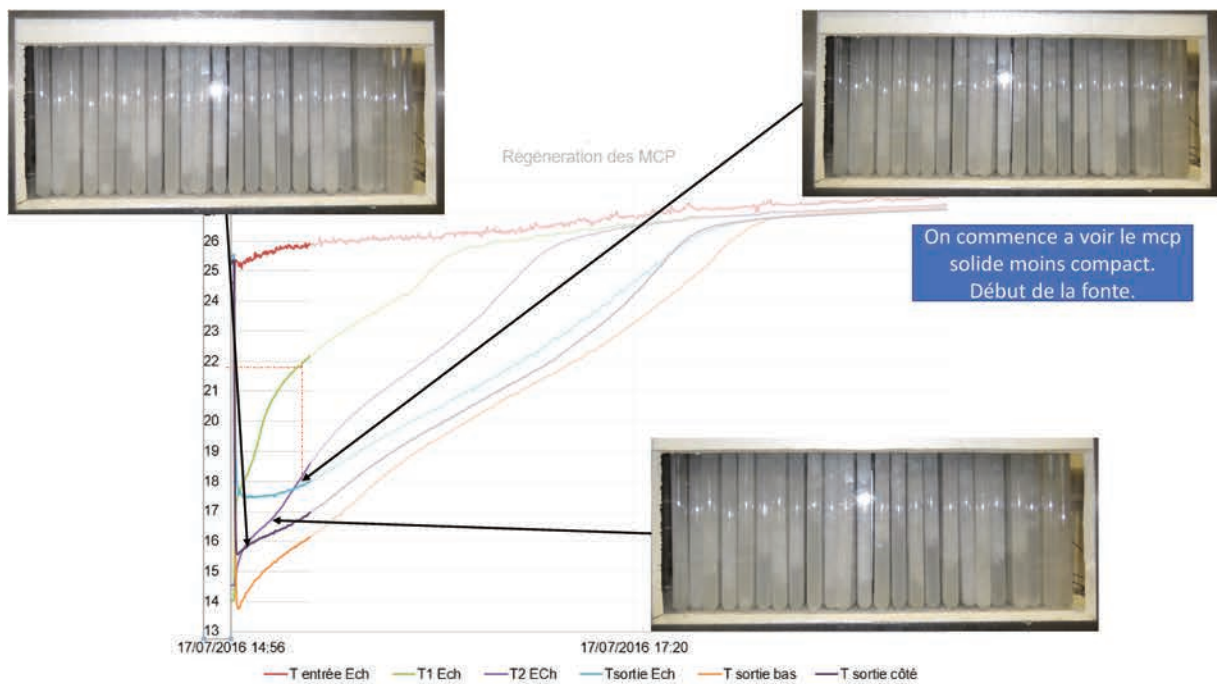


Figure D.12 – Visual tracking of the melting during the test performed on July 17<sup>th</sup>, 2016 at I2M. After 15 minutes of the solidification cycle, the PCM have started to solidify.

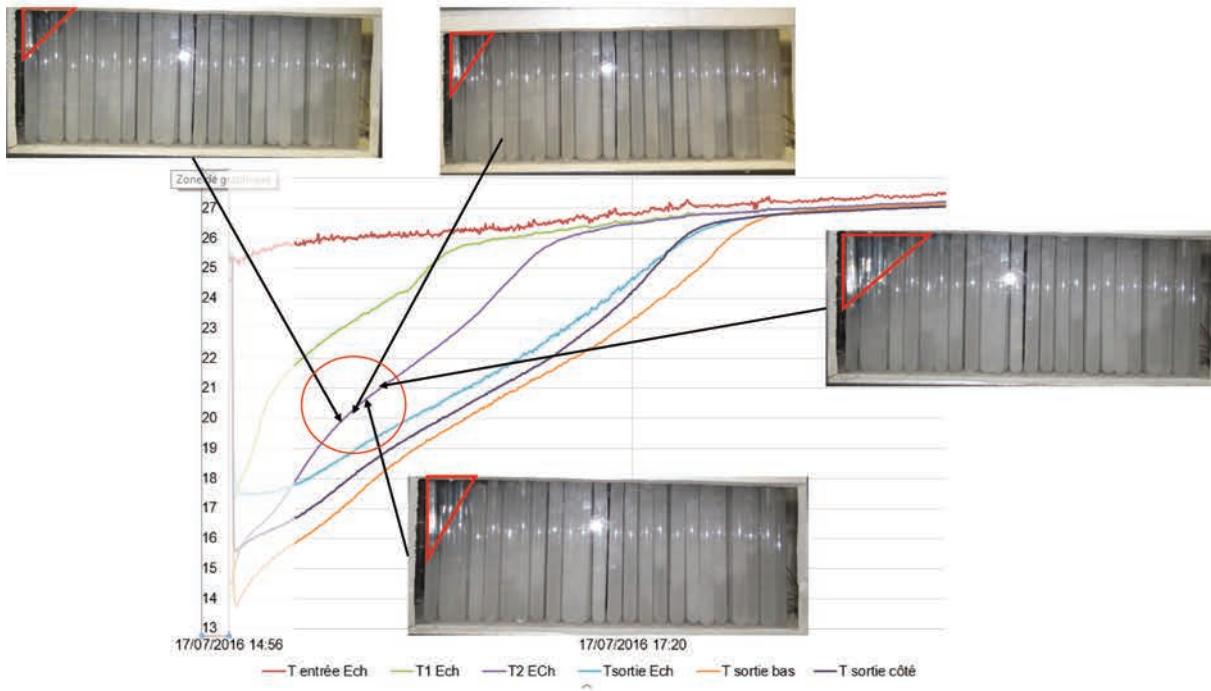


Figure D.13 – Visual tracking of the melting during the test performed on July 17<sup>th</sup>, 2016 at I2M. After 40 minutes from the beginning of the cycle, we start to observe the melting of the PCM. The melting front moves downward in the axial direction of the tube, beginning with the upper part.

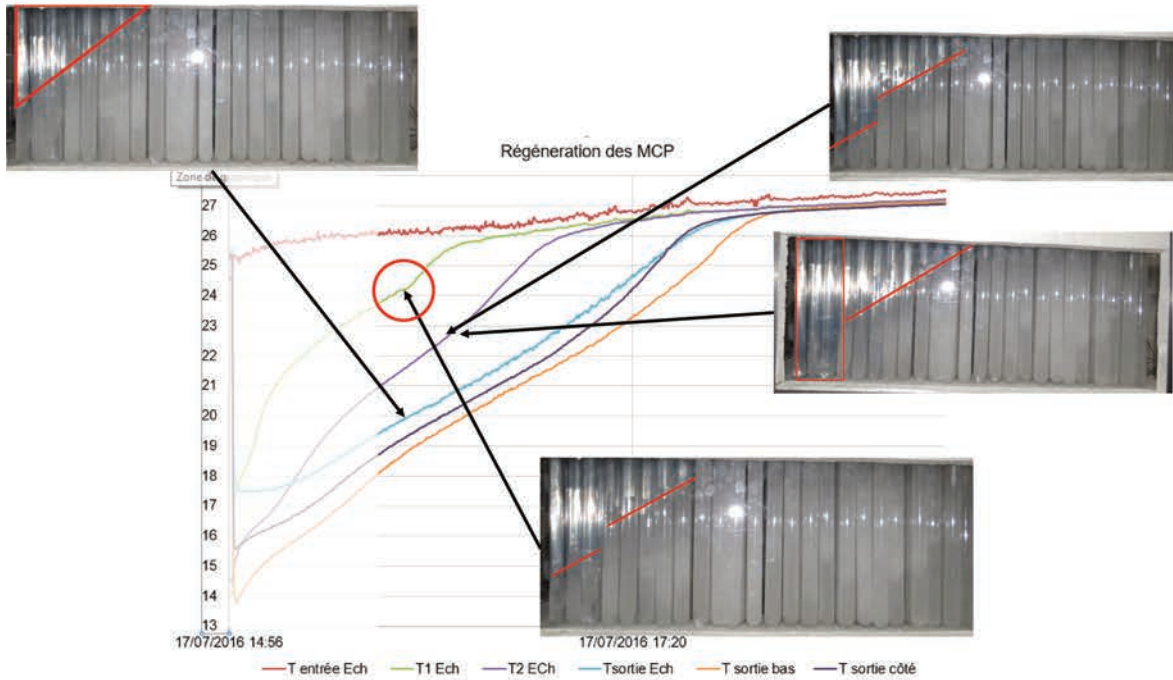


Figure D.14 – Visual tracking of the melting during the test performed on July 17<sup>th</sup>, 2016 at I2M. After an hour of the cycle, the melting front moves forward through the rows of the unit, keeping the downward movement in the axial direction of the tube, beginning with the upper part.



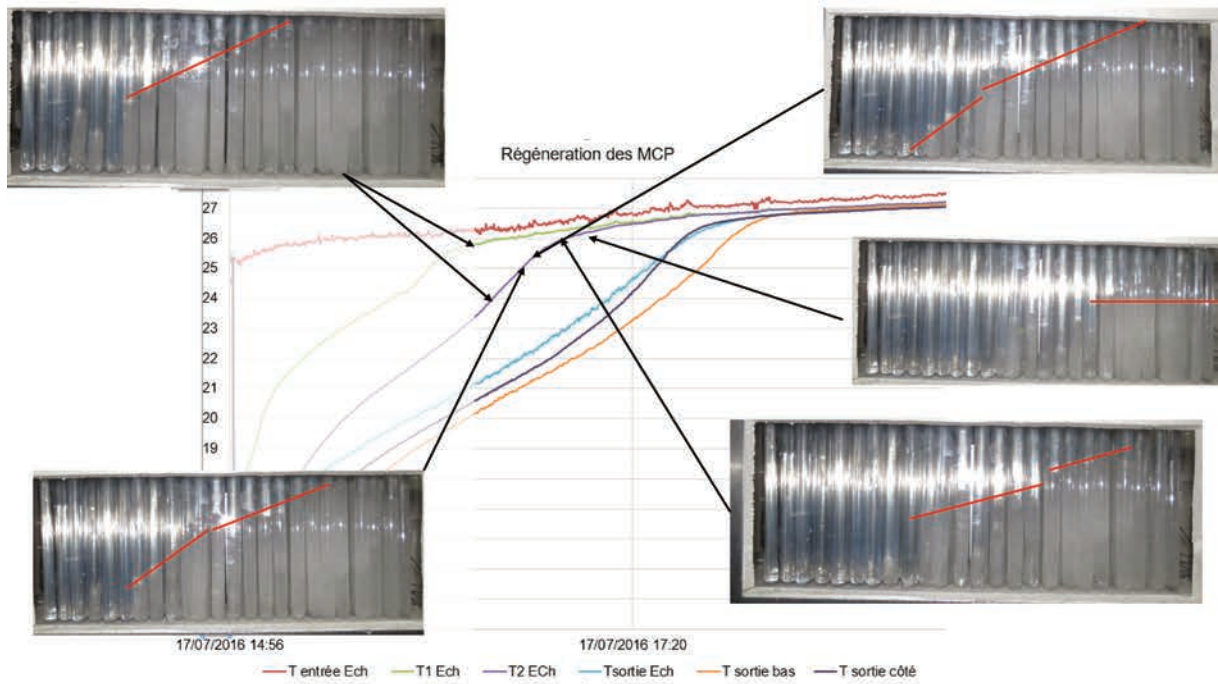


Figure D.15 – Visual tracking of the melting during the test performed on July 17<sup>th</sup>, 2016 at I2M. After an hour and a half of the cycle, the melting front have move forward through the rows of the unit, reaching the temperature measurement point located at one-third of the unit. In this figure, we can observe that at this moment the air temperature reaches the inlet conditions.

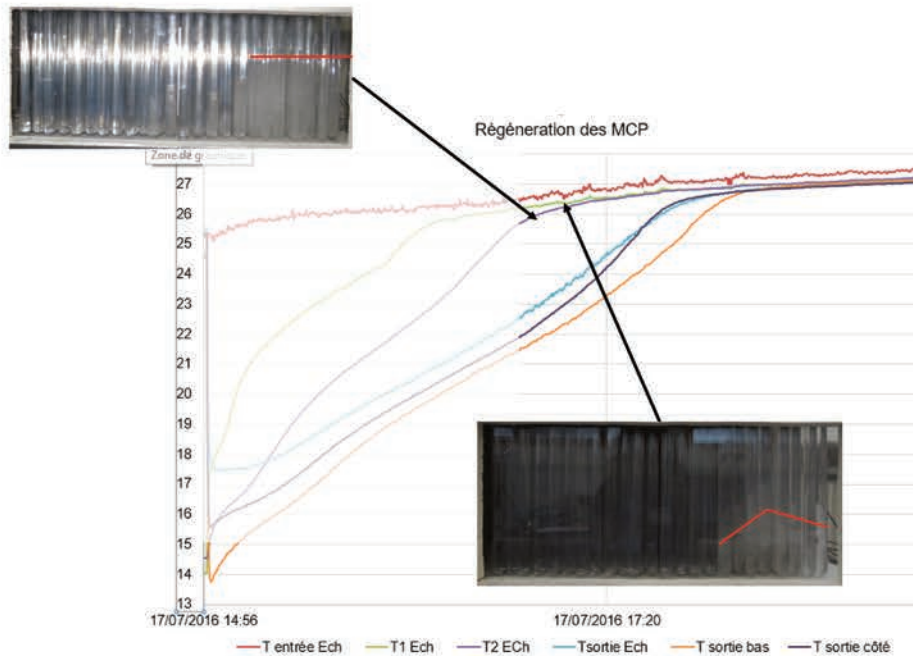


Figure D.16 – Visual tracking of the melting during the test performed on July 17<sup>th</sup>, 2016 at I2M. After two hour of the cycle, we can observe that almost all the PCM have been solidified.









# Index



# Contents

<b>Abstract</b>	<b>vii</b>
<b>Remerciements</b>	<b>xiii</b>
<b>Contents</b>	<b>xvii</b>
<b>Résumé détaillé de la thèse</b>	<b>xxiii</b>
<b>Nomenclature</b>	<b>1</b>
<b>Introduction</b>	<b>7</b>
Current Problematic: Global outlook . . . . .	7
Phase change materials for cooling and heating applications . . . . .	8
PCM systems for building applications developed by I2M of Bordeaux . . . . .	9
Box shape tube bundle: <i>Napevomo house</i> . . . . .	9
Slabs PCM system: <i>Sumbiosi house</i> . . . . .	11
Further Research . . . . .	12
Departure point for the present work . . . . .	13
Problem statement . . . . .	13
Thesis Objectives . . . . .	14
Thesis Structure and Methodology . . . . .	14
<b>1 Theoretical background and literature review</b>	<b>17</b>
1.1 Scope . . . . .	17
1.2 Phase Change Materials . . . . .	18
1.2.1 Organic materials . . . . .	18
1.2.2 Inorganic materials . . . . .	20
1.2.3 Eutectic materials . . . . .	20
1.3 Encapsulation of phase change materials . . . . .	21
1.4 Physical phenomena during phase change . . . . .	23



1.4.1	Dimensionless numbers associated with phase change . . . . .	25
1.4.2	Experimental Approaches . . . . .	26
1.4.3	Numerical Approaches . . . . .	29
1.4.4	Empirical correlations for conduction and convection during phase change	31
1.4.5	Visual tracking of the melting front . . . . .	34
1.5	Basic concepts in Image Processing . . . . .	36
1.6	Concluding Remarks . . . . .	39
<b>2</b>	<b>Air-PCM heat transfer unit definition</b>	<b>43</b>
2.1	Scope . . . . .	43
2.2	Design of an air-PCM heat exchanger unit . . . . .	44
2.2.1	Methodology for the design of an air-PCM unit . . . . .	44
2.2.2	System Overview . . . . .	45
2.2.3	Physical phenomena involved in phase change applications for cooling and heating . . . . .	46
2.2.4	General Analysis . . . . .	48
2.2.5	Functional Analysis . . . . .	49
2.2.6	Keywords search and analysis . . . . .	51
2.3	Concluding remarks and perspectives . . . . .	59
<b>3</b>	<b>Experimental Approaches</b>	<b>61</b>
3.1	Scope . . . . .	61
3.2	Experimental setup and procedures . . . . .	62
3.2.1	Design of the experiment . . . . .	62
3.2.2	Experimental setup . . . . .	64
3.2.3	Experimental Procedure . . . . .	71
3.3	Experimental results and discussion . . . . .	76
3.3.1	Melting cycle results . . . . .	77
3.3.2	Solidification cycle results: . . . . .	86
3.4	Thermal performance of the unit . . . . .	93
3.4.1	Data processing for thermal performance evaluation . . . . .	93
3.4.2	Results and Analysis of the thermal performance evaluation . . . . .	98
3.5	Physical phenomena identification . . . . .	111
3.5.1	Physical phenomena related to phase change . . . . .	111
3.5.2	Dimensionless numbers associated with an air-PCM heat exchanger . . . . .	112
3.5.3	Results from the phenomena identification by dimensionless numbers . . . . .	113
3.6	Concluding remarks . . . . .	113

---

<b>4</b>	<b>Modeling of a tube bundle type air-PCM unit</b>	<b>115</b>
4.1	Scope . . . . .	115
4.2	Experimental Correlations . . . . .	116
4.2.1	Previous analysis before obtaining the correlations . . . . .	116
4.2.2	Statistical tests to validate the multiple linear regression . . . . .	117
4.2.3	Results from the correlations for the melting fraction . . . . .	118
4.3	Thermal resistance model . . . . .	121
4.3.1	Problem statement for the model . . . . .	121
4.3.2	Resolution methodology . . . . .	121
4.3.3	Assumptions . . . . .	122
4.3.4	Mathematical formulation . . . . .	123
4.3.5	Initial and boundary conditions . . . . .	124
4.3.6	Numerical Resolution . . . . .	125
4.3.7	Validation of the model . . . . .	127
4.4	Non-isothermal phase change with natural convection model . . . . .	135
4.4.1	Main assumptions for the model . . . . .	135
4.4.2	Energy conservation in the air . . . . .	136
4.4.3	Energy conservation in the wall and PCM . . . . .	136
4.4.4	Supplementary assumptions . . . . .	136
4.5	Concluding remarks . . . . .	137
<b>5</b>	<b>Building Applications</b>	<b>139</b>
5.1	Scope . . . . .	139
5.2	Mobile air-PCM unit . . . . .	140
5.2.1	PCM containers . . . . .	141
5.2.2	Unit Structure . . . . .	142
5.2.3	Experimental setup and Procedure . . . . .	143
5.2.4	Results under controlled conditions : Office room at I2M laboratory . . . . .	146
5.2.5	Results under real conditions : Sumbiosi PEH . . . . .	150
5.3	Concluding Remarks . . . . .	155
	<b>General Conclusions</b>	<b>157</b>
	Limitation of the Research . . . . .	158
	Regarding the design . . . . .	158
	Regarding the experimental approaches . . . . .	158
	Regarding the modeling approaches . . . . .	159
	Regarding the building application . . . . .	159

Perspectives and future research . . . . .	159
Regarding the design . . . . .	159
Regarding the experimental approaches . . . . .	159
Regarding the modeling approaches . . . . .	160
Regarding the building application . . . . .	160
<b>Bibliography</b>	<b>161</b>
<b>List of Tables</b>	<b>173</b>
<b>List of Figures</b>	<b>175</b>
<b>A Calibration</b>	<b>185</b>
A.1 Temperature calibrations . . . . .	185
A.2 Velocity and airflow calibrations . . . . .	185
<b>B Modeling Results</b>	<b>189</b>
B.1 Melting correlations results . . . . .	189
B.2 1-D thermal resistance modeling results . . . . .	189
<b>C Pure conduction enthalpy method modeling</b>	<b>195</b>
C.1 Enthalpy method modeling . . . . .	195
C.1.1 Mathematical formulation . . . . .	195
C.1.2 Numerical Solution . . . . .	196
C.1.3 Conductivity value . . . . .	200
<b>D Mobile air-PCM unit</b>	<b>201</b>
D.1 Selection of the PET tubes . . . . .	201
D.1.1 Partnership for manufacturing . . . . .	202
D.1.2 Short-term reliability test . . . . .	202
D.2 Air-PCM unit Plans . . . . .	203
D.3 Visual tracking of phase change for the air-PCM unit . . . . .	205
D.3.1 Solidification cycle . . . . .	205
D.3.2 Melting cycle . . . . .	209
<b>Index</b>	<b>215</b>
<b>Contents</b>	<b>217</b>



## **Design and thermal analysis of a customizable latent heat thermal energy storage system for air-cooling in buildings**

### **Abstract**

The present work aims to design and study an air-PCM heat exchanger unit as a passive solution for thermal comfort assessment in buildings during summertime, providing tools to ease the design and building integration. The PCM present a large storage capacity per volume unit whereby, they can contribute to the reduction of the energy consumption related to cooling applications. Although, they show some drawbacks, as a low thermal conductivity in commercial PCM, so a well-thought design of these kind of systems is necessary to achieve adequate thermal performances. The first part of this thesis surveys the existing systems through a literature review, highlighting the geometry relation with the physics and thermal performance. This search provided the bases for the development of an air-PCM unit design, following a problem-solving methodology developed by the I2M laboratory. A keyword matrix was obtained from the physical phenomena and functional analysis of the unit. From this matrix, the patents analysis provided inspiration for the design resulting in a tube bundle air-PCM heat exchanger with vertical tubes aligned perpendicular to the airflow. The development of design and integration in buildings tools was sought through a modeling that can accurately predict the thermal performance of the system. Simplified models are preferred for this task. Nevertheless, they can under predict the actual performance if the physical phenomena involved is not properly accounted. Then, local and global experimental approaches were used to achieve an understanding of the physics associated with charging and discharging cycles in the unit. For this, a test bench was installed, measuring temperature and airflow under different inlet conditions, accompanied by a visual tracking through digital images. Image and data processing were used to obtain thermal performance indicators and equivalent correlations using known dimensionless numbers for convective-conductive heat transfer mechanisms in the PCM. These findings allowed the development of thermal models based on energy balances, that accounted the complexity of phenomena involved in the unit for performance prediction. Finally, the thermal performance of the system was tested in two buildings applications: as a mobile unit in a PEH house in Gradignan and at an office at I2M laboratory.

**Keywords:** phase change materials, cylindric, buildings, air-pcm heat exchangers, tube-bundle, design

---

## **Conception et analyse thermique d'un système de rafraîchissement d'air en applications de bâtiments à partir des matériaux a changement de phase**

### **Résumé**

Ces travaux de thèse visent à concevoir et étudier une unité air-MCP en tant que solution passive à la problématique du confort thermique dans les bâtiments pendant l'été, fournissant des lignes de conception et une intégration facile aux bâtiments. Les MCP présentent une grande capacité de stockage par unité de volume, ce qui leur permet de contribuer à la réduction de la consommation d'énergie liée aux applications de rafraîchissement. Bien qu'ils présentent certains inconvénients, en tant que faible conductivité thermique, notamment dans les PCM commerciaux, une conception bien détaillée est nécessaire pour atteindre des performances thermiques adéquates. La première partie de cette thèse examine les systèmes existants à travers d'une étude bibliographique, mettant en évidence la relation géométrique avec la physique et la performance thermique. Cette recherche a fourni les bases pour le développement d'une conception d'une unité air-MCP, suivant une méthodologie de résolution de problèmes développée par le laboratoire I2M. Une matrice de mots-clés a été obtenue à partir des phénomènes physiques et de l'analyse fonctionnelle de l'unité. A partir de cette matrice, l'analyse des brevets a inspiré la conception qui a abouti à un échangeur de chaleur air-PCM à faisceau tubulaire avec des tubes verticaux alignés perpendiculairement au flux d'air. Le développement d'outils de conception et d'intégration dans les bâtiments a été recherché au moyen d'une modélisation permettant de prédire avec précision les performances thermiques du système. Les modèles simplifiés sont préférés pour cette tâche. Néanmoins, ils peuvent sous-estimer les performances réelles si les phénomènes physiques impliqués ne sont pas correctement comptabilisés. Alors, des approches expérimentales locales et globales ont été utilisées pour parvenir à une compréhension de la physique associée. Pour cela, un banc d'essai a été installé, mesurant la température et le débit d'air dans différentes conditions d'entrée, accompagné d'un suivi visuel à travers des images. Les traitements d'images et des données ont été utilisés pour obtenir des indicateurs de performance thermique et des corrélations équivalentes en utilisant des nombres adimensionnels pour les mécanismes de transfert de chaleur convectifs-conducteurs dans le PCM. Ces découvertes ont permis de développer des modèles de résistance thermique qui rendent compte de la complexité des phénomènes impliqués. Enfin, la performance thermique du système a été testée dans deux applications de bâtiments : en tant qu'unité mobile dans une maison PEH à Gradignan dans un bureau du labo I2M.

**Mots clés :** matériau a changement de phase, bâtiments, stockage de chaleur, faisceau de tubes, conception

**Institut d'Ingénierie et Mécanique de Bordeaux - Département TREELE**

---

ENSAM – Esplanade des Arts et Métiers – 33405 TALENCE Cedex – France